MECHANICAL ALLOYING FOR FABRICATION OF ADVANCED ENGINEERING MATERIALS

by

M. Sherif El-Eskandarany

Al Azhar University
Cairo, Egypt

NOYES PUBLICATIONS

WILLIAM ANDREW PUBLISHING
Norwich, New York, U.S.A.

Library of Congress Catalog Card Number:
ISBN: 0-8155-1462-X
Printed in the United States

Published in the United States of America by
Noyes Publications / William Andrew Publishing
13 Eaton Avenue
Norwich, NY 13815
1-800-932-7045
www.williamandrew.com
www.knovel.com

10 9 8 7 6 5 4 3 2 1

Library of Congress Cataloging-in-Publication Data

El-Eskandarany, M. Sherif.
Mechanical alloying for fabrication of advanced engineering materials / Dr. M. Sherif El-Eskandarany.
p. cm.
Includes index.
ISBN 0-8155-1462-X (alk. paper)
1. Mechanical alloying. I. Title
TN698 .E44 2001
669'.95--dc21 2001032983

MATERIALS SCIENCE AND PROCESS TECHNOLOGY SERIES

Series Editors

Gary E. McGuire, Microelectronics Center of North Carolina
Stephen M. Rossnagel, IBM Thomas J. Watson Research Center
Rointan F. Bunshah, University of California, Los Angeles (1927–1999), founding editor

Electronic Materials and Process Technology

CHARACTERIZATION OF SEMICONDUCTOR MATERIALS, Volume 1: edited by Gary E. McGuire

CHEMICAL VAPOR DEPOSITION FOR MICROELECTRONICS: by Arthur Sherman

CHEMICAL VAPOR DEPOSITION OF TUNGSTEN AND TUNGSTEN SILICIDES: by John E. J. Schmitz

CHEMISTRY OF SUPERCONDUCTOR MATERIALS: edited by Terrell A. Vanderah

CONTACTS TO SEMICONDUCTORS: edited by Leonard J. Brillson

DIAMOND CHEMICAL VAPOR DEPOSITION: by Huimin Liu and David S. Dandy

DIAMOND FILMS AND COATINGS: edited by Robert F. Davis

DIFFUSION PHENOMENA IN THIN FILMS AND MICROELECTRONIC MATERIALS: edited by Devendra Gupta and Paul S. Ho

ELECTROCHEMISTRY OF SEMICONDUCTORS AND ELECTRONICS: edited by John McHardy and Frank Ludwig

ELECTRODEPOSITION: by Jack W. Dini

HANDBOOK OF CARBON, GRAPHITE, DIAMONDS AND FULLERENES: by Hugh O. Pierson

HANDBOOK OF CHEMICAL VAPOR DEPOSITION, Second Edition: by Hugh O. Pierson

HANDBOOK OF COMPOUND SEMICONDUCTORS: edited by Paul H. Holloway and Gary E. McGuire

HANDBOOK OF CONTAMINATION CONTROL IN MICROELECTRONICS: edited by Donald L. Tolliver

HANDBOOK OF DEPOSITION TECHNOLOGIES FOR FILMS AND COATINGS, *Second Edition:* edited by Rointan F. Bunshah

HANDBOOK OF HARD COATINGS: edited by Rointan F. Bunshah

HANDBOOK OF ION BEAM PROCESSING TECHNOLOGY: edited by Jerome J. Cuomo, Stephen M. Rossnagel, and Harold R. Kaufman

HANDBOOK OF MAGNETO-OPTICAL DATA RECORDING: edited by Terry McDaniel and Randall H. Victora

HANDBOOK OF MULTILEVEL METALLIZATION FOR INTEGRATED CIRCUITS: edited by Syd R. Wilson, Clarence J. Tracy, and John L. Freeman, Jr.

HANDBOOK OF PLASMA PROCESSING TECHNOLOGY: edited by Stephen M. Rossnagel, Jerome J. Cuomo, and William D. Westwood

HANDBOOK OF POLYMER COATINGS FOR ELECTRONICS, *Second Edition:* by James Licari and Laura A. Hughes

HANDBOOK OF REFRACTORY CARBIDES AND NITRIDES: by Hugh O. Pierson

HANDBOOK OF SEMICONDUCTOR SILICON TECHNOLOGY: edited by William C. O'Mara, Robert B. Herring, and Lee P. Hunt

HANDBOOK OF SEMICONDUCTOR WAFER CLEANING TECHNOLOGY: edited by Werner Kern

HANDBOOK OF SPUTTER DEPOSITION TECHNOLOGY: by Kiyotaka Wasa and Shigeru Hayakawa

HANDBOOK OF THIN FILM DEPOSITION PROCESSES AND TECHNIQUES: edited by Klaus K. Schuegraf

HANDBOOK OF VACUUM ARC SCIENCE AND TECHNOLOGY: edited by Raymond L. Boxman, Philip J. Martin, and David M. Sanders

HANDBOOK OF VLSI MICROLITHOGRAPHY: edited by William B. Glendinning and John N. Helbert

HIGH DENSITY PLASMA SOURCES: edited by Oleg A. Popov

HYBRID MICROCIRCUIT TECHNOLOGY HANDBOOK, *Second Edition:* by James J. Licari and Leonard R. Enlow

IONIZED-CLUSTER BEAM DEPOSITION AND EPITAXY: by Toshinori Takagi

MOLECULAR BEAM EPITAXY: edited by Robin F. C. Farrow

SEMICONDUCTOR MATERIALS AND PROCESS TECHNOLOGY HANDBOOK: edited by Gary E. McGuire

ULTRA-FINE PARTICLES: edited by Chikara Hayashi, R. Ueda and A. Tasaki

WIDE BANDGAP SEMICONDUCTORS: edited by Stephen J. Pearton

Other Related Titles

ADVANCED CERAMIC PROCESSING AND TECHNOLOGY, Volume 1: edited by Jon G. P. Binner

CEMENTED TUNGSTEN CARBIDES: by Gopal S. Upadhyaya

CERAMIC CUTTING TOOLS: edited by E. Dow Whitney

CERAMIC FILMS AND COATINGS: edited by John B. Wachtman and Richard A. Haber

CORROSION OF GLASS, CERAMICS AND CERAMIC SUPERCONDUCTORS: edited by David E. Clark and Bruce K. Zoitos

FIBER REINFORCED CERAMIC COMPOSITES: edited by K. S. Mazdiyasni

FRICTION AND WEAR TRANSITIONS OF MATERIALS: by Peter J. Blau

HANDBOOK OF ANALYTICAL TECHNIQUES IN CONCRETE SCIENCE AND TECHNOLOGY; Principles, Techniques, and Applications: edited by V. S. Ramachandran and James J. Beaudoin

HANDBOOK OF CERAMIC GRINDING AND POLISHING: edited by Ioan D. Marinescu, Hans K. Tonshoff, and Ichiro Inasaki

HANDBOOK OF HYDROTHERMAL TECHNOLOGY: edited by K. Byrappa and Masahiro Yoshimura

HANDBOOK OF INDUSTRIAL REFRACTORIES TECHNOLOGY: by Stephen C. Carniglia and Gordon L. Barna

HANDBOOK OF PHYSICAL VAPOR DEPOSITION (PVD) PROCESSING: by Donald M. Mattox

MECHANICAL ALLOYING FOR FABRICATION OF ADVANCED ENGINEERING MATERIALS: by M. Sherif El-Eskandarany

SHOCK WAVES FOR INDUSTRIAL APPLICATIONS: edited by Lawrence E. Murr

SOL-GEL TECHNOLOGY FOR THIN FILMS, FIBERS, PREFORMS, ELECTRONICS AND SPECIALTY SHAPES: edited by Lisa C. Klein

SOL-GEL SILICA: by Larry L. Hench

SPECIAL MELTING AND PROCESSING TECHNOLOGIES: edited by G. K. Bhat

SUPERCRITICAL FLUID CLEANING: edited by John McHardy and Samuel P. Sawan

NOTICE

To the best of our knowledge the information in this publication is accurate; however the Publisher does not assume any responsibility or liability for the accuracy or completeness of, or consequences arising from, such information. This book is intended for informational purposes only. Mention of trade names or commercial products does not constitute endorsement or recommendation for use by the Publisher. Final determination of the suitability of any information or product for use contemplated by any user, and the manner of that use, is the sole responsibility of the user. We recommend that anyone intending to rely on any recommendation of materials or procedures mentioned in this publication should satisfy himself as to such suitability, and that he can meet all applicable safety and health standards.

To Professor Kenji Suzuki

You have taught me how to enjoy the experiments and how to be a creative researcher. I owe a debt of gratitude that I cannot entirely repay.

Acknowledgment

The continual support and encouragement of my family is deeply and sincerely appreciated.

Contents

1 Introduction 1

1.1 BACKGROUND 1

1.2 HISTORY OF STORY OF MECHANICAL ALLOYING 2

1.3 MILLING 5

1.3.1 Factors Affecting the Mechanical Alloying 6

1.3.1.1 Types of Mills 7

1.3.1.2 Effect of Ball-to-Powder Weight Ratio 14

1.3.1.3 Effect of Milling Atmosphere 16

1.4 MECHANISM OF MECHANICAL ALLOYING 16

1.4.1 Ball-Powder-Ball Collision 16

1.5 NECESSITY OF MECHANICAL ALLOYING 19

REFERENCES 19

2 Fabrication of ODS Alloys 22

2.1 INTRODUCTION AND BACKGROUND 22

2.2 APPLICATIONS AND EXAMPLES 24

2.2.1 ODS Ni-Base Superalloys and Fe-Base High-Temperature Alloys 24

2.2.1.1 INCONEL MA 754 25

2.2.1.2 INCONEL MA 6000 25

2.2.1.3 INCOLOY MA 956 27

REFERENCES 33

3 Fabrication of Nanophase Materials 34

3.1 INTRODUCTION 34

3.2 INFLUENCE OF NANOCRYSTALLINITY ON MECHANICAL PROPERTIES: STRENGTHENING BY GRAIN SIZE REDUCTION 35

3.3 FORMATION OF NANOCRYSTALLINE MATERIALS BY BALL MILLING TECHNIQUE 36

3.3.1 Mechanism(s) 37

3.3.2 Selected Examples 38

3.4 CONSOLIDATION OF THE NANOCRYSTALLINE MILLED POWDERS 41

REFERENCES 43

4 Fabrication of Nanocomposite Materials 45

4.1 INTRODUCTION AND BACKGROUND 45

4.2 FABRICATION OF SiC_p/Al COMPOSITES BY MECHANICAL SOLID STATE MIXING 47

4.3 PROPERTIES OF MECHANICALLY SOLID-STATE FABRICATED SiC_p/Al COMPOSITES 48

4.3.1 X-Ray Analysis 48

4.3.2 Morphology and Metallography 49

4.3.3 TEM Observations 52

4.3.4 Consolidation 53

4.3.5 Properties 56

4.4 MECHANISM OF FABRICATION 58

4.4.1 Formation of Agglomerates Coarse Composite SiC_p/Al Powder Particles 58

4.4.2 Disintegration of the Agglomerates Composite SiC_p/Al Powder Particles 59

4.4.3 Formation of Nanocomposite SiC_p/Al Powder Particles 59

4.4.4 Consolidation of Nanocomposite SiC_p/Al Powder Particles 59

REFERENCES 60

5 Mechanically Induced Solid State Carbonization 62

5.1 INTRODUCTION 62

5.2 DIFFICULTIES OF PREPARATIONS 64

5.3 FABRICATION OF NANOCRYSTALLINE TiC BY MECHANICAL ALLOYING METHOD 65
5.4 PROPERTIES OF MECHANICALLY SOLID-STATE REACTED TiC POWDERS 68
5.4.1 Structural Changes with the Milling Time 68
5.4.2 Morphology 76
5.4.3 Consolidation 78
5.4.4 Mechanism of Fabrication 83
5.5 OTHER CARBIDES PRODUCED BY MECHANICAL ALLOYING 86
5.5.1 Fabrication of β-SiC Powders 86
5.5.2 Fabrication of Nanocrystalline WC Powders 88
5.5.3 Fabrication of Nanocrystalline ZrC Powders 89
REFERENCES 93

6 Mechanically Induced Gas-Solid Reaction 94
6.1 INTRODUCTION 95
6.2 FABRICATION OF NANOCRYSTALLINE TiN BY REACTIVE BALL MILLING 95
6.3 PROPERTIES OF REACTED BALL MILLED TiN POWDERS 96
6.3.1 Structural Changes with the Milling Time 96
6.3.2 Morphology 98
6.4 MECHANISM OF FABRICATION 108
6.4.1 RBM Technique for Preparing TiN Powders 108
6.5 OTHER NITRIDES PRODUCED BY RBM 109
6.6 FABRICATION OF NANOCRYSTALLINE SOLID SOLUTION NiTiH BY REACTIVE BALL MILLING 113
REFERENCES 117

7 Mechanically Induced Solid-State Reduction 118
7.1 INTRODUCTION 119
7.2 REDUCTION OF Cu_2O WITH Ti BY ROOM TEMPERATURE ROD MILLING 119
7.3 PROPERTIES OF ROD MILLED POWDERS 120
7.3.1 Structural Changes with the Milling Time 120
7.3.2 Metallography 125
7.3.3 DTA Measurements 126
7.4 MECHANISM OF MSSR 126

7.5 FABRICATION OF NANOCRYSTALLINE WC AND NANOCOMPOSITE WC-MgO REFRACTORY MATERIALS BY MSSR METHOD 129
7.5.1 Properties of Ball-Milled Powders 131
7.5.1.1 Structural Changes with the Milling Time 131
7.5.1.2 Temperature Change with the Milling Time 136
7.5.1.3 Hardness, Toughness, and Elastic Moduli of Consolidated WC and WC/MgO 139
REFERENCES 141

8 Mechanically Induced Solid-State Amorphization 142

8.1 INTRODUCTION 143
8.2 FABRICATION OF AMORPHOUS ALLOYS BY MECHANICAL ALLOYING PROCESS 144
8.3 CRYSTAL-TO-GLASS TRANSITION 146
8.3.1 The Metastable Phase Diagram 149
8.4 MECHANISM OF AMORPHIZATION BY MECHANICAL ALLOYING PROCESS 150
8.4.1 Structural Changes with the Milling Time 152
8.4.1.1 X-Ray Analysis 152
8.4.1.2 TEM Observations 154
8.4.2 Morphology and Metallography Changes with the Milling Time 157
8.4.3 Thermal Stability 161
8.4.3.1 Amorphization Process 161
8.4.3.2 Crystallization Process 169
8.4.3.3 Mechanism 172
8.5 THE GLASS-FORMING RANGE 175
8.6 AMORPHIZATION VIA MECHANICAL ALLOYING WHEN ΔH^{for} = ZERO; MECHANICAL SOLID-STATE AMORPHIZATION OF $Fe_{50}W_{50}$ BINARY SYSTEM 183
8.6.1 Structural Changes with the Milling Time 183
8.6.2 Magnetic Studies 186
8.6.3 Thermal Stability 187
8.6.4 Mechanism 190
8.6.4.1 The Stage of Composite FeW Powder Particles Formation 190
8.6.4.2 The Stage of Formation of FeW Solid Solution 191
8.6.4.3 The Stage of Amorphous FeW Formation 191
8.7 SPECIAL SYSTEMS AND APPLICATIONS 192

8.7.1 Amorphous Austenitic Stainless Steel 192
8.7.2 Fabrication Amorphous $Fe_{52}Nb_{48}$ Special Steel 194
8.7.3 Fe-Zr-B System 196

8.8 DIFFERENCE BETWEEN MECHANICAL ALLOYING AND MECHANICAL DISORDERING IN THE AMORPHIZATION REACTION OF $Al_{50}Ta_{50}$ IN A ROD MILL 198
8.8.1 Background 198
8.8.2 Procedure 199
8.8.3 Structural Changes with Milling Time 199
8.8.4 Morphological Changes with Milling Time 202
8.8.5 Thermal Stability 205
8.8.6 Mechanism of Formation of Amorphous $Al_{50}Ta_{50}$ via MD Method 208

8.9 MECHANICALLY-INDUCED CYCLIC CRYSTALLINE-AMORPHOUS TRANSFORMATIONS DURING MECHANICAL ALLOYING 209
8.9.1 Co-Ti Binary System 209
8.9.1.1 Structural Changes with the Milling Time 210
8.9.1.2 Thermal Stability 216
8.9.2 Al-Zr Binary System 217
8.9.2.1 Structural Changes with the Milling Time 218
8.9.2.2 Thermal Stability 221
8.9.3 Mechanism of Amorphous-Crystalline-Amorphous Cyclic Phase Transformations During Ball Milling 223

REFERENCES 225

Index 232

1

Introduction

Mechanical alloying is a unique process for fabrication of several alloys and advanced materials at room temperature.

1.1 BACKGROUND

Fundamentally, the term *milling* may be referred to as the breaking down of relatively coarse materials to the ultimate fineness. Apart from the milling of ores, milling is also used for preparing materials for some industrial applications, such as milling of quartz to fine powder (under 70 μm in diameter), milling of talc to produce body powder, milling of iron ore for preparation of pellets, and many others. Over the past three decades, ball milling has evolved from being a standard technique in mineral dressing and

powder metallurgy, used primarily for particle size reduction, to its present status as an important method for the preparation of either materials with enhanced physical and mechanical properties or, indeed, new phases, or new engineering materials. Accordingly, the term *mechanical alloying* (MA)[1] is becoming increasingly common in the materials science and metallurgy literatures.[2]

So far, the MA process, using ball-milling[3] and/or rod-milling techniques,[4] has received much attention as a powerful tool for fabrication of several advanced materials (Fig. 1.1), including equilibrium, nonequilibrium (e.g., amorphous, quasicrystals, nanocrystalline, etc.), and composite materials.[5]–[7] In addition, it has been employed for reducing some metallic oxides by milling the oxide powders with metallic reducing agents at room temperature.[8]–[10] In fact, MA is a unique process in that a solid state reaction takes place between the fresh powder surfaces of the reactant materials at room temperature. Consequently, it can be used to produce alloys and compounds that are difficult or impossible to be obtained by conventional melting and casting techniques.[11]

1.2 HISTORY OF STORY OF MECHANICAL ALLOYING

The MA process was developed in 1966 at The International Nickel Company (INCO) as part of a program to produce a material combining oxide dispersion strengthening with gamma prime precipitation hardening in a nickel-based superalloy intended for gas turbine applications. In fact, the original MA process was the by-product of research into different subjects. In the early 1960s, INCO had developed a process for manufacturing graphite aluminum alloys by injection of nickel-coated graphite particles into a molten bath by argon sparging. A modification of the same technique was tried to inoculate nickel-based alloys with dispersion of nickel-coated, fine refractory particles. The reason for nickel coating was to render the normally unwetted oxide particles wettable by a nickel-chromium alloy. Early experiments used metal-coated zirconium oxide purchased from an outside vendor. The examinations of these materials revealed no differences between the inoculated materials and uninoculated alloys. Examinations of the inoculants revealed that they were zirconia-coated nickel rather than nickel-coated zirconia. Attention was directed to ball milling as a means of coating oxide particles with nickel. Ball milling had been used for the coating of tungsten carbide with cobalt for well over 70 years.[12] Small amounts of nickel-coated thoria and zirconia were successfully produced in a small high-speed shaker

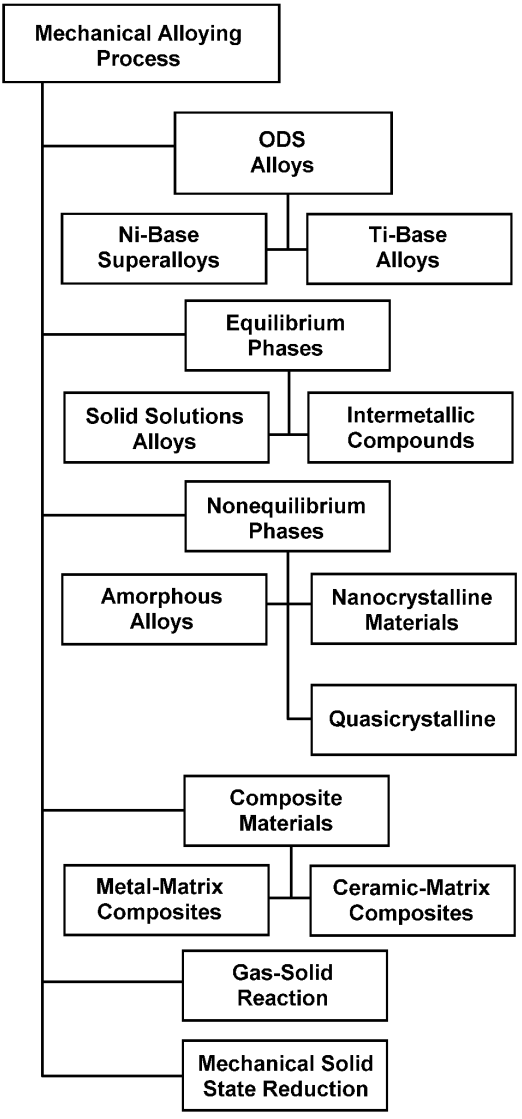

Figure 1.1. Mechanical alloying is a pioneer process for fabrication of a wide variety of alloys and compounds at room temperature. Fabrication of high thermal stable amorphous alloys, nanocrystalline and nanocomposite materials at room temperature are some advantages of this process.

mill. This process, in particular, was used to coat oxides with metals that could not be applied by chemical process due to their reactivity. Since the apparatus employed, a small high-energy ball mill, could produce only 1 cm^3 of powder per single milling run, these powders were used only for studies of the rate of rejection of oxide powders from molten alloys. Compacts of composite powders were partially melted in an arc melter, sectioned, and examined metallographically.

In mid-1966, attention was turned to the ball-milling process that had been used to make metal powders for wetting studies as a means of making the alloy itself by powder metallurgy. The reason was attributed to the capability of this process to coat hard phases (e.g., WC or ZrO_2) with a soft phase (Co or Ni).[13]

In 1970, Benjamin[1] introduced a pioneering development on ball-milling technique for producing complex oxide dispersion-strengthened (ODS) alloys that were used for high temperature structural applications, such as jet engine parts. This unique method could be successfully used for preparing fine, uniform dispersions of oxide particles (Al_2O_3, Y_2O_3, ThO_2) in nickel-base superalloys. It is worth noting that these materials cannot be obtained by the conventional powder metallurgy method.

During the 1970s, research programs concerned the nature and mechanism of the MA process itself and the design of special equipment for carrying out the process. At that time, MA was well known as a process for the fabrication of several ODS alloys.[14]–[22]

Apart from the fabrication of ODS alloys by the ball-milling technique, for their subsequent beneficiation, White[23] observed the formation of an amorphous phase by ball milling elemental Nb and Sn powders at room temperature. In 1983, Koch et al.[24] reported the first novel technique for formation of $Ni_{60}Nb_{40}$ amorphous alloy by high-energy ball milling of elemental Ni and Nb powders. Since then, the MA method has been successfully employed for the formation of a large number of amorphous alloys. This technique leads to the formation of several alloys that can not be prepared by liquid metallurgy, such as Al-Ta[25] and Al-Nb[26] binary systems.

An attractive application of the ball-milling technique has been demonstrated by El-Eskandarany et al., for preparing nitrides (e.g., Fe_4N,[27] AlTaN,[28] TiN,[29] and NbN[30]) by milling the elemental powder under nitrogen gas flow. This method, which is called reactive ball milling, has been employed for preparing several metal nitrides and hydrides.[31]

Within the last five years, the ball-milling technique has been proposed for formation of nanocrystalline materials at room tempera-

ture.[32]–[35] The end-product of the milled powder was consolidated into fully-dense nanocrystalline compacts which have unusual unique physical and mechanical properties.[36]

In 1998, El-Eskandarany[37] prepared homogeneous nanocomposite Al/SiC_p materials by milling the elemental powders of Al and β-SiC in a high-energy ball mill. It should be noted that this composite material is difficult to obtain by the conventional liquid metallurgy method due to the poor wettability between molten Al (or Al alloys) and the reinforcement material of SiC. In addition, the liquid metallurgy method usually leads to an undesirable reaction between SiC and molten Al, producing brittle phases of Al_4C_3 and Si.

More recently, ceramic/ceramic nanocomposite WC-14 % (at.) MgO material that combines two interesting properties of high hardness and fracture toughness values[38] has been fabricated by the ball-milling technique.[39]

1.3 MILLING

As mentioned above, the objectives of milling are particle size reduction (breaking down the minerals until every particle is either fully mineral or fully gangue), mixing and blending, and particle shaping. In this book we focus only on the application of milling (ball milling and rod milling) for fabrication of engineering materials via MA process. Benjamin[12] has defined the MA process as a method for producing composite metal powders with a controlled fine microstructure. It occurs by the repeated fracturing and rewelding of a mixture of powder particles in a highly energetic ball mill. As originally carried out, the process requires at least one fairly ductile metal to act as a host or binder.[17] Other components can consist of other ductile metals, brittle metals, and intermetallic compounds or nonmetals and refractory compounds.

The major process in MA for producing quality powders of alloys and compounds with well-controlled microstructure and morphology, is the repeated welding, fracture, and rewelding of the reactant mixed powders. Several types of mills have been employed for such purpose. The MA process can be successfully performed in both high-energy mills (attritor-type ball mill, planetary-type ball mill, centrifugal-type ball mill, and vibratory-type ball mill), and low-energy tumbling mills (e.g., ball and rod mills).

1.3.1 Factors Affecting the Mechanical Alloying

The MA process is affected by several factors that are playing very important roles in the fabrication of homogeneous materials.[40] It is well known that the properties of the milled powders of the final product, such as the particle size distribution, the degree of disorder, or amorphization, and the final stoichiometry, depend on the milling conditions and, as such, the more complete the control and monitoring of the milling conditions, the better end-product is obtained.[2][40][41] These factors can be listed as follows:

- Type of mills (e.g., high-energy mills and low-energy mills)
- The materials of milling tool (e.g., ceramics, stainless steel, and tungsten carbide)
- Types of milling media (e.g., balls or rods)
- Milling atmosphere (e.g., air, nitrogen, and an inert gas)
- Milling environment (e.g., dry milling or wet milling)
- Milling media-to-powder weight ratio
- Milling temperature
- Milling time

A summary of these chief factors that control the mechanical alloying process is schematically presented in Fig. 1.2.

1.3.1.1 Types of Mills

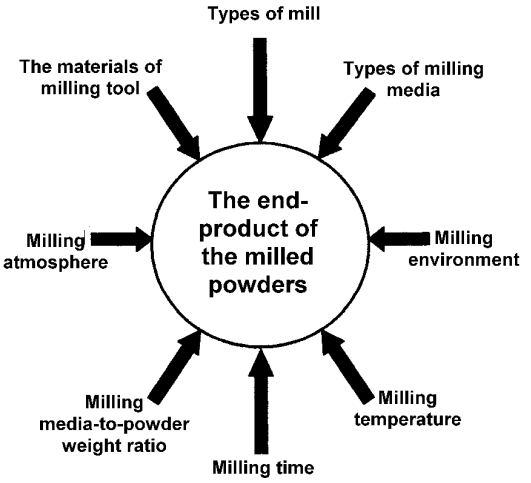

Figure 1.2. Schematic presentation of the main factors that affect the MA process.

High-Energy Ball Mills. ***Attritor or Attrition Ball Mill.*** Szigvari introduced this type of mill to the industry in 1922 in order to quickly attain fine sulfur dispersion for use in the vulcanization of rubber.[22] The illustration of this mill, also known as Szigvari attritor grinding mill, is shown in Fig. 1.3. In this mill, the milling procedure takes place by the stirring action of an agitator which has a vertical rotating central shaft with horizontal arms (impellers). The capacity (volume) of the attritor used for the MA process ranges between 3.8×10^{-3} m^3 to 3.8×10^{-3} m^3. The rotation speed of the central shaft is about 250 rpm (4.2 Hz).

Kimura and his coworker[42] at the National Defense Academy of Japan developed an attritor ball mill with a higher rotation speed of about 500

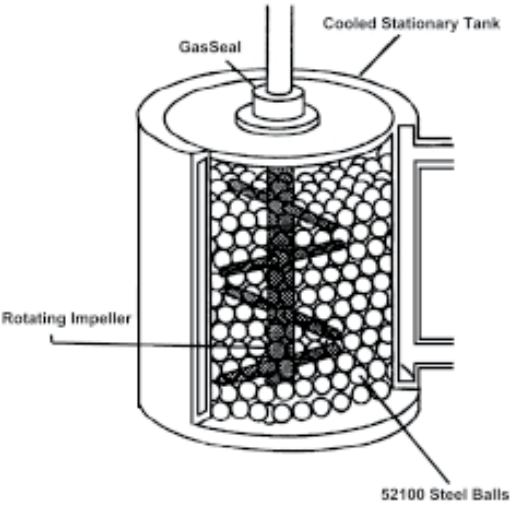

Figure 1.3. In the Szigvari attritor ball mill, the ball charge is activated by impellers radiating from a rotating vertical shaft which rotates at speeds up to 250 rpm. *(After Gilman et al.)*[22]

rpm. In addition, they equipped the mill with several devices to control and measure the applied torque during the MA process. They could minimize the oxygen contamination content during the MA experiments by continuous evacuation (using rotary and diffusion pumps) of the vial and introducing a continuous flow of an argon gas. In addition, the milling temperature could

be controlled by flushing the outermost shell of the vial with current water. They have proposed this milling tool for the synthesizing of several amorphous alloy powders.

Planetary Ball Mill. The Planetary Ball Mill is one of the most popular mills used in MA research for synthesizing almost all of the materials presented in Fig. 1.1. In this type of mill, the milling media have considerably high energy, because milling stock and balls come off the inner wall of the vial (milling bowl) and the effective centrifugal force reaches up to twenty times gravitational acceleration.

The centrifugal forces caused by the rotation of the supporting disc and autonomous turning of the vial act on the milling charge (balls and powders). Since the turning directions of the supporting disc and the vial are opposite, the centrifugal forces alternately are synchronized and opposite. Therefore, the milling media and the charged powders alternatively roll on the inner wall of the vial, and are lifted and thrown off across the bowl at high speed (360 rpm), as schematically presented in Fig. 1.4.

One advantage of this type of mill is the ease of handling the vials (45 ml to 500 ml in volume) inside the glove box (Fig. 1.5).

Vibratory Ball Mill. The vibratory ball mill is another kind of high-energy ball mill that is used mainly for preparing amorphous alloys. The vials capacities in the vibratory mills are smaller (about 10 ml in volume)

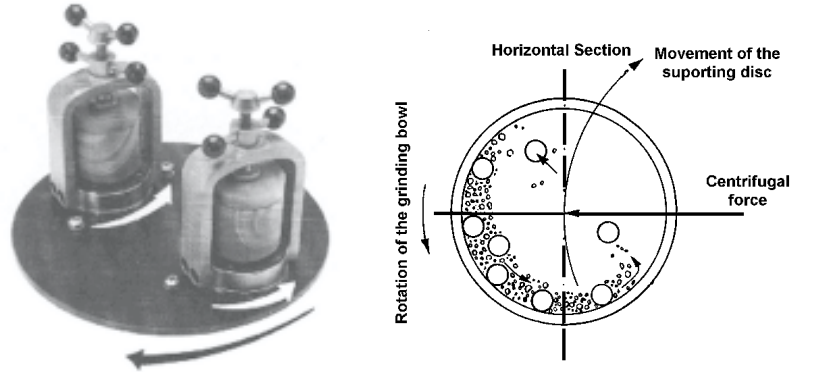

Figure 1.4. Schematic drawing of a high-energy planetary ball mill. The w_d and w_v are the angular velocities of the disc and the vials, respectively.

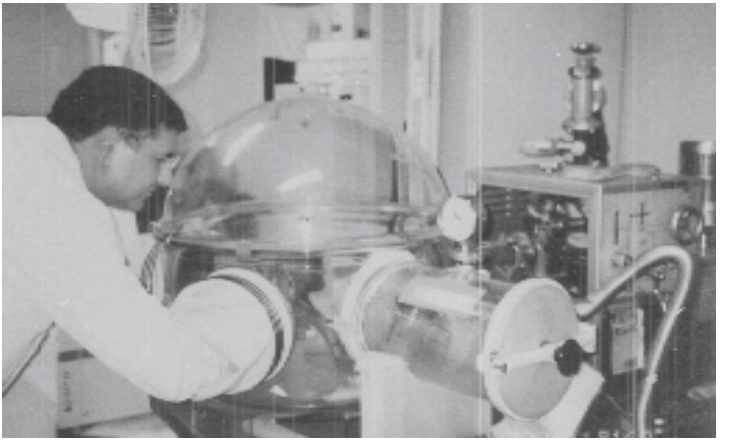

Figure 1.5. The milling tools (the vials and milling media), and the elemental powders of the starting materials for the MA experiments must be handled inside a glove box filled with an inert gas before starting the milling procedure. *(The photo was taken for the author at his laboratory, Faculty of Engineering, Al Azhar University, Cairo, Egypt.)*

compared to the previous types of mills. In this mill, the charge of the powder and milling tools are agitated in three perpendicular directions (Fig. 1.6) at very high speed, as high as 1200 rpm.

Another type of the vibratory ball mill, which is used at the van der Waals-Zeeman Laboratory, consists of a stainless steel vial with a hardened steel bottom, and a single hardened steel ball of 6 cm in diameter (Fig.1.7).

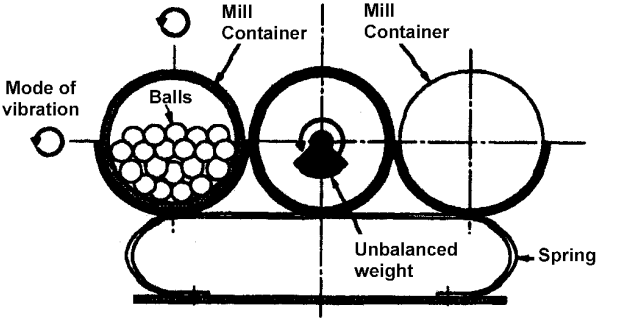

Figure 1.6. Schematic drawing of a high-energy vibratory ball mill. *(After Hashimoto et al.)*[43]

The mill is evacuated during milling to a pressure of 10^{-6} Torr, in order to avoid reactions with a gas atmosphere.[44] Subsequently, this mill is suitable for mechanical alloying of some special systems that are highly reactive with the surrounding atmosphere, such as rare earth elements.

Low-Energy Tumbling Mill. Tumbling mills are defined as cylindrically-shaped shells, which rotate about a horizontal axis. Loads of balls or rods are charged into the mill to act as milling media. The powder particles

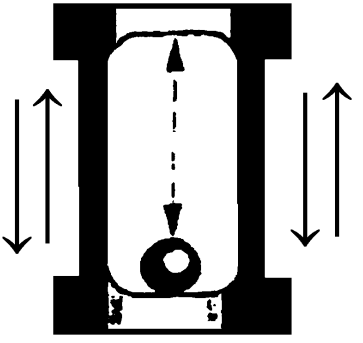

Figure 1.7. Schematic illustration of the vibratory ball mill, which is used at the van der Waals-Zeeman Laboratory.

of the reactant materials meet the abrasive and/or impacting force which reduce the particle size and enhance the solid state reaction between the elemental powders.

Tumbler Ball Mill. The tumbler ball mills date back to 1876[45] and are characterized by the use of balls (made of iron, steel, or tungsten carbide) as milling media. The capacities of these mills are governed by several variables (ratio of mill length to diameter, speed of mill, size of balls, particle size, etc.) that should be adjusted and balanced.

In these mills, the useful kinetic energy can be applied to the powder particles of the reactant materials[46] (Fig. 1.8) by

- Collision between the balls and the powders
- Pressure loading of powders pinned between milling media or between the milling media and the liner

- Impact of the falling milling media
- Shear and abrasion caused by dragging of particles between moving milling media
- Shock wave transmitted through crop load by falling milling media

The tumbler ball mills have been successfully used for preparing several kinds of mechanically alloyed powders. (See, for example, Ref. 41.) However, this kind of low-energy mill may lead to an increase in the required milling time for a complete MA process, it produces homogeneous and

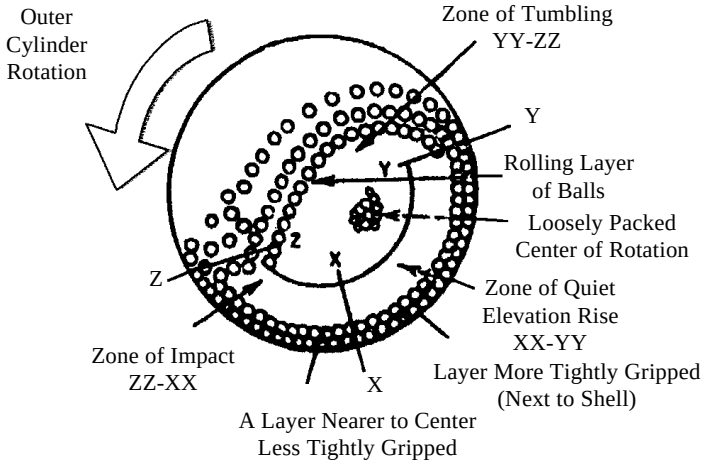

Figure 1.8. Schematic cross-section of tumbler ball mill showing ball movement.[46]

uniform powders.[47] In addition, it is cheaper than those of the high-energy mills and can be self-made with lower costs. Moreover, tumbling mills are operated simply with low maintenance requirements.

Tumbler Rod Mill. Our current knowledge of the materials which are fabricated by MA has shown that almost all ball-milled alloy powders are contaminated with iron, when stainless steel balls and vial are used; this is a natural consequence of the collision between milling media. Therefore, MA method is faced with a serious problem which has impeded progress. Since the ball-powder-ball collision in a tumbling, planetary, or vibrating mill can

be the main source of iron contamination, different kinds of mills, in which there is no collision between the milling media should be used.

In 1990, El-Eskandarany et al.[4] employed a laboratory scale rod mill for preparing a large amount (30 g) of homogeneous amorphous $Al_{30}Ta_{70}$ powder. In their experiments, they made a stainless steel (SUS 304) cylindrical shell and used 10 stainless steel (SUS 304) rods as milling media. In order to prevent jamming of the rods inside the shell, the shell has been designed so that its length (250 mm) is greater than its diameter (120 mm) and the rods have been cut to lengths (200 mm) less than the full length of the shell. The movement of the rods inside the shell was directly observed through a thick and transparent plastic plate sealing the window of the shell. This observation has shown that the milling occurs by the line contact of rod-powder-rod extending over the full length of the shell. The results have shown that a single phase of amorphous Al_xTM_{100-x} (TM; Ti, Zr, Hf, Nb, and Ta) powders with low iron contamination content can be formed via rod-milling technique.[48]–[50] They reported that rod-milling technique leads to the formation of high-thermal stable, homogeneous and low iron-contaminated amorphous alloys.

Figure 1.9 shows the concentration content of iron concentration in mechanically alloyed $Al_{30}Ta_{70}$ as a function of (*a*) rod-milling and (*b*) ball-milling times, as well as the effect of repeating the MA process. At the beginning of the first milling run, the milling media were used in the absence of mechanically alloyed powder coatings. After this run, the milling media which had been coated by the powders were used again in the second and the third milling runs. A drastic decrease in iron content from the first to the third milling runs was observed. It also shows that the amount of iron contamination in the rod-milled powders is lower than in the ball-milled powders.

In the ball-milling (BM) process the starting elemental powders usually agglomerate at the early stage of milling to form powder particles of greater diameters, as large as several hundred microns, and this is followed by continuous disintegration until the particle size is less than a few microns. As shown in Fig. 1.10, the rod milling (RM) leads to a similar behavior for the variation in powder diameters. In RM, however, the average diameter of the agglomerate powders is very small and the subsequent disintegration into fine powders proceeds at a high rate to provide a narrow size distribution.

1.3.1.2 Effect of Ball-to-Powder Weight Ratio

The effect of the ball-to-powder weight ratio (W_b:W_p) on the amorphization reaction of $Al_{50}Ta_{50}$ alloy powders in a low-energy ball mill,

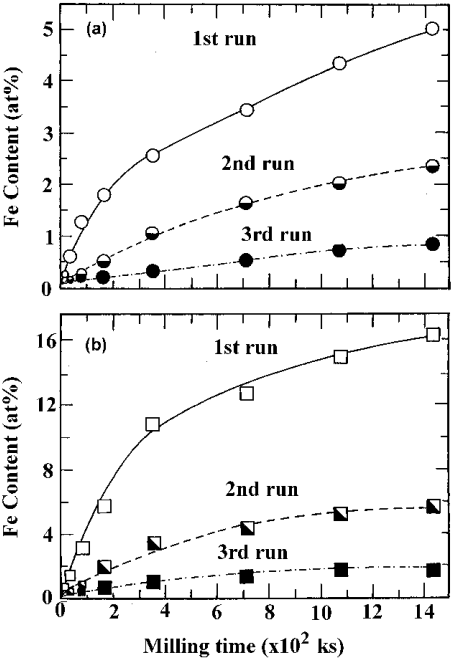

Figure 1.9. Iron contamination content in mechanically alloyed $Al_{30}Ta_{70}$ powders as a function of milling repetition of milling process, *(a)* rod-milling time and *(b)* ball-milling time. *(After El-Eskandarany et al.)*[4]

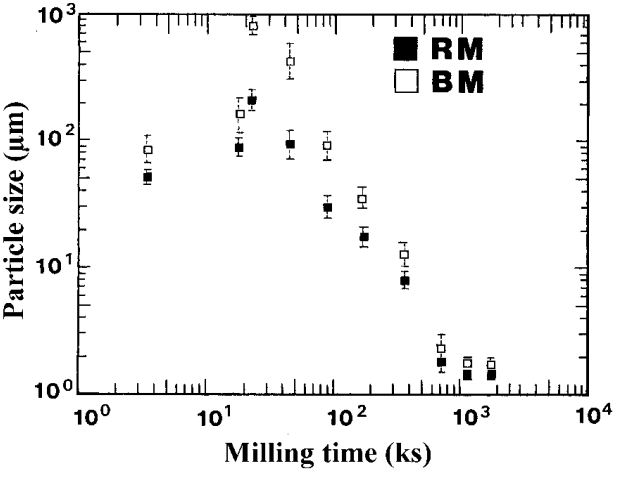

Figure 1.10. Particle size distribution of mechanically alloyed $Al_{30}Ta_{70}$ as a function of rod-milling (RM) and ball-milling (BM) times. *(After El-Eskandarany et al.)*[4]

was studied in 1991 by El-Eskandarany et al.[51] They have used 90 g, 30 g, 20 g, 10 g, and 3 g of powders to obtain W_b:W_p ratios of 12:1, 36:1, 54:1, 108:1, and 324:1, respectively. (See Fig. 1.11.)

The x-ray diffraction patterns (XRD) of mechanically alloyed $Al_{50}Ta_{50}$ powders as ball milled for 1440 ks (400 h) as a function of the W_b:W_p ratio. Single phase of amorphous alloys are obtained when ratios 36:1 and 108:1 were used. The Bragg peaks of elemental Al and Ta crystals still appear when the W_b:W_p ratio is 12:1, indicating that the amorphization

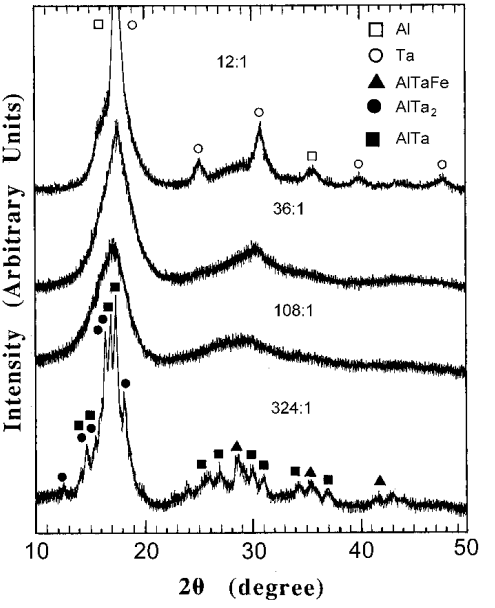

Figure 1.11. The x-ray diffraction patterns (XRD) of $Al_{50}Ta_{50}$ alloy powders as ball milled for 1440 ks (400 h) as a function of the ball-to-powder weight ratio, W_b:W_p. *(After El-Eskandarany et al.)*[51]

reaction is not completed. In contrast, when the W_b:W_p ratio is 324:1, the amorphous phase coexists with the crystalline phases of AlTa, $AlTa_2$, and AlTaFe.

Based on their results,[51] it is concluded that the rate of amorphization depends strongly on the kinetic energy of the ball mill charge and this depends on the number of opportunities for the powder particles to be reacted and interdiffused. Increasing the W_b:W_p ratio accelerates the rate of amorphization, which is explained by the increase in the kinetic energy of the

ball mill charge per unit mass of powders. It has been shown in this study that the volume fraction of the amorphous phase in the mechanically alloyed ball milled powders increases during the early stage of milling, 86–173 ks (48 h) with increasing W_b:W_p ratio. It is noted that further increasing this weight ratio leads to the formation of crystalline phases and this might be related to the high kinetic energy of the ball mill charge which is transformed into heat. When the W_b:W_p ratio was reduced to 12:1, however, the amorphization reaction was not completed. This indicates that the kinetic energy of the mill charge is insufficient for complete transition from the crystalline to the amorphous phase.

It is worth noting that powder particles reached the minimum of extreme fineness when using a high W_b:W_p ratio. One disadvantage of using such a high weight ratio is being the high concentration of iron contamination which is introduced to the milled powders during the MA process, as presented in Fig. 1.12.

1.3.1.3 Effect of Milling Atmosphere

The atmosphere of the mill is considered as one of the most important factors during ball and/or rod milling of the elemental powders. It has been shown[27] that very fine powders have relatively large surface areas and, thus,

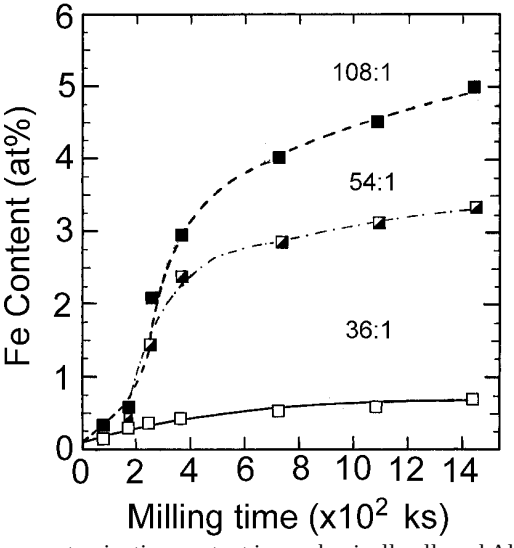

Figure 1.12. Iron contamination content in mechanically alloyed $Al_{50}Ta_{50}$ powders as a function of the ball-milling time and ball-to-powder weight ratio, W_b:W_p.*(After El-Eskandarany et al.)*[51]

are highly reactive not just with oxygen, but also with other gases, such as hydrogen or nitrogen.[2] This so-called reactive ball milling[29] will be discussed in another chapter of this book.

It has been suggested by Yavari et al.[52] that the amorphization reaction which takes place in a ball mill between immiscible A-B binary couples with $\Delta H_{mix}<0$ is attributed to the presence of some oxygen (~5 at. %) and the ternary mixtures are found to be miscible with $\Delta H_{mix}<0$.

1.4 MECHANISM OF MECHANICAL ALLOYING

As previously mentioned, the main process which takes place in a mill during the MA method to produce quality powders with controlled microstructure is the repeated welding, fracturing, and rewelding of a mixture of powders of the diffusion couples. It is critical to establish a *balance* between fracturing and cold welding in order to mechanically alloy successfully. Two techniques are proposed by Gilman and Benjamin[22] to reduce cold welding and promote fracturing. The first technique is to modify the surface of the deforming particles by addition of a suitable processing control agent (PCA) (wet milling) that impedes the clean metal-to-metal contact necessary for cold welding. The second technique is to modify the deformation mode of the powder particles so that they fracture before they are able to deform to the large compressive strains necessary for flattening and cold welding. Cooling the mill chamber is an approach to accelerate the fracture and establishment of steady-state processing (effect of milling temperature).[23]

We should emphasize that milling the powders of certain metals which cold-weld easily (e.g., Ti, Zr, Al, Pb, Zn, Ag, etc.) with an organic agent (PCA),[53] may lead to a undesired reaction between the PCA and the milled powders, specifically those pure metals of the 4*f* and 5*f* elements.

1.4.1 Ball-Powder-Ball Collision

The starting material powders that are mechanically alloyed can be two (or more) metallic powders, powders of intermetallic compound(s) or dispersoid powders. The MA process starts by blending the two (or more) individual powder constituents in order to obtain the final or so-called end-product after certain hours of milling (dry or wet). The morphology of the powders is modified when they are subjected to ball collisions (Fig. 1.13). It

is worth noting that the effects of collisions on the milled powders depend on the type of the constituent particles.

It has been shown that the initial ball-powder-ball collision causes the ductile metal powders to flatten and work harder when they are cold welded and heavily mechanically deformed. Therefore, they flatten, overlap, and atomically clean metal interfaces. They are brought into intimate contact,

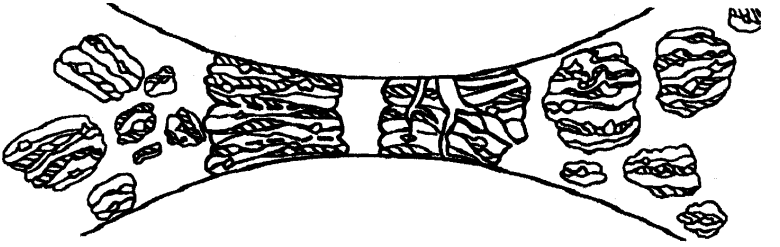

Figure 1.13. Ball-powder-ball collision of powder mixture during mechanical alloying. *(After Gilman et al.)*[22]

forming layered structure of composite particles consisting of various combinations of the starting ingredients, as schematically shown in Fig. 1.13. Further milling results in cold welding and deformation of the layered particles and a refined microstructure is obtained. Due to the initially low hardness of the starting elemental powders, the lamellar spacing of the agglomerated particles are quickly reduced upon further milling. Increasing the MA time increases the hardness and this leads to fracturing of the agglomerated powders into smaller particles. Further milling time leads to an interdiffusion reaction that takes place at the clean or fresh surfaces of the intimate layers in the powder particles, to form an alloy.

1.5 NECESSITY OF MECHANICAL ALLOYING

Mechanical alloying is a unique process for the formation of several alloys and compounds that are difficult or impossible to be produced by the

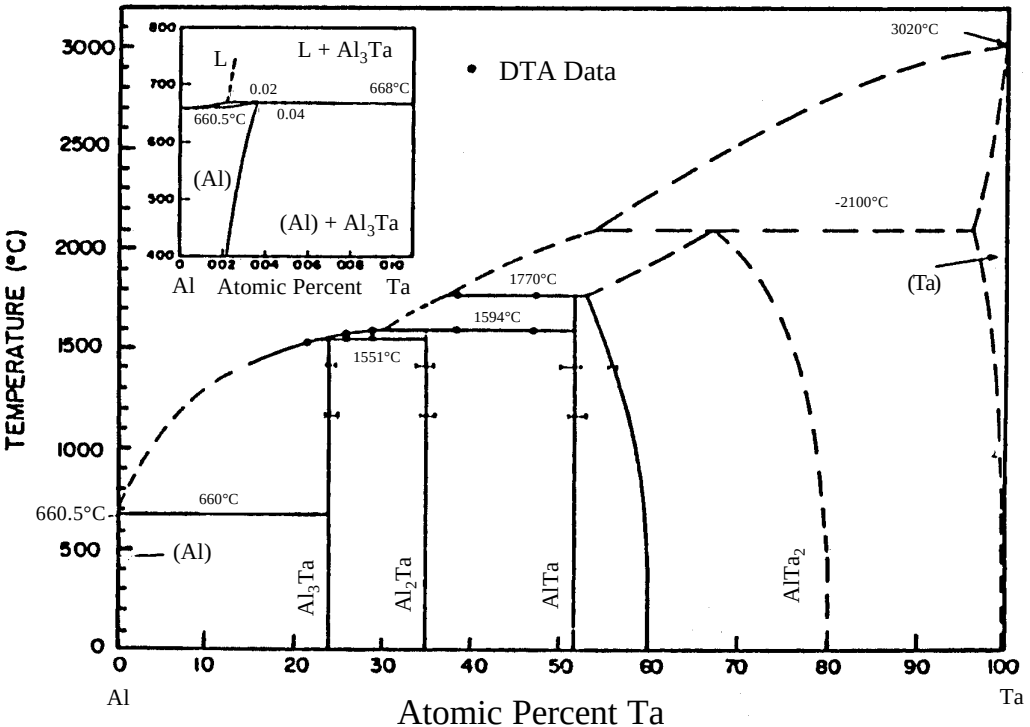

Figure 1.14. Phase relation of Al-Ta binary system. *(After Subramanian et al.)*[54]

conventional melting and casting technique. For example, Al-Ta binary system (Fig. 1.14) shows a remarkable gap difference between the melting points of Al (933 K) and Ta (3293 K). This gap difference restricts the production of such promising advanced materials that are used as capacitors in industrial applications. The MA method leads to the fabrication of such new amorphous material with a wide range of formation.

MA has also been used as a promising method for the fabrication of many nanocrystalline and nanocomposite materials (Chs. 3 and 4), especially the refractory materials of metal carbides (Ch. 5) and metal nitrides (Ch. 6), using very simple techniques. More recently, the MA method has been used for reducing several metal oxides (Ch. 7) at room temperature. Furthermore, it can also be used for the fabrication of many amorphous materials (Ch. 8) at room temperature.

REFERENCES

1. Benjamin, J. S., *Metall. Trans.*,1**:**2943 (1970)
2. Campbell, S. J., and Kaczmarek, W. A., *Mössbauer Spectroscopy Applied to Materials and Magnetism,* (G. J. Long and F. Grandjean, eds.) Plenum Press, New York, 2:273
3. Benjamin, J. S., *Scientific American*, 234**:**48 (1976)
4. El-Eskandarany, M. S., Aoki, K., and Suzuki, K., *J. Less-Common Met.*, 167:113 (1990)
5. El-Eskandarany, M. S., Aoki, K., and Suzuki, K., *J. Jpn Society of Powder and Powder Metallurgy*, 38:59 (1991)
6. Eckert, J., Schultz, L., and Urban, K., *Appl. Phys. Lett*., 55:117 (1989)
7. El-Eskandarany, M. S., *J. Alloys Comp*., 279:263 (1998)
8. Schaffer, G. B., and McCormick, P. G., *Metall. Trans. A*, 21**:**2789 (1990)
9. Matteazzi, P., and Le Caër, G., *Mater. Sci. Eng. A*, 149:135 (1991)
10. El-Eskandarany, M. S., *Materials Transactions, JIM*, 36:182 (1995)
11. El-Eskandarany, M. S., Itoh, F., Aoki, K., and Suzuki, K., *J. Non-Cryst. Solids*, 118:729 (1990)
12. Benjamin, J. S., *Sci. Forum*, 88–90:1 (1992)
13. Zbiral, J., Jangg, and Korb, G., *Sci. Forum*, 88–90:19 (1992)
14. Wright, L. G., and Wilcox, B. A., *Metall. Trans.*, 5:957 (1974)
15. Benjamin, J. S., and Volin, T. E., *Metall. Trans.*, 5:1929 (1974)
16. Gessinger, G. H., *Metall. Trans. A*, 7:1203 (1976)

17. Benjamin, J. S., and Bomford, M. J., *Metall. Trans. A*, 8:1301 (1977)
18. Gilman, G., and Nix, W. D., *Metall. Trans. A*, 12:813 (1981)
19. Benjamin, J. S., and Schelleng, R. D., *Metall. Trans. A*, 12:1827 (1981)
20. Benn, R. C., Benjamin, J. S., and Austin, C. M., *High Temperature Alloys: Theory and Design*, Warrendale, PA, TMS-AIME (1984)
21. Kang, S. K., and Benn, R. C., *Metall. Trans. A*, 18:747 (1987)
22. Gilman, P. S., and Benjamin, J. S., *Ann. Rev. Mater. Sci*., 13:279 (1983)
23. White, R. L., *The Use of Mechanical Alloying in the Manufacture of Multifilamentary Superconductor Wire*, Ph.D. Thesis, Stanford University (1979)
24. Koch, C. C., Cavin, O. B., McKamey, C. G., and Scarbourgh, J. O., *Appl. Phys. Lett.*, 43:1017 (1983)
25. El-Eskandarany, M. S., Aoki, K., and Suzuki, K., *J. Alloys Comp.*, 186:15 (1992)
26. El-Eskandarany, M. S., Aoki, K., and Suzuki, K., *Scripta Metall.*, 25:1695 (1991)
27. El-Eskandarany, M. S., Sumiyama, K., Aoki, K., and Suzuki, K., *Mater. Sci. Forum*, 88–90:801 (1992)
28. El-Eskandarany, M. S., Aoki, K., and Suzuki, K., *Appl. Phys. Lett.*, 60:1562 (1992)
29. El-Eskandarany, M. S., Sumiyama, K., Aoki, K., and Suzuki, K., *J. Mat. Res.*, 7:888 (1992)
30. El-Eskandarany, M. S., Sumiyama, K., Aoki, K., Masumoto, T., and Suzuki, K., *J. Mat. Res.*, 9:2891 (1994)
31. El-Eskandarany, M. S., and Ahmed, H. A., Sumiyama, K., and Suzuki, K., *J. Alloys Comp.*, 218:36 (1995)
32. Eckert, J., Holzer, J. C., Krill, C. E. III, and Johnson, W. L., *Mater. Sci. Forum*, 88–90:505 (1992)
33. Abe, Y. R., and Johnson, W. L., *Mater. Sci. Forum*, 88–90:513 (1992)
34. Kuyama, J., Ishihara, K. N., and Shingu, P. H., *Mater. Sci. Forum*, 88–90:521 (1992)
35. Morris, M. A., and Morris, D. G., *Mater. Sci. Forum*, 88–90:529 (1992)
36. El-Eskandarany, M. S., Omori, M., Konno, T. J., Sumiyama, K., Hirai, T., and Suzuki, K., *Metall. Trans. A*, 29:1973 (1998)
37. El-Eskandarany, M. S., *J. Alloys Comp.*, 279:263 (1998)
38. El-Eskandarany, M. S., *J. oAlloys Comp.*, 296:175 (2000)
39. El-Eskandarany, M. S., Omori, M., Konno, T. J., Sumiyama, K., Hirai, T. and Suzuki, K., *Metall. Trans. A*, (2000) (in press)

40. Campbell, S. J., and Kaczmarek, W. A., *Mössbauer Spectroscopy Applied to Materials and Magnetism*, (G. J. Long and F. Grandjean, eds.) Plenum Press, New York, 2:273
41. El-Eskandarany, M. S., *Solid State Amorphization of Ta-Based Alloy Powders by Mechanical Alloying*, Ph.D. Thesis, Tohoku University (1992)
42. Kimura, H., Kimura, M., and Ban, T., *Proceeding of the 2nd International Conference on Rapidly Solidified Materials*, San Diego, CA, published by ASM International, p. 172 (Mar. 7–8, 1988)
43. Hashimoto, H., and Watanabe, R., *Mater. Sci. Forum*, 88–90:89 (1992)
44. Bakker, H., Zhou, G. F., and Yang, T., *Prog. Mat. Sci*., 39:159 (1995)
45. Processing Handbook, American Institute of Mining, Metallurgical and Petroleum Engineers, Inc., (1985)
46. Taggart, A. F., *Handbook of Mineral Dressing: Ores and Industrial Minerals*, John Wiley & Sons Inc., New York (1927)
47. El-Eskandarany, M. S., *J. Alloys Comp.*, 284:295 (1999)
48. El-Eskandarany, M. S., Aoki, K., and Suzuki, K., *J. Appl. Phys.*, 72:2665 (1992)
49. El-Eskandarany, M. S., Aoki, K., and Suzuki, K., *Metall. Trans. A*, 23:2131 (1992)
50. El-Eskandarany, M. S., Aoki, K., and Suzuki, K., *J. Non-Cryst. Solids*, 150:472 (1992)
51. El-Eskandarany, M. S., Aoki, K., Itoh, H., and Suzuki, K., *J. Less-Common Met.*, 169:235 (1991)
52. Yavari, A. R., and Desré, P. J., *Mater. Sci. Forum*, 88–90:43 (1992)
53. Rairden, J. R., and Habesch, E. M., *Thin Solid Films*, 83:353 (1981)
54. Subramanian, P. R., Miracle, D. B., and Mazdiyasni, S., *Metall. Trans. A*, 21:539 (1991)

2

Fabrication of ODS Alloys

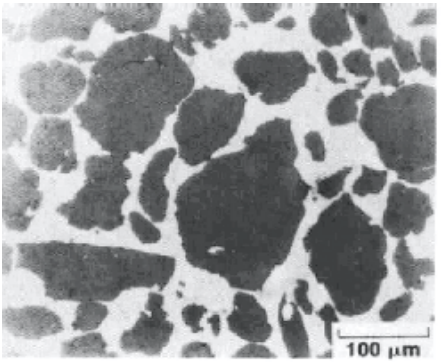

Two of the most important alloy systems to emerge from the mechanical alloying process are based on iron and nickel. The solid-state alloying process for these materials is designed to introduce fine dispersions of yttrium oxide particles. The mixture of metal powders and fine refractory oxide powders are milled together, extruded, and further deformed to achieve the required shape. The figure shows a micrograph of a well processed ODS superalloy powder. *(After Benjamin, J. S.,* Metall. Trans.*, 1:2943, 1970.)*

2.1 INTRODUCTION AND BACKGROUND

As pointed out in Ch. 1, the original mechanical alloying (MA)[1] process was the by-product of research into a different subject. This process was developed in 1966 at INCO's Paul D. Merica Research Laboratory as part of a program to produce an alloy combining the benefits of oxide

dispersion strengthening (ODS) with gamma prime precipitation hardening in a nickel-based superalloy intended for gas turbine applications.[2]

In the early 1960s, INCO had developed a process for manufacturing graphite aluminum alloys by injecting nickel-coated graphite particles into a molten bath by argon sparging. A modification of the same technique was tried to inoculate nickel-based alloys with a dispersion of nickel-coated, fine refractory oxide particles. The purpose of nickel coating was to render the normally unwetted oxide particles wettable by a nickel-chromium-based alloy.

Early experiments used metal-coated zirconium oxide purchased from outside vendors. Chemical analysis, metallographic analysis, and mechanical property measurements, however, revealed no differences between the inoculated materials and uninoculated alloys. Examination of the inoculants revealed that they were zirconia-coated nickel rather than nickel-coated zirconia.

A number of different processes were studied for production of the coated fine oxides required for this injection process. These processes included co-reduction of mixed oxides of nickel and thorium and ball milling of various oxides with nickel in order to form a coating of the ductile metal on the oxide, much as was done over 70 years ago[3] in the production of tungsten carbide-cobalt composite materials. The ball-milling process, in particular, was used to coat oxides with metals that could not be applied by chemical processes due to their reactivity. For example, zirconium oxide was coated with aluminum in one such experiment. Since the apparatus employed a small high-energy vibratory mill, and could produce only 1 cm^3 of powder per run, these powders were used only for studies of the rate of rejection of oxide powders from molten alloys. Compacts of the composite powders were partially melted in an arc melter, sectioned, and examined metallographically.

In 1966, attention was turned to the ball-milling process that had been used to make metal powders for wetting studies as a means of making the alloy itself by powder metallurgy. This choice is attributed to the fact that the ball-milling process could be employed to coat hard phases, such as tungsten carbide or zirconium oxide with soft phases such as cobalt or nickel. It was also considered that:

- Both welding and fracturing occur during ball milling of metallic powders.
- High-energy ball mills can greatly increase the rate of the grinding and fracture processes.

- Virtually any composition could be manufactured using a mixture of elemental and readily available powders instead of having to rely on atomized pre-alloy powders, which are relatively expensive.
- The thermodynamic activity of reactive gamma prime forming elements, such as aluminum and titanium**,** could be reduced in orders of magnitude by combining them with less reactive metals, such as nickel, in intermetallic compounds.

These key ideas led to the concept of establishing a kneading action which would refine the internal structure of powders while maintaining their overall particle size at a relatively coarse level, preventing pyrophoricity.[2]

2.2 APPLICATIONS AND EXAMPLES

2.2.1 ODS Ni-Base Superalloys and Fe-Base High-Temperature Alloys

The major commercial dispersion-strengthened Ni-base superalloys produced to date by mechanical alloying process are INCONEL alloys MA 754, MA 758, and MA 6000. The composition of these alloys is presented in Table 2.1.

Table 2.1. Composition of Ni-base ODS Superalloys Produced by Mechanical Alloying Process (in wt.%)[4]

Alloy	**Ni**	**Cr**	**Co**	**W**	**Mo**	**Ta**	**Al**	**Ti**	**Y_2O_3**
MA 754	Bal.	20	-	-	-	-	0.3	0.5	0.6
MA 758	Bal.	30	-	-	-	-	0.3	0.5	0.6
MA 6000	Bal.	15	-	4	2	2	4.5	2.5	1.1

2.2.1.1 INCONEL MA 754

In 1980, Weber[5] prepared a large amount of mechanically alloyed ODS superalloy (INCONEL MA 754). It is essentially a Ni-20% Cr alloy strengthened by about 1 vol % Y_2O_3. The Ni, Cr, and Y_2O_3 powders were milled until a homogeneous Ni-20% Cr alloy was formed in which the Y_2O_3 particles were uniformly distributed. The fabricated alloy powder was then consolidated by hot extrusion which was followed by hot rolling. A recrystallization step, often directional, followed consolidation that resulted in elongated, high-aspect-ratio grains that were very stable owing to the inert oxide pinning. After the directional crystallization, the grains had typical dimensions of ~ 500 to 700 μm parallel to the working direction and ~ 15 μm perpendicular to this direction. The typical BFI of the fabricated MA 754 is displayed in Fig. 2.1, which shows the oxide distribution in the metallic matrix. Benjamin et al.[6] have suggested that fine particles are a uniform dispersion of stable yttrium aluminates formed by the reaction between the added Y_2O_3, excess oxygen in the powder, and the aluminum added to getter oxygen. In Fig. 2.1, the larger particles are titanium carbonitrides. The dispersoids are typically 14 nm in diameter with an average spacing of 0.2 μm. The 1093°C stress rupture properties of INCONEL MA 754 are compared to those of other alloys in Fig. 2.2. The MA 754 alloy, like other ODS materials, has a very fine, flat, log stress-log rupture life slope compared to conventional alloys. The strength of MA 754, about 100 MPa for 100 hours life, is somewhat higher than both of the other ODS alloys and several times greater than conventional materials, MAR-M alloy 509 and alloy 80 A. Thus, while MA 754 alloy is comparable to TD (Thoria dispersed) NiCr, it has a non-radioactive dispersoid and high strength, so it is suitable for applications such as gas turbine vanes.

2.2.1.2 INCONEL MA 6000

INCONEL MA 6000 combines precipitation strengthening (gamma prime, γ', precipitates) from its Al, Ti, and Ta content for intermediate temperature strength with oxide dispersion strengthening from the Y_2O_3 addition for strength and stability at very high temperatures. It contains about 25% of γ' precipitates. The dispersoid dimensions are 30 nm average diameter and 0.1 μm average spacing. As in MA 754, the Y_2O_3 reacts with oxygen and aluminum to form uniform dispersions of yttrium aluminates, e.g., yttrium-aluminum garnet $5Al_2O_3 \cdot 3Y_2O_3$ (YAG). The YAG dispersoid appears to be very stable.

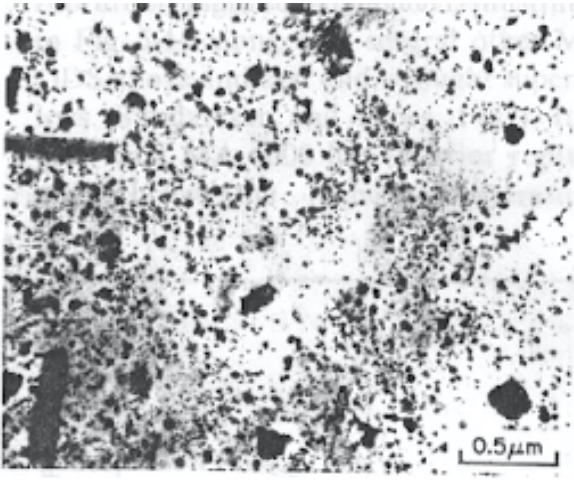

Figure 2.1. BFI micrograph of INCONEL MA 754 showing uniform distribution of the fine primary dispersion, the presence of coarser carbonitrides and microtwins. *(After Weber.)*[5]

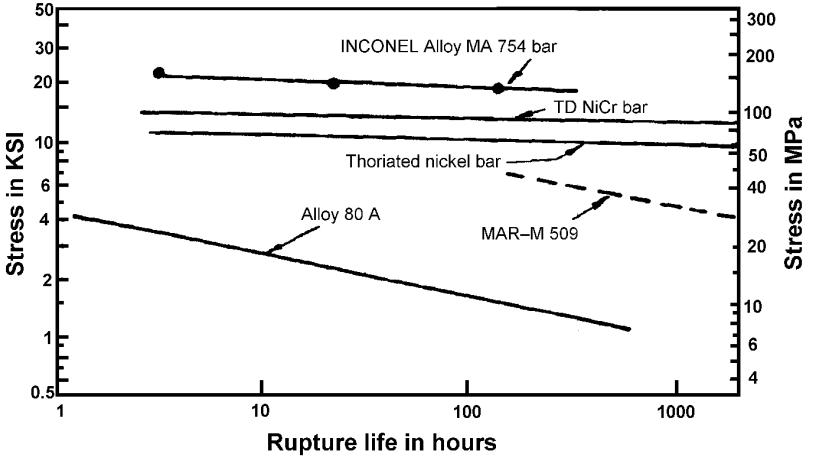

Figure 2.2. Stress rupture properties of MA 754 at 1093°C compared to those of other alloys. *(After Weber.)*[5]

Negligible coarsening is observed for stress rupture tests at ~750°C and only small coarsening for temperatures of 950 to 980°C at rupture lives beyond 10^4 hours. These changes cause no serious loss in the loadbearing capability of the alloy, for practical applications.[7] Figure 2.3 shows the 1000-hour creep rupture strength for MA 6000 alloy compared with several other MA ODS alloys.[8] It is clear that MA 6000 has superior rupture strength at the highest temperatures (less than 900°C) and comparable strength to MAR-M 200 at intermediate temperatures. MA 6000 alloy has been used to a small extent, so far, in gas turbine engine blades.

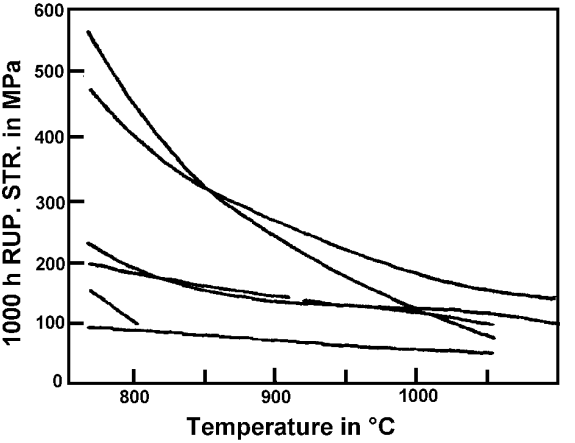

Figure 2.3. Creep rupture at 1000 h for MA alloys compared with cast and wrought superalloys: (1) MA 956, (2) MA 764, (3) MA 753, (4) MA 6000, (5) MAR-M 200, and (6) $Ni_{80}Al$. *(After Sundaresan et al.)*[8]

2.2.1.3 INCOLOY MA 956

The iron-base INCOLOY alloy MA 956 contains about 20% Cr, 4.5% Al, 0.5% Ti, and about 0.5% Y_2O_3. It can be used at operating temperatures of over 1300°C in a corrosive atmosphere.[8] MA 956 also has excellent fabricability. It can be cold-worked and can be joined by several welding techniques. MA 956 sheets can be bent more than 150° around a diameter equal to twice the sheet thickness.[5] The first ODS material designed as a structural system was SAP (Sintered Al Powder) as developed

by Irmann.[9] Sintered Al Powder (SAP) displayed a greater strength than pure Al and no changes were observed after extended heating near the melting point. In 1957, Benjamin et al.[10] developed further SAP. Bars of SAP were made by a mixture of 1 to 10% vol % Al_2O_3 powder in pure Al powder. The Al_2O_3 particles in SAP exhibit a wide distribution of sizes (~10 nm to 1 μm), as presented in Fig. 2.4. In order to maximize the strength of Al-Al_2O_3 ODS alloys it was desired to obtain a finer and more uniform distribution of the Al_2O_3 dispersion in the Al matrix.

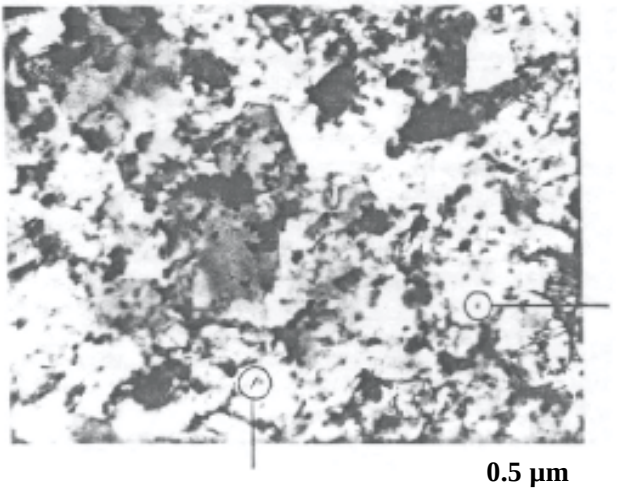

Figure 2.4. BFI of as-extruded MA Al. *(After Benjamin et al.)*[10]

Figure 2.5 shows the variation of ultimate tensile strength as a function of the combined volume fraction of Al_2O_3 and carbon and compares it to some SAP materials of comparable strength. The correlation between the ultimate tensile strength of MA Al and Al_2O_3 content alone is not as good; indicating that certain carbon dispersion contributes to the strengthening.[10] High tensile strengths of the heats were obtained with low dispersoid levels (less than 5.4 vol %). Sintered Al Powder (SAP) products containing this content of Al_2O_3 dispersoid typically show tensile strengths at room temperature of around 241 MPa.[11] Strengths of 310 MPa to 448 MPa are only obtained in SPA products with more than about 7 vol % Al_2O_3.[12]

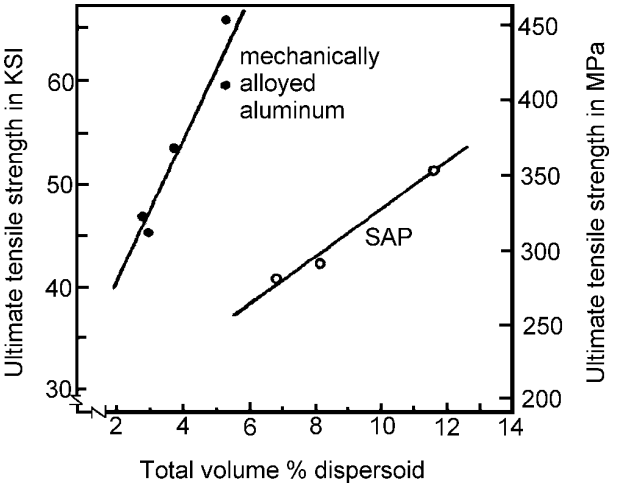

Figure 2.5. Room temperature tensile strength vs. dispersoid content for SAP and MA Al. *(After Benjamin et al.)*[10]

It was found necessary to use a process control agent, such as a stearic acid or methanol, to prevent excessive welding.[10] The decomposition of the process control agent during mechanical alloying and subsequent powder compaction by hot pressing and extrusion resulted in significant contamination by carbon. The carbon was believed present as Al_4C_3 dispersoids. Thus, dispersion strengthening in these materials comes from both Al_2O_3 and Al_4C_3 dispersoids.

Conventional Al-Mg alloys have inherently good corrosion characteristics and dispersion strengthening of such alloys through MA was seen to be of technological value. It was upon this basis that the MA process was extended to produce a dispersion-strengthened Al-4 vol % Mg alloy by Benjamin et al., in 1981.[13] A mixture of commercial Al and Mg powders is charged into a high-energy ball mill (Szegvari attritor)[14] filled with small steel grinding balls. The powder particles are trapped between colliding grinding balls and severe plastic deformation results. The surfaces of the starting Al and Mg powders are covered by adsorbed gases, hydrated oxides, and other thin amorphous compounds, such as carbonates. As displayed in Fig. 2.6, flattening during MA processing increases the surface-to-volume ratio of the powders and ruptures the surface films, exposing atomically clean metal.

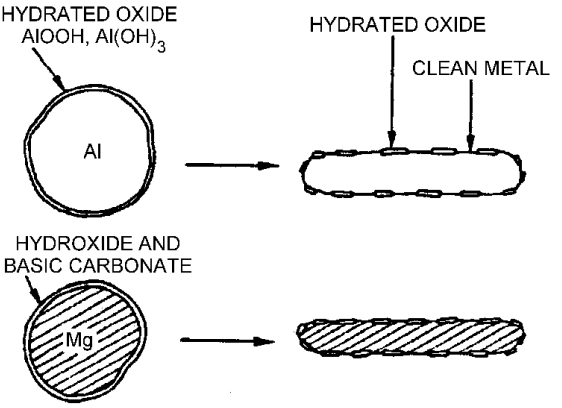

Figure 2.6. Rupture of surface contamination films by plastic deformation during MA process of Al and Mg powders. *(After Benjamin et al.)*[13]

As shown in Fig. 2.7(*a*), cold welds are forced between powder particles, building up composite particles and entrapping fragments of the surface films within the composites. Adding a control agent during MA process leads to increased oxygen and carbon contents of the powders. This pickup occurs by the formation of new adsorbed surface layers [Fig. 2.7(*b*)]. Further processing of the composite metal particles [Fig. 2.7(*c*)] caused further welding and plastic deformation. This thins the lamellae of the original starting powders, and causes further fragments within the composite particles. The internal homogeneity of the composite particles is improved by this thinning of the internal lamellae. In addition to welding, which tends to increase average particle size, fracturing occurs, which tends to decrease average particle size. The fracturing is assisted to some extent by the increased carbon and oxygen content, due to the occlusion of a process control agent.

With further processing, the internal structure of the powders continues to be refined. Local composition, from particle to particle and within the particle, approaches the average composition of the desired alloy. The end point of the MA process is reached when the surface film fragments are randomly distributed throughout the powder particles and metallic alloying has been completed on a submicron scale.

The microstructures of MA Al-Mg powders after partial and complete processing are shown in Fig. 2.8.

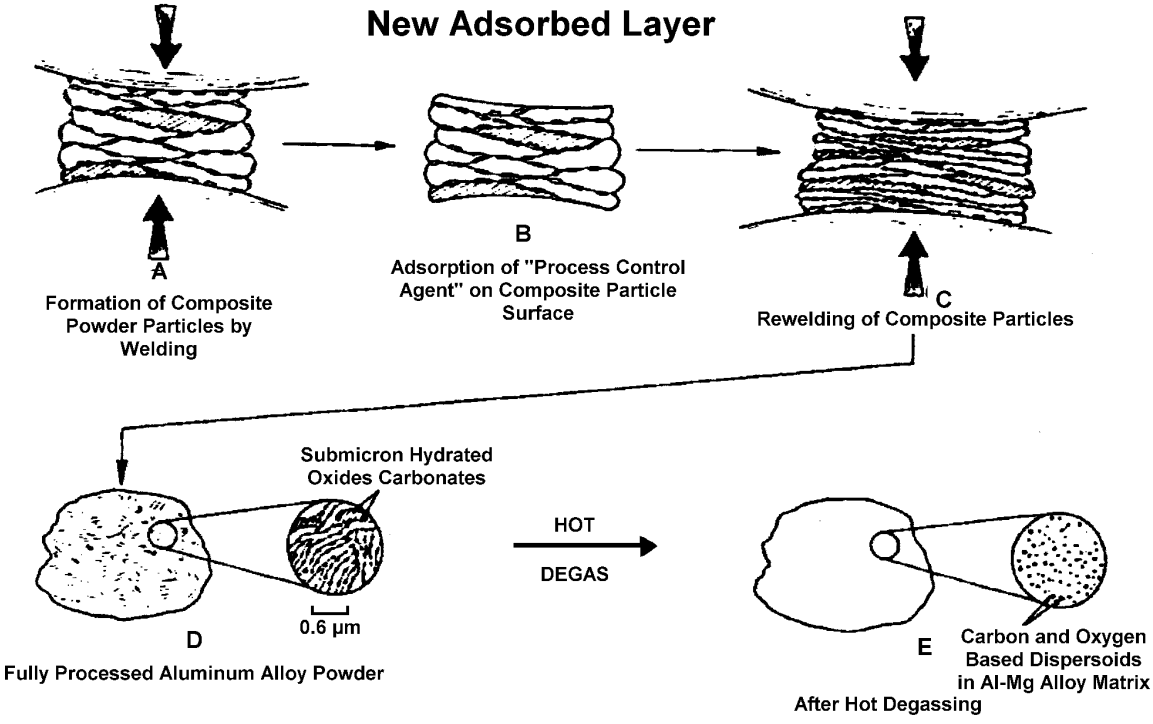

Figure 2.7. Schematic diagram of the MA process applied to Al-Mg alloys. *(After Benjamin et al.)*[13]

(a)

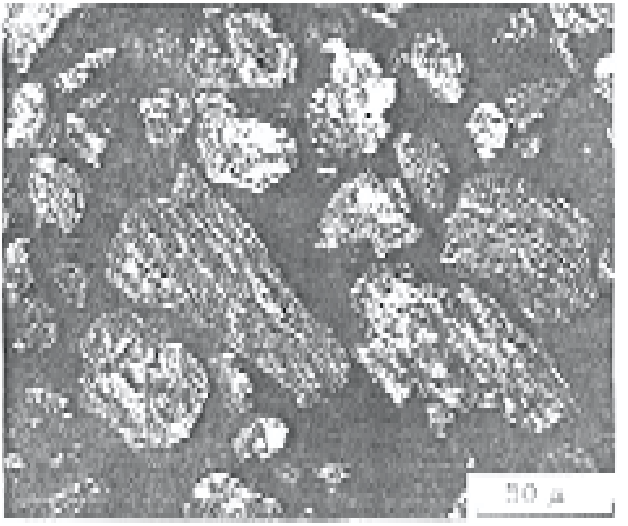

(b)

Figure 2.8. Microstructures of mechanically alloyed Al-Mg powders after *(a)* partial processing and *(b)* complete processing.

The Al-Mg, with uniform equaxed oxygen and carbon-based dispersoids, and Mg solid solution strengthening, gave tensile strengths of 520 to 585 MPa along with excellent resistance to corrosion and stress corrosion cracking.

REFERENCES

1. Benjamin, J. S., *Metall. Trans.*, 1:2943 (1970)
2. Benjamin, J. S., *Sci. Forum*, 88–90:1 (1992)
3. Hoyt, S. L., *AIM Trans*., 89:9 (1930)
4. Gilman, P. S., and Benjamin, J. S., *Ann. Rev. Mater. Sci*., 13:279 (1983)
5. Weber, J. H., *The 1980s-Payoff Decade for Advanced Materials*, 25:752, Azusa, CA, S.A.M.P.E. (1980)
6. Benjamin, J. S., and Volin, T. E., *Metall. Trans. A*, 5:1929 (1974)
7. Benn, R. C., Benjamin, J. S., and Austin, C. M., *High Temperature Alloys: Theory and Design*, Warrendale, PA, TMS-AIME (1984)
8. Sundaresan, R., and Froes, F. H., *Modern Developments in Powder Metallurgy*, 21:439 (1988)
9. Irmann, I. R., *Metallurgia*, 46:125 (1952)
10. Benjamin, J. S., and Bomford, M. J., *Metall. Trans. A*, 8:1301 (1977)
11. Bloch, E. A., *Met. Rev*., 6:193 (1961)
12. Hansen, N., *Metall. Trans.*, A1:545 (1970)
13. Benjamin, J. S., and Schelleng, R. D., *Metall. Trans. A*, 12:1827 (1981)
14. U.S. Patent No. 2,764,359, Szegvari, A. (1956)

3

Fabrication of Nanophase Materials

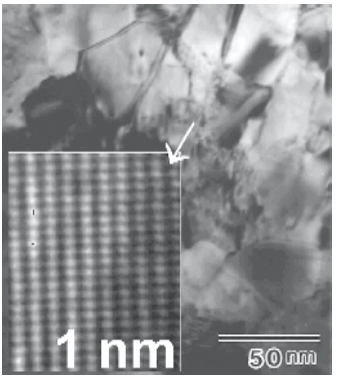

The figure shows a cross-sectional view of as-consolidated mechanically reacted WC powders. The fabricated WC materials via MA process have shown advanced and unique properties owning to their nanocrystalline structure. *(El-Eskandarany et al.,* Metall. Trans. A, *27:4210, 1996)*

3.1 INTRODUCTION

Most crystalline solids are composed of a collection of many small crystals or grains; termed polycrystalline. The term *nanocrystalline materials* (also known as nanostructured or nanophase materials)[1][2] is used to describe those materials that have a majority of grain diameters in the typical range from ~1 to 50 nm.[3] Whether it can be called a revolution or simply evolution, the nanocrystalline materials have received much attention as advanced engineering materials with unique physical and mechanical properties. The

mechanical properties of the nanocrystalline materials at room temperature are always superior (i.e., higher strength and toughness) to those of coarse-grained ones. Intensive research on these materials has been performed since the pioneering investigations of Gleiter.[1][4]

3.2 INFLUENCE OF NANOCRYSTALLINITY ON MECHANICAL PROPERTIES: STRENGTHENING BY GRAIN SIZE REDUCTION

One of the very basic results of the physical chemistry of solids is the insight that most properties of solids depend on the microstructure. The size of the grains (average grain diameter) in a polycrystalline material has pronounced effects on many of its physical and mechanical properties. A fine-grained material, or so-called nanostructured material, is harder and stronger than one that is coarse-grained (Fig. 3.1), since the former has a greater total grain boundary area to impede dislocation motion. For many materials the yield strength, σ_y, varies with grain size according to:

Eq. (3.1) $$\sigma_y = \sigma_0 + k_y d^{-1/2}$$

In this expression, termed the Hall-Petch equation, d is the average grain diameter, and σ_0 and k_y are constants for a particular material.

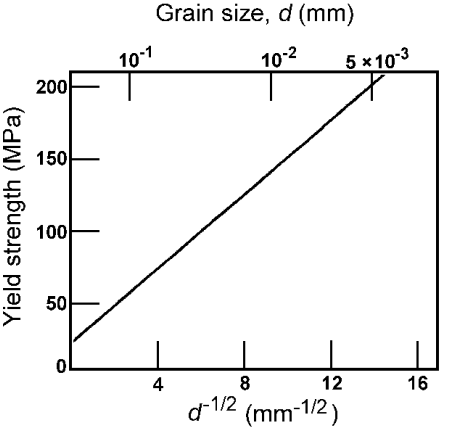

Figure 3.1. The influence of grain size on the yield strength of Cu-30% Zn brass alloy. *(After Suzuki.)*[5]

The information for the average grain diameters can be primarily obtained from TEM and/or HRTEM observations, and x-ray line broadening.

3.3 FORMATION OF NANOCRYSTALLINE MATERIALS BY BALL MILLING TECHNIQUE

Nanocrystalline materials can be successfully synthesized by several techniques, including inert gas condensation,[6] rapid solidification,[7] electrodeposition,[8] sputtering,[9] crystallization of amorphous phases,[10] and chemical processing.[11] (See Fig. 3.2.)

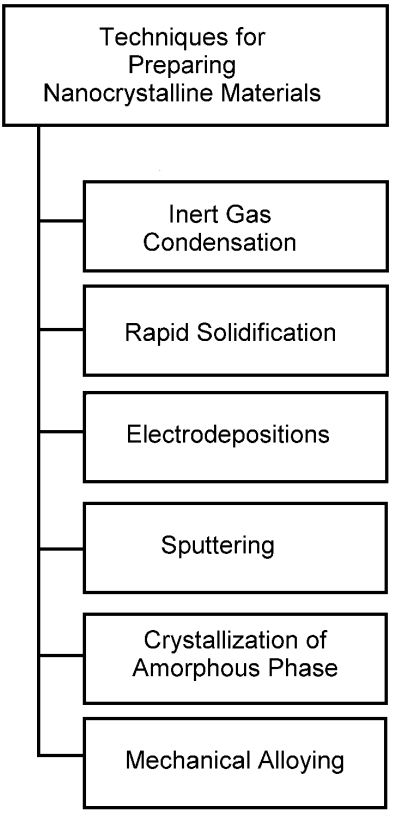

Figure 3.2. Nanocrystalline materials are a unique class of the advanced engineering materials that can be prepared by several methods.

It has been reported that composites of amorphous and nanocrystalline phases have unique properties when compared with those of amorphous phases.[12]

Amongst the different options for preparations, the mechanical alloying method has been considered the most powerful tool for nanostructured materials[13] because of its simplicity, relatively inexpensive equipment, and the possibility of producing large quantities, that can be scaled up to several tons.[14] The formation of nanocrystalline materials during MA of ceramics or metallic powders is attributed to the intense cold working on the ball milled powders. This leads to a dramatic increase in the number of imperfections (e.g., point and lattice defects) which leads to decreasing the thermodynamic stability of the starting materials. Based on the type of defects applied, different kinds of nanocrystalline materials, with different physical and mechanical properties, can be obtained.[12][15]

It is believed that the reduction in grain size during MA takes place similar to that suggested by the model for nanocrystalline materials fabricated by gas condensation.[6] It is worth noting that the enthalpy stored via high-energy ball milling is far above than that for the conventional cold working technique.[16] For example, the enthalpy stored through cold welding of metals and alloys does not exceed 2 kJ/mol and is only a small fraction of the heat of fusion, ΔH_f.[17] In the MA method, however, the enthalpy is larger and can reach higher values of crystallization enthalpies[17] of a metallic glass, as high as 0.4 times the heat of fusion. We should emphasize that such enthalpy storage, in the form of lattice and point defects, cannot be achieved in traditionally processed materials. Hence, the grain boundary energy of milled nanocrystalline powders is larger than the grain boundary energy of fully equilibrated grain boundary.[18]

3.3.1 Mechanism(s)

The mechanism for formation of nanocrystalline materials by the ball-milling technique has been proposed by Fecht,[19] who summarized the phenomenology of the grain size reduction into three stages.

First Stage. Plastic deformation that is produced in the crystal lattices of the ball milled powders by slip and twinning. This deformation is localized in shear bands containing a high dense network of dislocation. The local shear instability of a crystal lattice can be triggered by material heterogeneity and enhance instabilities.[16] It is worth noting that these instabilities result from a nonuniform heat transfer during the mechanically induced deformation of the

milled powders. During this stage of milling (early stage), the atomic level strain increases as a result of increasing the dislocation density.

Second Stage. Due to the successive accumulation of the dislocation density, the crystals are disintegrated into subgrains that are initially separated by low-angle grain boundaries. The formation of these subgrains is attributed to the decrease of the atomic level strain.

Third Stage. Further ball milling time leads to further deformation occurring in the shear bands located in the unstrained parts of the powders which leads to subgrain size reduction so that the orientation of final grains becomes random in crystallographic orientations of the numerous grains and hence, the direction of slip varies from one grain to another.

3.3.2 Selected Examples

Formation of Nanocrystalline Ni_xMo_{100-x} (x = 60 and 85 at. %). Trudeau et al.[20] have carried out a high resolution electron microscope (HRTEM) study of mechanically alloyed Ni_xMo_{100-x} (x = 60 and 85 at. %) powders which were prepared by milling pure Ni and Mo in a high-energy ball mill. The end products for both compositions are nanocrystalline fcc alloys. They have followed the reduction in the grain size for both alloys as a function of the milling time [see Fig. 3.3(*a*)].

Their results have indicated that the reduction in crystal size is taking place by increasing the ball milling time. By correlating the crystal size [Fig. 3.3(*a*)] and the strain values [Fig. 3.3(*b*)] we can conclude that a drastic fragmentation of the crystallites is achieved during the beginning of the MA process and the grains refined to be about 10–20 nm with a large increase on the internal strain. Upon further milling, the strain still increases in the lattice and reaches values that provoke, after 15 h of milling [Fig. 3.3(*b*)]. The strain drops afterwards and the crystal size decreases below 10 nm [Fig. 3.3(*b*)]. They have concluded that a large number of dislocations are present in the crystals when the internal elastic strain reaches its maximum value (10–15 h). The results of their work shows that when the size of the crystallites is less than 10 nm, the crystals are dislocation-free. Plastic deformation, in this case, takes place through a glide along the grain boundaries. After a long milling time, high-angle grain boundaries are formed.[20]

Formation of Nanocrystalline fcc Metals. Eckert et al.[21] carried out a systematic study for the grain reduction of pure metals with fcc structure during ball milling. The milling was carried out in a high-energy ball mill under an argon and hydrogen gas atmosphere, using hardened steel balls with

ball-to-powder weight ratio as 4:1 (for Al, Cu, Ni, and Pd) or 6:1 (for Rh and Ir). The structure of the milled powder was characterized by means of XRD and TEM techniques.

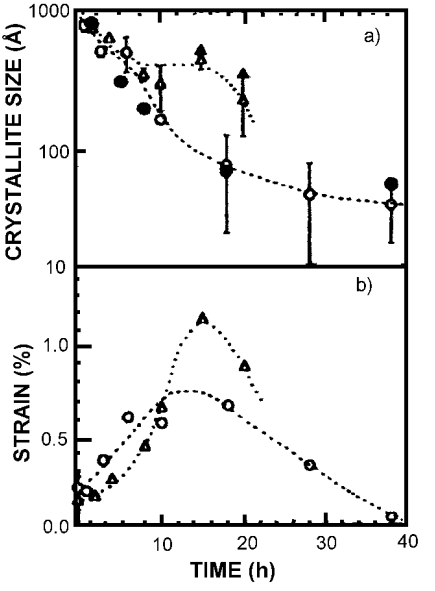

Figure 3.3. *(a)* Average grain size of the nickel crystallites size, L as a function of milling time measured by x-ray diffraction (open symbols) and direct TEM observations (full symbols) for (•ê) $Ni_{85}Mo_{15}$ and (!F) $Ni_{85}Mo_{15}$, *(b)* RMS strain measured by x-ray diffraction for the same alloys. *(After Trudeau et al.)*[20]

The XRD patterns of Pd powders before and after 20 hours of milling are shown in Fig. 3.4. The sharp Bragg peaks are remarkably broadened after ball milling, due to the refinement of the crystal size and an increase in internal strain, they have shown a correlation between the melting points of the metallic milled powders and the final average of the grain size (Fig. 3.5). Whereas, the grain size can be reduced to only 22 nm for Al, it decreases to values below 10 nm for the elements with high melting temperatures. This suggests that the recovery rates during the milling process correlate with the melting point of the specific metal, thus preventing very small grain sizes for low melting point elements.

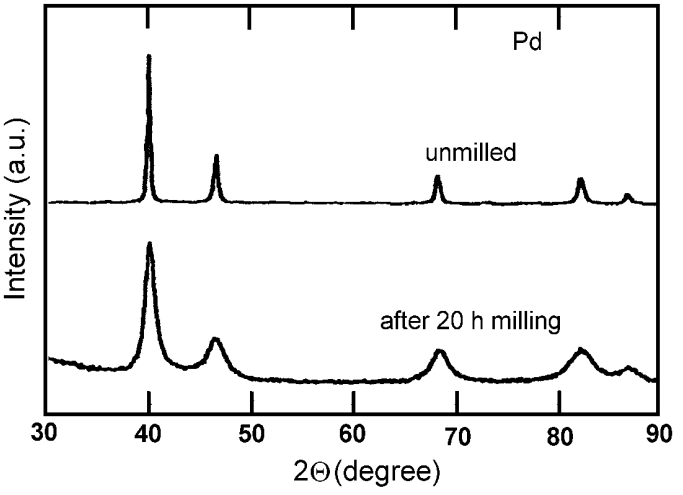

Figure 3.4. The XRD patterns of Pd powders *(a)* before milling and *(b)* after 20 h of milling. *(After Eckert et al.)*[21]

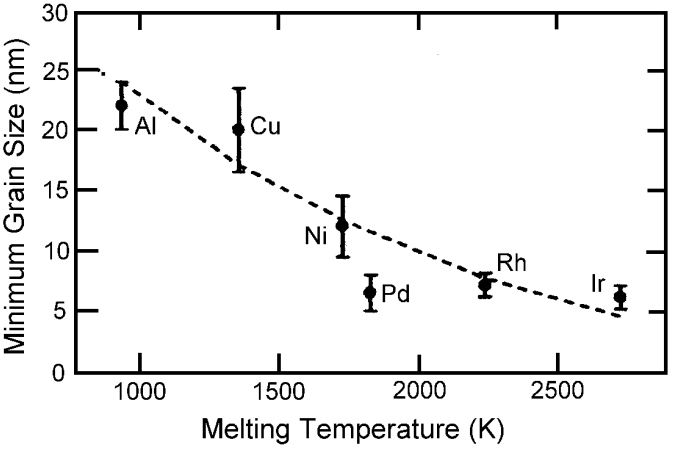

Figure 3.5. Minimum grain sizes for different metallic fcc metals vs. melting temperature. *(After Eckert et al.)*[21]

3.4 CONSOLIDATION OF THE NANOCRYSTALLINE MILLED POWDERS

Consolidation of milled powders is an important step for reliable and reproducible determination of the physical/mechanical properties of the fabricated materials and is required for most industrial applications.[22][23] Consolidation of the ball milled powders into bulk, full density compacts while retaining nanoscale grain size is a major challenge.[22] Many sintering techniques, e.g., hot pressing,[24][25] hot extrusion,[26] sintering forging,[27] and HIPing[28] have been employed to consolidate the mechanically alloyed powders. An attractive technique that has been used for consolidation of several metallic and ceramics powders is the plasma activated sintering, PAS. Recently, El-Eskandarany et al.[29]–[31] used this sintering technique for preparing bulk, fully dense nanocrystalline materials, using the mechanical alloying method as a source of the nanocrystalline powders.

In the PAS method, the powders are consolidated in vacuum at 1963 K under pressures ranging from 19.6 to 38.2 MPa for 0.3 ks. In order to avoid undesired grain growth, the sintering process is usually applied for only 0.18 ks. In fact, there are three important factors governing successful consolidation step via the PAS (Fig. 3.6). The first factor is the application of uniaxial load, the second factor is the application of pulsed voltage for plasma activation, and the last factor is the resistance heating of graphite crucible and powders.

In this consolidation technique, when the direct current pulse voltage is applied to the powders, micro discharge takes place among the powder particles, which generates a plasma. Hence, the atoms on the surface of each particle are activated, and the sintering procedure takes place in a short time (consolidation is achieved within 0.3 ks). Accordingly, grain growth during sintering can be minimized and the sintered powders (Fig. 3.7) maintain their unique nanocrystalline properties with improved physical and mechanical properties. In addition, the PAS technique does not result in any compositional and/or structural changes of the sintered powders. Thus, the as-milled and as-consolidated samples are identical in their properties.[33]

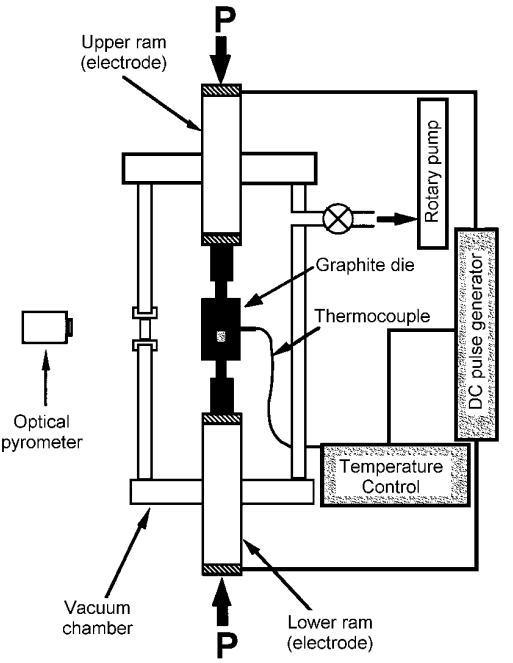

Figure 3.6. A schematic presentation of the plasma activated sintering (PAS) apparatus. *(After El-Eskandarany et al.)*[32]

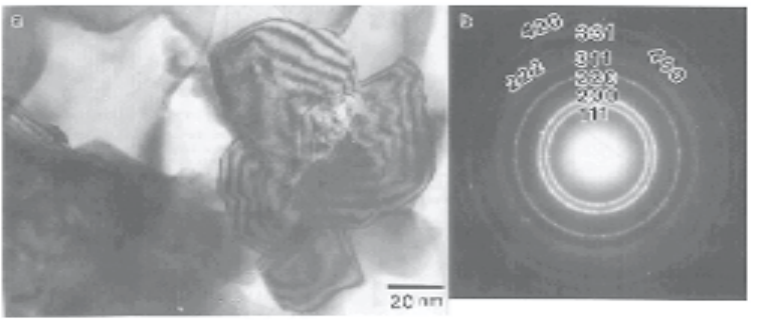

Figure 3.7. *(a)* Bright field image (BFI) and *(b)* the corresponding selected area diffraction pattern (SADP) of the as-PAS TiN powders after milling for 173 ks. The highly dense and the nanostructure characteristics of the sintered sample can be noted. *(After El-Eskandarany et al.)*[23]

REFERENCES

1. Gleiter, H., *Prog. Mat. Sci.,* 33:223 (1989)
2. Hahn, H., *NanoStruct. Mater.,* 9:3 (1997)
3. McHenry, M. E., and Laughlin, D. E., *Acta. Mater.,* 48:223 (2000)
4. Gleiter, H., in: "Deformation of Polycrystals," (N. Hansen, A. Horsewell, T. Leffers, and H. Lilholt, eds.), p. 15, *Proc. Second Riso Int. Symp. Metallurgy and Materials Science,* Roskilde (1981)
5. Suzuki, H., *The Relation Between the Structure and Mechanical Properties of Metals,* National Physical Laboratory, Vol. II, Symposium No. 15:524 (1963)
6. Birringer, R., Gleiter, H., Klein, H. P., and Marquardt, P., *Phys. Lett. A,* 102:3423 (1984)
7. Inoue, A., *Mater. Sci. Eng. A,* 179/180:57 (1994)
8. Hughes, R. O., Smith, S. D., Pande, C. S., Johnston, H. R., and Armstrong, R. W., *Scripta Metall.,* 20:93 (1986)
9. Li, Z. G., and Smith, D. J., *Appl. Phys. Lett.,* 55:919 (1989)
10. Lu, K.,Wei, W. D., and Wang, J. T., *Scr. Metall. Mater.,* 24:2319 (1995)
11. Kear, B. H., and Strutt, P. R., *NanoStruct. Mater.,* 6:227 (1995)
12. Gleiter, H., *NanoStruct. Mater.,* 6:3 (1995)
13. Koch, C. C., *NanoStruct. Mater.,* 2:109 (1993)
14. Koch, C. C., *NanoStruct. Mater.,* 9:13 (1997)
15. Froes, F. H., and Suryanarayana, C., *J. Metals,* 6:12 (1989)
16. Campbell, S. J., and Kaczmarek, W. A., *Mössbauer Spectroscopy Applied to Materials and Magnetism* (G. J. Long and F. Grandjean, eds.) Plenum Press, New York, 2:273 (2000)
17. Johnson, W. L., *Prog. Mat. Sci.,* 30:81 (1986)
18. Johnson, A., in: *New Materials by Mechanical Alloying Techniques,* (E. Arzt and L. Schults, eds.), p. 354, Informationsgesellschaft Verlag, Calw-Hirsau (1988)
19. Fecht, H. J., *NanoStruct. Mater.,* 6:33 (1995)
20. Trudeau, M. L., and Schulz, R., *Sci. Eng. A,* 134:1361 (1991)
21. Eckert, J., Holzer, J. C., Krill, C. E., III, and Johnson, W. L., *Mater. Sci. Forum,* 88–90:505 (1992)
22. He, L., and Ma, E., *J. Mater. Res.,* 11:73 (1996)
23. El-Eskandarany, M. S., Omori, M., Konno, T. J., Sumiyama, K., Hirai, T., and Suzuki, K., *Metall. Trans. A,* 29:1973 (1998)

24. Nash, P., Kim, H., Choo, H., Ardy, H., Hwang, S. J., and Nash, A. S., *Mater. Sci. Forum*, 88–99:603 (1992)
25. El-Mahdy, A. A., El-Eskandarany, M. S., Ahmed, H. A., and Amer, A. A., *J. Alloys Comp.* 299:244 (2000)
26. Hwang, S. J., Nash, P., Dollar, M., and Dymek, D., *Mater. Sci. Forum*, 88–99:611 (1992)
27. Jain, M., and Christman, T., *Acta. Metall. Mater.*, 42:1901 (1994)
28. Oehring, M., Appel, F., Pfullmann, Th., and Bormann, R., *Appl. Phys. Lett.*, 66:941 (1995)
29. El-Eskandarany, M. S., Omori, M., Ishikuro, M., Konno, T. J., Takada, K., Sumiyama, K., Hirai, T., and Suzuki, K., *Metall. Trans. A*, 27:4210 (1996)
30. El-Eskandarany, M. S., *J. Alloys Comp.*, 279:263 (1998)
31. El-Eskandarany, M. S., *J. Alloys Comp.*, 296:175 (2000)
32. El-Eskandarany, M. S., Omori, M., Kamiyama, T., Konno, T. J., Sumiyama, K., Hirai, T., and Suzuki, K., *Sci. Rep. Ritu*, Tohoku University, A43:181 (1997)
33. El-Eskandarany, M. S., *J. Alloys Comp.*, 305:219 (2000)

4

Fabrication of Nanocomposite Materials

The idea of combining two or more different materials resulting in a new material with improved properties dates back to 3000 years, when the Pharaohs of Egypt knew that plant fibers helped strengthen and prevent bricks and pottery from cracking. The figure shows a typical composite material, which consists of brick (dark-gray block matrix) where the plant fiber materials (light-gray needle-like material) are embedded. (*After El-Eskandarany,* Al Azhar University Engineering Journal*, 1:143, 1998.)*

4.1 INTRODUCTION AND BACKGROUND

Metal matrix composites (MMC) are an engineered combination of two or more materials in which tailored properties are achieved by bringing the combined advantages of both reinforcement and metallic matrix into full play, which gives us a rather high degree of freedom in

material design.[1] Structurally, reinforcements may be in the form of continuous fibers, short fibers, particles, or whiskers, and early interest in developing these materials was fueled by their potential for applications in aerospace, naval, and automotive structures.[2]

Some composite systems, like SiC/Al, have shown a significant improvement in their tensile strength and elastic modulus as well as wear resistance. Improved mechanical properties of particulate SiC_p/Al composites are due to the transfer of shear load at the matrix/reinforcement interface.

Unfortunately, the traditional technique of liquid metallurgy, which is the least expensive method for composite fabrications cannot be successfully applied for the synthesizing of some SiC/Al, due to the extreme gap difference in the thermal expansion coefficients between the two constituents and also due to the poor wettability between molten Al (or Al alloys) and SiC. According to various theoretical and experimental studies carried out thus far, SiC reacts with the molten Al to form Al_4C_3 and Si according to the following reaction:[3]

Eq. (4.1) $$4Al + 3SiC \rightarrow Al_4C_3 + 3Si$$

This reaction is known to have several undesirable effects on the overall composite properties:

- Mechanical properties of SiC will be degraded due to the formation of Al_4C_3
- Since the reaction product Al_4C_3 is unstable in some environments, such as water, methanol, HCl, etc.,[4][5] the composite can be susceptible to corrosive environments
- In addition, Si, formed as an interfacial reaction product, will produce Al-Si eutectic at the interface and the grain boundary regions, resulting in unintended mechanical properties of the composite

As a result, fabrication of SiC/Al composite devoid of Al_4C_3 has long been one of the major concerns.

There are various methods employed in fabricating metal matrix composites using different processing parameters, melt process, squeeze casting, powder metallurgy (PM) hot pressing, and spray forming. Among these processes, two methods have been proven to be effective in achieving the goal for fabricating the metal matrix composite (MMC).

- Si addition into the Al matrix[6]–[9]
- Artificial oxidation of SiC to produce a SiO_2 layer on the surface of SiC[10]–[12]

The basic principle behind both methods is to enhance the Si activity and thereby reduce the Al activity, by dissolving Si into the Al matrix. However, considering the forward reaction which is presented in Eq. (1), one can say that such interfacial reaction is also dependent on the temperature and holding time, etc., and can be the alternative solution to support the interfacial reaction.

4.2 FABRICATION OF SiC_p/Al COMPOSITES BY MECHANICAL SOLID STATE MIXING

The field of nanocomposites has recently attracted considerable attention as researchers strive to enhance composite properties and extend their utility by using nanoscale reinforcements instead of the more conventional particulate-filled composites.[13] While smaller reinforcements have a better reinforcing effect than larger ones, applying the ball-milling technique for composite fabrications must have the following merits:

- since ball milling is processed at room temperature, the disadvantages of the liquid metallurgy method for producing undesirable materials can be avoided
- moreover, the ball-milling process can produce homogeneous nanocomposite powders instead of the more conventional coarse particulate-filled composites

In 1998, El-Eskandarany[14] employed a high-energy ball mill to fabricate metal matrix, a composite of Al reinforced with SiC_p with distinct nanocrystalline characteristics. In his experiments, pure elemental powders of Al (99.99%, 10 mm) and SiC ($\beta + \alpha$ phases) (99.9%, 100 mm) were weighed to give the nominal composition of SiC_xAl_{100-x} (x = 2, 5, 7, and 10 vol %) and mixed in a glove box under a purified argon atmosphere, using sapphire mortar and pestle. The initial mixed powders were then charged and sealed in a stainless steel vial (SUS 316, 250 ml in volume) together with fifty stainless steel balls (SUS 316, 10 mm in diameter). The ball-to-powder weight ratio was maintained as 20:1. The ball-milling experiments were performed in a high-energy planetary ball mill at a rotation speed of 3.3 s^{-1}. To avoid the formation of any undesired contaminated phase(s), no

lubricant solutions that are mainly hydrocarbon compounds were added to the charge. The ball-milling experiments were stopped periodically (every 1.8 ks) and then resumed when the temperature of the vial decreased to about 300 K. The final product (86 ks of milling) of the mixed powders were then consolidated into compacts in vacuum at 823 K, which is far below the melting point of Al (934 K), with a pressure of 19.6–38.2 MPa for 0.3 ks, using a plasma activated sintering method (PAS). The as-milled and as-consolidated samples were characterized by means of x-ray diffraction (XRD) with CuKα radiation, scanning electron microscopy (SEM) using a 20 kV microscope, transmission electron microscopy (TEM) using a 200 kV microscope, and chemical analyses, using the induction coupled plasma emission and helium carrier fusion-thermal conductivity methods. The gas (oxygen, nitrogen, and hydrogen) and the iron, that was introduced to the samples from the milling tools, contamination contents in the end-product of composite SiC_p/Al were determined to be less than 0.07 and 0.2 (at. %), respectively. The density of the consolidated samples was determined by Archimedes' principle, using water immersion. The hardness of the compacted sample was determined using a Vickers indenter with a load of 10 kg. Moreover, the elastic properties of the bulk samples were investigated by a pulse-echo overlap ultrasonic technique, using an ultrasonic detector.

4.3 PROPERTIES OF MECHANICALLY SOLID STATE FABRICATED SiC_p/Al COMPOSITES

4.3.1 X-Ray Analysis

Figure 4.1 presents the typical XRD patterns of mechanically-mixed SiC_{10}/Al_{90} powder after (*a*) 0 ks of ball-milling time (starting material mixture of elemental Al and SiC powders) and (*b*) 86 ks of ball-milling time (the end-product). Obviously, the starting materials contain coarse polycrystalline grains of SiC and Al, suggested by the sharp diffraction peaks of the powder mixture. On the contrary, the Bragg peaks of both the reinforcement (SiC) and metallic matrix (Al) powders become broad towards the end stage of milling [Fig. 4.1(*b*)], indicating the formation of nanocomposite SiC_p/Al material. Remarkably, this end-product is still an intact mixture of polycrystalline SiC and Al and does not coexist with any reactive products, such as Al_4C_3 and Si, suggesting the absence of any undesirable reactions at the SiC/Al interfaces.

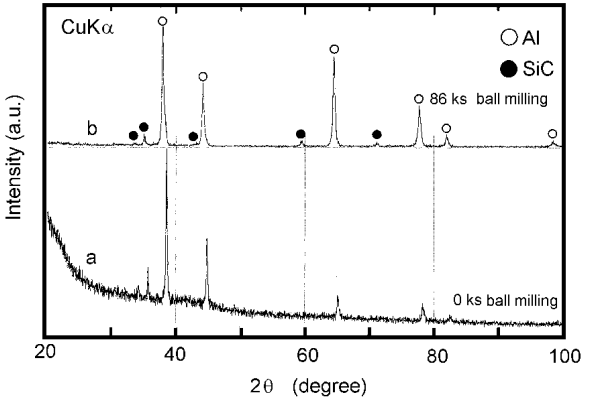

Figure 4.1. XRD patterns of mechanically mixed SiC_{10}/Al_{90} powder after *(a)* 0 ks and *(b)* 86 ks of the milling time. *(After El-Eskandarany.)*[14]

4.3.2 Morphology and Metallography

SEM technique was used to follow the characteristics of the powders during the several stages of ball milling. Figure 4.2 may summarize the morphology, topology, and size of mechanically mixed SiC_{10}/Al_{90} (vol %) powder after selected ball-milling time. The powders at the starting stage of milling [Fig. 4.2(*a*)] are bulky with random shape and size. The soft Al particles in the initial starting mixture are affected by the cold working and the impact and shear forces generated by the milling media, and tend to agglomerate to form larger powder particles with an average diameter of nearly 1000 μm, after 3.6 ks of the milling [Fig. 4.2(*b*)]. At this stage of milling, the hard particles of SiC are randomly embedded into the deformed Al soft matrix (host matrix) to form coarse composite SiC_p/Al powders, as shown in Fig. 4.3. Contrary to the Al powders, the SiC powders have been dramatically disintegrated to form finer particles with spherical-like morphology. During the subsequent disintegration stage (22 to 43 ks), the agglomerated powder particles are subjected to a continuous disintegration with fragmentation to form finer powders with extremely wide particle size distribution [Fig. 4.2(*c*)]. Towards the end of this stage (43 ks), the reinforcement SiC particles becoming finer (less than 1 μm in diameter) and more uniformly distributed in the Al matrix (Fig. 4.4). The powder of

the end-product (86 ks of milling time) of SiC_{10}/Al_{90} composite possesses excellent morphological appearance, characterized by the ultrafine (less than 0.5 μm in diameter), smooth (without any detailed structural relief on the powder surface), and the exactly spherical-like morphology, as shown in Fig. 4.2(*d*).

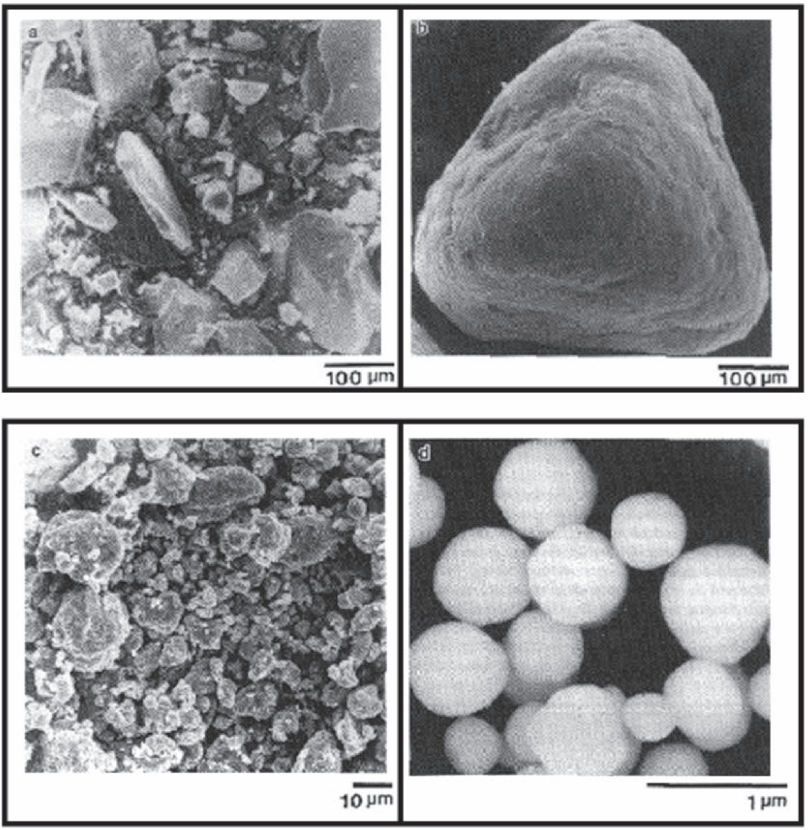

Figure 4.2. SEM micrographs of mechanically solid state mixed SiC_{10}/Al_{90} powder after *(a)* 0 ks, *(b)* 3.6 ks, *(c)* 22 ks, and *(d)* 86 ks of the ball-milling time. *(After El-Eskandarany.)*[14]

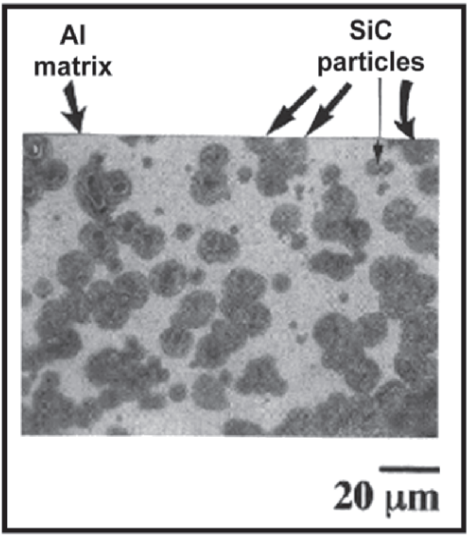

Figure 4.3. Optical micrograph of the polished and etched particle of mechanically solid state mixed SiC_{10}/Al_{90} after 3.6 ks of the ball-milling time. *(After El-Eskandarany.)*[14]

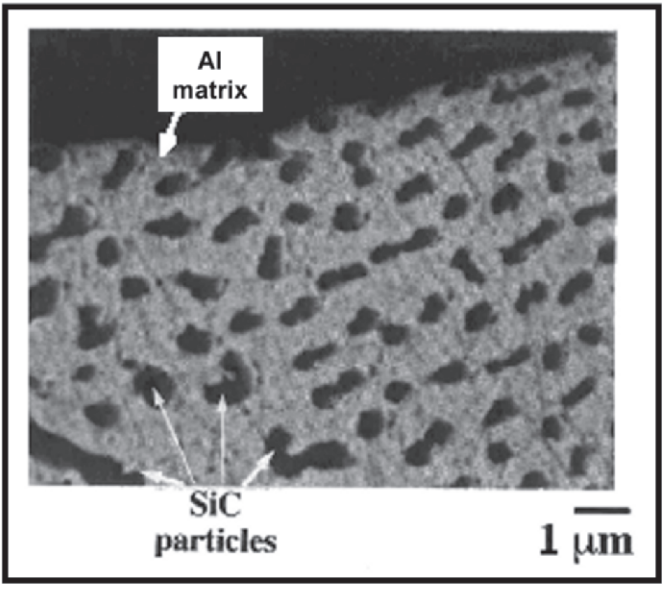

Figure 4.4. SEM micrograph of the cross-sectional view of a selected mechanically solid state mixed SiC_{10}/Al_{90} particle after ball milling for 43 ks. *(After El-Eskandarany.)*[14]

4.3.3 TEM Observations

To reveal more information, the internal structure of the mechanically-mixed powders has been investigated by the TEM technique. This technique provides information on the structure of the powder particles within small areas (less than 50 nm in diameter) in which SEM is not able to give such information.

Figure 4.5 shows the bright field images (BFI) and the selected-area diffraction patterns (SADP) of mechanically mixed powders after 3.6 ks of ball-milling time. Obviously, the large grains of SiC are embedded into the Al matrix that are heavily faulted, characterized by parallel rows of faults which appear as multiple fringes, as shown in Fig. 4.5(*a*). The SADP [Fig. 4.5(*b*)] shows a sharp ring-spot pattern that is characteristic of several simultaneity diffracting polycrystalline β-SiC (fcc) and Al (fcc). It is worth mentioning that there is no evidence of the formation of any reactive products such as Al_4C_3 and Si phases.

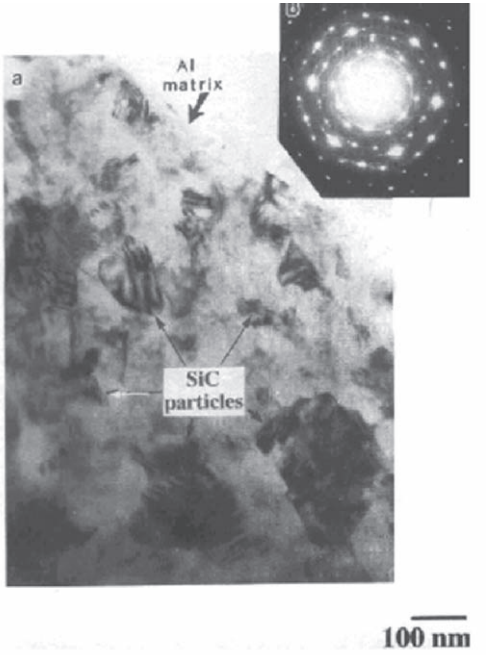

Figure 4.5. *(a)* BFI and *(b)* the corresponding SADP of mechanically solid state mixed SiC_{10}/Al_{90} composite particle after 3.6 ks of the ball-milling time. *(After El-Eskandarany.)*[14]

Figure 4.6 displays the BFI and the corresponding SADP of mechanically-mixed powders after 86 ks of ball-milling time. Obviously, the end-product is a typical nanocomposite material, containing only the two starting phases of SiC (granular fine grains) and metallic Al (overall matrix). No more sharp ring-spot patterns appeared [Fig. 4.6(*b*)], suggesting the formation of fine powders.

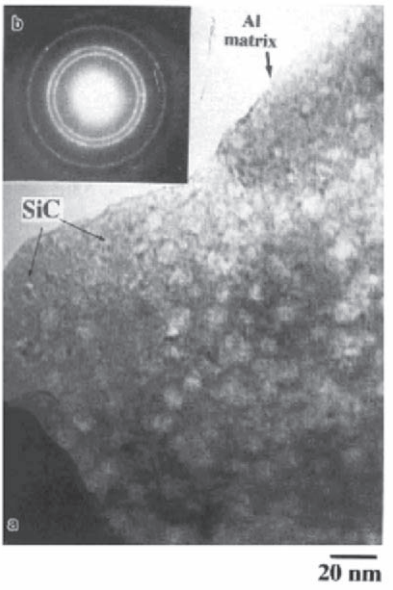

Figure 4.6. *(a)* BFI and *(b)* the corresponding SADP of mechanically solid state mixed SiC_{10}/Al_{90} composite particle after 86 ks of the ball-milling time. *(After El-Eskandarany.)*[14]

4.3.4 Consolidation

In order to determine some of the physical and mechanical properties of fabricated composite powders, the PAS method has been applied to consolidate the final product of the milled powders into compacts (20 mm in diameter and 20 mm in thickness). The XRD pattern of the end-product of as-consolidated mechanically mixed powders, exemplified by

SiC_{10}/Al_{90} compact is shown in Fig. 4.7. Comparing this pattern with that for the milled powders [Fig. 4.1(*b*)], one can conclude that this consolidation step does not lead to a remarkable grain growth of the sintered powders, and the materials still maintain their unique nanocrystalline structure.

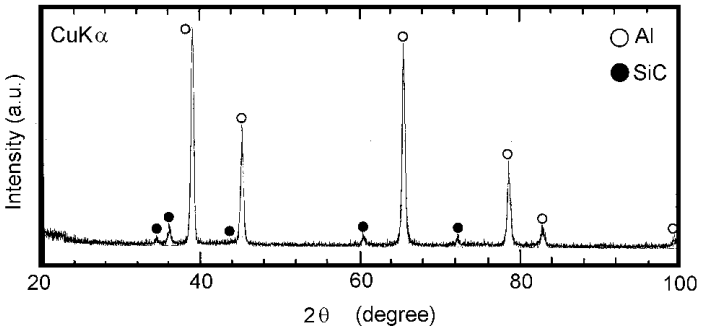

Figure 4.7. The typical XRD pattern of as-consolidated mechanically solid state mixed SiC_{10}/Al_{90} that ball milled for 86 ks. *(After El-Eskandarany.)*[14]

TEM technique has also been used to investigate both the grain size and the phases that may be formed during the consolidation procedure. The BFI and corresponding SADP of as-consolidated SiC_{10}/Al_{90} are shown together in Fig. 4.8. Comparing this micrograph with the one in Fig. 4.6, we can say that this consolidation step leads to slight or moderate grain growth for both the reinforcements (SiC) material and Al matrix. Since the average grain size of the composite consolidated sample is less than 100 nm (about 20 nm in diameter or less) one can say that the sintered sample maintains its nanocrystalline character. No reaction layers can be detected at the SiC/Al interfaces, using the shown magnification. It has also emphasized that this consolidation step does not lead to the formation of any reactive product(s), and the fabricated nanocomposite bulk material combines only the two starting materials of SiC and Al, as suggested by the SADP that is shown in Fig. 4.8(*b*).

The SEM (back scattering) micrograph and the elemental dot mapping of Al and Si of as-consolidated SiC_{10}/Al_{90} compact, are shown in Fig. 4.9. Remarkably, the SiC particles (sharp-edged light-gray particles) are embedded and distributed along the Al matrix (dark-gray background

matrix). Apparently neither voids nor cracks can be detected, indicating an excellent SiC/Al interfacial bonding [Fig. 4.9(*a*)]. Moreover, no reacted product of amorphous or an intermediate phase can be identified, suggested by segregation of the elements of Al and Si in the composite sample on a micron scale, as shown in Figs. 4.9(*b*) and 4.9(*c*).

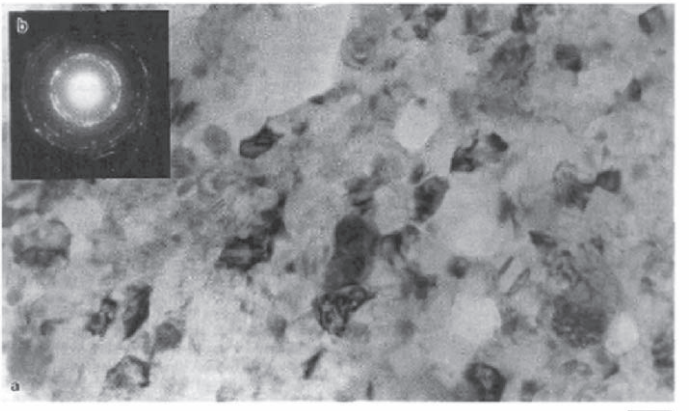

Figure 4.8. The *(a)* BFI and *(b)* the corresponding SADP of as-consolidated mechanically solid state mixed SiC_{10}/Al_{90} that ball milled for 86 ks. *(After El-Eskandarany.)*[14]

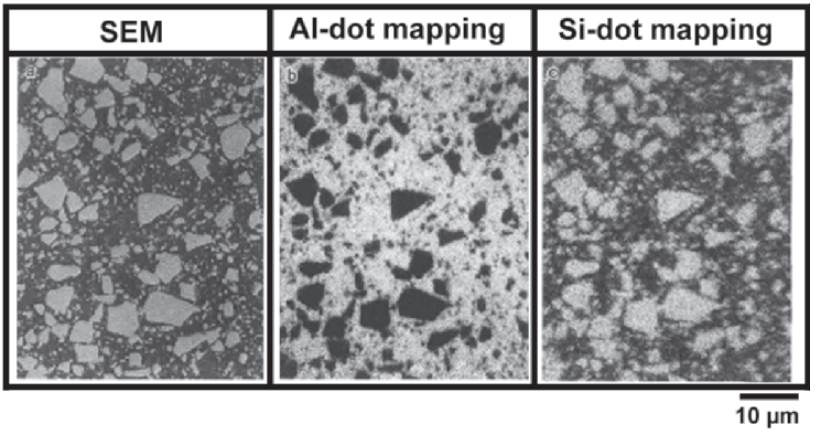

Figure 4.9. *(a)* The SEM micrograph and dot mapping of *(b)* Al and *(c)* Si of as-consolidated mechanically solid state mixed SiC_{10}/Al_{90} that ball milled for 86 ks. *(After El-Eskandarany.)*[14]

4.3.5 Properties

The bulk density of the as-consolidated SiC_x/Al_{100-x} composite samples is plotted as a function of the SiC content, *x*, in Fig. 4.10.

Obviously, the densities increase monotonically with an increase in the volume fraction of the reinforcement material, to have a maximum value of about 2.77 Mg m^{-3} for the sample which contains 10 vol % SiC, just above the theoretical density of pure Al (2.70 Mg m^{-3}). It is worth noting that the densities of all the consolidated samples presented in Fig. 4.10 are about 99.5% of the theoretical density, suggesting the formation of a fully dense SiC_x/Al_{100-x} composite material.

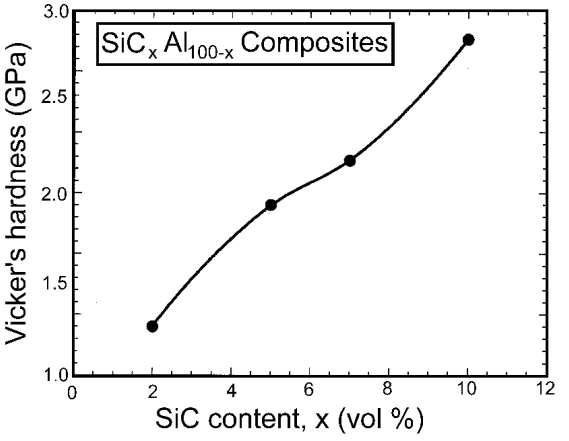

Figure 4.10. Influence of SiC concentration content on the bulk density of as-consolidated mechanically solid state mixed SiC_x/Al_{100-x} that ball milled for 86 ks. *(After El-Eskandarany.)*[14]

Figure 4.11 illustrates the effect of the SiC additives on the Vickers hardness of the consolidated samples. As expected, the hardness increases linearly with an increase in the volume fraction of the harder phase (SiC) in the soft matrix of metallic Al, to have a maximum value of about 2.6 GPa for the sample that contains 10 vol % SiC, which is well above the measured hardness of pure Al (about 0.95 GPa) under the same measurement conditions. Remarkably, the hardness values for all the SiC_x/Al_{100-x} samples have a narrow distribution range indicating a homogeneous distribution of the reinforcement particles in the Al matrix.

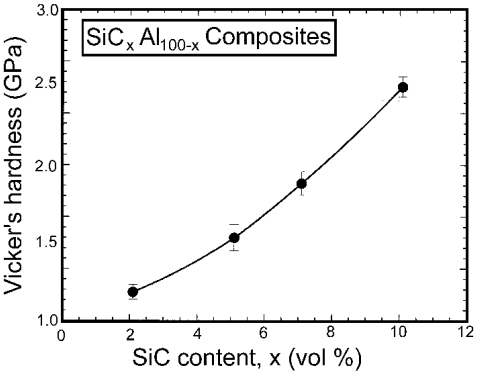

Figure 4.11. Correlation between SiC concentration content, *x*, and Vickers hardness of consolidated SiC_x/Al_{100-x} powders that ball milled for 86 ks. *(After El-Eskandarany.)*[14]

The elastic moduli presented by the bulk modulus, Young's modulus, and the shear modulus, of the consolidated mechanically-mixed SiC_x/Al_{100-x} composites, is shown as a function of the SiC content in Fig. 4.12. We should emphasize that the values of the elastic moduli of the consolidated samples have been estimated from the measured samples densities and the constant parameters of the non-destructive testing apparatus, as was explained elsewhere.[15][16] These values increase significantly with increasing the SiC content, suggesting the formation of a composite material that contains a brittle phase (SiC) which embedded in the ductile Al matrix.

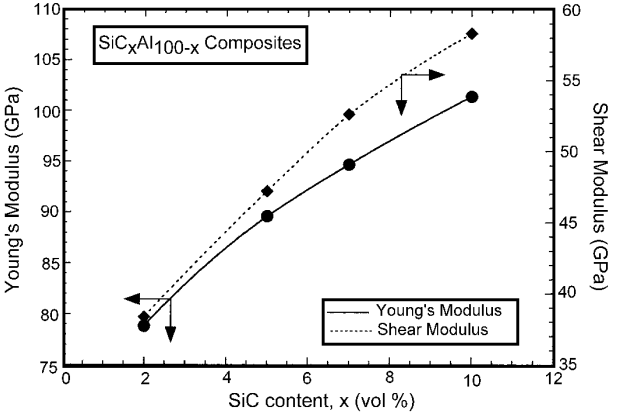

Figure 4.12. Dependence of the elastic moduli on the SiC concentration content, *x*, for consolidated SiC_x/Al_{100-x} powders that ball milled for 86 ks. *(After El-Eskandarany.)*[14]

4.4 MECHANISM OF FABRICATION

In this section, the mechanism for synthesis of this type of important engineering composite material will be discussed. In addition, the mechanism of powder consolidation into nanocrystalline compacts is explained as well. The challenge in processing SiC/Al composites is to promote wetting and interface formation between SiC and Al. Contrary to the liquid metallurgy technique, that may lead to the formation of undesirable brittle phases of Al_4C_3 and Si, the ball-milling technique shows the possibility of fabrication of nanocomposite SiC_xAl_{100-x} without the existence of these reactive products. Synthesizing nanocomposite SiC_p/Al by mechanical-mixing via ball-milling technique can receive much attention. This may be due to the simplicity in the technique and the huge amount of homogeneous composite powders that can be produced on an industrial scale at room temperature. Based on the above results, well bonded nanocomposite SiC_xAl_{100-x} powder particles are yielded by milling elemental Al and SiC powders in a high energy ball mill at room temperature. Neither solid solutions nor reactive products could be detected during the milling process.

First, it may be useful to classify the milling process into four stages according to the structure and morphological characteristics of the powder particles.

4.4.1 Formation of Agglomerates Coarse Composite SiC_p/Al Powder Particles

This refers to the first stage of the mechanical-mixing (0–22 ks). During the first few kiloseconds of milling, all the Al powder particles are stacked on the surface of the milling tools as a result of cold welding. Meanwhile, most of the hard particles of refractory SiC powders are disintegrated and do not blend with the agglomerated Al powders. As the milling time increased (3.6 ks), those hard particles of SiC that are refined (nearly 20 μm in diameter) and changed in shape to a spherical-like morphology penetrated and embedded into the soft deformed metallic matrix of Al particles to form coarse composite particles of about 1,000 μm in diameter.

4.4.2 Disintegration of the Agglomerates Composite SiC_p/Al Powder Particles

The first stage of milling is followed by a second stage (22 ks to 43 ks) in which the agglomerated composite particles are shattered and disintegrated into several particles apparently irregular in size [Fig. 4.2(*c*)]. The disintegration of the powder occurred as a result of continuous shear and impact forces generated by ball-powder-ball collisions. However, the morphology and composition of the individual composite powder at this milling time may differ remarkably from particle to particle and within the particle itself, the SiC particles have not separated from the host Al matrix and no free SiC and/or Al powders could be detected in the mill-product at this stage of milling. This is attributed to the well bonding between SiC and Al that was improved by the mechanical mixing.

4.4.3 Formation of Nanocomposite SiC_p/Al Powder Particles

Towards the end of the mechanical mixing processing (43 ks to 86 ks) a complete homogenization of the composite powder particles takes place. At this stage of milling, the powders become ultrafine and the size of the individual particles is less than 0.5 μm in diameter. In addition, the particle size distribution of the powders has become very narrow, indicating the formation of a homogeneous and uniform composite powder. The final product of the powder (86 ks) contains internal extraordinary equiaxed fine sphere grains of SiC about 3 nm in diameter.

4.4.4 Consolidation of Nanocomposite SiC_p/Al Powder Particles

An attractive technique that has been used for consolidation of several metallic and ceramics powders is the PAS. Nanocrystalline materials with grain size of less than 100 nm are receiving much attention due to their unique mechanical properties. The ball-milling technique has been considered a powerful tool for preparing such a class of materials. The important steps during the PAS process are

- the application of uniaxial load
- the application of pulsed voltage for plasma activation
- the resistance heating of graphite crucible and powders

As DC pulse voltage is applied to the powder, a micro-discharge takes place among the composite powder particles, which generates plasma. Hence, the atoms on the surface of each particle are activated, and the sintering procedure takes place in a short period of time (consolidation is achieved within a few kiloseconds, 0.3 ks). Accordingly, grain growth during sintering can be minimized and the sintered maintain their nanocrystalline properties.

Another important factor in PAS that governs the grain size of the consolidated samples is the source of the milled materials powders. When the as-milled powders, which are introduced to the PAS, have spherical homogeneous shape with fine nanocrystalline grains, the PAS step leads in parallel to the formation of nanocrystalline fully dense compacts.

It is worth noting that the PAS technique does not result in the formation of any undesirable reactive products, such as Al_4C_3 and Si. These products are usually obtained when the sintering temperature is above the melting point of pure Al.

REFERENCES

1. Zhang, J. S., Liu, X. J., Cui, H., Duan, X. J., Sun, Z. Q., and Chen, G. L., *Metall. Trans. A*, 28:1261 (1997)
2. Kalambur, A., and Hall, J. W., *Scripta Metall.*, 37:193 (1997)
3. Lee, J. C., Byun, J. Y., Oh, C. S., Seok, H. K., and Lee, H. I., *Acta. Metall. Mater.*, 45:5303 (1997)
4. *CRC Handbook of Chemistry, Physics*, 74th edition and CRC Press, p. 4–36 (1992)
5. *The MRCK INDEX*, 10th edition, Mrck & Co., p. 50 (1983)
6. Ferro, A. C., and Derby, B., *Acta. Metall. Mater.*, 43:3061 (1995)
7. Viala, J. C., Fortier, P., and Bouix, J., *J. Mater. Sci.*, 25:1842 (1990)
8. Narciso, J., Garacia-Cordovilla, C., and Louis, E., *Mater. Sci. Eng. B*, 15:148 (1992)
9. Ribes, H., Suery, M., L'sperance, G., and Legoux, G., *Metall. Trans. A*, 26:2637 (1995)
10. Lloyd, D. J., Lagace, H., McLeod, A., and Morris, P. L., *Mater. Sci. Eng. A*, 107:73 (1989)
11. Bartos, G., and Xia, K., in: *Proc. 4th Int. Conf. on Semi-Solid Processing of Alloys and Composites*, p. 290, University of Sheffield, England (1996)

12. Witulski, T., Winkelmann, A., and Hirt, G., in: *Proc. 4th Int. Conf. on Semi-Solid Processing of Alloys and Composites*, University of Sheffield, England, p. 242 (1996)
13. Novak, B. M., *Adv. Mater.*, 5:422 (1993)
14. El-Eskandarany, M. S., *J. Alloys Comp.*, 279:263 (1998)
15. El-Eskandarany, M. S., *J. Jpn Society of Powder and Powder Metallurgy*, 44: 547 (1997)
16. El-Eskandarany, M. S., Omori, M., Sumiyama, K., Hirai, T., and Suzuki, K., *J. Jpn Society of Powder and Powder Metallurgy*, 44:1143 (1997)

5

Mechanically Induced Solid State Carbonization

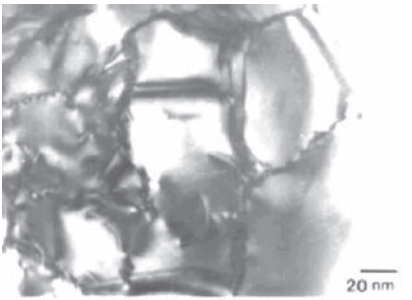

Carbides have a unique set of properties that are necessary for cutting tools. This is not only because they have great hardness and wear resistance, but also because they have good thermal shock resistance and thermal conductivity. In addition, they have good oxidation resistance. All of these properties are necessary for considering materials to serve as cutting tools.

5.1 INTRODUCTION

Carbides, especially those of the transition-metal carbides of IV and V groups in the periodic table, possess unusual properties that make them desirable and useful engineering materials for many industrial applications[1] (Fig. 5.1). They have great hardness values, ranging between 20 and 30 GPa, between alumina and diamond. Most of the carbides have extremely high melting points (2000ºC–3000ºC). For example, TaC has the

highest melting point known for any material (about 3983ºC), within a few degrees less than the sublimation point of graphite (4000ºC).

One important property of the metal carbides is their chemical stability at room temperature; they are attacked slowly when subjected only to very concentrated acidic media. The metal carbides are generally very strong at high temperatures with extremely high values of Young's modulus, however, they are brittle at room temperature. They undergo a brittle-to-ductile transformation at around 1000ºC. In fact, metal carbides are unique in that they combine the characteristic properties of metals and ceramics.

IV		V	
TiC	3067	VC	3648
	4.91		5.65
	29		29
ZrC	3420	NbC	3600
	6.59		7.79
	26		24
HfC	3928	TaC	3983
	12.67		14.5
	27		25

Figure 5.1. Selected properties[2] for metal carbides of the fourth and fifth groups in the periodic table.

From the above-mentioned characteristics of metal carbide, one can describe them as hard-stable materials. Thus, their properties place them on top of the refractory materials, which can find a wide range of industrial applications as cutting tools. In fact, carbides have a unique set of properties which are necessary for cutting tools. This is not only because they have great hardness and wear resistance, but also because they have good thermal shock resistance and thermal conductivity. In addition, they have a good oxidation resistance. All of these properties are necessary for considering the materials to be serviced as cutting tools.

The melting point (T_m) in ºC, density (ρ) in g/cm^3, and hardness (H) in GPa, for each metal carbide are presented as:

Eq. (5.1) $$\frac{T_m}{\frac{\rho}{H}}$$

As well as their applications in cutting tools, metal carbides are employed as wear resistant parts in wire drawing and extrusion and pressing dies. They are also used as drilling tools and bits for mining and petroleum field applications.

5.2 DIFFICULTIES OF PREPARATIONS

In the industrial scale of production, the technique of powder metallurgy is usually used for preparing polycrystalline metal carbides. In this process, a direct reaction between the powder form of metallic elements or their hydrides with graphite takes place at extremely high temperatures. Tables 5.1 and 5.2 summarize the different ways of obtaining the metal carbides, and the reaction temperature of selected systems.

Recently, a significant amount of attention has been focused on another technique for preparing metal carbides, using a method called self-propagating high-temperature synthesis (SHS).[3] In this process, a successful reaction between the reactant materials that are a mixture of elemental metals and graphite takes place only at a temperature well above the melting points of the metallic elements.[4]

Table 5.1. The Possible Methods for Fabrication of Transition-Metal (TM) Carbides via the Technique of Powder Metallurgy*

Method	Reaction
Direct reaction between metallic elements or metallic hydrides and graphite, under vacuum or inert gas.	$TM + C \rightarrow TMC$
	$TMH + C \rightarrow TMC + H_2$
Reduction of the metal oxide by graphite, under vacuum or inert gas.	$TMO + C \rightarrow TMC + CO$
Reaction of the metal with carbonizing gas.	$TM + C_nH_{1-n} \rightarrow TMC + H_2$
	$TMC + CO \rightarrow TMC + CO_2$

**(After Schwarzkopf et al.)*[2]

Table 5.2. The Reaction Temperatures for the Formation of Selected Transition-Metal Carbides from Elements via Powder Metallurgy Way of Fabrication*

REACTION	TEMPERATURE (°C)
$Ti + C \rightarrow TiC$	1700–2100
$Zr + C \rightarrow ZrC$	1800–2200
$Hf + C \rightarrow HfC$	1900–2300
$V + C \rightarrow VC$	1100–1200
$Nb + C \rightarrow NbC$	1300–1400
$Ta + C \rightarrow TaC$	1300–1500
$W + C \rightarrow WC$	1400–1600

**(After Schwarzkopf et al.)*[2]

From the above, it can be concluded that the preparation of homogeneous metal carbides with high purity via the traditional ways of fabrications is a difficult task. This is attributed to the application of high temperatures that may restrict the fabrication process, especially in developing countries where the facilities of high-temperature furnaces are limited. Accordingly, the high cost of this process is considered a major disadvantage for these processes and this increases the price of the end-product.

5.3 FABRICATION OF NANOCRYSTALLINE TiC BY MECHANICAL ALLOYING METHOD

Since all metal carbides are prepared at high temperatures (see Table 5.2), the possibility for preparing large amounts of homogeneous nanocrystalline TiC powders at room temperature has been proposed by El-Eskandarany.[6] Unlike all other techniques that are used for fabrication of metal carbides (see Table 5.1), MA leads to the production of metal carbides with nanoscale dimensions. These nanostructured refractory materials must receive tremendous attention due to their expected unique physical and mechanical properties that can add more advanced properties to this class of important material (see Ch. 3).

In this method, pure (99.9%) elemental Ti (30 μm) and carbon powders (5 μm) were used as the starting reactant materials and mixed to give the desired average composition of $Ti_{44}C_{56}$, then sealed in a sapphire vial (80 ml in volume) together with sapphire balls (10 mm in diameter) in a glove box under an Ar atmosphere. The ball-to-powder weight ratio was 10:1. The milling process was carried out at room temperature using high-energy ball mill (Laboratory Centrifuge Mill, P6, Germany). The ball-milling experiments were interrupted after selected milling times and a small amount of the powder was taken from the vial in the glove box. An individual MA experiment was carried out in order to determine the milling temperature during the solid-state reaction between the diffusion couples of Ti and C. This was achieved by fixing the end of a thermocouple at the outermost surface of the vial. The ball mill was then operated without interruption and the temperature of the vial was recorded after selected milling times. X-ray diffraction (XRD) with Cu$K\alpha$ radiation and transmission electron microscopy (TEM) operated at 200 kV have been used to monitor the structural changes of the powders after several ball-milling times; however, some samples have been characterized by high-resolution transmission electron microscopy (HRTEM) operated at 200 kV. The samples of TEM and/or HRTEM have been prepared by mixing the powders with a small amount of pure alcohol (2 ml in volume) and stirring for 30 s. Two or three drops of the suspension were placed on a Cu-microgrid and then well dried for about 1.8 ks before mounting the microgrid onto the TEM sample holder. The morphological (shape and size) changes of the powder after selected milling times were determined by scanning electron microscopy (SEM), operated at 20 to 30 kV, and optical microscope. In order to determine the Ti content and the contamination degree of Al (that might be introduced to the milled powders upon using the sapphire milling tools), the powders of the final product (720 ks) have been analyzed by the induction coupled plasma emission method. On the other hand, the concentration of C and oxygen contamination content, that is introduced to the powders during the milling procedure and/or during the powder handling outside the glove box, has been determined by the helium carrier fusion-thermal conductivity method.

The mechanically reacted powders were then consolidated in vacuum at 1963 K under pressure ranging from 19.6 to 38.2 MPa for 0.3 ks, using a plasma activated sintering (PAS) method. In order to avoid undesired grain growth, the sintering process was applied for only 0.18 ks.

No binding material was used in this consolidation procedure. The as-consolidated samples were also characterized by means of XRD, transmission TEM, SEM, and chemical analyses, using the same experimental conditions as previously shown. Selected samples (the end-product) have been investigated by high-resolution transmission electron microscope (HRTEM). The density of the consolidated TiC was determined by Archimedes' principle using water immersion. Vickers indenter, with a load of 50 kg, was used to determine the hardness of the compacted samples which milled for selected MA times. The hardness values reported below are averaged from ten indentation results. In addition, some mechanical properties of the consolidated samples have been determined by non-destructive tests.

Table 5.3 shows the chemical analyses of the as-milled and as-consolidated samples of TiC. Obviously, the as-sintered sample gains 0.10 at. % oxygen during the consolidation procedure, however, the sintering was achieved under high vacuum, as high as 6.0×10^{-6} torr. This may be attributed to some leaks in the vacuum system of the PAS, nevertheless, the total contamination content of the bulk sample is 0.38 at. %, acceptable for several industrial applications.

Table 5.3. Chemical Analyses of As-Milled and As-Consolidated Mechanically Reacted TiC After 720 ks of Ball-Milling Time

Sample	Ti content (at.%)	C content (at.%)	Al content (at.%)	O content (at.%)
As-Milled	44.80	54.93	0.03	0.24
As-Consolidated	44.45	55.17	0.03	0.35

5.4 PROPERTIES OF MECHANICALLY SOLID STATE REACTED TiC POWDERS

5.4.1 Structural Changes with the Milling Time

The XRD patterns of ball-milled $Ti_{44}C_{56}$ powders are presented in Fig. 5.2 after selected MA times. After 2 ks [Fig. 5.2(*a*)], the powders are mixtures of the starting reactant materials, characterized by the sharp Bragg peaks of elemental Ti and C. Increasing the MA time (6 ks to 8 ks) leads to a remarkable decrease in the intensity of the Bragg peaks for pure graphite crystals [Figs. 5.2(*b*)–(*c*)] that can be hardly seen after 11 ks of the MA time [Fig. 5.2(*d*)]. This is attributed to a solid state diffusion of the C atoms that have small atomic radii in the lattice of hcp-Ti. Moreover, the Bragg peaks for pure Ti crystals shifted to the low angle side, suggesting the formation of an interstitial hcp-TiC solid solution [Fig. 5.2(*d*)]. After 15 ks of MA time [Fig. 5.2(*e*)], a new phase, corresponding to NaCl-TiC is yielded, characterized by the Bragg peaks of TiC (111), TiC (200), TiC (220), TiC (311), and TiC (222) reflections. After 22 ks of the MA time, the Bragg peaks of the reactant materials (Ti and graphite), surprisingly, disappeared and the reflections that come from TiC crystals become sharp and pronounced, indicating the completion of the MA process [Fig. 5.2(*f*)].

The lattice parameter (a_0) of the formed phase for TiC was calculated after 40 ks [Fig. 5.2(*g*)] of the MA time and found to be 0.4326 nm, in good agreement with the reported value (0.4327 nm).[7] It is worth noting that the intensity ratios of these Bragg peaks are almost in good agreement with those of the TiC powder,[7] suggesting that the crystal structure of the obtained powders is of the NaCl type. Increasing the MA time to 80 ks [Fig. 5.2(*h*)] leads to an increase in the mechanical deformation that is generated by the milling tools, causing a remarkable decrease in the grain size of the milled powders, suggested by the broadening of the Bragg peaks at this stage of milling. Further milling (720 ks) leads to the formation of nanocrystalline TiC, indicated by very broad Bragg peaks, as shown in Fig. 5.2(*i*). This formed phase of TiC does not transform to any other phase(s) even after longer milling times, as long as 1,000 ks.

Detailed TEM analyses have been performed in order to understand the local structure changes of the mechanically reacted powders during the several stages of the MA process. The HRTEM micrograph of the powders that milled for 2 ks of the MA time is shown in Fig. 5.3. The powders are mixtures of pure Ti (zone I) and graphite (extended thin veins in zone II). The lattice fringe spacing in zone II of Fig. 5.3 is measured to

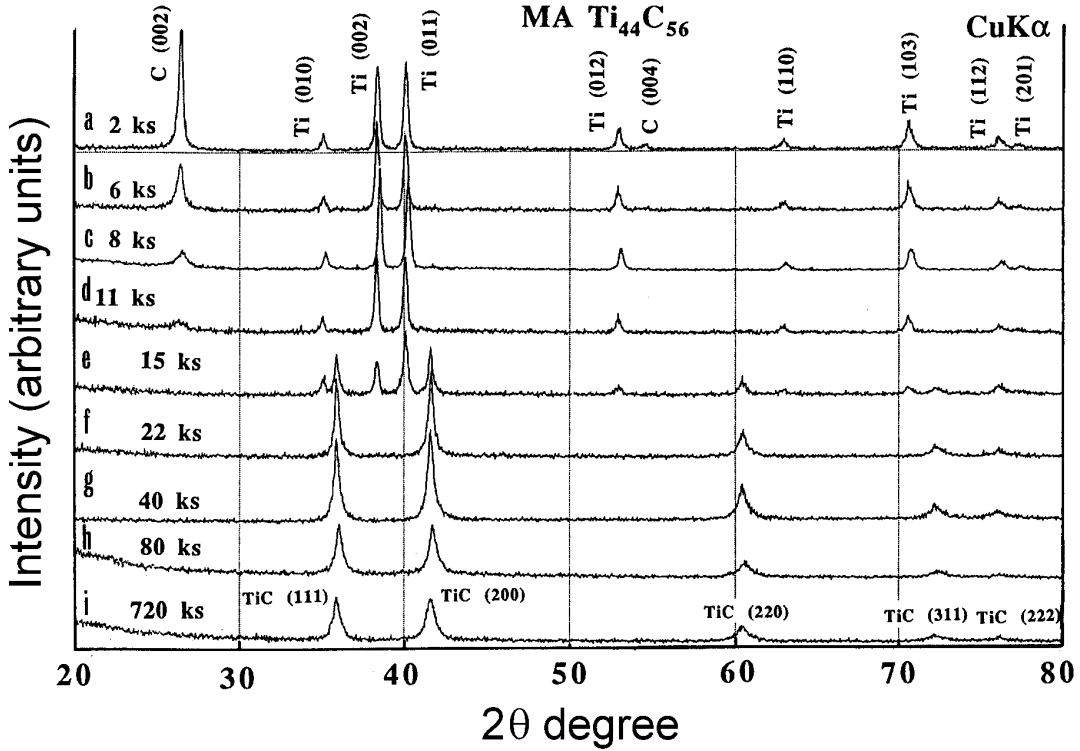

Figure 5.2. XRD patterns of mechanically alloyed $Ti_{44}C_{56}$ powders after selected MA time. *(After El-Eskandarany, et al.)*[6]

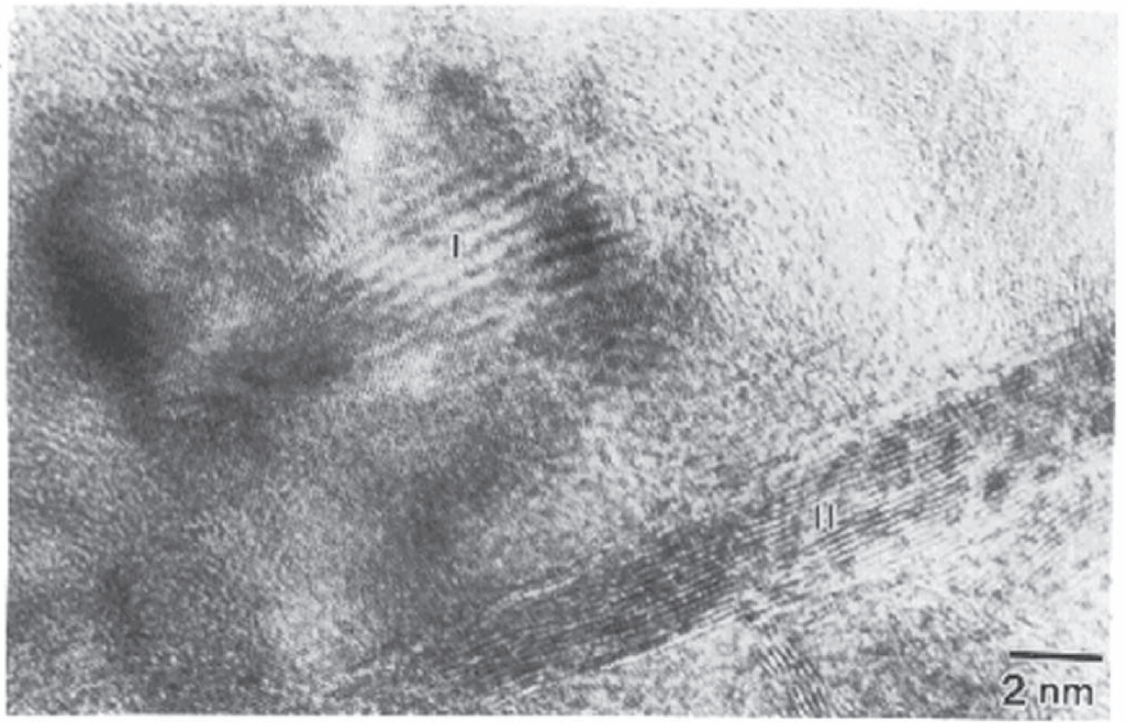

Figure 5.3. HRTEM image of mechanically alloyed $Ti_{44}C_{56}$ powders after 2 ks of the ball-milling time. *(After El-Eskandarany.)*[6]

be 0.335 nm, which matches the plane (002) of carbon (0.338 nm). The existence of the TiC phase could not be detected at this stage of milling. The bright field image (BFI) of the powders that milled for 11 ks is shown in Fig. 5.4. Obviously, the particle is a typical Ti/C composite, containing thin veins (less than 10 nm in thickness) of C layers embedded in the soft matrix of Ti. A mechanical solid state reaction takes place at the interfaces of these fresh layers and a new phase of TiC results after further milling time. Figure 5.5 shows the bright field image (BFI) of the powders that milled for 15 ks of MA time. The structure of the particle is somewhat fine; however, several faults and defects, such as twins and nanotwins, are observed. The presented BFI is classified into three zones, i.e., I, II, and III, and the corresponding selected area diffraction patterns (SADPs) [Figs. 5.5(*b*), (*c*), and (*d*)] are shown as insets in the micrograph. At this stage of milling, the powders differ widely in internal structure from region to region with a heterogeneous structure.

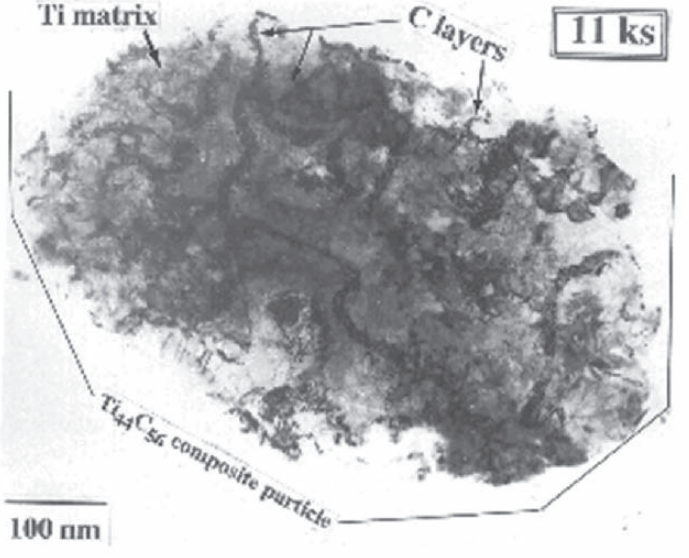

Figure 5.4. BFI image of mechanically alloyed $Ti_{44}C_{56}$ powders after 11 ks of the ball-milling time. *(After El-Eskandarany.)*[5]

The SADP presented in Fig. 5.5(*b*) (corresponding to zone I), consists of sharp rings that correspond to the coarse fcc-TiC grains (the obtained product), coexisting with unprocessed hcp-Ti (sharp spots). Zone II is a TiC-rich region, which coexisted with small mole fractions of unprocessed Ti crystals (sharp spot patterns), as shown in Fig. 5.5(*c*). Zone III, however, shows the existence of a single phase of fcc-TiC [Fig. 5.5(*d*)].

The BFI and the corresponding SADP of the powders which were milled for 40 ks, are shown, together in Fig. 5.6. Overall, the sample consists of rather coarse lenses or cells with wide size distribution, ranging from 20 to 60 nm [Fig. 5.6(*a*)]. Remarkably, a single phase of NaCl-type TiC is detected, characterized by the Debye-Scherrer rings corresponding to TiC, as indicated in Fig. 5.6(*b*). No free Ti and/or C crystals could be observed after this stage of milling.

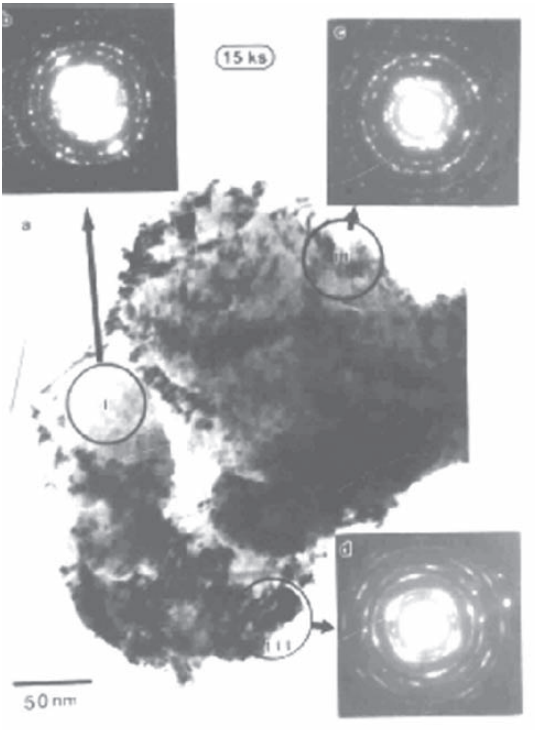

Figure 5.5. *(a)* BFI and *(b–d)* the corresponding SADPs of a mechanically alloyed sample after milling for 15 ks. The sample differs widely in structure within the particle itself. *(After El-Eskandarany.)*[6]

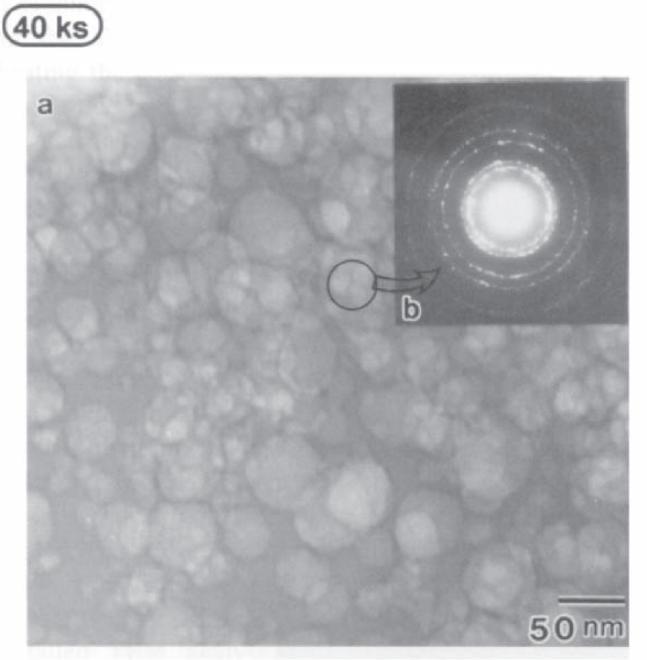

Figure 5.6. *(a)* The BFI and *(b)* the corresponding SADP for the sample that is obtained after 40 ks of the MA time. The micrograph shows cell structure morphology with lens-like morphology of about 35 nm in diameter. *(After El-Eskandarany.)*[6]

After 80 ks of the MA time, the powders have nanocrystalline spherical grains of about 4 nm (or less) [Fig. 5.7(*a*)] in diameter. The indexed SADP still shows clear fcc-rings of the obtained TiC [Fig. 5.7(*b*)]. The absence of the spots in the SADP indicates the formation of fine grain TiC powders.

The HRTEM image of the final-product for TiC that was ball milled for 720 ks of the MA time is presented in Fig. 5.8. HRTEM observations show the lattice fringe image of TiC alloy. This lattice fringe spacing was measured to be about 0.250 nm which matches well with the interplanar spacing of TiC (111).[7]

The crystalline size of mechanically alloyed $Ti_{44}C_{56}$ powders has been determined directly by using TEM techniques at different MA times. The results are compared with those results obtained from the XRD analyses, using the Scherrer equation and are plotted in Fig. 5.9 as a function

of the MA time. The figure shows that the MA process for formation of nanocrystalline TiC consists of four stages. In the first stage (0 to 11 ks), called the stage of formation of composite Ti/C particles, the grain size of these composite cells is slightly decreased to an average size of about 1000 nm in diameter.

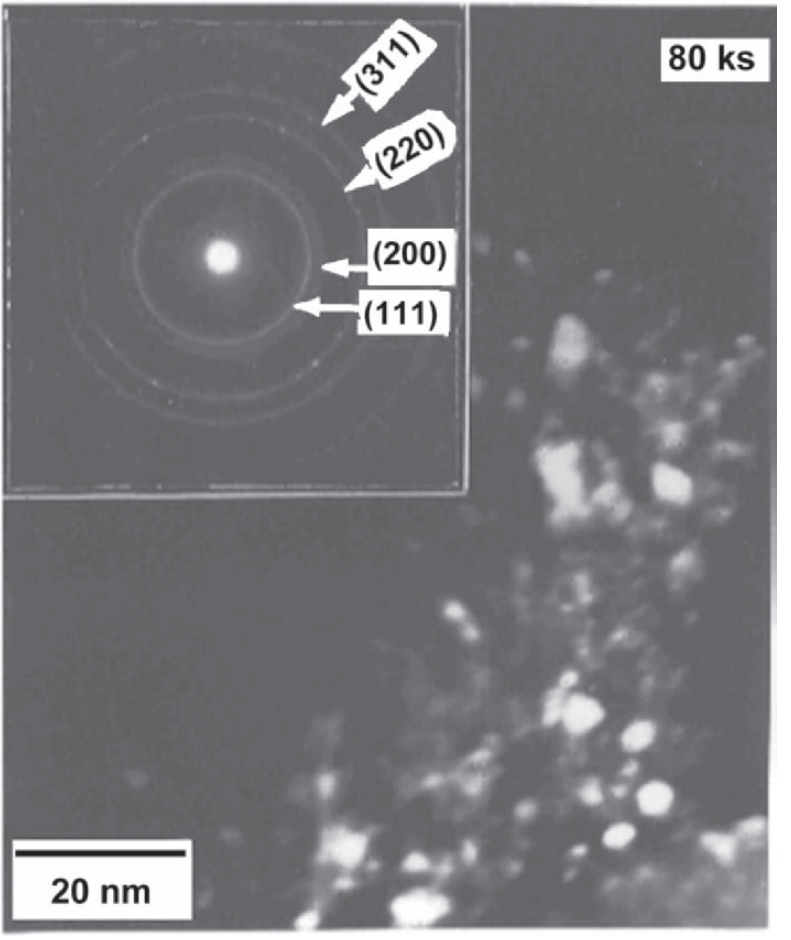

Figure 5.7. *(a)* The dark field image and *(b)* the corresponding SADP for the sample at the final stage of MA (80 ks). At this stage of milling, their powders contain nanocrystalline spherical cells of less than 4 nm in diameter *(a)* with fcc-structure corresponding to the TiC-phase *(b). (After El-Eskandarany.)*[5]

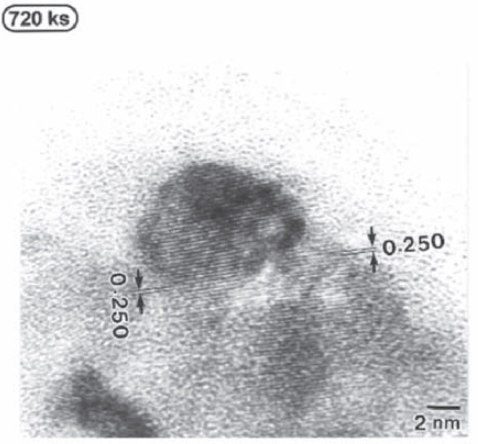

Figure 5.8. HRTEM image of sample at the refining stage of milling (720 ks). The micrograph shows the lattice fringe spacing (0.250 nm) that matches well with the interplanar spacing of TiC (111). *(After El-Eskandarany.)*[6]

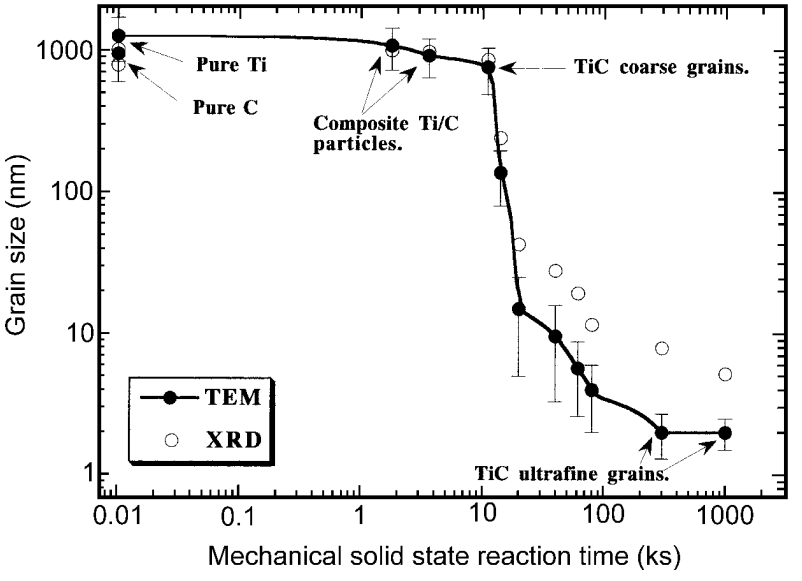

Figure 5.9. Dependence of the crystalline size of mechanically alloyed $Ti_{44}C_{56}$ powders on the MA time. *(After El-Eskandarany.)*[5]

In the second stage (11 to 20 ks), almost all the reactant materials of Ti and C are completely reacted and very coarse grains of TiC, ranging from 800 to 1000 nm, are formed. This stage is followed by the third stage (20 to 80 ks) in which the grains of TiC are disintegrated dramatically to form rather fine grains with wide distribution (ranging from 100 to 5 nm diameter). Toward the last stage of milling, which is called the refining stage or homogenization stage (80 to 1000 ks), extraordinarily fine grains (about 2 nm in diameter) of TiC alloy powders are formed, with narrow size distribution (± 1 nm or less).

5.4.2 Morphology

The SEM technique was used to follow the changes in shape and size of the milled powders during the different stages of MA process. Figure 5.10 shows the SEM micrographs of the milled powders after selected MA times. At the starting stage (0 ks), the powders of the reactant materials of Ti/C [Fig. 5.10(*a*)] are bulky, with random shape and size.

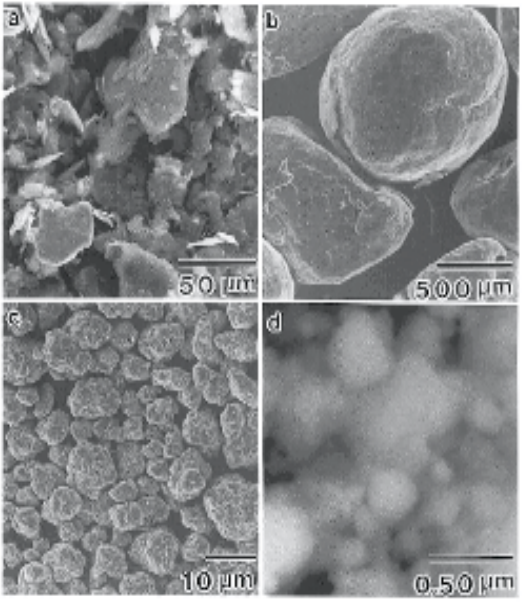

Figure 5.10. The SEM micrographs of the powders of mechanically alloyed TiC powders after *(a)* 0 ks, *(b)* 11 ks, *(c)* 40 ks, and *(d)* 720 ks of the ball-milling time. *(After El-Eskandarany.)*[6]

During the early stage of milling (11 ks), the powders tend to agglomerate and form large composite Ti/C particles of about 1000 μm in diameter [Fig. 5.10(*b*)]. The metallographical examinations of the polished and etched particles show that the individual particle contains many thick layers of the diffusion couples of Ti and C powders (Fig. 5.11). A solid state reaction takes place at the clean-interfaces of these layers, and a new single phase of TiC (product) is formed after 20 ks of milling. This is confirmed by the surprising disappearance of the reactant layers, as displayed in Fig. 5.11.

After 40 ks of milling, the large composite particles are disintegrated into smaller powders with an average diameter of 10 μm, as shown in Fig. 5.10(*c*). Toward the end of the MA process (refining stage), the powders possess excellent morphological properties, such as homogeneous shapes with fine and smooth surface relief and uniform size (less than 0.3 μm in diameter), as shown in Fig. 5.10(*d*).

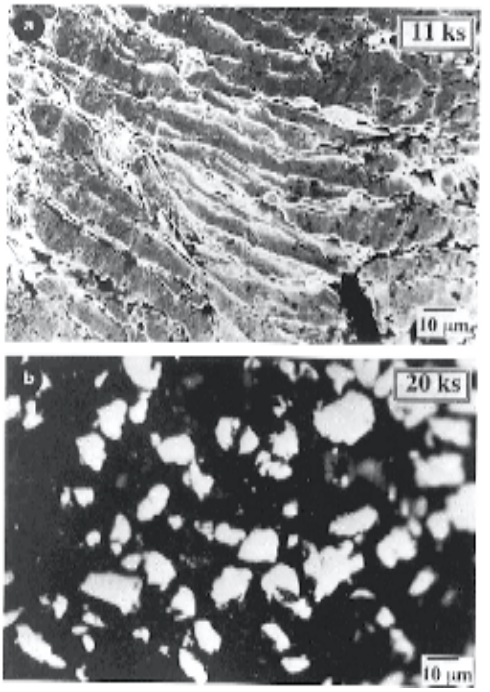

Figure 5.11. Cross-sectional view of polished and etched particles of mechanically alloyed TiC after *(a)* 11 ks and *(b)* 20 ks of the ball-milling time. *(After El-Eskandarany.)*[5]

5.4.3 Consolidation

A sintering step using PSA technique (see Ch. 3) is applied to consolidate the powders after a selected MA time. Figure 5.12 shows the cross-sectional view of as-consolidated powders that were milled for 15 ks [Fig. 5.12(*a*)], 40 ks [Fig. 5.12(*b*)], and 720 ks [Fig. 5.12(*c*)]. As was previously presented in the x-ray analysis [Fig. 5.2(*e*)], after 15 ks of the MA time, the as-milled powder consists of two phases: unreacted metallic Ti and fully reacted fcc-TiC. Since the consolidation procedure took place at 1963 K [just above the melting point of Ti (1943 K)] and far below the melting point of TiC (3373 K), the particles of TiC in the mixed powders [the agglomerated particles in the center of Fig. 5.12(*a*)] are embedded in the molten Ti matrix to form composite Ti/TiC compact. Thus, the consolidated samples, after this stage of milling, are either rich or poor in TiC. During Vickers hardness measurements, the sample hardness varies from few (nearly 2.5 GPa) to 29 GPa, as shown in Fig. 5.14.

The microstructure of the consolidated sample for the end-product (40 ks) shows a high-density structure with nearly equiaxed grains of about 15 μm in diameter, as shown in Fig. 5.12(*b*). The microstructure of the consolidated powders after the refining stage of MA (720 ks) possess fine grains (less than 5 μm in diameter) and dense structure, as presented in Fig. 5.12(*c*). It should be noted that the irregular grain edges in some cases, shown in Figs. 5.12 (*b*) and (*c*), arise from the long etching time used during the sample preparation.

The BFI and corresponding SADP of the as-consolidated sample that milled for 720 ks of the MA time, are shown in Fig. 5.13. The highly dense and the nanostructure characteristics of the sintered sample can be noted. Comparing this micrograph with the one in Fig. 5.7, we can conclude that the consolidation step leads to moderate grain growth. Since the average grain size of this consolidated sample is less than 100 nm (about 60 nm in diameter), one can say that the sintered sample maintains its nanocrystalline character. In addition, this consolidation step does not lead to any structural changes, and the sintered TiC bulk material maintains its fcc-structure, as shown by the indexed SADP in Fig. 5.13(*b*).

The dependence for the hardness of the consolidated TiC samples on the MA time and the grain size is displayed in Fig. 5.14. As was previously displayed in Figs. 5.6 and 5.7, increasing the MA time leads to refine the grains of the milled powders. At a specific MA time, the grain size of the compact sample is dependent on the original grain size of the as-milled powders that are used as source for the consolidation procedure. This

correlation can be understood from the plot of the grain size for as-milled and as-consolidated samples against the MA time (Fig. 5.15). One can conclude that increasing the MA time leads to a decrease in the grain size of the powders which leads to a remarkable decreasing in the grain size of the sintered samples.

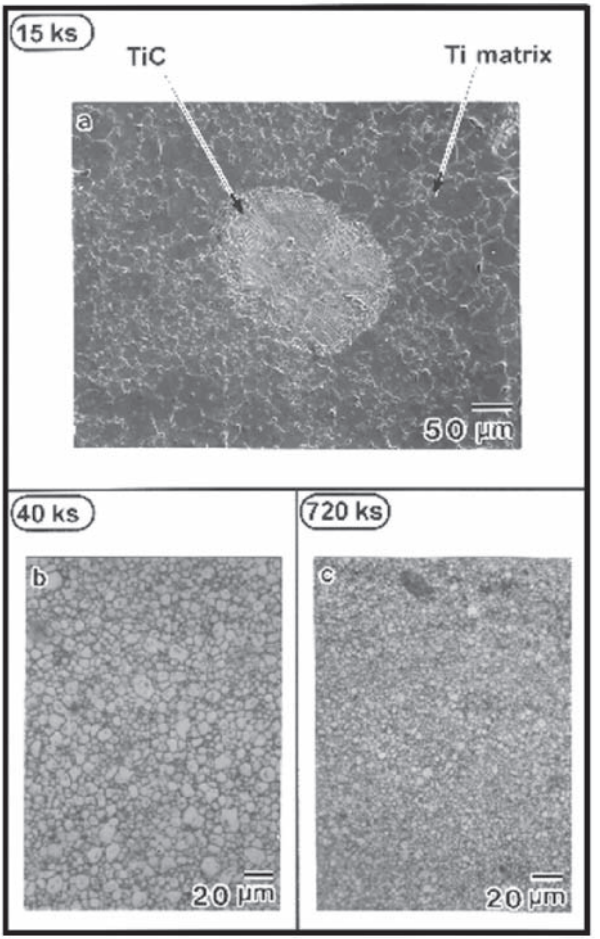

Figure 5.12. Cross-sectional views of the as-consolidated powders which milled for *(a)* 15 ks, *(b)* 40 ks, and *(c)* 720 ks of the MA time. During the consolidation of the powders of the early stage of milling, the TiC particles are embedded in the molten Ti matrix to form composite Ti/TiC compact *(a)*. The micrographs of the final and refining stages reveal the fine structure of single phase of TiC. *(After El-Eskandarany.)*[6]

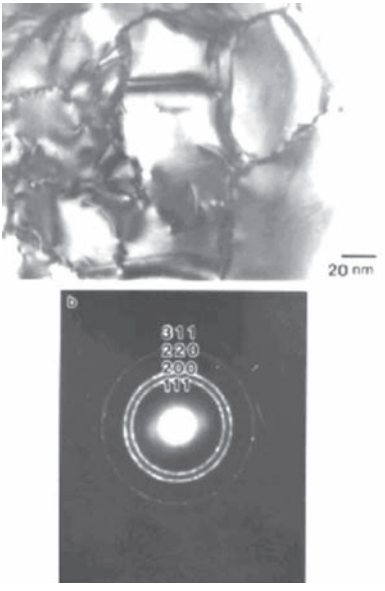

Figure 5.13. *(a)* BFI and *(b)* the corresponding SADP of the as-consolidated TiC powders after milling for 720 ks. The highly dense and the nanostructure characteristics of the sintered sample can be noted. *(After El-Eskandarany.)*[6]

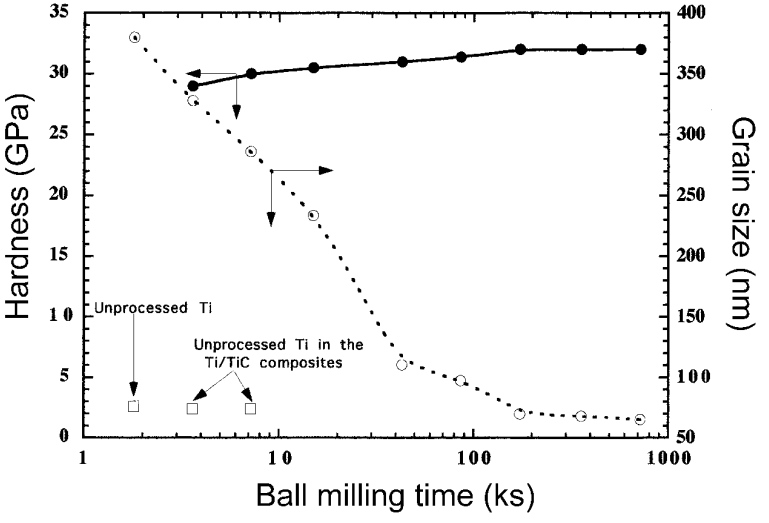

Figure 5.14. Correlation between the hardness, grain size, and the MA time, for as-consolidated TiC bulk alloys. *(After El-Eskandarany.)*[6]

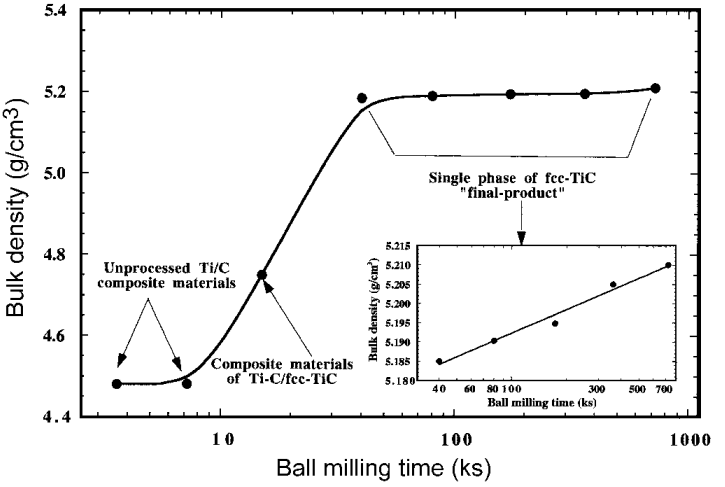

Figure 5.15. Correlation between the bulk density of the consolidated samples and the MA time. The densities vs. the MA time for the as-consolidated samples at the final and refining stages of milling, shown in a different scale, inset the figure. The slight increase in the values of densities (5.185 to 5.210 g/cm^3) at these two stages of milling, may be attributed to the grain refining, which can play an important role for getting higher density materials. *(After El-Eskandarany.)*[6]

Thus, the MA time can play an important role for obtaining nanocrystalline bulk material with improved grain size strengthening. As the grain size of the compacted samples decreased, the Vickers hardness value increased, to be about 32 GPa after 720 ks of MA time. It is worth noting that the high hardness value of this sample is attributed to the grain boundary hardening effect due to Hall-Petch assumption.

The bulk density of the as-consolidated samples is plotted as a function of the MA time in Fig. 5.15. During the early and intermediate stages of milling (3 to 40 ks), the bulk density increases monotonically by increasing the MA time, suggesting the existence of the higher density phase (TiC). That portion of the relation between the MA time and the density at the final and refining stages of the MA (40 to 720 ks), is presented in a larger scale inset of Fig. 5.15. The densities of the consolidated samples at this stage of milling are increased linearly in a range from 5.185 to 5.210 g/cm^3. This slight increase may be attributed to grain refining which can play an important role in obtaining higher density materials. Comparing the values of the densities for the samples at the refining stage (5.210 g/cm^3) with the theoretical density of TiC indicates that the sintered TiC is fully dense.

The Poisson's ratio and the elastic modulii of the consolidated powders have been estimated from measured sample densities and the constant parameters of the nondestructive testing apparatus and plotted as a function of MA times in Figs. 5.16 and 5.17, respectively. Increasing the MA time leads to an increase in the fraction of TiC vs. that of unreacted Ti. This leads to a monotonic decrease in the value of Poisson's ratio to approximately 0.261 after 720 ks of the MA time. This value is smaller than one for unprocessed metallic Ti (0.321), suggesting the formation of brittle phase of TiC.

The elastic modulii presented by the bulk modulus, Young's modulus, and the shear modulus, of the consolidated mechanically reacted TiC powders are shown as a function of the MA time in Fig. 5.17. These values increase significantly during the early and intermediate stages of milling (0 to 40 ks), suggesting an increase of the TiC in the milled powders. Toward the end of the MA process (40 to 720 ks), the values of the elastic moduli are almost saturated or slightly increased, indicating the formation of a single homogeneous phase of TiC.

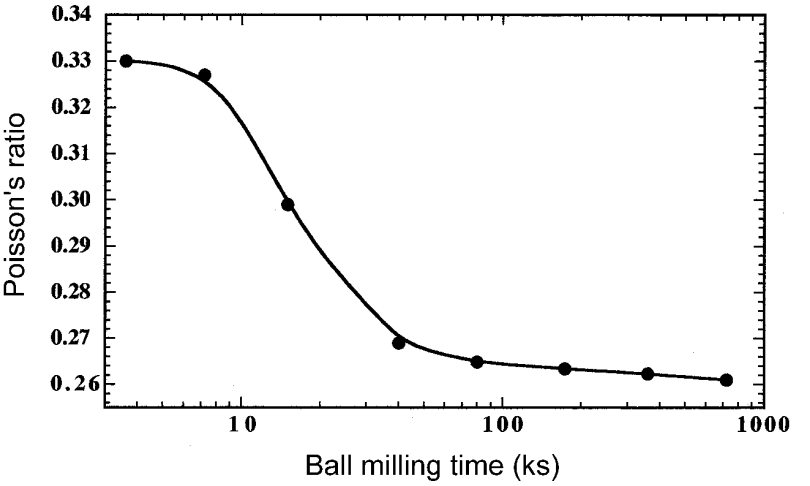

Figure 5.16. Dependence of Poisson's ratio of the consolidated powders on the MA time. The remarkable decrease in this ratio indicates the progress of the solid state reaction and the increasing of TiC phase in the milled powders. *(After El-Eskandarany.)*[6]

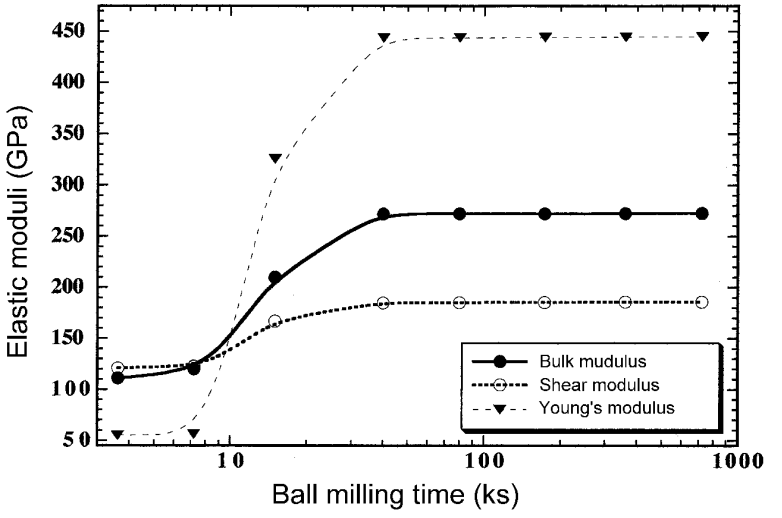

Figure 5.17. Relationship between the elastic modulii of the consolidated powders and the MA time. The remarkable increase in these values suggests monotonical increasing of a hard phase of TiC. *(After El-Eskandarany.)*[6]

5.4.4 Mechanism of Fabrication

In fact, Ti-C is a typical exothermic reaction with a large negative heat of formation (-77 kJ/mol).[8] Based on the results of the present study, $Ti_{44}C_{56}$ is yielded upon high-energy ball milling of elemental Ti and graphite powders at room temperature. Neither solid solution nor amorphous phases could be detected at the end stage of the milling process. In this section, the mechanism for formation of TiC alloy powders by MA method will be discussed. In addition, the consolidation of the product powders into nanocrystalline compacts is explained.

Figure 5.18 presents the dependence of the vial's temperature on the MA time. We should emphasize that the measured temperature here cannot be used to tell us the actual temperature that occurs at the ball-powder-ball collision or the heat liberated during the reaction of Ti with C. This is because the actual temperature decreased when transferred from the reacted zones in the innermost portion of the vial to the outermost surface of the vial. Hence, the measured temperature here can just be used to express the kinetics of the reaction during the several stages of milling.

These experiments have been done using an agate vial containing the milling charge of reactant materials of Ti and C powders, together with the milling media (the agate balls). The data was obtained by fixing the end of a thermocouple at the outermost surface of the vial; the ball mill was then operated without any interruptions. The temperatures of the vial were recorded at selected MA times (solid line). In order to observe the relative temperature rise during the reaction, the same experiments were done using the same vial but containing the milling media only (broken line).

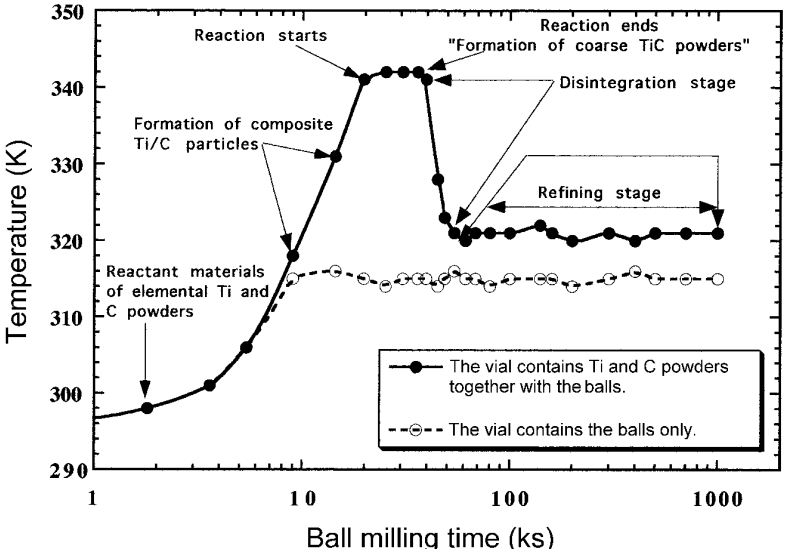

Figure 5.18. Dependence of the vial's temperature on the MA time and the vial contents during the ball-milling process. *(After El-Eskandarany.)*[6]

Obviously, the temperature of the vial that contains the milling media only is monotonically increased by increasing the milling time to obtain a value of 315 K after 9 ks of milling time. No remarkable change in this value could be observed even after a longer milling time (1000 ks). The situation differs when the ball mill contains both the balls and the reactant materials. In this case, the vial's temperature increased monotonically during the first few kiloseconds of milling (0 to 9 ks). During the second stage of milling (9 to 15 ks), however, the temperature is dramatically increased to get a maximum value of 332 K after 15 ks of MA time.

During this early stage of milling the powder particles of Ti and C are blended together and grown in size to form composite particles of a larger diameter (about 800 μm) as a result of cold welding. A partial reaction between the reactant powders takes place, and a small mole fraction of TiC is formed after 11 ks of milling. At this stage, the solid state reaction starts and considerable amounts of the product (TiC) are formed.

The previous stage of milling is followed by a second stage (14 to 40 ks), in which a complete solid state reaction takes place between the diffusion couples of Ti and C in the composite particles and a new phase of NaCl-$Ti_{44}C_{56}$ is formed. Here, all the reactant materials have already reacted completely, and a single phase of TiC is formed after about 22 ks. During this stage of milling, the vial's temperature is increased to about 342 K (Fig. 5.18). This reaction is accompanied by the evolution of heat. Thus, the heat liberated on reacting Ti with C, which transferred to the surface of the vial, is measured to be 28 K (net temperature). It should be noted that the net temperature of the vial during this stage equals the difference between the temperature of the vial when it contains the milling charge of the balls and the powders and the temperature of the vial when it contains the balls only. The temperature of the vial saturated at this value for a duration of MA time equals 40 ks.

After the reaction is completed, the temperature of the vial decreases drastically during the disintegration stage (40 to 54 ks), to have a minimum value of 328 K after 54 ks of the MA time. Once the temperature of the vial is decreased, the powder particles are no longer welded on the surface of the ceramics milling tools so that the powders are forwarded to the effect zone of the milling media (balls). Thus, a drastic decreasing in the particle size could be achieved. During this disintegration stage (40 to 80 ks), the powder particles have a smooth surface relief, spherical-like morphology, and individual particle sizes of about 1 μm in diameter. In addition, the particles consist of fine cells with an average grain size of about 35 nm in diameter.

During the refining stage of the MA (80 to 720 ks), a complete homogenization of the powder particles takes place. At this stage of milling, the powders become ultrafine and the size of the individual particles is less than 0.8 μm in diameter. Moreover, the particle size distribution of the powders has become very narrow, indicating the formation of homogeneous and uniform powder particles. This final-product contains internal extraordinarily fine crystallites of about 4 nm in diameter. The vial's temperature is almost saturated at a value close to 320 K during this last stage of milling which extends from 54 to 1,000 ks.

5.5 OTHER CARBIDES PRODUCED BY MECHANICAL ALLOYING

In this section, selected examples are given of carbide synthesis by mechanical alloying of elemental component powders which produce the phase predicted by the equilibrium phase diagram.

5.5.1 Fabrication of β-SiC Powders

Among ceramics composites, the cubic form of SiC (β-SiC) has received much attention as a promising semiconductor for high-temperature, high-frequency, and high-power, electronic devices, due to its wide band gap, high-saturated electron velocity, excellent thermal stability, and high-breakdown field.[9] Moreover, its intrinsic resistance to oxidation, corrosion, and creep, at high temperatures also makes it a desirable protective coating for devices operating at elevated temperatures.[10] Single crystal β-SiC thin films are conventionally grown on Si(100) substrate by the chemical vapor deposition (CVD) process using cold-wall or hot-wall techniques.

In 1995, El-Eskandarany et al.[11] could prepare stoichiometric β-SiC powders by solid state reaction of elemental silicon and carbon powders via the room temperature mechanical alloying process. The MA process was performed in a high-energy ball mill similar to the one used for preparing TiC powders (see Sec. 5.3). Complete fcc-SiC alloy powders were obtained after 1080 ks of milling (300 h). The XRD patterns of the end-product of as ball-milled $Si_{50}C_{50}$ powders is shown in Fig. 5.19 after 1080 ks of MA time. The Bragg peaks for this end-product are broad, suggesting the formation of fine grain alloy powders. The lattice parameter (a_0) of the formed β-SiC was calculated to be 0.4357 nm,[12] in excellent agreement with the reported value (0.4358).[13]

Figure 5.20 illustrates the infrared transmission of $Si_{50}C_{50}$ powders at (*a*) starting stage (0 ks), (*b*) final stage (as-milled for 1080 ks), and (*c*) as-milled, for 1080 ks then annealed under vacuum at 1773 K for 86 ks. At the starting stage of milling [Fig. 5.20(*a*)], there is no evidence of any oxide phase(s), such as SiO_2. Contrary to this, a narrow absorption band is observed at about 9.5×10^2 cm^{-1}, suggesting the existence of longitudinal optical (LO)-like phonon mode. In addition, the existence of transverse optical (TO)-like phonon mode is observed at lower energy (about 8.4×10^2 cm^{-1}), as shown in Fig. 5.20(*b*). It can be concluded that a complete β-SiC phase is formed after 1080 ks. This formed phase has a nanocrystalline

structure with an average grain size of about 7 nm in diameter (Fig. 5.21). We should emphasize that almost the same TO- and LO- like phonon modes corresponding to the β-SiC phase are observed in the alloy powders after annealing the final product in vacuum at 1773 K for 86 ks. The other absorption bands centered at 10.9×10^2, 7.8×10^2, and 4.75×10^2 cm^{-1} are due to the existence of the SiO_2 phase in the as-annealed powders [Fig. 5.20(*c*)].

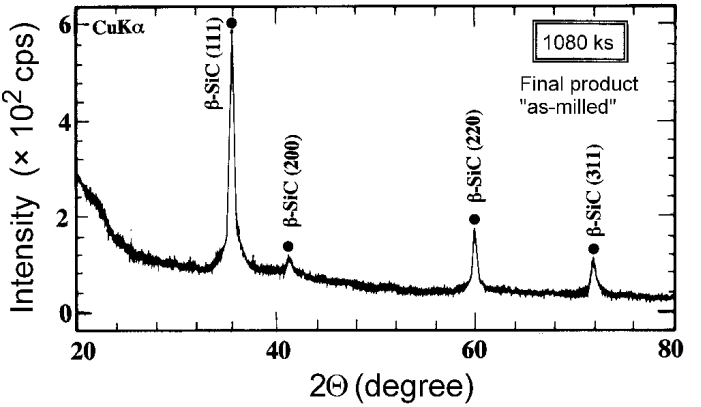

Figure 5.19. The XRD pattern of as-ball milled $Si_{50}C_{50}$ powders after the final stage of mechanical alloying (1080 ks). *(After El-Eskandarany.)*[11]

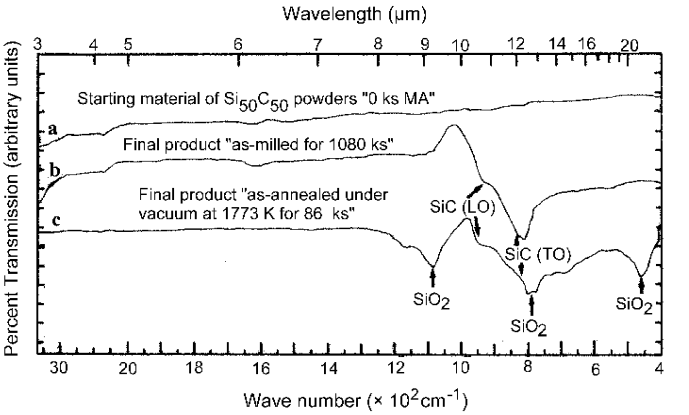

Figure 5.20. Infrared transmission spectra of *(a)* unmilled $Si_{50}C_{50}$ powders, *(b)* final product of β-SiC powders which were obtained after 1080 ks of milling, and *(c)* final product of β-SiC powders after 1080 ks of milling, then annealed under vacuum at 1773 K for 86 ks. *(After El-Eskandarany.)*[11]

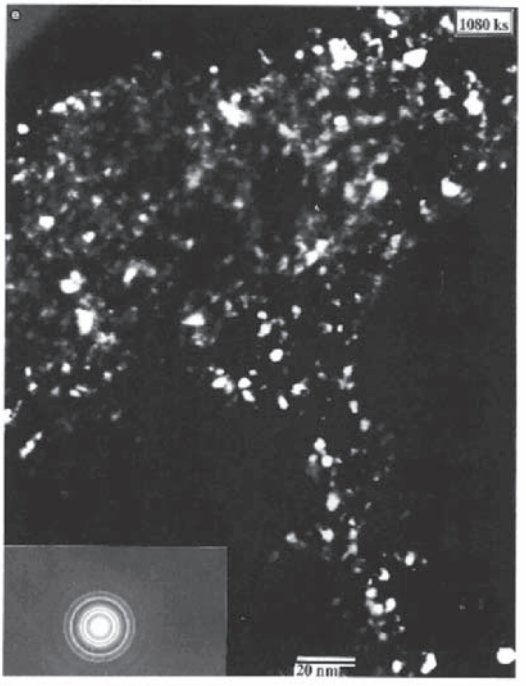

Figure 5.21. The DFI and corresponding SADP of the end product of β-SiC phase after 1080 ks of ball-milling time.

5.5.2 Fabrication of Nanocrystalline WC Powders

It has been reported by some authors[14][15] that a single hcp phase of WC can be fabricated by high-energy ball milling of elemental W and carbon powders. The end-product (432 ks) of as-mechanically alloyed WC powders possesses nanocrystalline characteristics, with an average grain size of less than 5 nm,[15] as indicated by the broad Bragg peaks of hcp-WC which are presented in Fig. 5.22(*a*). Hot pressing of the mechanically alloyed WC powders at 1773 K leads to slight grain growth and the compact sample still retains its nanocrystalline characteristics, with an average grain size of about 45 nm [Fig. 5.22(*b*)]. Contrary to this, consolidation of the powders at a higher temperature (1973 K) leads to a dramatic grain growth and the compact sample loses its unique nanocrystalline characteristics [Fig. 5.22(*b*)].

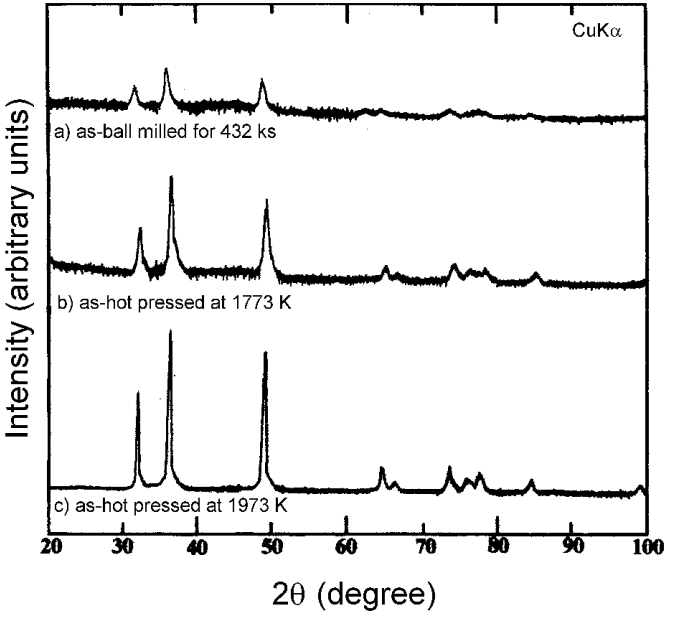

Figure 5.22. XRD patterns of the end product of WC after *(a)* ball milling for 432 ks, *(b)* milling for 432 ks and then hot pressed at 1773 K, and *(c)* milling for 432 ks and hot pressed at 1973 K phase. *(After El-Eskandarany et al.)*[15]

5.5.3 Fabrication of Nanocrystalline ZrC Powders

Mahdy et al.[16] successfully synthesized nanocrystalline powders of $Zr_{56}C_{44}$ by high-energy ball milling of elemental Zr and C powders at room temperature. They have reported that a complete single phase of fcc-ZrC was obtained after 173 ks of milling time. The fabricated ZrC powders possess excellent morphological characteristics, such as a homogeneous shape (spherical-like morphology) with fine and smooth surface relief, and uniform size (less than 0.5 μm in diameter).

The fabricated refractory ZrC powders have fine cell-like structure with nanoscale dimensions of about 5 nm in diameter.[16] Cold- and hot-pressing techniques have been used to consolidate the end-product of the milled powders (259 ks) into fully dense (>99.5%) compacts. In the consolidation procedure, the powders were pressed at 1573 K with a pressure of 1.0–1.5 GPa for 43 ks.

The BFI (near-edge) of as-consolidated ZrC at a temperature of 1573 K, is presented in Fig. 5.23. Obviously, the compact is fully dense and practically free of voids and/or cracks. Moreover, the sample contains nearly equiaxed grains with an average size of 95 nm in diameter. We should emphasize that while preparing the sample for TEM observations (polishing, ion milling, and etching), some grains resulted with a thickness of more than 100 nm. These grains, especially those that are at the far edge (right-hand lower side), reflect dark-contrast images, as shown in Fig. 5.23.

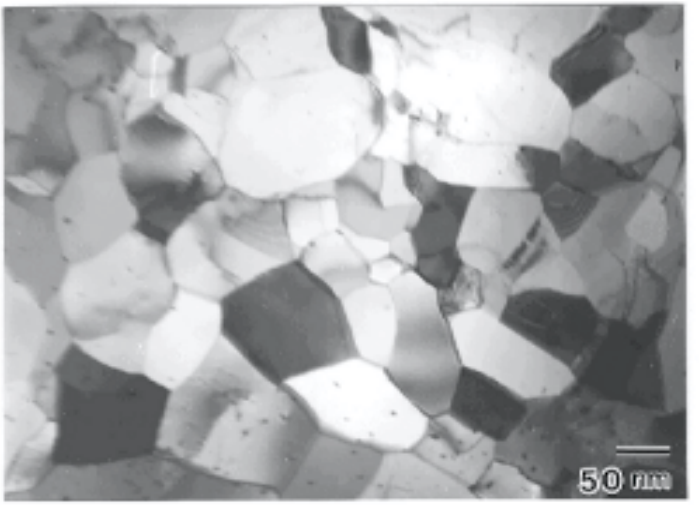

Figure 5.23. The BFI of as-hot-pressed ZrC powders of the final product, 259 ks of milling. *(After Mahdy et al.)*[16]

Figure 5.24 shows the grain size distribution which was determined from at least 150 representative grains taken from several BFI micrographs of the consolidated ZrC compact that was hot-pressed at 1573 K. The average grain size is estimated to be 95 nm, far below the one which calculated from an XRD diffraction pattern (130 nm) of the same consolidated sample (Fig. 5.25), using the Scherrer equation. It is worth noting that

those few larger grains (much larger than 100 nm, i.e., submicrons) are very few when compared with those grains that are less than 100 nm in diameter.

A well-known empirical dependence of strength and hardness on porosity and grain size for ceramics materials is given in Refs. 17–20.

Eq. (5.2) $H = Kd^{-a}e^{-bP}$

where H is the hardness value, d is the grain size, P is the specimen porosity, and K, a, and b are the empirical constants. The constant, a, can be approximated to be 0.5.[21]

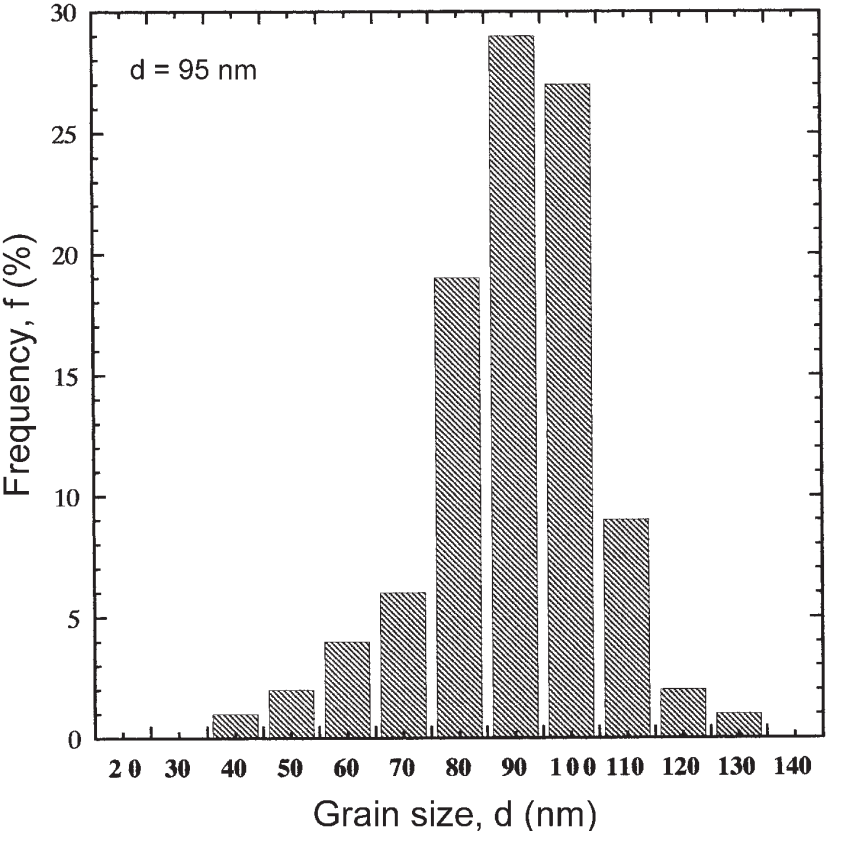

Figure 5.24. Grain size distribution of consolidated $Zr_{56}C_{44}$ (259 ks of milling time) at 1573 K (1.5 GPa) as determined from several TEM micrographs. *(After Mahdy et al.)*[16]

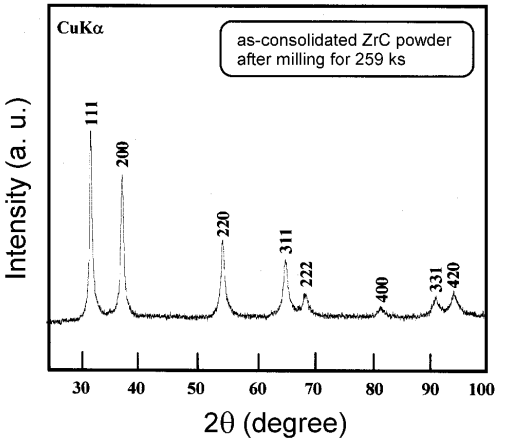

Figure 5.25. XRD pattern of consolidated $Zr_{56}C_{44}$ (259 ks of milling time) at 1573 K (1.5 GPa). The sample reveals fcc structure without the existence of any reacted product. *(After Mahdy et al.)*[16]

Figure 5.26 shows the correlation between the *P* of the consolidated samples that were hot-pressed at various temperatures, and the combined effect of *H* and *d*. It can be noted that the hardness increases with an increase in the values of density (low porosity values) and grain size. A linear relation obtained with a slope, $b = 5.575$, is similar to that found for a variety of materials (3.7 [17]–[19] 6.6–6.7[20][21]).

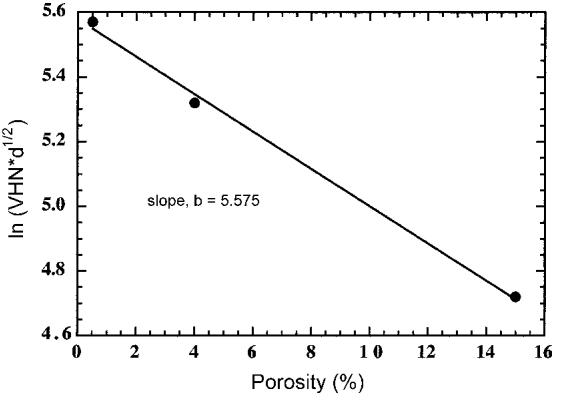

Figure 5.26. Dependence of the Vickers hardness on porosity and grain size of bulk $Zr_{56}C_{44}$ (259 ks of milling time) material. *(After Mahdy et al.)*[16]

REFERENCES

1. Storms, E. K., *The Refractory Carbides*, Academic Press, New York (1967)
2. Schwarzkopf, P., and Kieffer, R., *Refractory Hard Metals*, Macmillan, New York (1953)
3. Munir, Z. A., *Ceramic. Bull.*, 67:342 (1988)
4. Munir, Z. A., and Anselmi-Tamburini, U., *Mater. Sci. Rep.*, 3:277 (1989)
5. El-Eskandarany, M. S., *Metall. Trans. A*, 27:2374 (1996)
6. El-Eskandarany, M. S., *J. Alloys Comp.*, 305:219 (2000)
7. ASTM Card No. 32-1383, *ASTM*, Philadelphia, PA
8. de Boer, F. R., Boom, R., Mattens, W. C. M., Miedema, A. R., and Niessen, A. K., *Cohesion in Metals-Transition Metal Alloys*, 1:127, 1st Ed. North-Holland, Amsterdam (1988)
9. Chiu, C. C., Desu, S. B., and Tsai, C. Y., *J. Mater. Res.*, 8:2617 (1993)
10. Sasaki, K., Samkuma, E., Misawa, S., Yoshida, S., and Gonda, S., *Appl. Phys. Lett.*, 45:72 (1984)
11. El-Eskandarany, M. S., Sumiyama, K., and Suzuki, K., *J. Mater. Res.*, 10:659 (1995)
12. El-Eskandarany, M. S., Konno, T. J., Sumiyama, K., and Suzuki, K., *Mater. Sci. Eng. A*, 217/218:265 (1996)
13. *ASTM* Card No. 1-1119
14. Wang, G. M., Millet, P., Calka, A., and Campbell, S. J., *Mater. Sci. Forum*, 179/181:183 (1995)
15. El-Eskandarany, M. S., Mahdy, A. A., Ahmed, H. A., and Amer, A. A., *J. Alloys Compounds*, 312:315 (2000)
16. Mahdy, A. A., El-Eskandarany, M. S., Ahmed, H. A., and Amer, A. A., *J. Alloys Comp.*, 299:244 (2000)
17. Ryshkewitch, E., *J. Am. Ceram. Soc.*, 36:65 (1953)
18. Duckworth, W., *J. Am. Ceram. Soc.*, 36:68 (1953)
19. Knudsen, F. P., *J. Am. Ceram. Soc.*, 42:376 (1959)
20. Rice, R. W., *Mater. Sci. Eng.*, 73:215 (1985)
21. He, L., and Ma, E., *J. Mater. Res.*, 11:72 (1996)

6

Mechanically Induced Gas-Solid Reaction

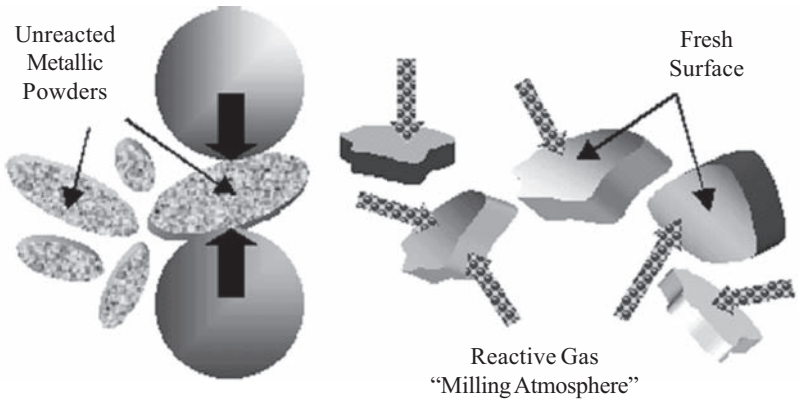

Ball-Powder-Ball Collisions Formation of Fresh Active Surfaces

Reactive ball-milling (RBM) technique has been considered as a powerful tool for fabrication of metallic nitrides and hydrides via room temperature ball milling. The flowchart shows the mechanism of gas-solid reaction through RBM that was proposed by El-Eskandarany. In his model, the starting metallic powders are subjected to dramatic shear and impact forces that are generated by the ball-milling media. The powders are, therefore, disintegrated into smaller particles, and very clean or fresh oxygen-free active surfaces of the powders are created. The reactive milling atmosphere (nitrogen or hydrogen gases) was gettered and absorbed completely by the first atomically clean surfaces of the metallic ball-milled powders to react in a same manner as a gas-solid reaction owing to the mechanically induced reactive milling.

6.1 INTRODUCTION

Nitrides possess unique properties which are highly desirable for a variety of applications. They are technologically important materials because of their hardness, stability at high temperatures, and electrical and optical properties.[1] Titanium nitride (TiN) alloys are used for cutting tools, tool coatings, solar-control films, and microelectronics applications. It is harder than alumina and thermally stable to about 3300 K. TiN is chemically stable with respect to most etching solutions, has a low receptivity, and provides an excellent diffusion barrier against metals.[1]

The cubic form of TiN can be obtained by several methods, such as activated reactive evaporation,[2] self propagating combustion method[3] under high nitrogen pressure (10^5 atm), and high temperature (1500 K), and the plasma spray method[4] under nitrogen gas flow. Moreover, a chemical vapor deposition technique has been also used for TiN preparation by reacting the titanium tetrachloride ($TiCl_4$) with ammonia (HN_3) at temperatures above 1300 K. In addition, the low-temperature physical vapor deposition and atmospheric pressure chemical vapor deposition,[1] and reactive sputtering[5] techniques are used widely for the preparation. The high costs of preparation and the excess of contamination in the end-product are the disadvantages of these methods.

6.2 FABRICATION OF NANOCRYSTALLINE TiN BY REACTIVE BALL MILLING

The formation of metal nitrides at room temperature was proposed by El-Eskandarany et al.[6] when they milled metallic powders of Ti or Fe under a flow of nitrogen gas atmosphere using a high-energy ball mill. So far this technique, which is called reactive ball milling (RBM),[7] has been employed for preparing some other metal nitrides[8][9] and hydrides.[10]

In this method, pure elemental Ti powder (99.5 at. %) and purified nitrogen gas (99 wt %) have been used as starting reacting materials. The powder was charged into a stainless steel (SUS 316) vial (250 ml in volume) together with twenty five stainless steel (SUS 316) balls (10 mm in diameter) and sealed in a glove box under a purified argon (99.99 wt %) atmosphere. The ball-to-powder weight ratio was 10 to 1. The reactive milling took place by mounting the vial in a high-energy ball mill (Fritsch P6) equipped with a rotary pump and a gas flow system. The vial was evacuated for about 4 ks and then a flow (1.0 ml s^{-1}) of nitrogen gas was

passed through the inlet of the vial via a plastic pipe. The outlet of the vial was connected with an oil bubbler. Once the gas bubbles were observed, the RBM experiment started with a milling rate of 4.2 s^{-1} at room temperature. Milling was stopped periodically, after selected ball-milling times and the powders were completely discharged from the vial in the glove box. Large amounts (90 vol %) of the mechanically reacted powders were then consolidated in vacuum at 1963 K under pressures ranging from 19.6 to 38.2 MPa for 0.3 ks, using a PAS method. In order to avoid undesired grain growth, the sintering process was applied for only 0.18 ks. The as-milled and as-consolidated samples were characterized by means of x-ray diffraction (XRD) with Cu$K\alpha$ radiation, transmission electron microscopy (TEM) using a 200 kV microscope, scanning electron microscopy (SEM) using a 20 kV microscope, optical microscopy, and chemical analysis. The hardnesses of the compacted samples were determined using a Vickers indenter with a load of 50 kg. In addition, densities of the consolidated samples were determined by Archimedes' principle, using water immersion. Some mechanical properties of the consolidated samples have been determined by non-destructive testing.

6.3 PROPERTIES OF REACTED BALL MILLED TiN POWDERS

6.3.1 Structural Changes with the Milling Time

The XRD analysis has been used to follow the progress of the gas-solid reaction during milling of elemental Ti powder under flow of nitrogen gas (Fig. 6.1). At the starting stage of RBM time (0 ks), the XRD pattern displays sharp Bragg peaks reflections corresponding to polycrystalline hcp-Ti powder, as shown in Fig. 6.1(*a*). After 22 ks of the RBM time, a new phase, corresponding to NaCl-type TiN appears [Fig. 6.1(*b*)]. The Bragg peaks corresponding to the TiN become sharp and pronounced after 43 ks of RBM time [Fig. 6.1(*c*)], indicating an increasing of TiN fraction in the milled powder. At this stage of milling, the structure of the powder differs widely from particle to particle and within particles. After 173 ks of RBM time, all the Bragg peaks corresponding to the metallic Ti disappeared and a single phase of nanocrystalline TiN appears, indicated by the broad Bragg peaks in Fig. 6.1(*d*). The lattice parameter, a_0, of this phase was calculated from (111) and (200) reflections and found to be 0.4243 nm, which is in agreement with the reported value of pure TiN (0.4242 nm).[11]

The dark field image (DFI) and the selected area diffraction pattern (SADP) of the end-product of TiN powder is shown in Fig. 6.2. The powder consists of fine grains (about 5 nm in diameter or less) with cell-like morphology [Fig. 6.2(*a*)] indicating the formation of nanocrystalline TiN powder. Moreover, the SADP [Fig. 6.2(*b*)] indicates the formation of a single phase of NaCl-type TiN. No hcp-Ti crystals could be detected, as presented in Fig. 6.2(*b*).

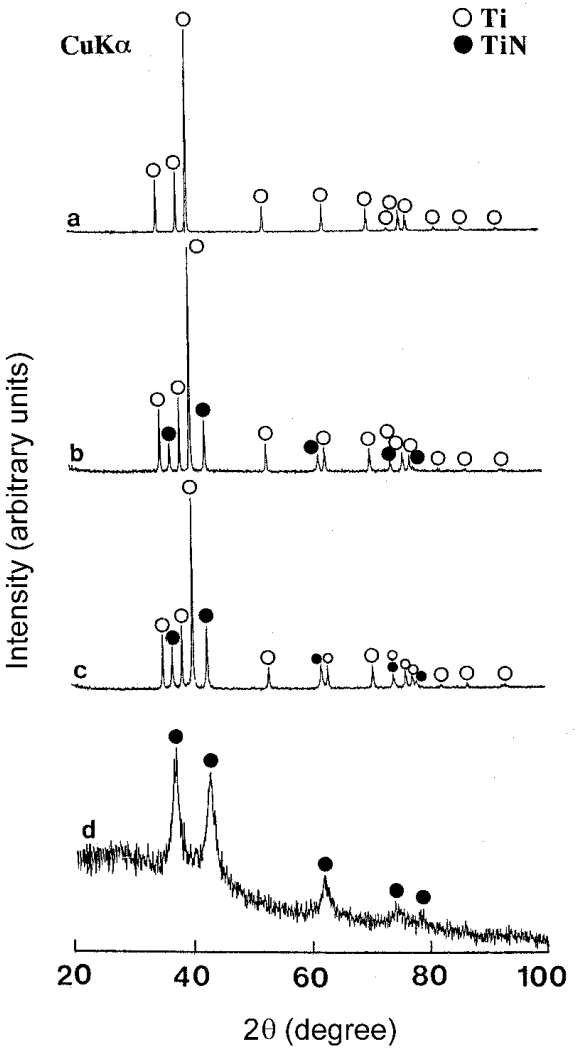

Figure 6.1. XRD patterns of Ti powders milled under flow of nitrogen after *(a)* 0 ks, *(b)* 22 ks, *(c)* 43 ks, and *(d)* 173 ks of RBM time. *(After El-Eskandarany et al.)*[12]

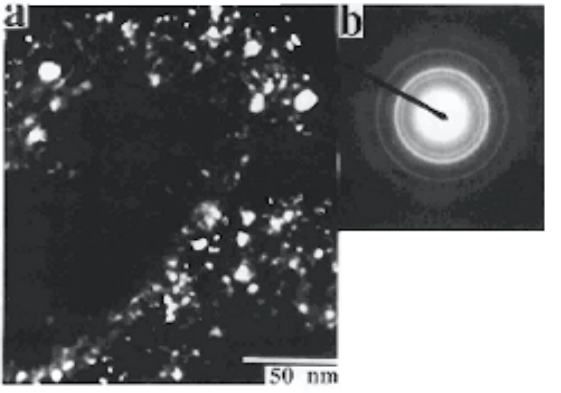

Figure 6.2. *(a)* DFI of the end-product of NaCl-TiN powders, and *(b)* the corresponding SADP. *(After El-Eskandarany et al.)*[7]

6.3.2 Morphology

SEM was used to follow the morphological and metallographical changes of powders during the different stages of the RBM. The starting Ti powder has a flake-like morphology and a wide particle size distribution, as shown in Fig. 6.3(*a*). After 3.6 ks of RBM time, the Ti powders agglomerate due to the success of the cold welding and form larger powder particles with an average particle size of about 400 μm, as shown in Fig. 6.4(*a*). These agglomerated particles are disintegrated upon further milling (7.2 ks) and this leads to the formation of powder particles that have fresh or active surfaces [Fig. 6.3(*b*)] with a lath-like topology [Fig. 6.3(*c*)]. Metallographical examination of the powders after 11 ks of RBM time show that individual agglomerated particles contain cracks and tend to be separated into smaller particles along the crack zones [Fig. 6.4(*b*)]. Finally, and after 22 ks of RBM time, the larger particles are divided into smaller powder (less than 40 μm in diameter), as presented in Fig. 6.4(*c*). As the RBM time increases (43 ks), a drastic decrease in the size of the powder occurs, being in the range of 5 μm to 30 μm [Fig. 6.3(*d*)]. Towards the end of the RBM process (86 ks to 173 ks), the powder of the end-product of TiN has homogeneous spherical-like morphology with an average particle size of about 0.4 μm (or less), as shown in Fig. 6.5.

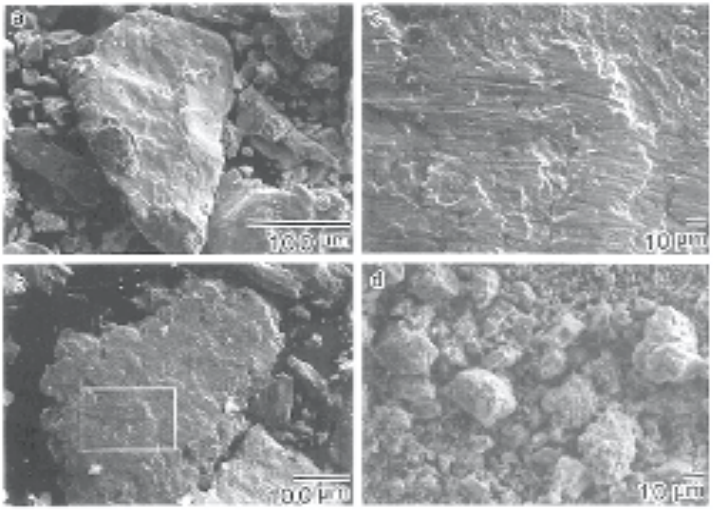

Figure 6.3. SEM micrographs of Ti powders milled under flow of nitrogen for *(a)* 0 ks, *(b and c)* 7.2 ks and *(d)* 43 ks of the RBM time. The indexed area in *(b)* is shown in another scale in *(c)*. *(After El-Eskandarany et al.)*[12]

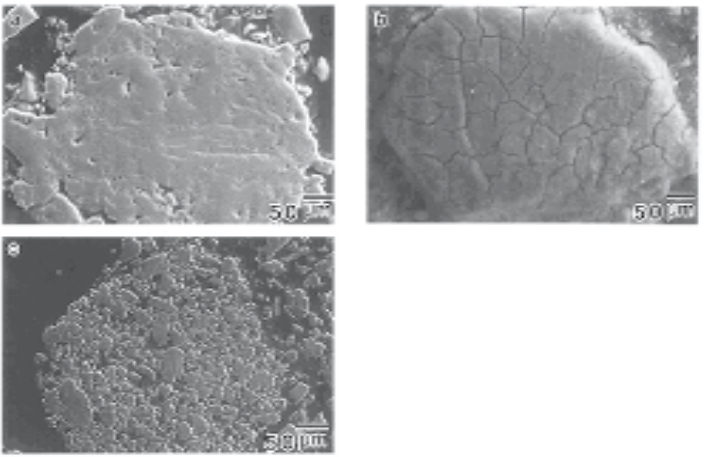

Figure 6.4. SEM micrographs of the cross sectional view of Ti powders milled under flow of nitrogen for *(a)* 3.6 ks, *(b)* 11 ks, and *(c)* 22 ks of RBM time. *(After El-Eskandarany et al.)*[12]

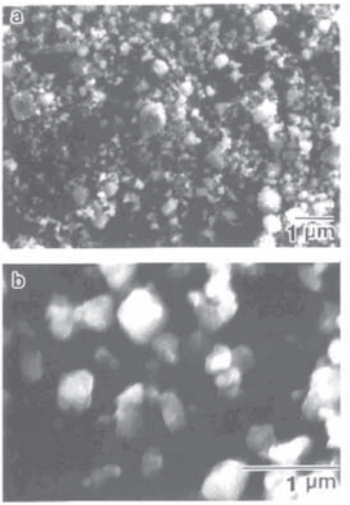

Figure 6.5. SEM micrographs of Ti powders milled under flow of nitrogen for *(a)* 86 ks and *(b)* 173 ks of RBM time. The presented powders here are fully reacted TiN. *(After El-Eskandarany et al.)*[12]

A sintering step is applied to consolidate the powders after selected RBM times. Figure 6.6 shows a SEM micrograph of the cross-sectional view of as-consolidated powder that has been RBM for 43 ks. As was presented in the previous section [see Fig. 6.1(*c*)], after 43 ks of the RBM time, the as-milled powder consists of two phases; unreacted metallic Ti and fully reacted TiN powders. Since the consolidation of the powder took place at 1963 K, just above the melting point of pure Ti (1943 K) and far below the melting point of TiN (3563 K), the TiN particles in the mixed powder (the agglomerated particles in the center of Fig. 6.6) are embedded in the molten Ti matrix to form composite Ti/TiN compact. Thus, the consolidated samples for this stage of RBM (11 ks to 86 ks) are either rich or poor in TiN. During the Vickers hardness measurements, the sample hardness varies from a few GPa to nearly 20 GPa, as shown in Fig. 6.7. In addition to sample hardnesses found from the early and intermediate stages of RBM, the sample milled for 86 ks and then consolidated into a compact contains a single phase of TiN with fine grain structure (about 25 μm in diameter), as shown in Fig. 6.8(*a*). Moreover, the hardness value of this sample has a narrow distribution range of about 19 GPa, as shown in Fig. 6.7.

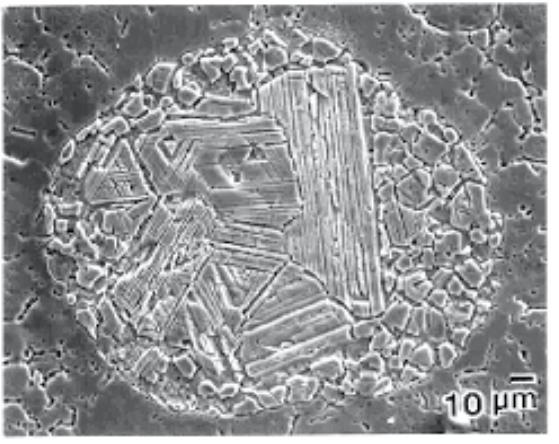

Figure 6.6. SEM micrographs of the cross-sectional view of as-consolidated Ti powders which milled under flow of nitrogen for 43 ks of RBM time. The micrograph shows the formation of composite Ti/TiN compact (see text). *(After El-Eskandarany et al.)*[12]

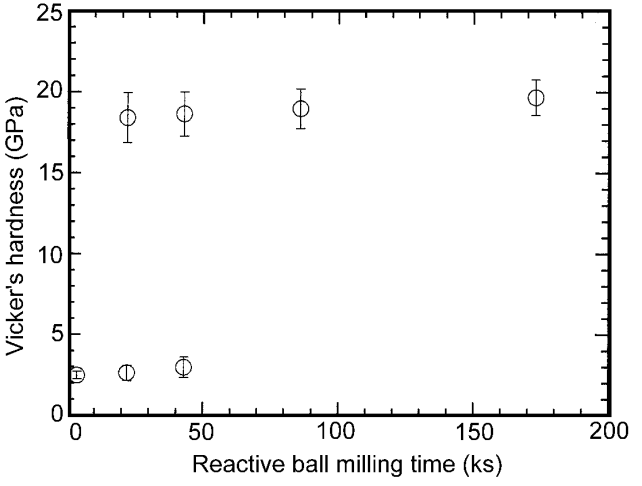

Figure 6.7. Dependence of Vicker's hardness of the as-consolidated mechanically reacted Ti powders on the RBM time. The measurements of the hardness were done using 50 kg. The symbols that have low hardness values (less than 5 GPa) are corresponding to the Ti matrix in the composite Ti/TiN compact (see text). *(After El-Eskandarany et al.)*[12]

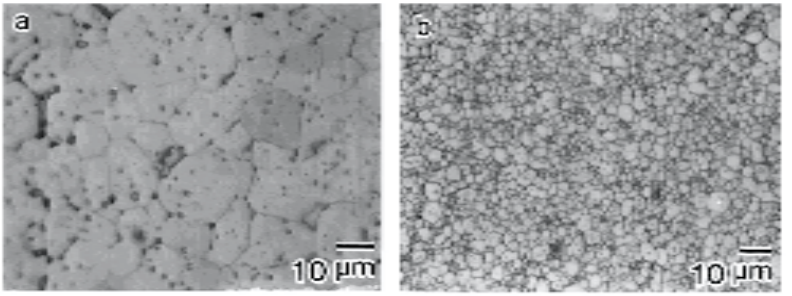

Figure 6.8. Optical micrographs of the cross-sectional view of as-consolidated Ti powders which were milled under flow of nitrogen for *(a)* 86 ks and *(b)* 173 ks of RBM time. The micrographs reveal a fine structure of single phase of NaCl TiN. *(After El-Eskandarany et al.)*[12]

The microstructure of the consolidated sample for the end-product (173 ks) shows a high dense structure with fine equiaxed grains of about 7 μm (or less) in diameter, as shown in Fig. 6.8(*b*). It should be noted that the irregular grain edges in some cases [see Fig. 6.8(*b*)] arises from the long etching time used during the sample preparation. The hardness of this sample lies in a narrow range of about 20.5 GPa (Fig. 6.7), suggesting the formation of a single phase TiN. Moreover, the SEM micrograph of the fracture surface of this sample can be used to show that the PAS technique leads to the formation of compacts with high density and uniform microstructure (Fig. 6.9).

The BFI and the corresponding SADP of the end-product (173 ks) after consolidation was previously shown in Fig. 3.7. Comparing this micrograph with that one in Fig. 6.2, we can say that the consolidation procedure for TiN powder leads to moderate grain growth. Since the average grain size of this consolidated sample is less than 100 nm (about 60 nm in diameter) one can say that the sintered sample maintains its nanocrystalline character. We emphasize that this consolidation step does not lead to any structural changes, and the TiN material maintains the NaCl, as shown by the indexed SADP in Fig. 3.7(*b*).

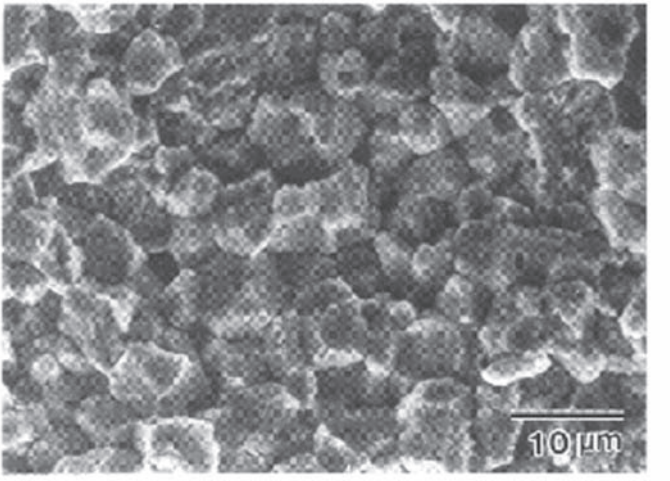

Figure 6.9. SEM micrograph of the fracture surface for the as-consolidated TiN (end-product, 173 ks). The micrograph shows that the compacted sample is fully-dense. *(After El-Eskandarany et al.)*[12]

The bulk density of the as-consolidated samples is plotted as a function of the RBM time in Fig. 6.10. During the first and intermediate stages of RBM, the bulk density increases monotonically with increasing the RBM time, suggesting the existence of high dense phase (TiN). At the final stage of RBM (86 to 173 ks), the densities of the consolidated samples are in a range between 5210 kg/m^3 to 5330 kg/m^3. Comparing these values with the theoretical density of TiN compound (5440 kg/m^3),[11] indicates that the consolidated TiN samples are fully dense.

The Poisson's ratio and the elastic moduli of the consolidated powders of TiN have been estimated from the measured samples densities and the constant parameters of the non-destructive testing apparatus, and plotted as a function of RBM times in Figs. 6.11 and 6.12, respectively. Increasing the RBM time leads to an increase in the fraction of TiN vs. that of unreacted Ti. This leads to a monotonic decrease in the value of Poisson's ratio to a value of 0.222. This value is smaller than one for pure metallic Ti (0.321), suggesting the formation of TiN.

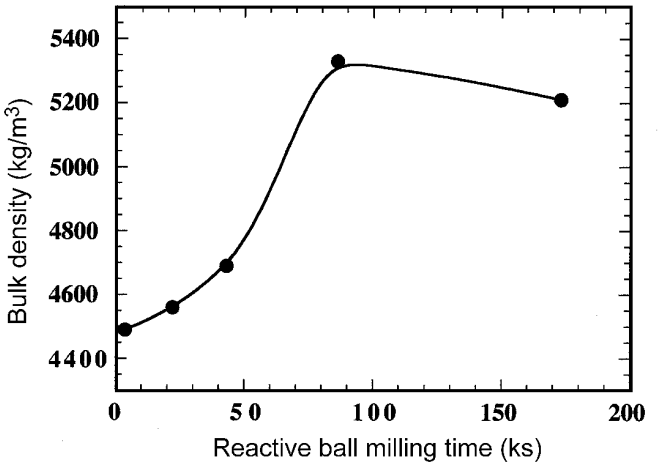

Figure 6.10. Correlation between the bulk density of the consolidated powders and the RBM time. *(After El-Eskandarany et al.)*[12]

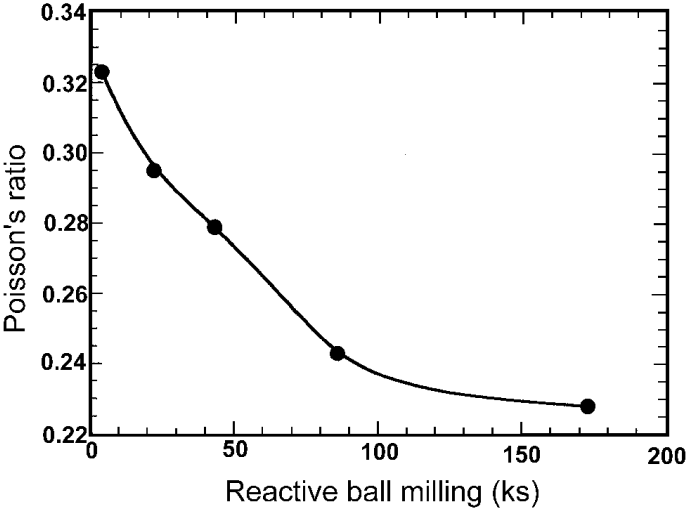

Figure 6.11. Dependence of Poisson's ratio of the consolidated powders on the RBM time. *(After El-Eskandarany et al.)*[12]

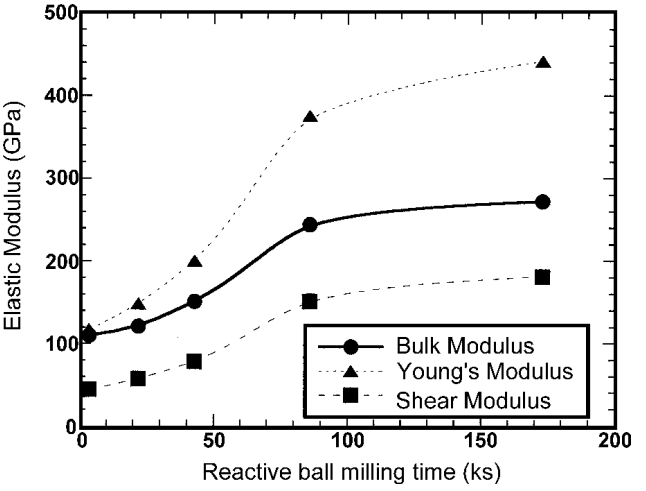

Figure 6.12. Relationship between the elastic moduli of the consolidated powder and the RBM time. *(After El-Eskandarany et al.)*[12]

The elastic moduli presented by the bulk modulus, Young's modulus, and the shear modulus of the consolidated mechanically reacted TiN powder is shown as a function of the RBM time in Fig. 6.12. These values increase significantly during the early and intermediate stages of RBM time (0 ks to 86 ks), suggesting an increase of TiN in the milled powder. Towards the end of the RBM time (86 ks to 173 ks), these values are almost saturated or slightly increased, indicating the formation of a single homogeneous phase of TiN.

Figure 6.13 displays the nitrogen content of the as-milled (closed symbols) and as-consolidated (open symbols) powders as a function of the RBM time. This figure can be used to illustrate the progress of the gas-solid reaction between Ti and nitrogen that took place in the ball mill. After a few kiloseconds of RBM time (22 ks), the powder contains considerable amount of nitrogen (13 at. %). Increasing the RBM time leads to an increase in the amount of the nitrogen content in the milled powder to about 40 at. % after 86 ks. The nitrogen content of the end-product is about 44 at. %, being in good agreement with the reported value of NaCl-TiN.[11] It is worth noting that the consolidation step does not lead to any compositional changes of the samples, as indicated by the near values of nitrogen content for the as-milled and as-consolidated samples.

The contamination content (iron, oxygen, carbon, and hydrogen) in the as-milled and as-consolidated samples is shown as a function of the RBM time in Figs. 6.14(*a*) and 6.14(*b*), respectively. Iron contamination is introduced to the milled powder due to the use of stainless steel milling tools. In order to decrease the iron contamination during RBM, metallic Ti powder was milled before charging the reactant material to form an iron-resistance wear on the surface of the milling tools. However, iron contamination content increases monotonically with an increase in the RBM time, [Fig. 14(*a*)]. The concentration of iron in the end-product of the TiN is less that 0.26 at. %. Comparing this value with the one in the as-received Ti powder (0.12 at. %) indicates the iron contamination that was introduced to the powder during the RBM is 0.16 at. %. The as-received Ti powder already contained a small amount of another contaminant, such as oxygen (0.08 at. %), hydrogen (0.02 at. %), and carbon (0.04 at. %), as displayed in Fig. 6.14(*a*). The concentrations of these contamination elements increases with increasing RBM times. This may be attributed to the existence of these elements in the nitrogen and/or argon gas used in the present study, or may be introduced to the powders during handling outside the glove box. These contamination contents do not seem to present a serious problem since they are under the level of 1 at. % in the end-product.

It is worth noting that during the consolidation procedure, the concentration of these contaminants did not increase [Fig. 6.14(*b*)].

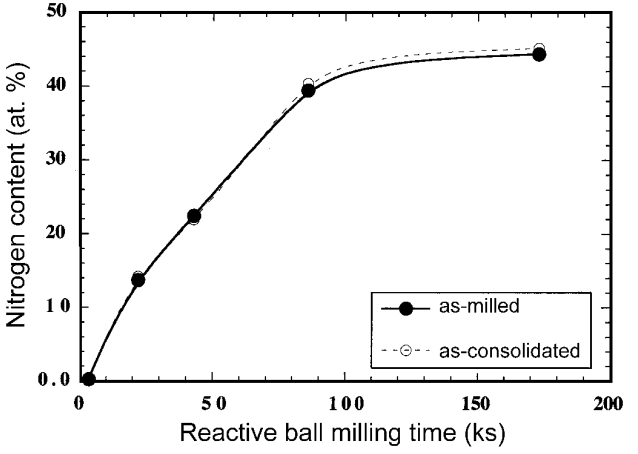

Figure 6.13. Dependence of the nitrogen content in the Ti powders on the RBM time. *(After El-Eskandarany et al.)*[12]

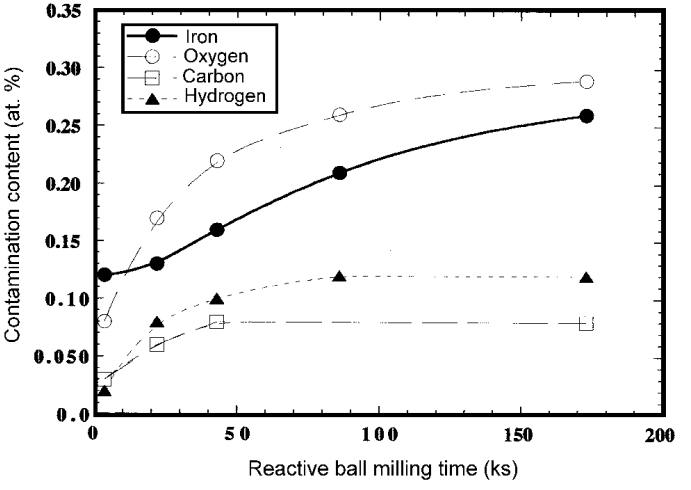

(a)

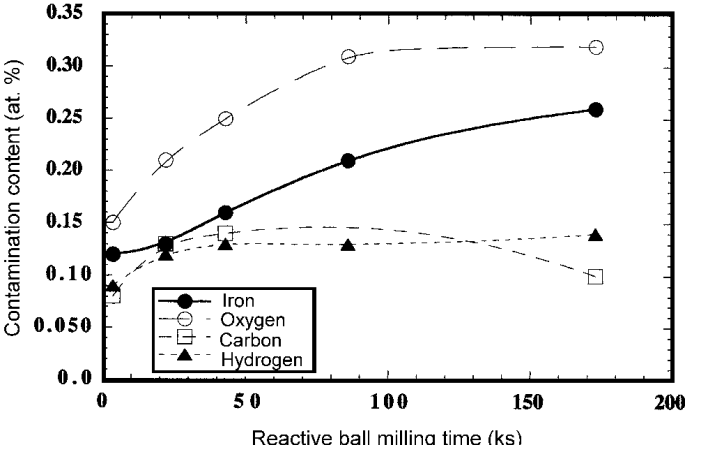

(b)

Figure 6.14. *(a)* Relation between the contamination content in the milled powders and the RBM time, and *(b)* dependence of the consolidation process and RBM on the contamination of the compacted samples. *(After El-Eskandarany et al.)*[12]

6.4 MECHANISM OF FABRICATION

A high-energy ball mill operated at room temperature under a nitrogen gas flow can be successfully employed for preparing a single phase NaCl structure TiN powder. The as-milled powders were consolidated into bulk samples, using a PAS method.

6.4.1 RBM Technique for Preparing TiN Powders

Results have shown that the RBM process can be classified mainly into four stages. The end-product of each stage varies widely in terms of structure and morphology.

6.4.1.1 The Early Stage of RBM.

In this stage of RBM (0 ks to 3.6 ks)—referred to as the first milling stage—powder particles of Ti agglomerate, as a result of cold welding, to form larger particles. The as-received Ti powder contains about 0.08 at. % oxygen and, hence, the powder is already coated with a thin layer of titanium oxide. These layers likely prevent the Ti powder from reacting with the surrounding milling atmosphere (nitrogen) or even with the other gas contaminants (e.g., hydrogen and oxygen gas). During this stage, the surface area of the particles is too small to react simultaneously with the nitrogen gas which is continuously introduced into the vial. The hardness of the consolidated samples taken from this stage is almost the same as pure metallic Ti and the bulk density is, likewise, that of elemental Ti. In addition, the material's elastic values are also the same as pure Ti. All of these observations, and the XRD patterns as well, signify the absence of TiN.

6.4.1.2 The Second Stage of RBM.

The previous stage of RBM is followed by a second stage (3.6 ks to 22 ks) in which the agglomerated particles of Ti are shattered and disintegrated into several particles apparently irregular in shape and size. The disintegration of the powder occurred as a result of the continuous shear and impact forces generated by ball-powder-ball collisions. The active surfaces of Ti particles react with nitrogen to form TiN and coexist with unreacted Ti powder. Thus, the consolidated samples of this stage are composite Ti/TiN. Accordingly, the hardnesses of these samples have two

values; a low one, that correlates to the unreacted metallic Ti, and a high one, corresponding to the fully reacted TiN. Moreover, the bulk density of this sample increases due to the existence of TiN.

6.4.1.3 The Third Stage of RBM.

This stage of milling (22 ks to 86 ks) can be defined as the intermediate stage of RBM, in which the unprocessed Ti particles continuously disintegrate and react with nitrogen in a typical gas-solid reaction. Increasing the mole fraction of NaCl-TiN at this stage causes an increase in the bulk density of the consolidated sample. Since, the consolidated sample of this stage contains a considerable amount of the unreacted metallic Ti, no remarkable change in the hardness value could be noted, and the sample still contains rich and poor zones of TiN. As the TiN increases, the value of Poisson's ratio decreases. Moreover, the existence of TiN causes a remarkable increase in the value of elastic moduli.

6.4.1.4 The Fourth Stage of RBM.

During this, the final stage of milling (86 ks to 173 ks), all of the metallic Ti particles react with nitrogen to form single-phase nanocrystalline TiN powders. The powders are uniform with respect to shape and size. The nitrogen content of the material saturates in this stage and the bulk density of the consolidated samples is indicative of full-dense TiN. In addition, the hardness of the as-consolidated samples is uniform throughout.

6.5 OTHER NITRIDES PRODUCED BY RBM

A metastable phase of fcc-NbN alloy powders has been fabricated by milling pure Nb powders in a high-energy ball mill under a nitrogen gas flow.[7] The nonequilibrium phase that shows a superconducting behavior with high T_c, is considered as a promising industrial material that can be used in the field of electronics.

The XRD patterns of elemental bcc-Nb powders and fcc-NbN alloy powders after 720 ks of the RBM time are shown in Fig. 6.15(*a*) and (*b*), respectively. Toward the end of the RBM processing time (720 ks), the Bragg peaks of pure bcc-Nb powders have disappeared completely and a new phase that related to the fcc-NbN alloy appeared clearly. The lattice

parameter, a_0, of the unit cell for this new phase is calculated to be 0.4330 nm. The grain size of this alloy powder, that was calculated from TEM and XRD, shows nanocrystalline characteristics (less than 5 nm in diameter) of the fabricated alloy. It is worth noting that no remarkable change in the crystal structure of this metastable phase can be observed, even after heating to 950 K, as illustrated in Fig. 6.15(*c*). At 1150 K, however, the metastable fcc-NbN phase transforms to mixed phases of hcp-Nb_4N_3 and hcp-NbN, as presented in Fig. 6.15(*d*).

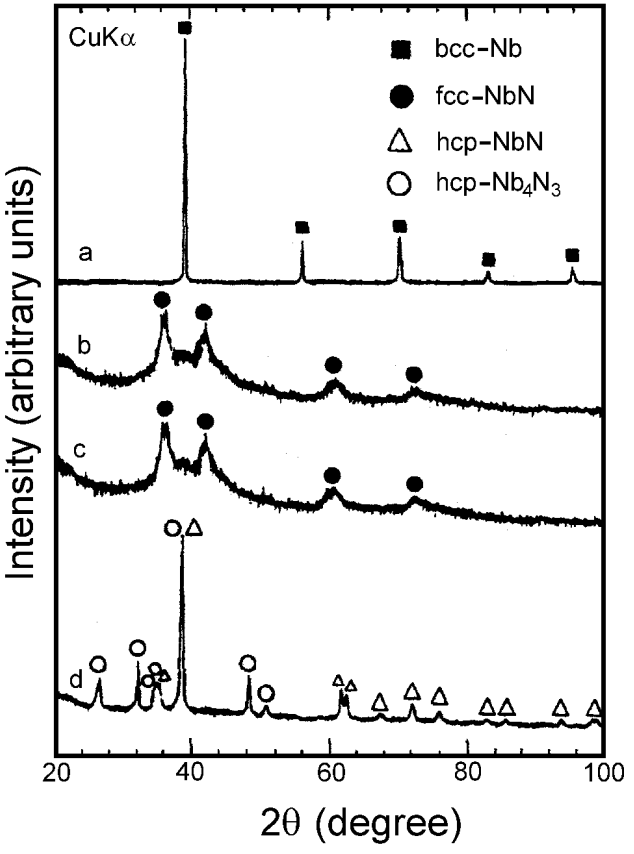

Figure 6.15. The typical XRD patterns of *(a)* pure Nb, *(b)* milled NbN alloy powders after 720 ks, *(c)* milled NbN alloy powders after 720 ks, then heated up to 950 K, and *(d)* milled NbN alloy powders after 540 ks, then heated up to 1150 K. *(After El-Eskandarany et al.)*[7]

The DTA technique has been used to get more information about the thermal stability and the behavior of the NbN alloy powders at several temperatures. Figure 6.16 illustrates the DTA curve of the metastable-fcc-NbN after 720 ks of RBM time. During the first heating run (solid line), four reactions are detected, at about 1025 K, 1100 K, 1490 K, and 1680 K. The first two reactions are exothermic and attributed to the phase-transformation of metastable-fcc-NbN to hcp-Nb_4N_3 and hcp-NbN, as was shown in Fig. 6.15(*d*). These phases melt at 1490 K and 1680 K, and are characterized by clear sharp endothermic peaks, as shown in Fig. 6.16. During the second and third heating runs (dashed lines), the exothermic reactions have already disappeared and two endothermic reactions are permanent and appear clearly, as shown in Fig. 6.16. This suggested a complete disappearance of the metastable-fcc-NbN alloy powders and formation of a mixture of hcp-Nb_4N_3 and hcp-NbN.

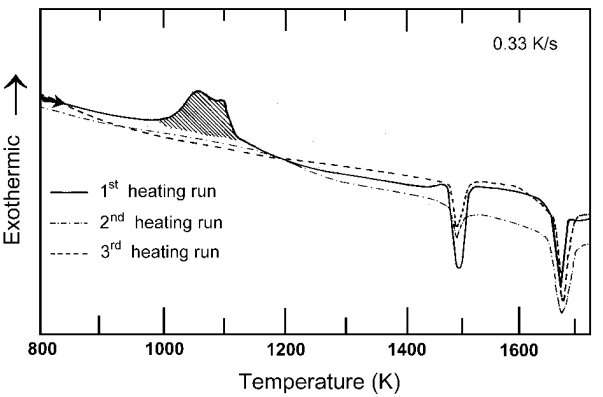

Figure 6.16. Typical DTA curves for Nb powders milled in a nitrogen gas flow for 720 ks of the RBM time. *(After El-Eskandarany et al.)*[7]

The first metallic amorphous nitride phase was fabricated by El-Eskandarany et al.[8] when they milled pure elemental powders of Al and Ta in a high-energy ball mill under nitrogen gas flow. The XRD patterns of the milled powders showed the formation of bcc-AlTa solid solution after 43 ks of RBM time (Fig. 6.17). The bcc-AlTa solid solution, which was obtained after 86 ks, contained 18 at. % nitrogen

and coexisted with unprocessed Ta powders. This bcc-Ta powder reacted with the nitrogen atmosphere to yield hcp-TaN that was embedded into the matrix of bcc-AlTa (Fig. 6.18). At the final stage of milling (72 ks) the bcc metastable phase is transformed completely to an amorphous phase, suggested by the diffuse haloes and smooth peaks which are shown in Fig. 6.17.

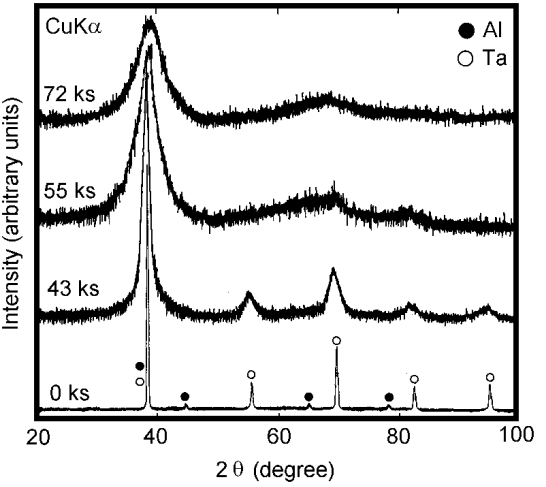

Figure 6.17. Typical XRD patterns of AlTaN alloy powders after selected RBM times. *(After El-Eskandarany.)*[9]

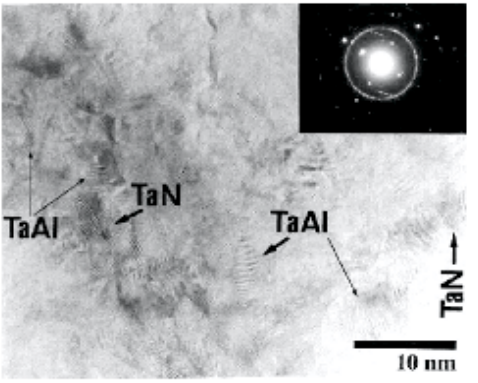

Figure 6.18. HRTEM image of mechanically reacted AlTaN powders after 86 ks of the ball milling time. *(After El-Eskandarany.)*[9]

In fact, recently, the fabrication of metallic nitrides via RBM at room temperature has been widely used for preparing many other metal nitrides, like FeN,[6][13] ZrN,[14] VN,[15] BN,[16] and amorphous NiZrN.[17]

6.6 FABRICATION OF NANOCRYSTALLINE SOLID SOLUTION NiTiH BY REACTIVE BALL MILLING

Where all metal hydrides are usually prepared by passing a flow of reactive hydrogen over the metallic materials under high vacuum pressure and at temperatures usually well above room temperature (static hydrogenous reaction), El-Eskandarany et al.[10] have prepared supersaturated fcc-$NiTiH_3$ solid solution by milling an equi-atomic mixture of elemental Ni and Ti powders in a ball mill under a hydrogen gas atmosphere.

Figure 6.19 displays the XRD patterns of NiTi powders after several stages of ball milling under a reactive hydrogen gas atmosphere. At the initial stage of milling [Fig. 6.19(*a*)], the initial powder consists of polycrystalline fcc-Ni and hcp-Ti. After 11 ks of the milling time, almost all the Bragg peaks corresponding to hcp-Ti surprisingly disappeared and a new phase of fcc-TiH_2 was detected, indicating a solid-gas reaction between the milling atmosphere (hydrogen) and the metallic Ti powder [Fig. 6.19(*b*)]. The cross-sectional view of a selected, polished, and etched particle shows a typical composite structure of TiH_2 (gray grains) which are embedded in the matrix of metallic Ni (Fig. 6.20). At the intermediate stage of milling (43 ks), the minor Bragg peaks of Ti have completely disappeared, indicating a *complete* phase transformation of hcp-Ti to fcc-TiH_2, as presented in Fig. 6.19(*c*). Moreover, the positions of the Bragg peaks for crystalline fcc-Ni have shifted, remarkably, to smaller angles, suggesting the formation of fcc-$NiTiH_3$ solid solution.

After 173 ks of the milling time, all the major peaks of TiH_2 disappeared, suggesting a solid state reaction between fcc-Ni and fcc-TiH_2, as displayed in Fig. 6.19(*d*). The product of this stage of milling is a single phase of fcc-$NiTiH_3$ solid solution, suggested by the fringe images and selected area diffraction pattern (SADP) of the powder particles (Fig. 6.21).

Increasing the milling time to 360 ks leads to the formation of nanocrystalline materials with an average grain size of about 10 nm in diameter, as shown in the dark field image (DFI) in Fig. 6.22.

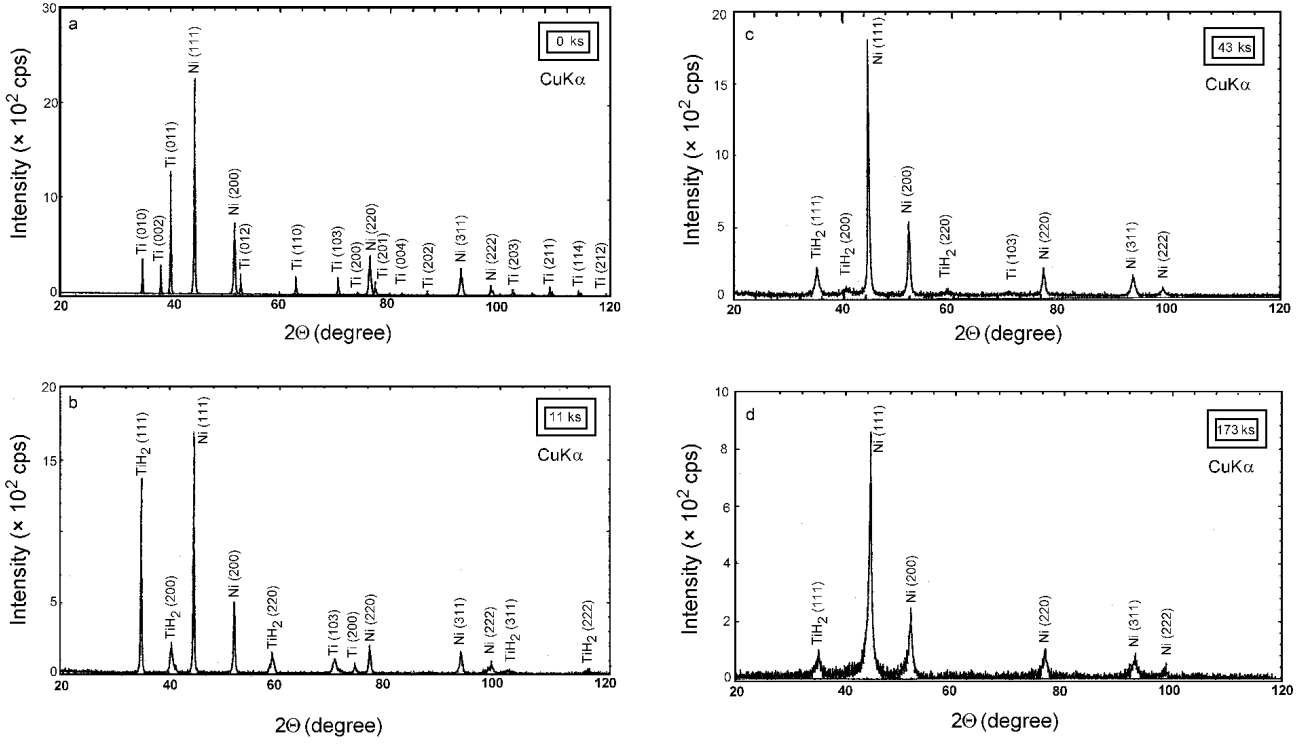

Figure 6.19. XRD patterns of NiTi powders at the *(a)* initial stage, *(b)* early stage, and *(c)* and *(d)* intermediate stage of RBM. *(After El-Eskandarany et al.)*[10]

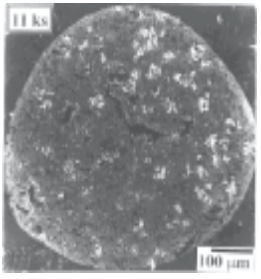

Figure 6.20. Optical micrograph for the polished and etched surface of a mixture of NiTi that ball milled under hydrogen gas for 11 ks. *(After El-Eskandarany et al.)*[10]

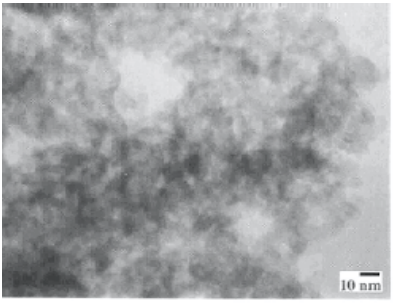

Figure 6.21. HRTEM micrograph for a mixture of NiTi that ball milled under hydrogen gas for 173 ks. *(After El-Eskandarany et al.)*[10]

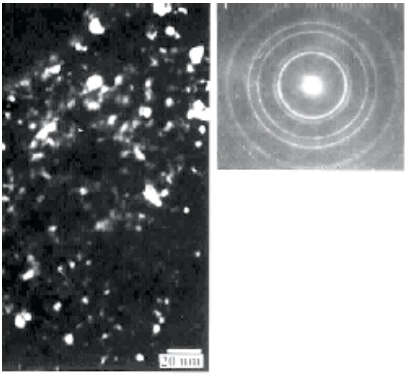

Figure 6.22. DFI and the corresponding SADP of NiTi powders that milled under hydrogen gas atmosphere for 173 ks. *(After El-Eskandarany et al.)*[10]

The XRD patterns for the end product of $NiTiH_3$ (360–720 ks), are presented in Fig. 6.23. Obviously, the Bragg peaks of the end product [Fig. 6.23(*a*)] become broader, indicating the formation of nanocrystalline $NiTiH_3$ solid solution. The lattice parameter (a_0) of the final product was calculated to be 0.35403 nm. This value is larger than pure fcc-Ni (0.35240 nm), suggesting an interstitial solubility of TiH_2 in Ni. We should emphasize that the final product of $NiTiH_3$ does not change to any other phase(s), even after milling for times as long as 720 ks, as displayed in Fig. 6.23(*b*). The XRD patterns of the end product (720 ks), after annealing in a differential scanning calorimeter under a flow of argon gas at 993 K, are presented in Fig. 6.23(*c*). The Bragg peaks of $NiTiH_3$ have become more pronounced and sharper, suggesting the formation of coarse grains. Comparing these peaks in Fig. 6.23(*c*) with those in Fig. 6.23(*a*) and (*b*), one can say that the $NiTiH_3$ phase is very stable, even at this relatively high temperature.

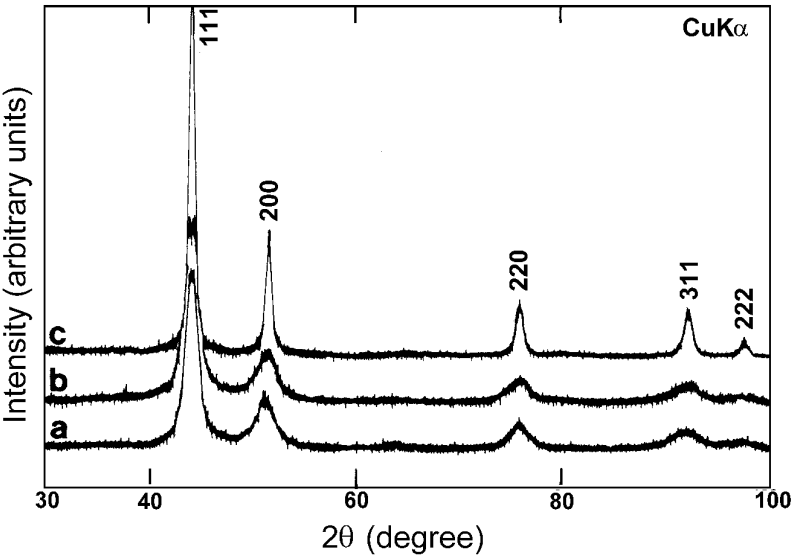

Figure 6.23. XRD patterns of the final products for $NiTiH_3$ alloy powders after *(a)* 360 ks, *(b)* 720 ks and *(c)* 720 ks of milling and then annealing under flow of argon at 993 K. *(After El-Eskandarany et al.)*[10]

REFERENCES

1. Musher, J. N., and Gordon, R. G., *J. Mater. Res.*, 11:989 (1996)
2. Nakamura, K., Inagawa, K., Tsuruoka, K., and Komiya, S., *Thin Solid Films*, 40:155 (1977)
3. Deevi, S., and Munir, Z. A., *J. Mater. Res.*, 5:2177 (1990)
4. Tsunekawa, Y., Hirai, H., Okumiya, M., and Niimi, I., *J. of Thermal Spraying Soc. of Jpn*, 26:1150 (1989)
5. Inoue, Y., Tanimoto, S., Tsujimura, K., Yamashita, Y., Ibara, Y., Yamashita, Y., and Yoneda, K., *J. Electrochem. Soc.*, 141:1056 (1994)
6. El-Eskandarany, M. S., Sumiyama, K., Aoki, K., and Suzuki, K., *Mater. Sci. Forum*, 88–90:801 (1992)
7. El-Eskandarany, M. S., Sumiyama, K., Aoki, K., Masumoto, T., and Suzuki, K., *J. Mater. Res.*, 9:2891 (1994)
8. El-Eskandarany, M. S., Aoki, K., and Suzuki, K., *Appl. Phys. Lett.*, 60:1562 (1992)
9. El-Eskandarany, M. S., *J. Alloys Comp.*, 203:117 (1994)
10. El-Eskandarany, M. S., Ahmed, H. A., Sumiyama, K., and Suzuki, K., *J. Alloys Comp.*, 218:36 (1995)
11. *ASTM* Card No. 38–1420.
12. El-Eskandarany, M. S., Omori, M., Konno, T. J., Sumiyama, K., Hirai, T., and Suzuki, K., *Metall. Trans. A*, 29:1973 (1998)
13. Koyano, T., Lee, C. H., Fukunaga, T., and Mizutani, U., *Mater. Sci. Forum*, 88–90:809 (1992)
14. Calka, A., *Appl. Phys. Lett.*, 59:1568 (1992)
15. Calka, A., and Williams, J. S., *Mater. Sci. Forum*, 88–90:787 (1992)
16. El-Eskandarany, M. S., unpublished results.
17. Aoki, K., Memezawa, A., and Matsumoto, T., *J. Mater. Res.*, 8:307 (1993)

7

Mechanically Induced Solid-State Reduction

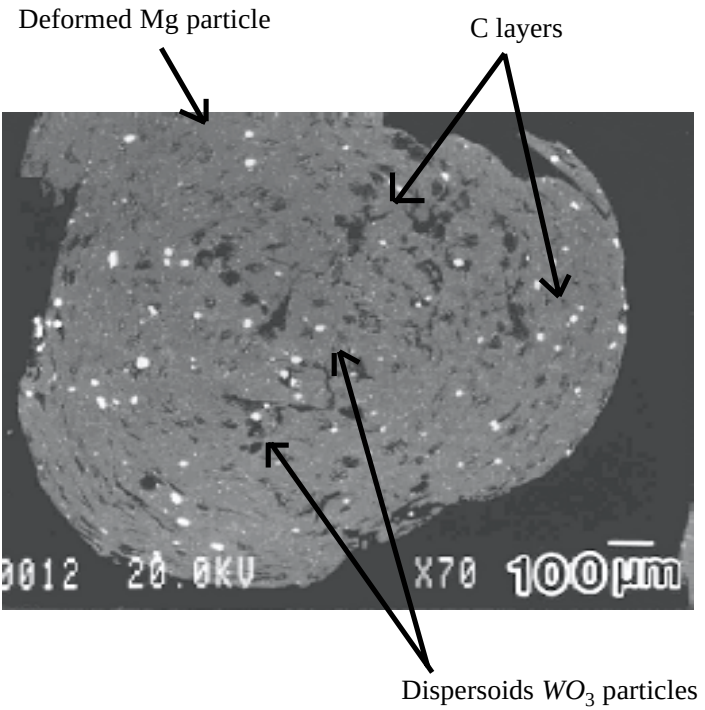

$$WO_3 + 3Mg + C \xrightarrow{\text{Room Temperature Ball Milling}} WC + 3MgO$$

[*After El-Eskandarany et al.,* Metall. Trans. A., *27:4210 (1996)*]

7.1 INTRODUCTION

As was shown in the previous chapters, most solid-state chemical reactions involve the formation of one (or more) product phases between the reactants, which, therefore, become specially separated. All the solid-state reaction rates are controlled by diffusion of the reacting species through the product material. Therefore, the activities of solids are dependent on initial contact areas, hence, particle size, on factors which influence diffusion rates, such as defect densities and local temperatures, and on product morphology.[1]–[3] In conventional thermally activated systems, the reactants remain substantially unchanged and specially separated during the course of the reaction. A significant increase in reaction rate could result if a means were found to agitate the reaction mass and continually bring unreacted material into contact, preventing the products from dividing the reactants. In fact, mechanical alloy processing is able to provide such a potential.

The displacement reactions of the type

$$A_xO + vB \rightarrow xA + B_vO$$

have been observed during MA processing of a simple metal oxide and a strong metallic reducing agent, such as elemental Ca, Mg, Ti, Fe, Ni, and Al powders.[4]–[7] This process is known as mechanical solid state reduction (MSSR).[8] In addition, the MSSR has been employed to fabricate nanocomposite WC/MgO materials by milling elemental Mg with WO_3 powders in a high-energy ball mill.[9]

7.2 REDUCTION OF Cu_2O WITH Ti BY ROOM TEMPERATURE ROD MILLING

In 1995, the room temperature rod-milling technique was employed for reducing Cu_2O with elemental Ti powders.[8] In this experiment, Cu_2O (99.9%, 50 μm) and Ti (99.5%, 100 μm) powders were mixed in a glove box under a purified argon atmosphere to give the desired starting average composition of $(Cu_2O)_xTi_{1-x}$. The mixed powders were then charged and sealed in a cylindrical stainless steel shell (SUS 304, 120 mm in diameter) together with stainless steel rods (SUS 304, 10 mm in diameter). The rod-to-powder weight ratio was controlled to about 30:1. The inlet of the shell was connected with a rotary pump and evacuated for about 4 ks. After evacuation,

a flow of argon gas was passed into the rod mill through a plastic pipe. Once the rod mill was filled with 1 atm of argon the inlet of the vial was closed and the MSSR process was carried out at room temperature by mounting the rod mill on a rotator at the rate of 1.4 s^{-1}. The MSSR was interrupted at selected intervals and a small amount of the rod-milled powder was taken out of the vial in the glove bag. The powders were characterized by x-ray diffraction (XRD) with CuKα, transmission electron microscopy (TEM) using a 200 kV microscope and differential thermal analysis in an argon gas atmosphere at a heating rate of 0.33 Ks^{-1}. The metallographic characterizations of the milled powders were studied by an optical microscope. Moreover, the induction coupled plasma (ICP) emission method was used to detect the degree of Fe contamination in the milled powders. After 360 ks of milling, the iron contamination content in the alloy powders was determined to be 0.25 at. %.

7.3 PROPERTIES OF ROD MILLED POWDERS

7.3.1 Structural Changes with the Milling Time

The XRD patterns of Cu_2O milled with Ti are presented in Fig. 7.1 after selected MSSR times. At the initial stage of MSSR process (0 ks), the powders consist of unreacted polycrystalline fcc-Cu_2O and hcp-Ti [Fig. 7.1(*a*)]. The intensities of the peaks corresponding to Cu_2O and Ti crystals decrease remarkably after 43 ks, as displayed in Fig. 7.1(*b*). Increasing the milling time to 173 ks enhances the solid state reaction of the reactants (Cu_2O and Ti) which translates into a MSSR between Cu_2O and Ti, as shown in Fig. 7.1(*c*). At this intermediate stage of milling, new phases corresponding to bcc-Cu and tetragonal-TiO_2 appear, suggesting an increase in the chemical kinetics of MSSR reaction. The yield product at this stage of milling coexisting with unreacted Cu_2O and Ti powder particles, is displayed in Fig. 7.1(*c*). Figure 7.1(*d*) shows the XRD patterns of the end-product of the MSSR process after 360 ks of rod milling time. Obviously, the Bragg peaks that correspond to bcc-Cu become more pronounced, suggesting an increase in the mole fraction of metallic Cu in the yield product. Remarkably, these peaks of bcc-Cu are broad, indicating the formation of nanocrystalline Cu with an average crystallite size of 7 nm. Moreover, the starting materials (reactants) of Cu_2O and Ti powders no longer appear, suggesting the completion of MSSR process.

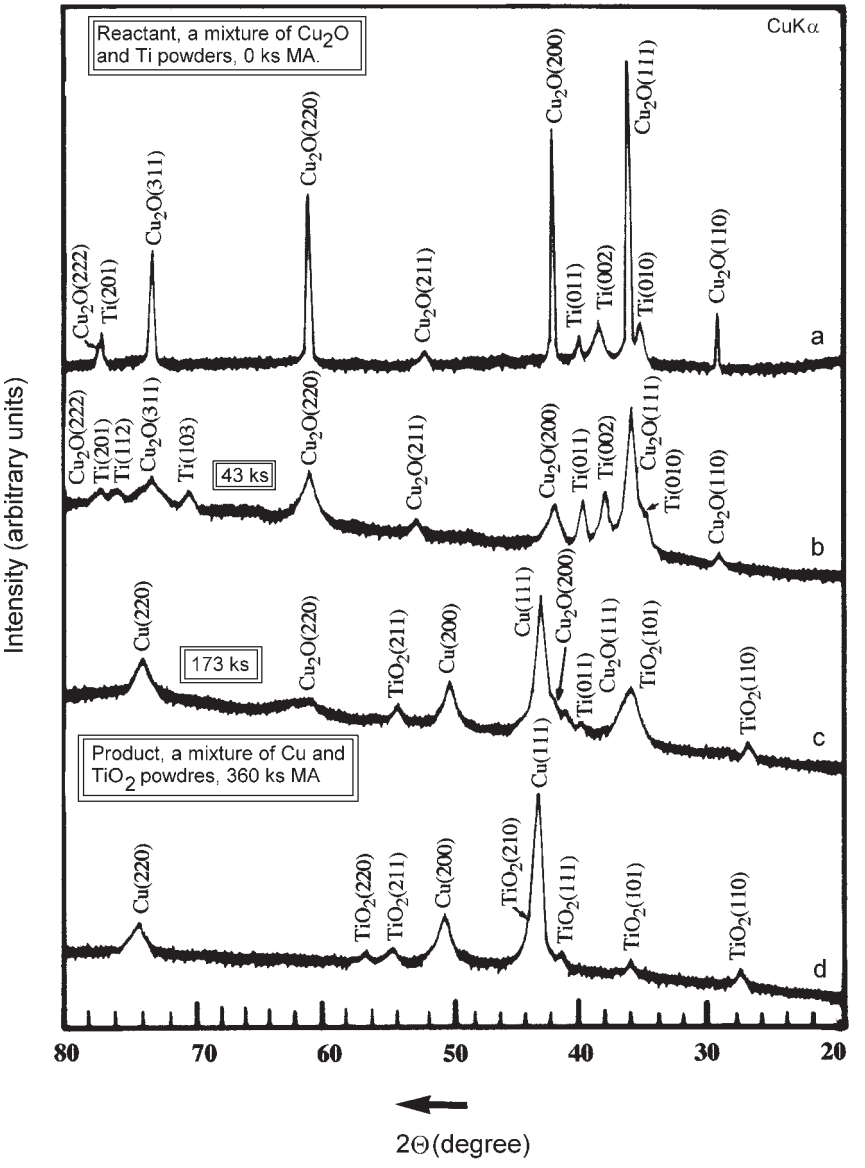

Figure 7.1. XRD patterns of mechanically alloyed Cu_2O and Ti powders after *(a)* 0 ks, *(b)* 43 ks, *(c)* 173 ks, and *(d)* 360 ks of the rod milled times. *(After El-Eskandarany.)*[8]

Figure 7.2 displays the change in the concentration of a reactant (Ti) and a product (Cu) with the rod milling time. The concentrations of Ti and Cu were calculated by measuring the areas under the diffraction peaks of Ti (011) and Cu (111) reflections. During the first few kiloseconds (0–43 ks), no remarkable change in the concentrations of Ti and Cu can be observed. Increasing the milling time (43–256 ks) increases the rate of the reaction. Thus, the concentration of Cu increases monotonically with a dramatic decrease of the concentration of Ti, as shown in Fig. 7.2. Toward the end of the MSSR process (360 ks) the reduction of Cu_2O to Cu is completed.

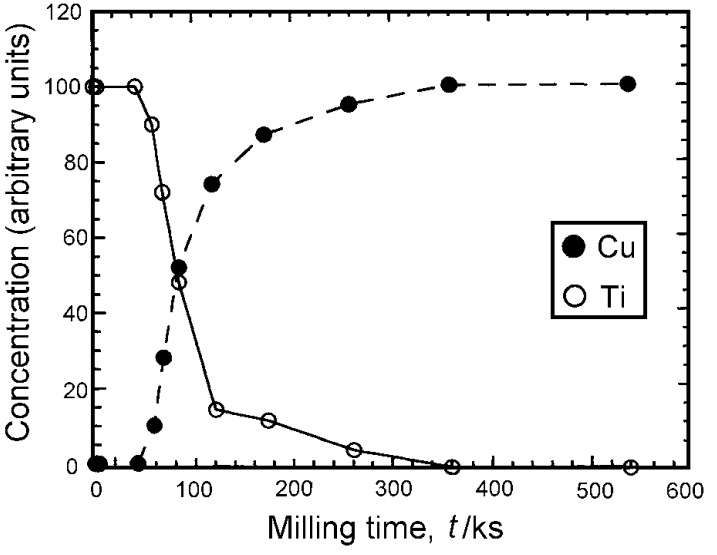

Figure 7.2. Effect of the milling time on the concentration of Cu and Ti in the yield product during rod milling of a mixture of Cu_2O and Ti powders. The concentrations of Ti and Cu were calculated by measuring the areas under the diffraction peaks of the Ti (011) and Cu (111) reflections.

Detailed TEM analyses were performed in order to follow the progress of the MSSR process with variation in the rod milling time. The bright-field images (BFIs) and the selected-area diffraction patterns (SADPs) of rod milled Cu_2O-Ti powders after selected milling times are shown in Figs. 7.3 through 7.5.

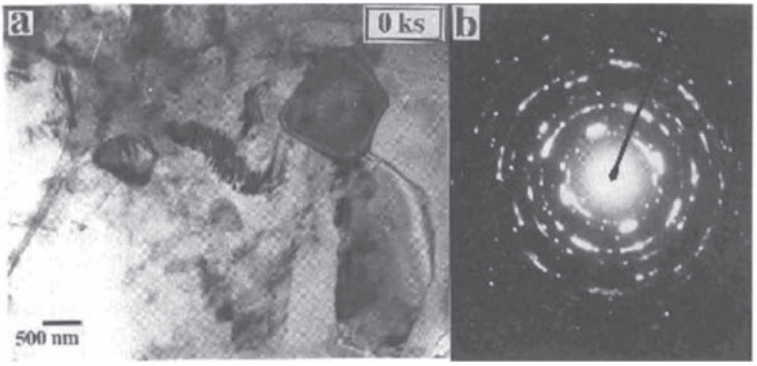

Figure 7.3. *(a)* BFI and *(b)* SADP of the reactant materials of Cu_2O and Ti powders at the starting stage (0 ks) of rod milling time. *(After El-Eskandarany.)*[8]

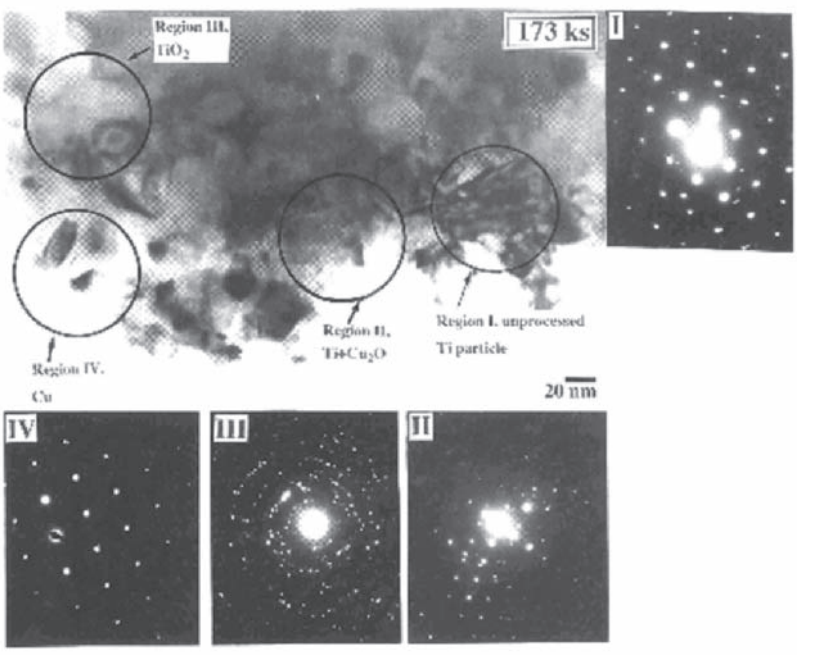

Figure 7.4. BFI and the corresponding SADPs of several regions for mechanically alloyed Cu_2O and Ti powders after 173 ks of the rod milling time. *(After El-Eskandarany.)*[8]

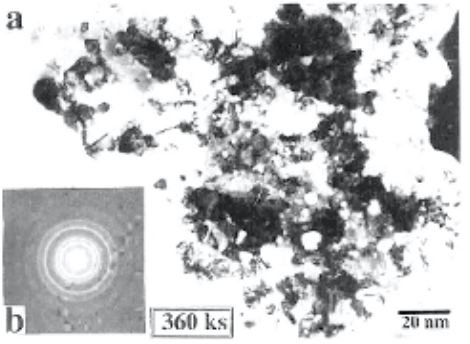

Figure 7.5. *(a)* BFI and *(b)* SADP of the powder particles at the end stage of the MSSR process (360 ks of the rod milling time). *(After El-Eskandarany.)*[8]

Figure 7.3 shows the (*a*) BFI and (*b*) corresponding SADP of a mixture of Cu_2O-Ti powders (reactant) at the starting stage of milling. Obviously, the powders contain large grains of about 500 nm in diameter. The SADP shows a ring-spot pattern that is characteristic of the polycrystalline fcc-Cu_2O and hcp-Ti.

The BFI and the corresponding SADPs of the powders milled for 173 ks of rod milling are shown in Fig. 7.4. At this intermediate stage of the MSSR process, the structures of the particles are extremely heterogeneous, shown by the different features of the powders in Fig. 7.4, suggested by SADPs taken at regions I (unprocessed Ti), II (diffracting polycrystalline Ti and Cu_2O), III (TiO_2), and IV (Cu). It is worth noting that the powder particles consist of somewhat fine grains, ranging from 10 to 50 nm in diameter. Increasing the rod milling time leads to an increase in the shear force generated by the rods and this causes several mechanical defects in the powder particles which translate into a continuous decrease in the unprocessed Cu_2O and Ti powders. Thus, atomically clean surfaces are created and brought into intimate contact so that MSSR takes place and the mole fraction of Cu and TiO_2 increase against the concentration of the reactant material of Cu_2O and Ti.

The BFI and corresponding SADP for the end-product of the MSSR process are shown in Fig. 7.5(*a*) and (*b*), respectively. The powders are a mixture of polycrystalline Cu (agglomerated dark grains) and TiO_2 (the light fine spherical grains). The reactant powders no longer appear, suggested by the ring diffraction patterns of fcc-Cu coexistent with tetragonal-TiO_2, as shown in Fig. 7.5(*b*).

7.3.2 Metallography

Figure 7.6 shows a cross-sectional view of polished and etched powder particles of Cu_2O and Ti, the reactant materials that were milled together for (*a*) 43 ks and (*b*) 360 ks of the MSSR time. Obviously, after 43 ks of MSSR processing time, the powder is a mixture of Cu_2O grains (dark gray sub-micron grains) and flaky Ti particles, as presented in Fig. 7.6(*a*). At the final stage of MSSR (360 ks), Cu_2O was reduced completely by Ti and the end product of this stage contained fine powders of Cu (gray particles) together with a relatively fine equiaxed cross section of TiO_2 grains (dark gray), as presented in Fig. 7.6(*b*).

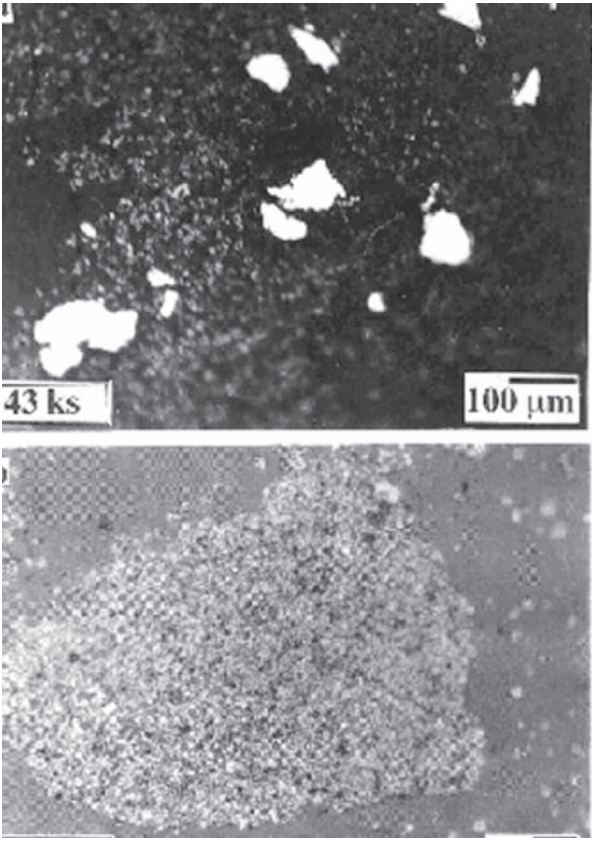

Figure 7.6. Optical micrograph of a cross-sectional view of polished and etched powder particles of Cu_2O and Ti, being the reactant materials that were milled together for *(a)* 43 ks and *(b)* 360 ks of the MSSR time. *(After El-Eskandarany.)*[8]

7.3.3 DTA Measurements

The DTA curves for Cu_2O milled with Ti are presented in Fig. 7.7 after (*a*) 0 ks and (*b*) 360 ks of rod milling times. All the samples were heated to about 1370 K (first heating run) and cooled to about 310 K. Then, second heating runs (dashed lines) were performed, in order to get a base line. At the starting stage of the MSSR process (0 ks), two reactions between the reactant materials (Cu_2O and Ti powders) took place, characterized by two exothermic peaks which appear at about 773 K and 973 K, as displayed in Fig. 7.7(*a*). These reactions occur due to the reduction of Cu_2O with Ti at such high temperatures. The products of these reactions, as indicated by XRD, contain TiO_2 and metallic Cu that melts at about 1356 K, characterized by a sharp endothermic peak [Fig. 7.7(*b*)]. At the second heating run, a single sharp endothermic peak appears, due to the melting of pure Cu powders in the yield product. Moreover, no exothermic reactions could be detected, suggesting the completion of the reduction process via DTA. We conclude that Cu_2O can be reduced to Cu using Ti as an RA (reducing agent) at temperatures higher than 973 K.

Figure 7.7(*b*) displays the DTA traces for the end-product of milled Cu_2O with Ti powders after 360 ks of rod milling time. Obviously, during heating of the sample, an endothermic reaction takes place, characterized by a single sharp endothermic peak centered at 1356 K. This is attributed to the melting of Cu powders in the end-product. Moreover, the exothermic reaction peaks that relate to the reaction of unprocessed Cu_2O with Ti powders [Fig. 7.7(*a*)] have already disappeared. This indicates the formation of new phases (Cu and TiO_2) without the existence of any other unprocessed reactant materials of Cu_2O or Ti.

7.4 MECHANISM OF MSSR

The reduction process reported in the previous section is considered a new application of the MA method for reducing metal oxide using a metallic reducing agent (RA) via rod-milling technique. This application was reported earlier by Schaffer et al.[4] when they reduced cupric oxide (CuO) to pure copper metal by several metallic RAs, e.g., Ca and Mg. Our results[8] have shown that Cu_2O could completely be reduced to metallic Cu by milling a mixture of Cu_2O and elemental Ti powders (due to the stoichiometry of reaction)[10] in a rod mill filled with argon atmosphere at room temperature. The completion of the so-called mechanical solid state

reduction (MSSR) process takes 360 ks of milling time. For MSSR, the basic change that occurs during milling the reactants (Cu_2O and Ti powders) can be described in terms of the transfer of electrons, as presented in the following reaction;

$$2\ Cu_2O\ (s) + Ti\ (s) \rightarrow TiO_2\ (s) + 4\ Cu\ (s)$$

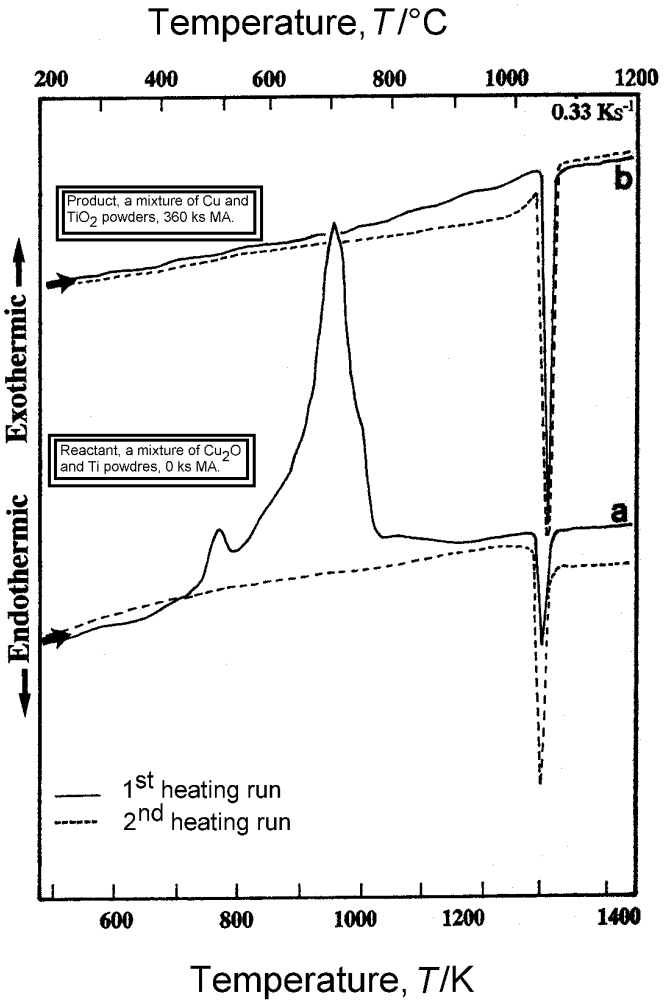

Figure 7.7. DTA curves for Cu_2O milled with Ti after *(a)* 0 ks and *(b)* 360 ks of rod milling times. The solid and dashed lines represent the first and the second heating runs, respectively. *(After El-Eskandarany.)*[8]

Principles of physics and of physical chemistry always lie at the root of every individual application of the MA technique. Obviously, the previous reaction is a typical oxidation-reduction reaction that involves the oxidation of Ti to TiO_2. The oxygen atoms required for this oxidation come from Cu_2O which is reduced to Cu. The formation enthalpy, ΔH^{for}, for TiO_2 (-315 kJ/mol)[11] is about five times larger than that for Cu_2O (-57 kJ/mol).[11] In other words, TiO_2 is more stable than Cu_2O so that the above mentioned reaction is a forward reaction and occurs during the rod milling of Cu_2O and Ti. It is shown that the chemical kinetics of the reaction indexed by the rate of MSSR increases monotonically by increasing the milling time (the rate at which the concentration of Cu and TiO_2 increases). However, this rate depends on several known factors such as the nature and concentration of the reacting species, and it can be controlled by the type of mill used. A high energy ball mill (attritor, vibrating or planetary mills) may increase the reduction rate due to the generated temperature caused by the collisions between the balls. One drawback of using these high energy mills comes from the fact that iron contamination could be brought from the milling media during the milling process, especially when using hard reactant materials.[12] Thus, the MSSR will face a serious problem presented by the existence of such foreign material in the end product. Moreover, this foreign material can be alloyed with the end product and a complex phase may be formed. In addition, the gradual oxidation-reduction reaction can be followed easily by low energy mills which allow us to study the characteristics of the yield product during the different stages of the MSSR process. For these reasons, the rod milling technique has been used in the present investigation.

For a successful MSSR via rod-milling technique, the elemental particles of RA powders should disintegrate during milling into smaller particles in which fresh surfaces are continuously created. These new particles, with their fresh surfaces, are very active and react immediately with Cu_2O. We should emphasize that these new surfaces play a very important role in the MSSR process, no reduction can occur without the presence of these surfaces. For example, magnesium (Mg) is a well known reactive RA with two electrons in the outermost shell [$(Ne)3s^2$], however, during rod milling of a mixture of Cu_2O and Mg under the same mentioned milling conditions, no reaction between Cu_2O and Mg could be detected.[13] This is attributed to the fact that Mg is a very soft metal with a low melting temperature (compared with Ti) and is stacked on the milling tools (due to the cold welding). In contrast to Schaffer et al.[4] during rod milling, Mg powders are being isolated from Cu_2O powders. We should emphasize that

the milling or grinding processes are necessary steps in extractive metallurgy. The possibility of performing pre-reduction stages by the MSSR method may be applied.

7.5 FABRICATION OF NANOCRYSTALLINE WC AND NANOCOMPOSITE WC-MgO REFRACTORY MATERIALS BY MSSR METHOD

Among hard alloys, WC alloys find wide industrial applications as tips for cutting tools and wear resistant parts. The intrinsic resistance to oxidation and corrosion at high temperatures also makes them desirable as a protective coating for devices at elevated temperatures. In the industrial scale of production, the hexagonal phase of WC is usually obtained by a direct alloying of elemental W and graphite at temperatures ranging from 1673 to 1873 K.[14][15] Accordingly, the high cost of preparation is a disadvantage of this process. It has been shown by El-Eskandarany[9][16] that nanocrystalline WC can be obtained by reducing WO_3 through ball milling this material in the presence of Mg and graphite. The Mg reduces the oxide, and the resulting metallic W reacts with graphite to form WC. The oxide phase of MgO is simply removed by selective leaching. Mi et al.[17] have reported the formation of fine-grained WC by ball milling the elemental powders of W and C.[17] They have also shown the possibility of synthesizing composite WC-Co by milling their previously reacted WC particles with elemental Co powder.

However, because the hexagonal phase of WC alloy possesses high hardness (23 GPa),[16] it is rarely used in industrial applications in its native form. This is due to its relatively poor shock resistance, high values of elastic moduli and bulk density, and low fracture toughness. Thus, a binding material (usually Co) is often added to WC during sintering in order to improve the mechanical properties. Co is desirable because it will wet the surface of WC while maintaining negligible solubility in the carbide phase. The present section will present the formation of a new nanocomposite WC/MgO material for use in industrial applications. In this method, a WC/MgO end-product forms during ball milling of WO_3, Mg, and C, and is subsequently consolidated into a nanocomposite bulk compact, using a plasma activated sintering method.

One purpose of the present section is to describe a unique process for forming fully dense, nanocomposite materials. The significant technological potential of the present work derives from a relatively inexpensive

and simple process for synthesizing ceramic/ceramic composite materials for applications in cutting tools, tips for drilling tools, and wear resistant parts used in wire drawing, extrusion and pressing dies. Finally, this work demonstrates a viable process for preparing bulk, fully dense, nanocomposite refractory material using MSSR as a source of nanophase powder.

In the experiments, elemental (99.5%) powders of WO_3 (5 μm), Mg (750 μm) and graphite (5 μm) with an atomic ratio of 1:3:1 respectively, were mixed in a glove box under argon gas atmosphere and sealed in a cylindrical sapphire vial together with fifty sapphire balls (10 mm in diameter). The ball-to-powder weight ratio was maintained at the level of 10:1. The ball-milling experiments were carried out at room temperature, using a Fritsch P6 high-energy ball mill at a rotation speed of 4.2 s^{-1}. The milling experiments were interrupted at regular intervals and small amounts of the milled powders were taken out of the vial in the glove box. The powders were characterized by means of x-ray diffraction (XRD) with CuKα radiation, scanning electron microscope (SEM), transmission electron microscope (TEM) using 200 kV microscope, and/or high-resolution transmission electron microscope (HRTEM). The powders were chemically analyzed to determine their concentrations of W and Mg, using the induction coupled plasma emission method. The sample of the end-product contains about 18 at. % MgO. The oxygen and carbon concentrations were investigated by the helium carrier fusion-thermal conductivity method.

Since WC is chemically stable at room temperature and cannot be attacked, even by strong acid solutions, the MgO powder is simply removed from selected samples, using a mixture of HCl (7 mol) and H_3PO_4 (3 mol). The as-leached product, which is pure WC powder, is consolidated into a bulk sample using a plasma activated sintering (PAS) method. The same sintering technique has been employed to consolidate the as-milled powder of composite WC-18% MgO material (before leaching). All the consolidation procedures of the present work took place in a vacuum at 1963 K with a pressure of 19.6 to 38.2 MPa. In order to avoid undesired grain growth, the sintering process was applied for only 0.18 ks without adding any binding materials. The densities of consolidated WC and WC-MgO materials were determined by Archimedes' principle, using water immersion, and found to be 15.60 g/cm^3 and 13.10 g/cm^3, respectively. Comparing these values with those for pure WC (theoretical density, 15.77 g/cm^3)[14] and the calculated one for WC-18% MgO (using the rule of mixtures principal, 13.21 g/cm^3), indicates the formation of fully dense bulk materials. Vickers indenter with a load of 50 kg was employed to determine the hardness of the compacted samples. The size of the indentation cracks was used to determine

the fracture toughness (K_c) of the sample.[18] The hardness and K_c values reported below are averaged from at least ten indentations. The elastic properties of the bulk samples were determined by a nondestructive test using the pulse-echo overlap ultrasonic technique using an ultrasonic detector.

7.5.1 Properties of Ball-Milled Powders

7.5.1.1 Structural Changes with the Milling Time

Figure 7.8 presents the XRD patterns of the (*a*) starting reactant materials, (*b*)–(*d*) as-milled, (*e*) as-leached powders (pure WC powder) and (*f*) consolidated sample (bulk WC material). At the starting stage of milling (0 ks) the powders are a mixture of elemental WO_3, Mg, and C materials with sharp Bragg peaks [Fig. 7.8(*a*)]. After 22 ks of milling, Bragg peaks of metallic W and MgO crystals appear, indicating the starting of a mechanical solid state reduction, MSSR, which takes place between Mg (reducing agent) and WO_3 powders [Fig. 7.8(*b*)]. In parallel to the MSSR process, a solid state reaction, SSR occurred between W and C powders to yield a refractory phase of hcp-WC. The Bragg peaks of these reacted phases have become pronounced and their intensities increased after 43 ks [Fig. 7.8(*c*)], suggesting an increase in the product materials. No free atoms of the starting reactant materials and/or metallic W powders could be detected after 173 ks of milling, suggesting the completion of both MSSR and SSR processes [Fig. 7.8(*d*)]. When the end-product of this stage (nanocomposite WC/MgO material) is leached with an acidic agent (see Sec. 7.5), the Bragg peaks of MgO completely vanish and the residual product is nanocrystalline WC with an average grain size of 7 nm [Fig. 7.8(*e*)]. The XRD pattern of the as-consolidated WC powder is shown in Fig. 7.8(*f*). Comparing this pattern with that one shown in Fig. 7.8(*e*), one can conclude that this consolidation step does not lead to a dramatic change in the grain size and the as-sintered sample still maintains its unique nanocrystalline properties. Moreover, this sintering procedure does not lead to any phase changes and/or transformations and the sample is a single phase of hcp-WC.

Figure 7.9 displays the XRD pattern of the as-consolidated WC-18% MgO powder (before leaching). Obviously, the compact sample contains two phases of WC and MgO without the presence of any reactive products. Again, one can conclude that the compacted sample is nanocomposite, characterized by a broadening in the Bragg peaks for both WC and MgO phases.

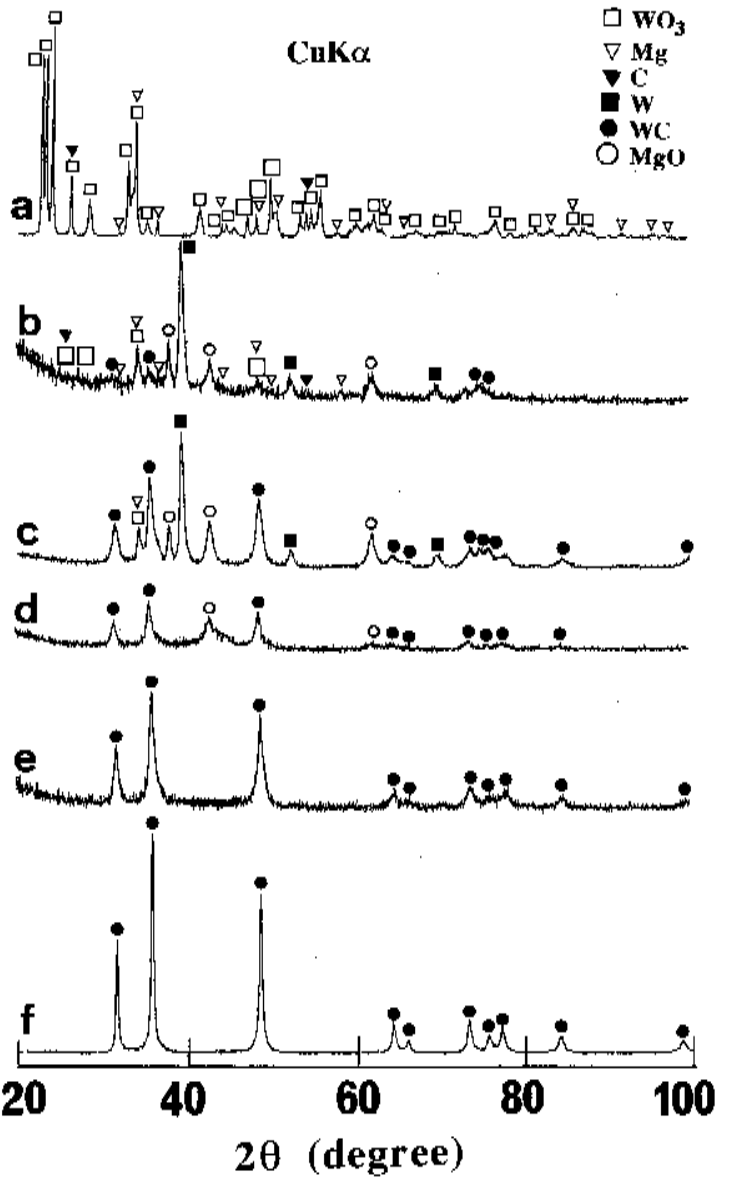

Figure 7.8. Typical XRD patterns of ball milled WO_3, Mg and C powders at *(a)* 0 ks, *(b)* 22 ks, *(c)* 43 ks, *(d)* 173 ks of the milling time, *(e)* the end-product after leaching and *(f)* the end-product after leaching and consolidation. *(After El-Eskandarany.)*[9]

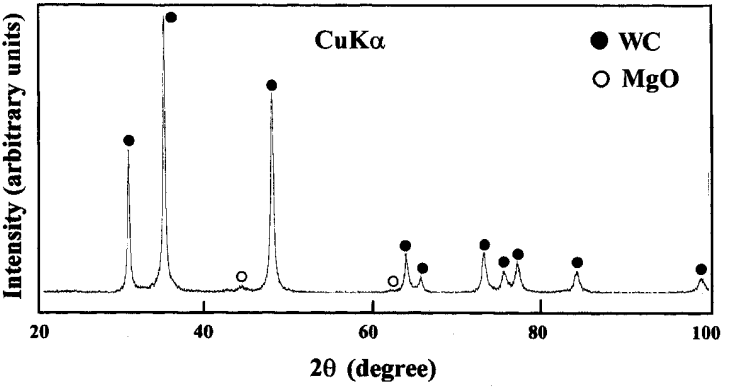

Figure 7.9. XRD pattern of as-consolidated WC-18% MgO (end-product, 173 ks of milling) before leaching. *(After El-Eskandarany.)*[9]

The bright field image (BFI) and the dark field image (DFI) of the powder that milled for 1.8 ks is shown, together with the selected area diffraction pattern (SADP), in Fig. 7.10. Obviously, the powders still contain the reactant elemental phases of WO_3, Mg, and graphite, with sharp spot diffraction patterns, as displayed in Fig. 7.10(*c*).

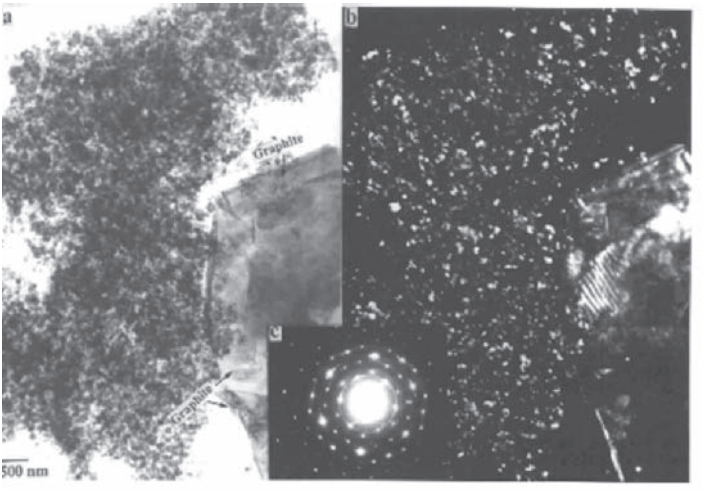

Figure 7.10. *(a)* BFI, *(b)* DFI, and *(c)* the corresponding SADP of the as-milled powders after 1.8 ks of the ball milling time. *(After El-Eskandarany.)*[9]

Figure 7.11 shows the (*a*) BFI of the milled powders after 3.6 ks, (*b*) and (*c*) the corresponding SADPs of two regions. The hard oxide phase of WO_3 and cubic graphite powders [Fig. 7.11(*b*)] are embedded into the soft metallic matrix of the agglomerated Mg [Fig. 7.11(*c*)] particles to form a composite-reactant material with ellipsoid-like morphology [Fig. 7.11(*a*)].

Figure 7.12 presents the BFI of the final-product (173 ks) of the milled powders (before leaching). The micrograph shows a typical nanocomposite material consisting of the host ceramic matrix of WC and uniform spherical nanoscale grains of MgO (reinforcement materials) that are embedded into the matrix.

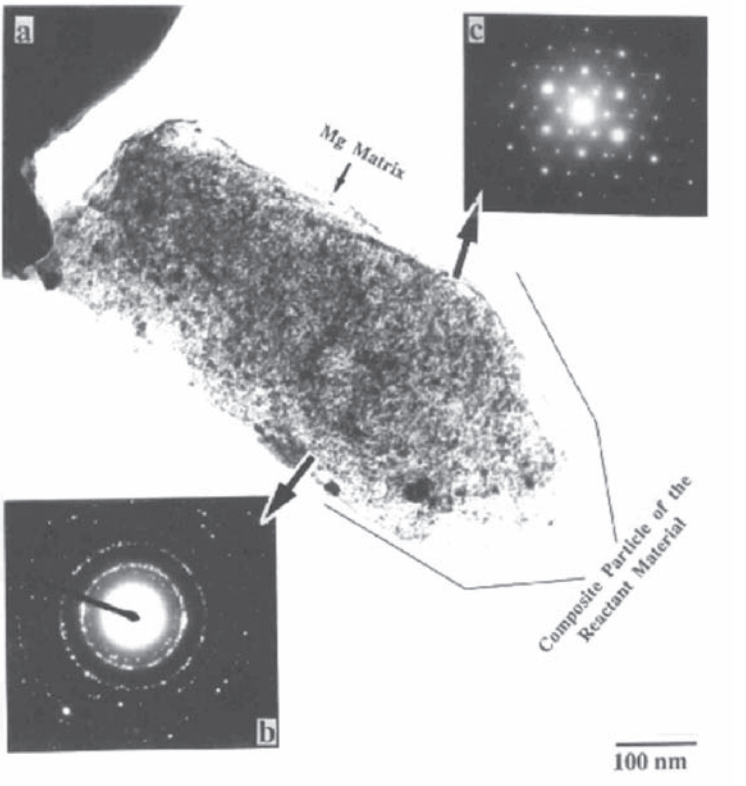

Figure 7.11. *(a)* BFI, *(b)* and *(c)* the corresponding SADPs of the as-milled powders after 3.6 ks of the ball-milling time. The micrograph presents a typical individual agglomerated reactant particle. *(After El-Eskandarany.)*[9]

Figure 7.12. BFI of as-milled powder after 173 ks (end-product). The spherical grains of MgO, with about 7 nm in diameter, are embedded in the WC matrix to form nanocomposite WC-MgO powders. *(After El-Eskandarany.)*[9]

The BFI and SADPs of the as-leached powder are shown together in Fig. 7.13. The powder has the fine structure [Fig. 7.13(*a*)] of a single phase of WC, as indicated by SADPs which were taken from several zones [Fig. 7.13(*b*), (*c*), and (*d*)].

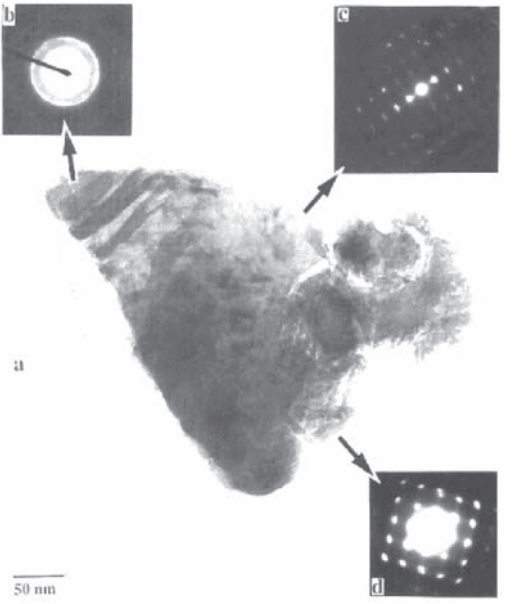

Figure 7.13. *(a)* BFI and *(b), (c),* and *(d)* the corresponding SADPs of the end-product after leaching. *(After El-Eskandarany.)*[9]

Figure 7.14 shows the BFI of the cross-sectional view of the as-consolidated WC (*a*) and composite WC/MgO (*b*) powders. Obviously, the consolidation procedure leads to the formation of nanocrystalline WC with an average grain size of about 25 nm in diameter. It can be noted that the consolidated sample of composite WC/MgO contains nanocrystalline grains of WC (dark region) and MgO (light gray region) of not more than 50 nm in diameter. The dense structure and the absence of any voids and/or cracks in the consolidated samples can be depicted.

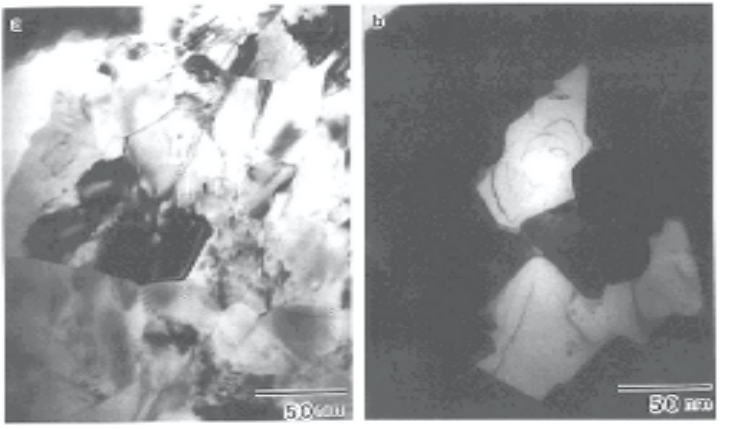

Figure 7.14. BFI planner view of the as-consolidated end-product *(a)* after leaching and *(b)* before leaching. *(After El-Eskandarany.)*[9]

7.5.1.2 Temperature Change with the Milling Time

Figure 7.15 shows the change of the vial's temperature during the milling time. It has been shown in a previous work[20] that this temperature did not increase more than 314 K, when the same mill was operated without charging the reactant powders. During the first few kiloseconds (0 to 3.6 ks), the temperature of the vial increased slightly, and the starting reactant materials of WO_3, Mg, and C, which have irregular shape and wide particle size distributions [Fig. 7.16(*a*)], agglomerated to form larger particles. The cross sectional view for these particles [Fig. 7.16(*b*)], shows the formation of composite powders consisting of WO_3 (fine white grains about 20 μm in diameter), C (black grains about 100 μm in diameter), and

Mg (the gray matrix about 1800 μm in diameter). The formation of such composite powder is attributed to the cold welding performed at this stage of milling in which the ductile Mg particles are deformed to form soft matrices containing rather hard particles of WO_3 and C powder. Increasing the milling time (3.6 to 43 ks) enhances the MSSR and SSR between the reactant materials, hence, the heat liberated by these reactions is transferred to the surface of the vial and leads to an increase in its temperature to about 370 K (Fig. 7.15). Toward the end of this stage (43 ks), a small mole fraction of WC is formed as a result of an SSR between the W and C powders. A complete SSR takes place between W and C powders at the second stage of milling (43 to 86 ks) and the vial's temperature drops to about 325 K. At the end of the MA time (173 ks), the vial's temperature remains at a constant value of about 320 K, suggesting the completion of both reactions and the formation of the final product, which is a composite WC/MgO powder which has spherical-like morphology, with an average particle size of about 0.5 μm [Fig. 7.16(*c*)].

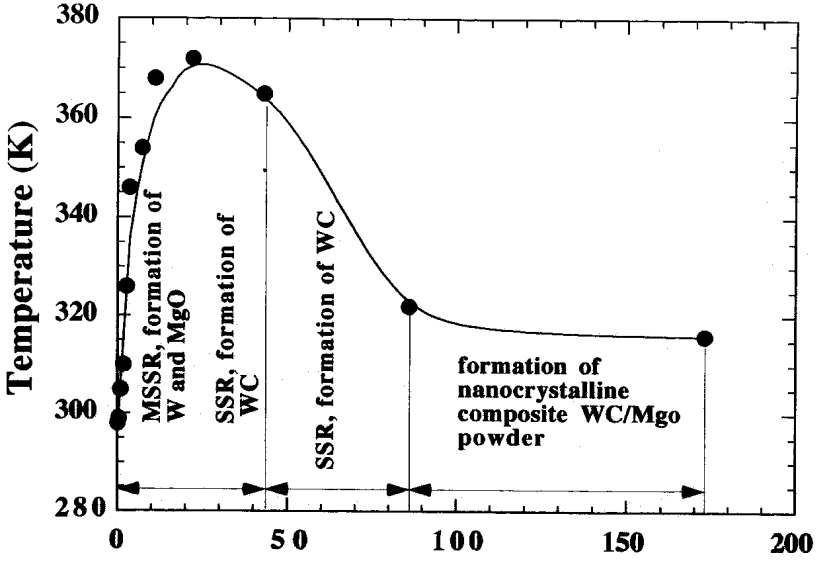

Figure 7.15. The correlation between the vial's temperature and the milling time during the ball milling elemental mixture of (WO_3+3Mg+C) powders. *(After El-Eskandarany.)*[9]

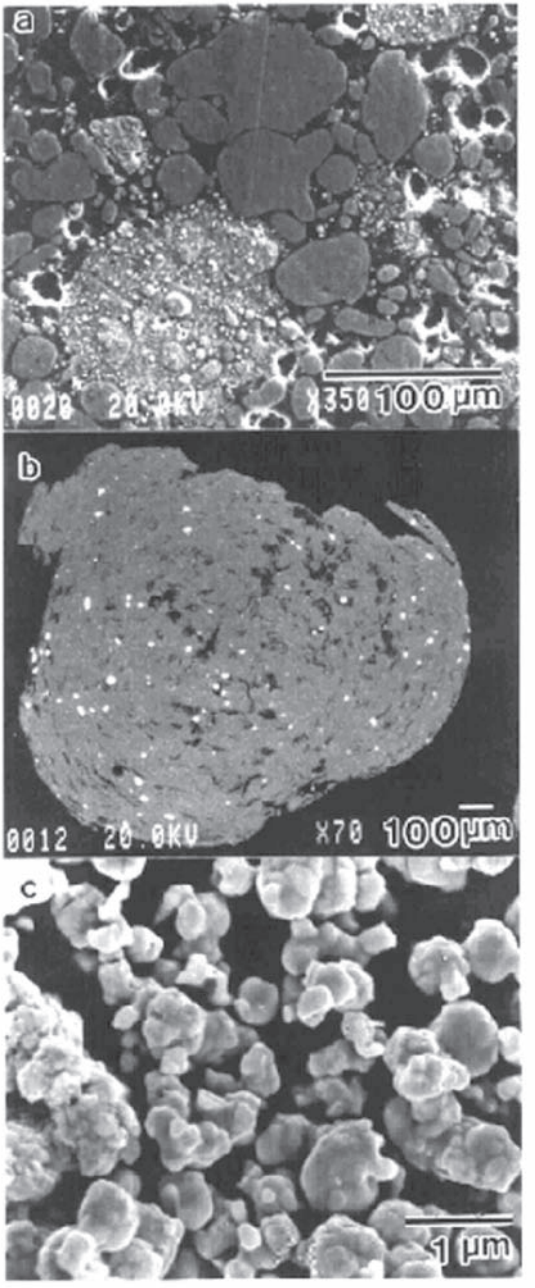

Figure 7.16. SEM micrographs of the as-milled powders after *(a)* starting stage, *(b)* 3.6 ks, and *(c)* 173 ks of the ball milling time. *(After El-Eskandarany.)*[9]

7.5.1.3 Hardness, Toughness, and Elastic Moduli of Consolidated WC and WC/MgO

A SEM micrograph of Vickers hardness indentation of the consolidated sample appears in Fig. 7.17. The hardness of this compact sample was measured to be 15 GPa, taking the average of at least ten indentations. It is worth noting that this value is higher than that for bonded WC–14% Co (13.2 GPa).[21] The cracks displayed in the micrograph, which developed in the product during indentation and extended 250 to 350 μm away from it, were used as indicators for estimating the fracture toughness, K_C, via the model that was suggested by Anstis et al.[18] This value is found to be 14 MPa·m$^{1/2}$, well above that for commercial WC/Co composites (12 MPa·m$^{1/2}$). This indicates the possibility of producing high fracture toughness WC/MgO nanocomposite materials.

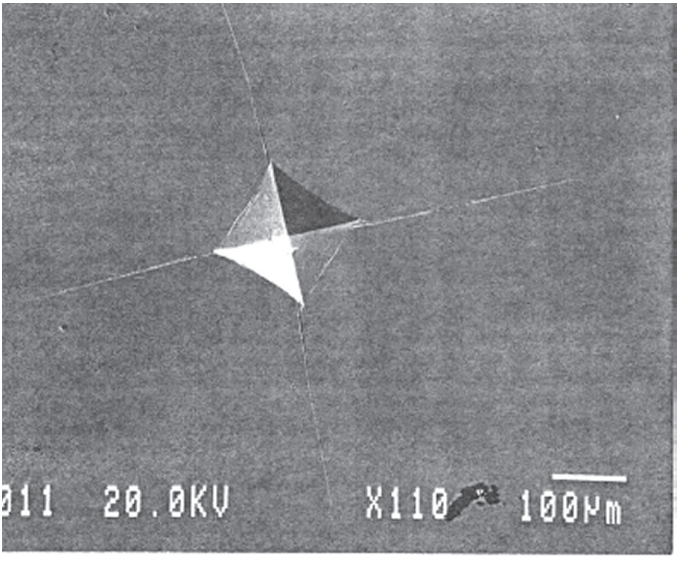

Figure 7.17. SEM micrograph of Vickers hardness indentation developed by applying a load of 50 kg on the consolidated sample of the end-product (173 ks). The presented radial cracks, induced during the indentation procedure with extensions of 250 to 350 μm away from the indentation, were used to estimate the fracture toughness, K_C. *(After El-Eskandarany.)*[9]

Table 7.1 summarizes the results of some mechanical properties for the consolidated samples. However, pure nanocrystalline WC possesses extraordinarily high values of hardness (23 GPa), Young's and shear moduli (813.5 and 405.1, respectively), and has a low value of K_C (4 MPa·m$^{1/2}$), making it difficult for use as a cutting tool. Contrary to the WC material, composite WC/MgO combines unique properties of high hardness value (15 GPa) and an extremely high value of K_C (14 MPa·m$^{1/2}$) with reasonable values of Young's (413 GPa) and shear (171 GPa) moduli. In fact, composite WC/MgO material is a unique material in that it can combine two opposite properties, high hardness and high fracture toughness. This may be understood when recognizing that the fabricated WC/MgO material consists of fine grains (less than 50 nm in diameter) that are able to improve the mechanical properties of the fabricated materials and introduce materials with unique properties.

Table 7.1. Some Measured Physical and Elastic Moduli of the Fabricated Nanocrystalline WC and Nanocomposite WC/MgO Materials

	Consolidated sample of as-mechanically reacted and then leached WC	Consolidated sample of as-mechanically reacted WC-18 at. % MgO
Density (g/cm^3)	15.6	13.1
Poisson's ratio	0.004	0.209
Young's modulus (GPa)	813.5	413
Shear modulus (GPa)	405.1	171
Bulk modulus (GPa)	273.4	237
Hardness (GPa)	23	15
Fracture toughness (MPa·m$^{1/2}$)	4	14

REFERENCES

1. Gomes, W. P., and Dekeyser, W., in: *Treatise on Solid State Chemistry*, (N. B. Hamny, ed.) Plenum Press, New York, 4:61 (1976)
2. Carter, R. E., *J. Chem. Phys.*, 34:2010 (1961)
3. Rapp, R. A., Yurek, A., and Yurek, G. J., *Metall. Trans.*, 4:1283 (1973)
4. Schaffer, G. B., and McCormick, P. G., *Appl. Phys. Lett.*, 55:45 (1989)
5. Schaffer, G. B., and McCormick, P. G., *Scripta Metall.*, 23:835 (1989)
6. McCormick, P. G., Whartom, V. N., and Schaffer, G. B., *Proc. Int. Symp. Phys. Chem. Powder Metall. Production and Processing*, TMS, (1990)
7. Schaffer, G. B., and McCormick, P. G., *Metall. Trans. A*, 21:2789 (1990)
8. El-Eskandarany, M. S., *Materials Transactions*, JIM, 36:182 (1995)
9. El-Eskandarany, M. S., *J. Alloys Comp.*, 296:175 (2000)
10. Benjamin, J. S., *Metall. Trans. A*, 1:2943 (1970)
11. de Boer, F. R., Boom, R., Mattens, W. C. M., Miedema, A. R., and Niessen, A. K., *Cohesion in Metals-Transition Metal Alloys*, North-Holland, Amsterdam (1988)
12. El-Eskandarany, M. S., Aoki, K., and Suzuki, K., *J. Less-Common Met.*, 167:113 (1990)
13. El-Eskandarany, M. S., unpublished work.
14. Yih, S. W. H., and Wang, C. T., *Tungsten*, Plenum Press, NY, p. 392 (1979)
15. Toth, L. E., *Transition Metal Carbides and Nitrides*, Academic Press, NY and London (1971)
16. El-Eskandarany, M. S., Omori, M., Ishikuro, M., Konno, T. J., Takada, K., Sumiyama, K., Hirai, T., and Suzuki, K., *Metall. Trans. A*, 27:4210 (1996)
17. Mi, S., and Courtney, T. H., *Scripta Metall.*, 38:171 (1997)
18. Anstis, G. R., Chantikul, P., Lawn, B. R., and Marshall, D. B., *J. Am. Ceram. Soc.*, 64:533 (1981)
19. El-Eskandarany, M. S., Omori, M., Konno, T. J., Sumiyama, K., Hirai, T., and Suzuki, K., *Metall. Trans. A*, 32:157 (2001)
20. El-Eskandarany, M. S., *J. Alloys Comp.*, 279:263 (1998)
21. *Fracture Mechanics Applied to Brittle Materials*, (S. W. Freiman, ed.) ASTM Spec. Tech. Publ., No. 678, Philadelphia (1979)

8

Mechanically Induced Solid-State Amorphization

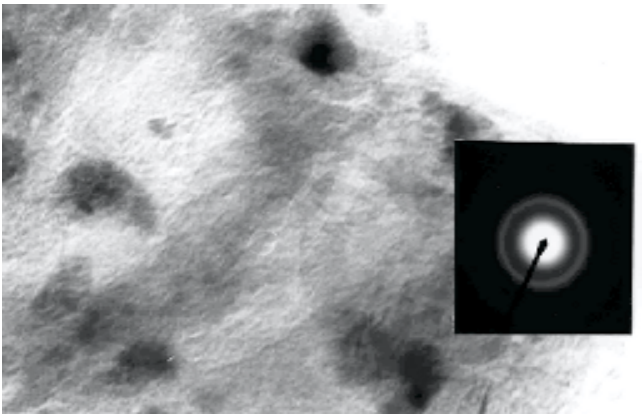

Mechanical alloying process has been employed for preparing homogeneous amorphous alloy powders at room temperature. One advantage of this technique appears to be that there is a very large composition range for which amorphous metallic alloys may be fabricated. The figure shows a bright field image and the corresponding diffraction pattern of amorphous Al-50 at. % Zr alloy powders fabricated by rod-milling technique. [*After El-Eskandarany et al.,* Metall. Trans. A, *23:2131 (1992)*]

8.1 INTRODUCTION

Ionic and covalent glasses are often formed when the corresponding melt fails to crystallize during relatively slow cooling, of the order of 1 K/s. Naturally occurring oxide glasses, such as obsidian, were first known to man who, as early as 70,000 BC, used them to make tools. Around 5,000 BC the Phoenicians discovered oxide-glass making.

The field of glassy metals or metallic glass has seen enormous development during recent years. For the uninitiated, the notion of a metallic glass may be rather unusual, since one would primarily associate glass with transparent and insulating window material. However, the term glass is nowadays almost unanimously used for an amorphous substance which is obtained by cooling the corresponding melt. Metallic glasses are new substances with exciting properties which are of interest not only for basic solid-state physics, but also for metallurgy, surface chemistry, and technology. Metallic glasses have properties which are quite different from solid metals making them promising candidates for technical applications. The following is a list of some of the important properties that can be found in metallic glasses;

- high mechanical ductility and yield strength
- high magnetic permeability
- low coercive forces
- unusual corrosion resistance
- temperature-independent electrical conductivity

Since the first pioneer investigation for preparing amorphous metallic alloys during the 1950s,[1] almost all amorphous materials are exclusively synthesized by one of the following techniques;

- rapid solidification of melts or vapors[2]
- atomic disordering of crystalline lattices[3]
- solid-state amorphization reaction between pure elements[4][5]
- solid-state transformations from metastable[6]

Several different methods for the preparation of amorphous alloys have been discovered since 1983. Yeh et al.[7] reported that the dissolution of hydrogen gas in crystalline Zr_3Rh results in amorphous $Zr_3RhH_{5.5}$. It was shown that chemical energies could be used to drive a crystal-to-amorphous transformation in the solid state. The hydrogen atoms, being small, can

easily diffuse in crystalline intermetallics of large unit cells, allowing for the reaction to occur at a temperature below the crystallization temperature of the amorphous hydride. So far, this method has been used for preparing various amorphous alloys.[8][9]

Another kind of solid-state amorphization reaction was reported by Herd et al.[4] They reported that metals can diffuse at low temperatures into amorphous semiconductors, such as tellurium, selenium, and silicon. Schwarz and Johnson gave the first example of two pure crystalline metals reacting to form a single-phase amorphous alloy.[5] In this experiment, thin films of pure gold and lanthanum, a few tenths of a nanometer in thickness, were fully reacted at 343 K within a few kiloseconds. Two requirements are proposed for the solid-state amorphizing reaction:

- The two reacting metals must have a large negative heat of mixing.
- The two metals must have vastly different diffusivities in each other and in the amorphous alloy to be formed.

The first condition ensures that a thermodynamic driving force for the reaction exists. The second condition ensures that the amorphous alloy will form in preference to crystalline intermetallics, which have lower free energies. This kinetic selection of the reaction path is possible because one species diffusing in the other and in the amorphous alloy is sufficient for the solid-state amorphizing reaction. The micro-mechanism of the solid-state amorphizing reaction in multilayers was studied by Rutherford back-scattering spectroscopic (RBS) marker experiments on a Ni/Zr diffusion couple[10] and transmission electron microscopy (TEM) on Co/Zr.[11] These experiments reveal that the smaller atom in the diffusion couple is the moving species. The growth rate of the amorphous layer, which is formed at the interface of the two atomic species, turned out to be determined by the diffusion coefficient through this amorphous layer.

8.2 FABRICATION OF AMORPHOUS ALLOYS BY MECHANICAL ALLOYING PROCESS

A different technique for synthesizing amorphous materials at temperatures below the crystallization temperature was suggested in 1979 by White[12] when he milled an elemental mixture of Nb and Sn powders. This technique, called mechanical alloying (MA), was then established by Koch et al.[13] for the synthesis of amorphous $Ni_{60}Nb_{40}$ powders by milling

a mixture of pure elements. In the typical experiments for the preparation of an amorphous $Ni_{60}Nb_{40}$ alloy, elemental powders of Ni and Nb were milled for about 40 ks in air or in helium (using a Spex Mixer/Mill Model 8000 and steel balls as a milling media). The XRD patterns for the end-product of amorphous $Ni_{60}Nb_{40}$ alloy powders of as-milled elemental powders in air and helium, prepared by melt spinning, are shown together in Fig. 8.1.

The positions of the maximum of the principal peak in the patterns of the alloys obtained by milling under helium and of the quenched $Ni_{60}Nb_{40}$ are similar ($2\theta = 42.6^{o}$). For the samples that were milled in air, this maximum is at a somewhat higher angle ($2\theta = 43^{o}$).

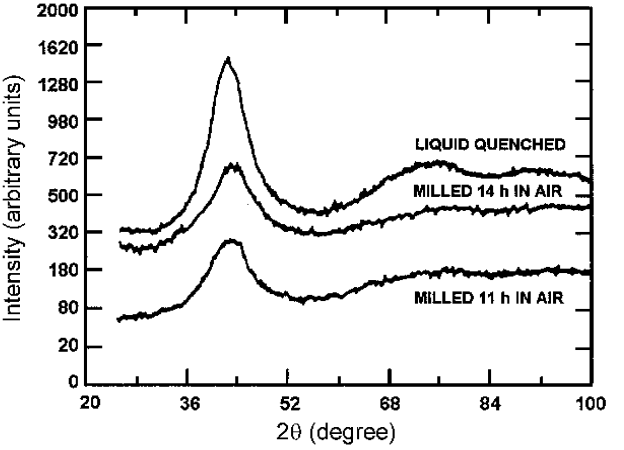

Figure 8.1. XRD patterns of amorphous $Ni_{60}Nb_{40}$ alloys prepared by liquid quenching, MA (14 h) in air, and MA (11 h) in helium. *(After Koch et al.)*[13]

The exothermic crystallization peaks of amorphous $Ni_{60}Nb_{40}$, using different preparation techniques, measured by differential scanning calorimetry (DSC), are not the same (Fig. 8.2). The onset of the first crystallization peak of the melt-spin and the in-helium MA $Ni_{60}Nb_{40}$ are at $T_x = 920$ K. The onset of the second crystallization peak of the helium MA is about 30 K lower than when rapidly cooled. In contrast, the in-air MA $Ni_{60}Nb_{40}$ has one broad crystallization peak with an onset at 850 K. These differences can be explained by the different oxygen concentrations in the alloys. Milling in air resulted in an oxygen concentration of about 3.4 wt %, while milling in helium resulted in a concentration of 0.46 wt % oxygen. These oxygen impurities lower the crystallization temperatures.[13]

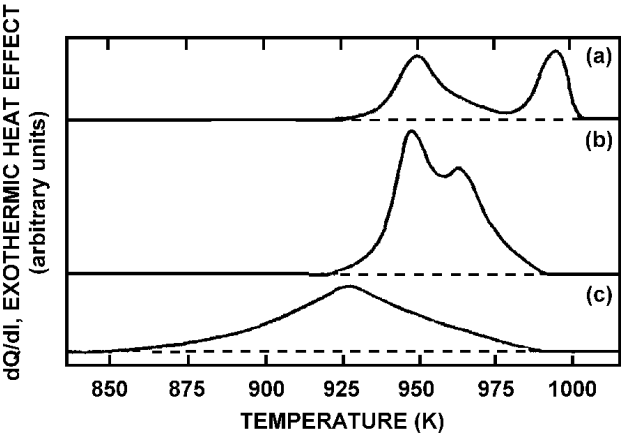

Figure 8.2. DSC plots (heating rate 40 K/min) of amorphous $Ni_{60}Nb_{40}$ prepared by *(a)* liquid quenching, *(b)* MA in helium, and *(c)* MA in air. *(After Koch et al.)*[13]

The effect of iron contamination content on the crystallization temperature, T_x, has also been studied by El-Eskandarany et al.[14] Figure 8.3 illustrates the DTA curves for (*a*) rod-milled (RM) and (*b*) ball-milled (BM) $Al_{30}Ta_{70}$ powders that were milled in an argon gas atmosphere. However, both the RM and BM amorphous alloys are crystallized through single sharp exothermic peaks; the onset of the final RM amorphous $Al_{30}Ta_{70}$ alloy (1440 ks) is 1216 K [Fig. 8.3(*a*)], higher than that for the BM $Al_{30}Ta_{70}$ alloy (1170 K) after the same milling time. This difference is attributed to the existence of high iron concentrations in the BM amorphous powders (2.0 at. %) compared with that for the RM $Al_{30}Ta_{70}$ alloy powders (less than 1 at. %).[14]

8.3 CRYSTAL-TO-GLASS TRANSITION

A free-energy diagram can successfully predict the products that are a result of solid-state amorphization reaction, SARR, for the initial and final products evaluated at the reaction temperature.[5][15] The free enthalpy of the equilibrium crystalline state (G_x) is always much lower than that of the amorphous state (G_a) for metallic systems below the melting temperature (T_m). The amorphous state is a metastable state, i.e., an energy barrier

exists which prevents amorphous metals from spontaneous crystallization.[16] In order to synthesize an amorphous metallic phase via SARR, it is necessary to create an initial crystalline state (G_0) with a high free enthalpy as proposed by the model illustrated in Fig. 8.4.[17]

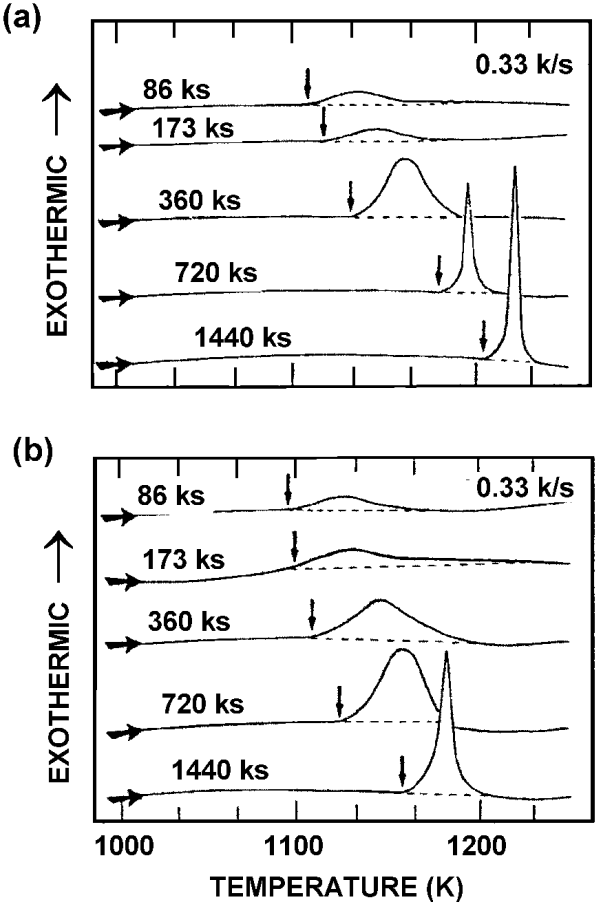

Figure 8.3. The DTA curves for mechanically alloyed $Al_{30}Ta_{70}$ powders as a function of the *(a)* rod-milling, RM, and *(b)* ball-milling, BM, times. *(After El-Eskandarany et al.)*[14]

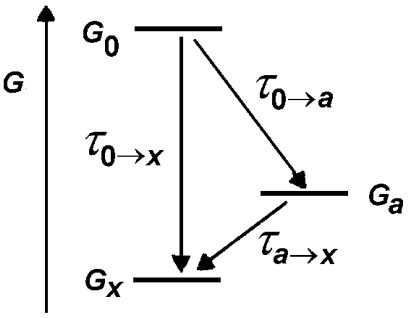

Figure 8.4. Basic principles of glass formation by a solid-state reaction. *(After Johnson.)*[17]

Starting from this initial state, G_0, the free enthalpy of the system can be lowered either by the formation of the metastable amorphous phase or by the formation of the crystalline intermetallic phase. Energetically favored is, of course, the crystalline equilibrium phase, but the kinetics of the phase formation decides which phase is, in fact, formed. To evaluate this, the time scales of the possible reactions must be examined. The formation of the amorphous phase is possible and likely if the formation reaction for the amorphous phase is much faster than that for the crystalline phase;

$$\tau_{0\text{-}a} << \tau_{0\text{-}x}$$

($\tau_{i\text{-}j}$ is the characteristic time scale of the reaction). During this reaction the amorphous phase should not crystallize:

$$\tau_{0\text{-}a} << \tau_{a\text{-}x}$$

It means that the reaction temperature, T_r, must be well below the crystallization temperature, T_x.

8.3.1 The Metastable Phase Diagram

Amorphization by mechanical alloying occurs by an interdiffusion reaction at relatively low temperature in the milled powders. The powder particles are repeatedly cold welded by the colliding balls [Fig. 8.5(*a*)].[16] Thus, the composite powder particles with a characteristically layered microstructure (Fig. 8.6)[18] are formed [Fig. 8.5(*a*)].[16]

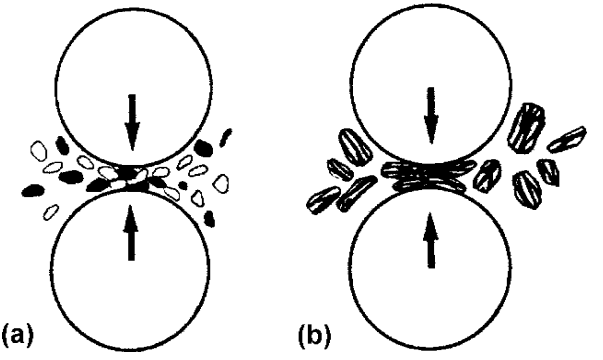

Figure 8.5. Schematic presentation of the mechanical alloying process: *(a)* at the beginning of the milling and *(b)* after some collision events. *(After Schultz.)*[16]

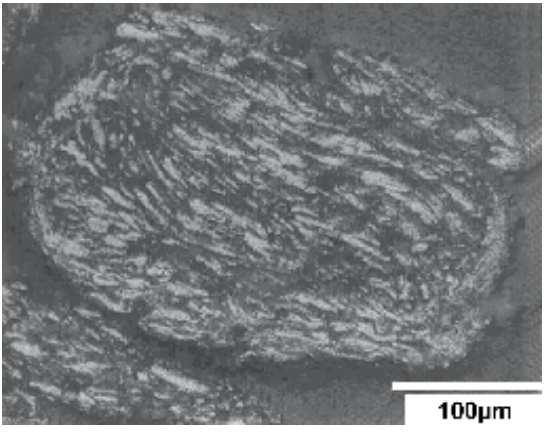

Figure 8.6. Cross-sectional view of mechanically alloyed $Al_{50}Zr_{50}$ powders after 86 ks of milling. *(After El-Eskandarany et al.)*[18]

During this interdiffusion reaction, intermetallic crystalline phases do not form, although these are thermodynamically stable phases. The metastable phase diagram can be deduced using free-energy curves.[19] Figure 8.7 shows the thermodynamically stable phase diagrams of a hypothetical A-B alloy and the free energy curves at a temperature T_r. The free-energy curves show extended primary phases α and β. The phase boundaries are obtained from the double-tangent construction at the free-energy curves. At the temperature T_r, the free-energy curve for the liquid or (assuming that T_r is below the glass transition temperature, T_g) the amorphous phase is always above the composed curve for the stable state. Therefore, the amorphous phase is not present in the phase diagram at T_r. If we consider the experimental fact that during the amorphization reaction the γ phase does not form, we must ignore the free-energy curve for the γ phase in Fig. 8.7. The free-energy curve for the amorphous phase is then lowest in the central part and the metastable phase diagram must be constructed using the free-energy curves for α and β, and by applying the double-tangent construction to these curves (broken lines in Fig. 8.7). As a result, we find extended solubilities for α and β, a broad glass-forming range in the central part and the two two-phase regions as α plus amorphous and β plus amorphous. Contrary to melt spinning, where glass formation would be expected in two composition ranges close to the two eutectics and not at the composition of the γ phase, glass formation by mechanical alloying preferentially occurs in the central part of the phase diagram, i.e., at the composition of the high-melting intermetallic phase. The eutectic compositions of the stable phase diagram are not involved.

The modified phase diagram in Fig. 8.7 resembles a very deep eutectic diagram with the phases α and β in which the eutectic temperature is below the glass transition temperature. Therefore, amorphization by mechanical alloying can also be regarded as a eutectic melting.[17]

8.4 MECHANISM OF AMORPHIZATION BY MECHANICAL ALLOYING PROCESS

The amorphization process during ball milling or rod milling has been proposed by several authors for the following binary systems:

- Ni-TM (TM: Ti,[20]–[23] Zr,[24][25] and Nb[26])
- Fe-TM (TM: Zr,[27] and Nb[28])

- Al-TM (TM: Ti,[29][30] Zr,[29][31] Hf,[32][33] Nb,[29][34][35] and Ta[36]–[40])

As a typical example, we will describe, in detail, the formation of amorphous Al_xHf_{100-x}.[33]

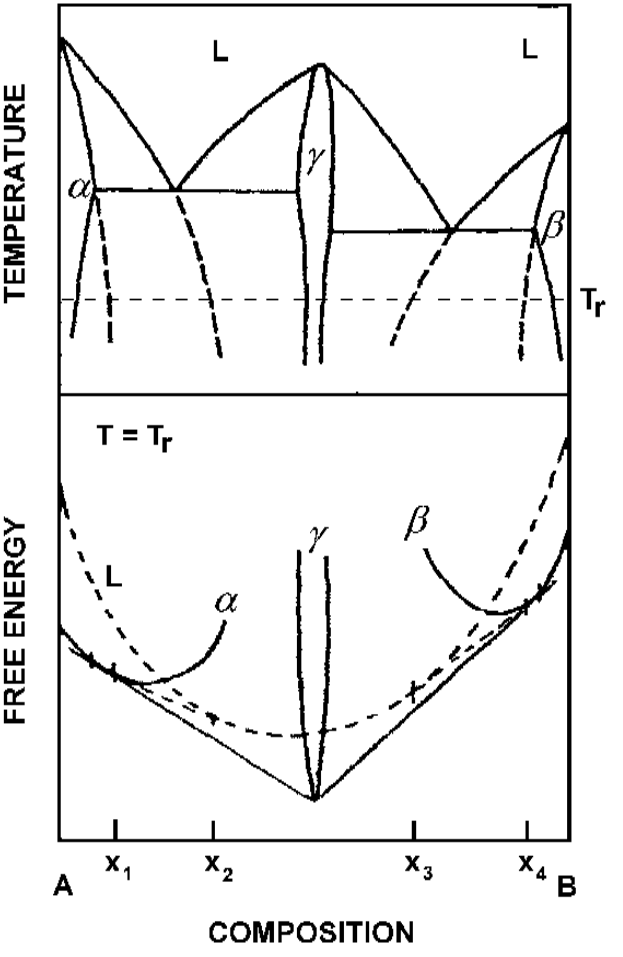

Figure 8.7. Free-energy curve and the resulting stable (solid line) and metastable (broken line) phase diagram. *(After Schwarz.)*[19]

8.4.1 Structural Changes with the Milling Time

8.4.1.1 X-Ray Analysis

Figure 8.8 displays the XRD patterns of the end-product of mechanically alloyed Al_xHf_{100-x} powders at different atomic concentrations of Al, x. Obviously, a wide amorphization range ($33 \leq x \leq 75$) can be obtained after rod milling the elemental diffusion couples for 720 ks of the MA time. For x = 20 and 80, the final products are a mixture of the amorphous phase coexistent with unprocessed elemental Al and/or Hf crystals. No amorphous phases could be detected in the rich sides of the reactant materials (when x = 10 or 90) and the end-products here are nanocomposites Al/Hf powders.

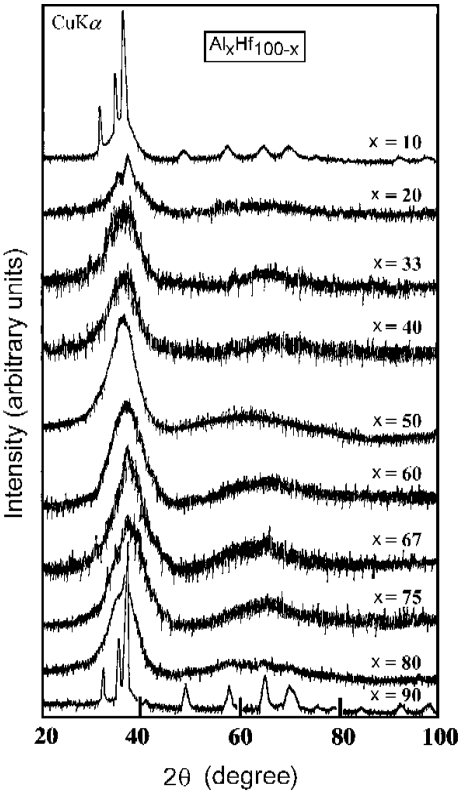

Figure 8.8. The typical XRD patterns of the end-products (720 ks of the MA time) for rod-milled Al_xHf_{100-x} powders. *(After El-Eskandarany.)*[33]

In order to understand the effect of MA time on the total structure of the rod-milled powders, different samples were taken after selected MA times for x-ray analyses. Figure 8.9 presents the correlation between the MA time and the powder's structural changes, taking $Al_{50}Hf_{50}$ alloy as a typical example. In spite of the intact mixture of polycrystalline fcc-Al and hcp-Hf [Fig. 8.9(*a*)], at the early and the intermediate stages of MA time (0 –173 ks), the Bragg peaks for Al and Hf reflections become wider and their intensities are drastically decreased [Fig. 8.9(*b*) and (*c*)]. During the next stage of MA (360 ks), these peaks become broader, with clear diffuse haloes, suggesting the formation of an amorphous phase coexisting with Al and Hf crystals, as illustrated in Fig. 8.9(*d*). At the end of rod-milling time (720 ks), a single homogeneous amorphous phase is yielded, characterized by diffuse haloes and smooth peaks, as displayed in Fig. 8.9(*e*).

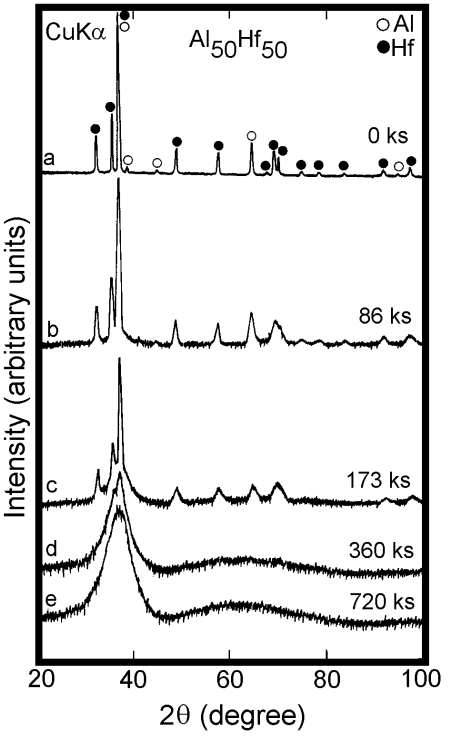

Figure 8.9. XRD patterns of mechanically alloyed $Al_{50}Hf_{50}$ powders after selected rod-milling processing times. *(After El-Eskandarany.)*[33]

8.4.1.2 TEM Observations

TEM analyses have been used to understand the local structure of the rod-milled powders, including the heterogeneity and homogeneity of the powders during the different stages of MA.

Figure 8.10 presents the bright field image, BFI [Fig. 8.10(*a*)], and the selected-area diffraction pattern, SADP [Fig. 8.10(*b*)], for rod-milled $Al_{50}Hf_{50}$ powder particles after 6 ks of MA time. Neither amorphous nor metastable (e.g., solid solution) phases could be detected after this stage of milling, and the powders are just polycrystalline mixtures of coarse cells of Al and Hf, indicated by the sharp spot patterns as shown in Fig. 8.10(*b*). The BFI and the corresponding SADPs of rod-milled powders at the intermediate stage of MA time (173 ks) are shown together in Fig. 8.11. Numerous faults with grain boundary fringes and heavy dislocations in the boundary appear clearly in the powders as a result of the shear stress generated by the milling media (rods), as displayed in Fig. 8.11(*a*). A remarkable significant heterogeneity in the local structure of the powders can be distinguished [Fig. 8.11(*a*)]. According to this variety in the local structure, two different morphological regions (I and II) are chosen as SADPs and presented in Fig. 8.11(*b*) and (*c*), respectively. A fine structure is observed at the right upper edge of the particle (region I), as presented in Fig. 8.11(*a*). The corresponding SADP [Fig. 8.11(*b*)] shows a clear halo pattern, indicating the formation of an amorphous phase in the rod-milled powders at this stage of milling. In region II, however, several defects with grain boundary movement are clearly visible near the center and at the lower edge of the micrographs [Fig. 8.11(*a*)]. The oriented particle has twin and nanotwin boundaries on unprocessed Al and Hf, suggested by the Laue spots presented in Fig. 8.11(*c*). The BFI and the corresponding SADP of the end-product (720 ks) of $Al_{50}Hf_{50}$ powders are shown together in Fig. 8.12. Overall, the sample appears to have a homogeneous fine structure with no dominant facet structure [Fig. 8.12(*a*)]. Moreover, the SADP [Fig. 8.12(*b*)] shows a typical halo-pattern of an amorphous phase in good agreement with the XRD pattern that is presented in Fig. 8.9(*e*).

EDS measurements, using an electron beam of 5 nm, have been used to determine the local composition and the degree of homogeneity for the end-product of the amorphous alloy. For this purpose, the sample that is shown in Fig. 8.13 was classified into a rectangular grid containing 50 circular regions (with a diameter of about 50 nm). Each region was divided into 10 zones and the content of Al in each zone was analyzed. Since such measurements were achieved over several days, the examined sample was

kept under vacuum in the TEM apparatus until the completion of all of the analyses. The results of these experiments were used to construct an isochemical contour map of Al in the examined sample of Fig. 8.12(*a*), using a contour interval of 0.2, as displayed in Fig. 8.13. Overall, the sample appears to have very close values of Al and varies slightly from 49.0 to 50.6 at. %, suggested by the slight gradient change of the Al isochemical line. This suggests the formation of a single homogeneous phase of $Al_{50}Hf_{50}$ alloy powder.

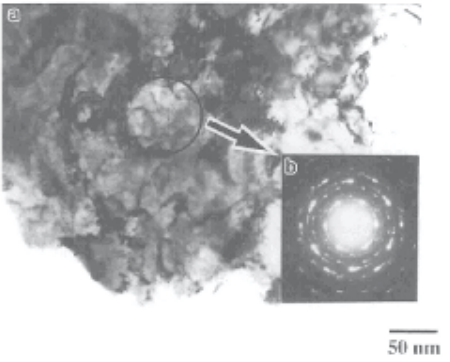

Figure 8.10. *(a)* BFI and *(b)* the corresponding SADP of a mechanically alloyed $Al_{50}Hf_{50}$ powder at the early stage of the rod-milling time (6 ks). *(After El-Eskandarany.)*[33]

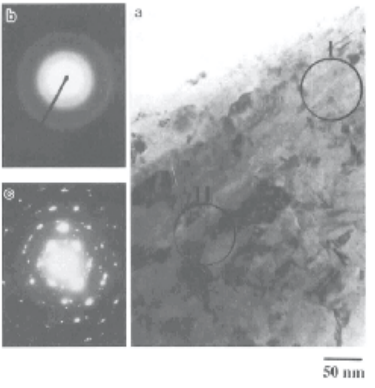

Figure 8.11. *(a)* BFI and *(b* and *c)* the corresponding SADPs of two selected zones (I and II) of a mechanically alloyed $Al_{50}Hf_{50}$ powder at the intermediate stage of the rod-milling time (173 ks). *(After El-Eskandarany.)*[33]

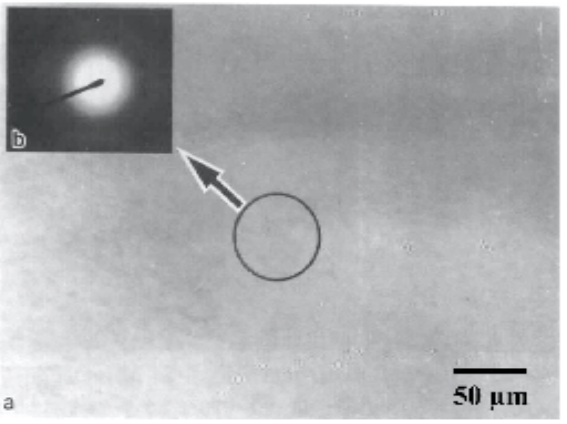

Figure 8.12. *(a)* BFI and *(b)* SADP of a mechanically alloyed $Al_{50}Hf_{50}$ powder at the final stage of the rod-milling time (720 ks). *(After El-Eskandarany.)*[33]

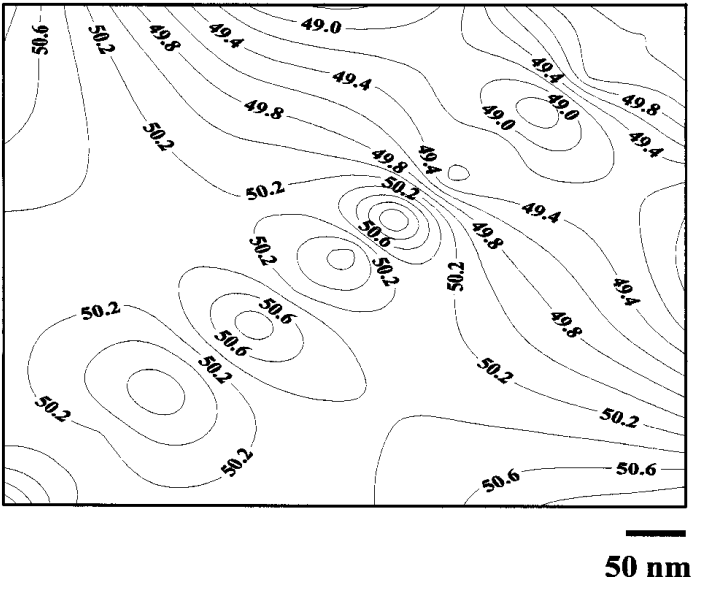

Figure 8.13. Isochemical contour map of Al concentration (at. %) of the sample shown in Fig. 8.12*(a)*. *(After El-Eskandarany.)*[33]

8.4.2 Morphology and Metallography Changes with the Milling Time

Detailed SEM observations were performed to understand the topology and metallography of the rod-milled powders after the different stages of MA. Figure 8.14 shows the SEM micrographs of rod-milled $Al_{50}Hf_{50}$ powders after selected MA times. After a few kiloseconds of milling (22 ks), the starting ductile powders of Al and Hf tend to form globe-shaped agglomerate composite particles (nearly 700 μm in diameter), as shown in Fig. 8.14(*a*).

The metallographical examinations of the cross section for the polished and etched particles that were milled for 86 ks show that the powders contain many intimate layers of elemental Al and Hf (Fig. 8.15). Contrary to the numerous thin layers of the equiatomic particles [Fig. 8.15(*b*)], the number of layers in both Hf and Al rich sides [Fig. 8.15(*a*) and (*c*)] are still fewer and wider in thickness. Further milling (173 ks) enhances the shear forces generated by the rods, leading to the formation of finer powders (about 25 μm in diameter) with cabbage leaf-like morphology, as presented in Fig. 8.14(*b*). After 360 ks of MA time, the powders are dramatically decreased in diameter (about 2 μm or less) and tend to have nearly spherical-like morphology, as shown in Fig. 8.14(*c*). The powder of the end-product (720 ks) comprises homogeneous and smooth spheres with an average size of about 0.75 μm in diameter, as presented in Fig. 8.14(*d*).

Figures 8.16 and 8.17 summarize the SEM observations of rod-milled powders at different stages of milling. Obviously, the MA process performed by the rod-milling technique can be classified into three stages, that is to say, early or agglomeration, intermediate or disintegration, and final or homogenization stages. At the agglomeration stage (0–22 ks) the alloying elemental powders of Al and Hf are agglomerated and grow in size, as a result of repeated cold welding. During this stage of milling, the powders vary widely in size from 150 to about 680 μm (Fig. 8.16). This, accompanied by an increase in the layer thickness and the number of layers for the individual particles, is presented in Fig. 8.17. During the subsequent disintegration stage (43–86 ks), the agglomerated powder particles are subjected to a continuous disintegration with fragmentation to form relatively finer powders with sizes less than 100 μm in diameter. This stage of milling provides very fine Al/Hf composite powder particles with narrow size distribution, as shown in Fig. 8.16. Furthermore, the layer thickness of the particles is dramatically decreased, indicating an increase in the interfaces between the reactant diffusion couples of Al and Hf, as

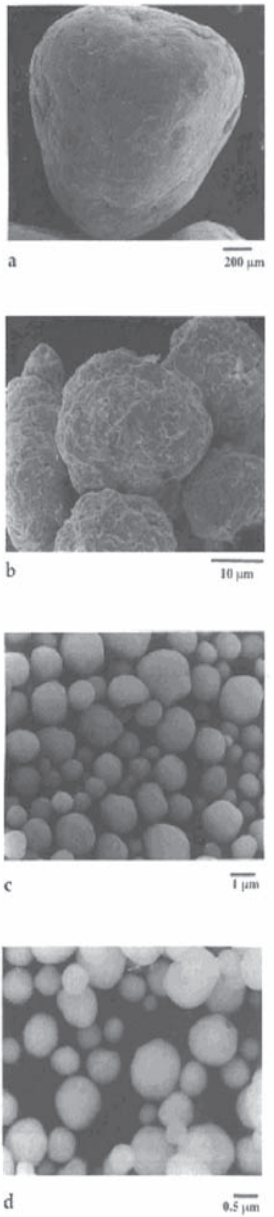

Figure 8.14. Detailed SEM micrographs of mechanically alloyed $Al_{50}Hf_{50}$ powders after *(a)* 22 ks, *(b)* 173 ks, *(c)* 360 ks, and *(d)* 720 ks of the rod-milling time. *(After El-Eskandarany.)*[33]

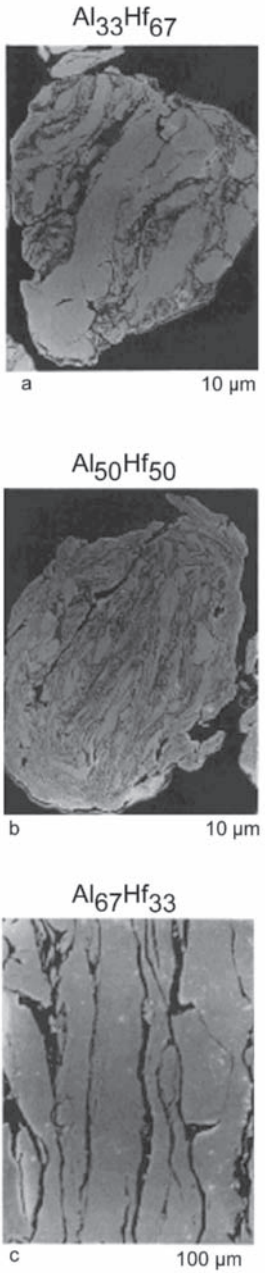

Figure 8.15. SEM micrographs of the cross-sectional view for mechanically alloyed *(a)* $Al_{33}Hf_{67}$, *(b)* $Al_{50}Hf_{50}$, and *(c)* $Al_{67}Hf_{33}$ after 86 ks of the rod-milling time. *(After El-Eskandarany.)*[33]

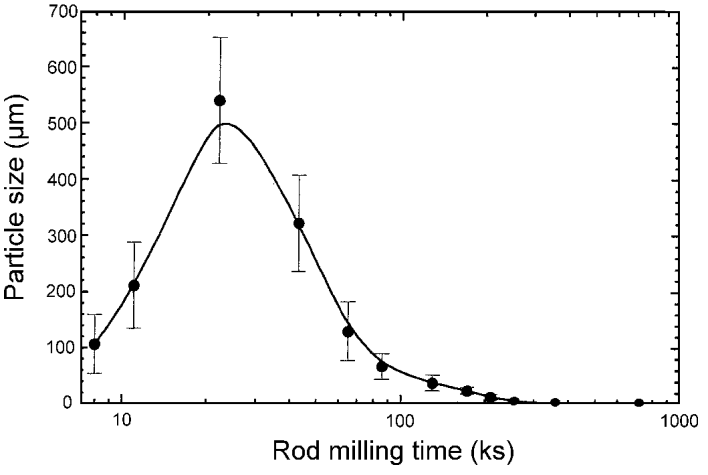

Figure 8.16. Influence of rod-milling time on the particle size distribution of mechanically alloyed $Al_{50}Hf_{50}$ powder. *(After El-Eskandarany.)*[33]

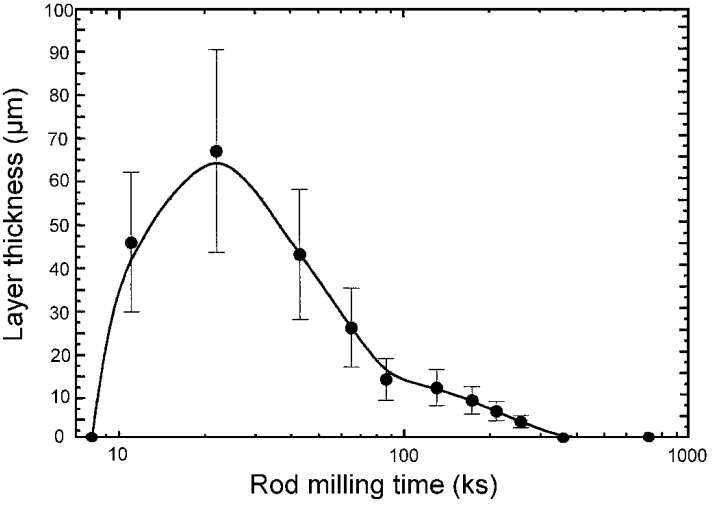

Figure 8.17. Effect of the rod-milling time on the layer thickness distribution of mechanically alloyed $Al_{50}Hf_{50}$ powders. *(After El-Eskandarany.)*[33]

displayed in Fig. 8.17. The final or so-called homogenization stage (360–720 ks) refers to the last stage of MA, in which all the particles are uniform in shape and size without any metallographical details (layered-structure morphology), suggesting the completion of the solid-state reaction and the formation of an amorphous phase.

8.4.3 Thermal Stability

8.4.3.1 Amorphization Process

The typical DTA thermograph of rod-milled $Al_{50}Hf_{50}$ powders is presented in Figs. 8.18 and 8.19 after selected MA times. These measurements were made at a constant heating rate of 0.33 K/s under an argon gas atmosphere. All the samples were heated to 1200 K (first run) and cooled to about 400 K. Then, second heating runs (dashed lines) were performed, in order to establish the base line.

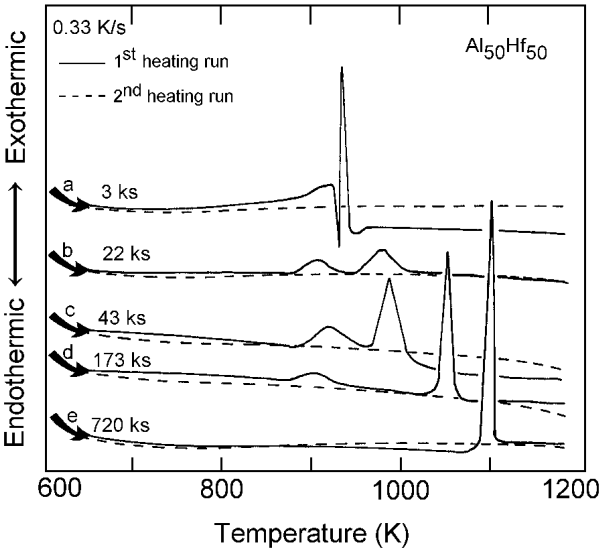

Figure 8.18. DTA curves of mechanically alloyed $Al_{50}Hf_{50}$ powders after *(a)* 11 ks, *(b)* 22 ks, *(c)* 43 ks, *(d)* 173 ks, and *(e)* 720 ks of the rod milling time. *(After El-Eskandarany.)*[33]

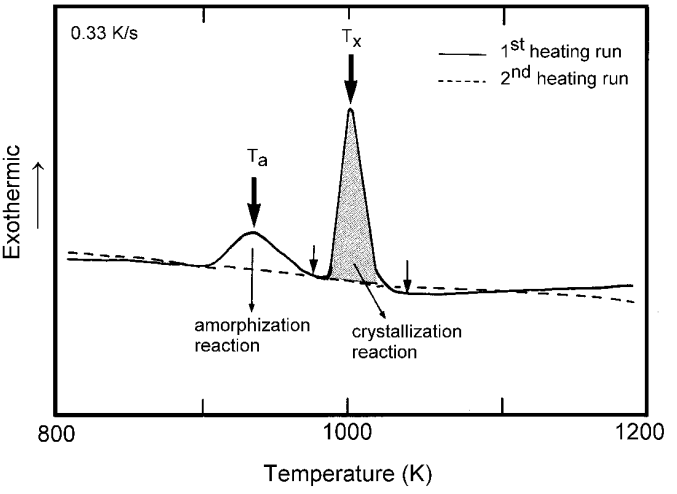

Figure 8.19. DTA thermogram associated with the amorphization reactions (the plain low temperature peak) and crystallization reactions (the shady high temperature peak) for mechanically alloyed $Al_{50}Hf_{50}$ powder after 86 ks of the rod milling time. *(After El-Eskandarany.)*[33]

After 11 ks, the scan reveals two reactions: the first reaction, observed at about 940 K, is endothermic and occurs due to the melting of pure Al in the starting reactant mixture of $Al_{50}Hf_{50}$ powders, and the second reaction (exothermic), occurs at about 980 K and is attributed to a partial reaction of the unprocessed materials of Al and Hf powders [Fig. 8.18(*a*)]. After 22 ks, 43 ks [Fig. 8.18(*b*) and (*c*)], and 86 ks (Fig. 8.19) of MA time, however, these reactions are replaced by a new reaction, that takes place exothermally. The first exothermic reaction appears at a relatively low temperature (about 900 K) and does not change remarkably by changing the milling time. In spite of the first reaction, the second one takes place at a relatively high temperature and its position shifts remarkably to the high temperature side by increasing the MA time. The origin of these reactions, exemplified by the rod-milled 86 ks sample (see Fig. 8.19), has been investigated by XRD, TEM/EDS, and metallographical examinations. The sample that was rod milled for 86 ks of the MA time is heavily dislocated and contains polycrystalline grains of Al and Hf, as suggested by the BFI and its corresponding SADP that is presented in Fig. 8.20(*a*).

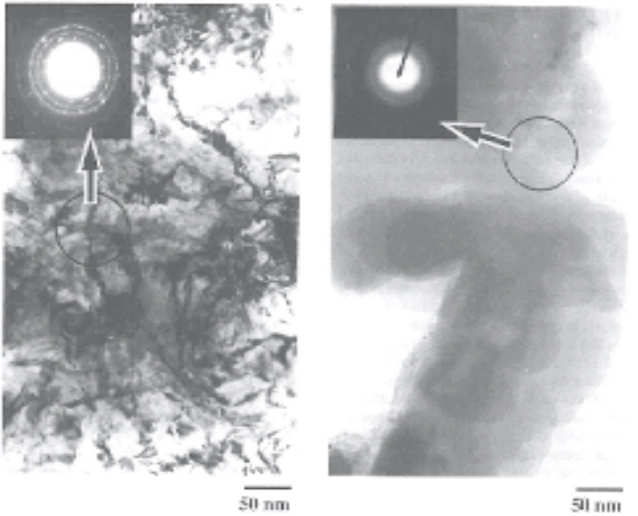

Figure 8.20. BFIs and the corresponding SADPs of $Al_{50}Hf_{50}$ powders after *(a)* rod milling for 86 ks, and *(b)* rod milling for 86 ks and then heating to 980 K in a DTA under Ar gas atmosphere. *(After El-Eskandarany.)*[33]

The metallographical examination of this sample reveals an intimate layered-structure of the diffusion couples of Al and Hf, as presented in Fig. 8.21(*a*). These layers disappear upon heating the sample to 980 K (just above the first exothermic peak in Fig. 8.19), suggesting the formation of a single phase, as displayed in Fig. 8.21(*b*). Moreover, the BFI of this sample shows the formation of fine and featureless images, and a clear halo pattern, as presented in Fig. 8.20(*b*). Consequently, it is concluded that the first exothermic reaction occurs due to a crystalline-amorphous phase transformation conducted by a so-called *TASSA* reaction. The XRD patterns of the sample that was annealed just above the second exothermic reaction[41] show the formation of a crystalline phase, indicating that the high temperature peak resulted from crystallization of the amorphous phase(s) in the milled powder. As the milling time increases, the crystallization peak moves to the high temperature side, becoming more pronounced and sharp; the amorphization peak, however, is hardly seen, as displayed in Fig. 8.18.

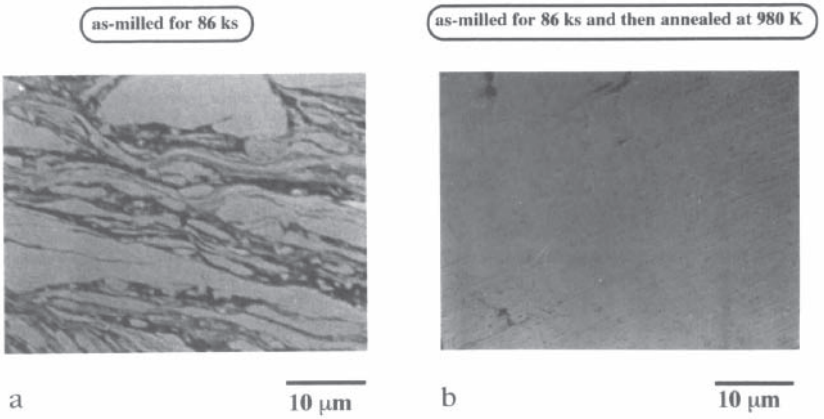

Figure 8.21. SEM micrographs of the polished surface of $Al_{50}Hf_{50}$ after *(a)* rod milling for 86 ks, and *(b)* rod milling for 86 ks and then heating to 980 K in a DTA under Ar gas atmosphere. *(After El-Eskandarany.)*[33]

In order to understand the local composition and the degree of homogeneity of the amorphous phase that formed via the *TASSA* process, EDS analyses have been performed for the sample milled for 86 ks and then annealed at 980 K. Figure 8.22 shows (*a*) the BFI and (*b*) the corresponding isochemical contour map of Al in the examined sample. The sample has been classified into 30 circular regions with a diameter of about 50 nm for each examined region. The results, which were obtained from the local analyses of at least 300 points (10 for each region, using an electron beam of 5 nm), were employed to construct the isothermal lines of Al concentration in the examined sample with a contour interval of 1 at. %, as shown in Fig. 8.22(*b*). In contrast to the results presented in Fig. 8.13, the Al concentration of this sample varies widely from region to region and even within the individual region itself, suggested by the dramatic changes of the values for the isochemical lines (35 to 48 at. %) and the narrow distance between the contour lines. It is worth noting that at this stage of milling (86 ks), a considerable amount of the Al powder is still stacked on the milling tools due to the cold welding effect. Annealing such material leads to the formation of heterogeneous amorphous alloys so that the sample is either poor in Al content (shaded area) or approaches near equiatomic values (plain area). It can be concluded that the amorphous alloy formed via *TASSA* is heterogeneous in composition, containing several compositions of amorphous Al_xHf_{100-x} powders.

(a)

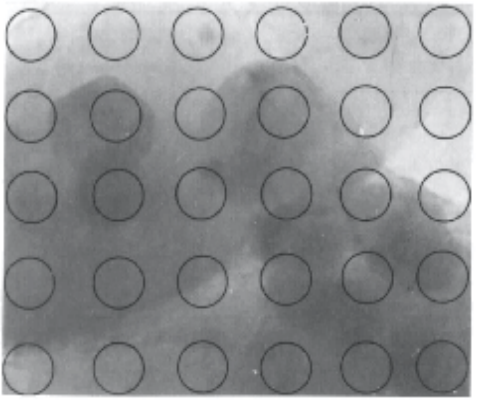

(b)

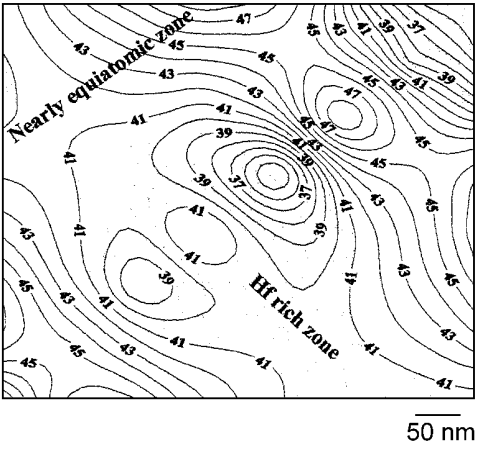

Figure 8.22. *(a)* BFI and *(b)* the corresponding isochemical contour map of Al concentration (at. %) of $Al_{50}Hf_{50}$ powder that was rod-milled for 86 ks and then heated to 980 K in a DTA under Ar gas atmosphere. *(After El-Eskandarany.)*[33]

The DTA measurements allow us to obtain the approximate values of the enthalpy of amorphization (heat release of the crystalline-to-amorphous phase transformation), ΔH_a, and the enthalpy of crystallization (heat release of the amorphous-to-equilibrium crystalline phase transformation), ΔH_x. The amorphization temperature, T_a, and the crystallization temperature, T_x, for amorphous Al_xHf_{100-x} powders have been investigated as well.

In the present study, the term ΔH_a^{TASSA} is used to refer to the heat formation of the amorphous phase (enthalpy of amorphization) via *TASSA* that was directly measured from the area under the amorphization peaks and plotted in Fig. 8.23 as a function of the rod-milling time of selected Al_xHf_{100-x} powders. In all the compositions, ΔH_a^{TASSA} decreases drastically to approach minimum values and then increases dramatically to zero. Compared to the alloy of the equiatomic composition (x = 50), the ΔH_a^{TASSA} for the alloys at the Hf-rich side (x = 20) and Al-rich side (x =80) take longer times to appear and also to vanish. This is attributed to the fact that the starting composite particles at the rich elemental sides contain such very thick elemental metallic layers that *TASSA* can not be performed between them.[42] Increasing the rod-milling time leads to refinement of the layers and, hence, *TASSA* takes place at the interfaces of these fine reactant layers.

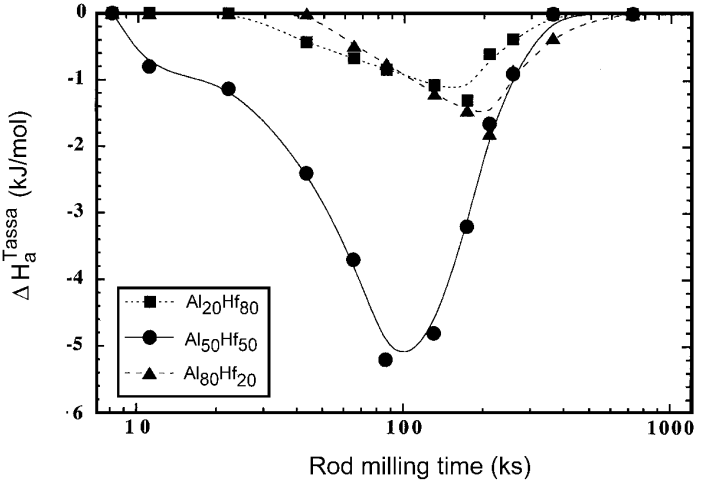

Figure 8.23. Dependence of rod-milling time and the Al concentration on the heat formation of amorphization via *TASSA*, ΔH_a^{TASSA} of selected mechanically alloyed Al_xHf_{100-x} powders. *(After El-Eskandarany.)*[33]

In the present study, the term ΔH_a^{MDSSA} is used to refer to the heat formation of an amorphous phase via *MDSSA*. However, ΔH_a^{MDSSA} is not a measurable value; it can be estimated only during the final stage of milling (when the amorphization peaks are absent, i.e., $\Delta H_a^{TASSA} = 0$), using the following relation:[43]

Eq. (8.1) $\Delta H_{for} = \Delta H_a + \Delta H_x$

Here ΔH_{for} is the reported value of the enthalpy of formation for an intermetallic compound at specific concentrations of Al(x) based on Miedema's model,[44] ΔH_a is the total heat formation of amorphous phases formed by *TASSA* and *MDSSA* processes, and the term ΔH_x is the sum total of enthalpy of crystallization for the amorphous phases caused by the two processes, *TASSA* and *MDSSA*.

Thus, ΔH_a can be given as follows:

Eq. (8.2) $\Delta H_a = \Delta H_a^{TASSA} + \Delta H_a^{MDSSA}$

Here, ΔH_a^{TASSA} and ΔH_a^{MDSSA} are the heat of formation of amorphous phases formed by *TASSA* and *MDSSA*, respectively. Similarly, ΔH_x may be also written as

Eq. (8.3) $\Delta H_x = \Delta H_x^{TASSA} + \Delta H_x^{MDSSA}$

Thus, Eq. (8.1) can be written as

Eq. (8.4) $\Delta H_{for} = (\Delta H_a^{TASSA} + \Delta H_a^{MDSSA}) + (\Delta H_x^{TASSA} + \Delta H_x^{MDSSA})$

During the final stage of milling (the stage in which the amorphous phase is formed due to the *MDSSA* process, i.e., when the amorphization reaction peaks are absent), both ΔH_a^{TASSA} and ΔH_x^{TASSA} equal zero. Hence, the relation of Eq. 8.4 can be rewritten as

Eq. (8.5) $\Delta H_{for} = \Delta H_a^{MDSSA} + \Delta H_x^{MDSSA}$

The value of ΔH_a^{MDSSA} can then be estimated directly from the following relation:

Eq. (8.6) $\Delta H_a^{MDSSA} = \Delta H_{for} - \Delta H_x^{MDSSA}$

In fact, this value is very difficult to estimate at the intermediate stage of milling in which the amorphization peaks are present. At the intermediate stage, measured value of ΔH_x is caused by the crystallization of two amorphous phases resulting from *TASSA* and *MDSSA* together.

The correlation between the minimum values of ΔH_a^{TASSA} and ΔH_a^{MDSSA} with the Al content are presented in Fig. 8.24 as a function of the

Al concentration, *x*. For all *x*, ΔH_a^{MDSSA} is larger than ΔH_a^{TASSA}, especially at the Al and Hf rich sides.

The amorphization ratios, $\Delta H_a^{MDSSA}/\Delta H_a^{TASSA}$, for amorphous Al_xHf_{100-x} alloy powders are listed in Table 8.1. Since the alloys of the rich sides of Al ($x \geq 75$) and Hf ($x \leq 33$) form composite particles with extremely thick layer structures (see Fig. 8.15), the *TASSA* process takes place slowly. Thus, only a small mole fraction of amorphous phase(s) can result upon annealing these composites. Accordingly, the value of ΔH_a^{TASSA} for these alloys is lower than those alloys that are laid near the equiatomic composition ($33 \leq x \leq 75$), as previously presented in Fig. 8.24 and Table 8.1. Hence, the $\Delta H_a^{MDSSA}/\Delta H_a^{TASSA}$ ratio has large values (more than 14) for the rich Al and Hf alloys, suggesting that the amorphous phases for these alloys are formed mainly due to the *MDSSA* process, which means long milling intervals are necessary.

The values of ΔH_a^{MDSSA} were estimated using Eq. (8.6), whereas, ΔH_a^{TASSA} was measured directly using DTA.

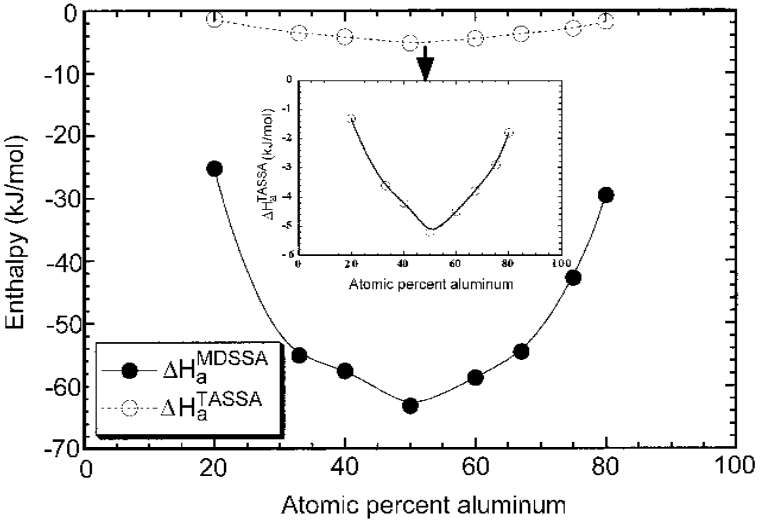

Figure 8.24. Correlation between the heat formation (enthalpy change) of amorphization via *TASSA*, ΔH_a^{TASSA} and *MDSSA*, ΔH_a^{MDSSA} for mechanically alloyed Al_xHf_{100-x} powders. The ΔH_a^{TASSA} of Al_xHf_{100-x} powders is shown inset in the figure in another scale. *(After El-Eskandarany.)*[33]

Table 8.1. The heat formation of amorphization via *MDSSA*, ΔH_a^{MDSSA} and *TASSA*, ΔH_a^{TASSA}, and the relative enthalpy of amorphization ratio, $\Delta H_a^{MDSSA}/\Delta H_a^{TASSA}$, for amorphous Al_xHf_{100-x} alloy powders. *(After El-Eskandarany.)*[33]

Al concentration, x (at. %)	ΔH_a^{MDSSA} (kJ mol^{-1})	ΔH_a^{TASSA} (kJ mol^{-1})	$\frac{\Delta H_a^{MDSSA}}{\Delta H_a^{TASSA}}$
20	-25.2	-1.3	19.4
33	-55.1	-3.6	15.3
40	-57.6	-4.2	13.7
50	-63.2	-5.2	12.2
60	-58.7	-4.5	13.0
67	-54.6	-3.8	14.4
75	-42.8	-2.9	14.8
80	-29.6	-1.8	16.4

8.4.3.2 Crystallization Process

The crystallization characteristics of selected Al_xHf_{100-x} alloy powders indexed by the crystallization temperature, T_x, and the enthalpy change of crystallization, ΔH_x, are presented as a function of the rod milling time, in Figs. 8.25 and 8.26, respectively. It can be seen in Fig. 8.25 that the T_x increases monotonically with an increase in the milling time during the early stage in which the amorphization process occurs only due to the *TASSA* process. This may suggest a gradual compositional change in the milled powders. It then increases dramatically during the intermediate stage in which the amorphous phases are formed due to the amorphization via *TASSA* and *MDSSA* together. This increase in the value of T_x indicates a drastic compositional change in the amorphous phases. During the final stage of milling, however, the amorphous phases are formed by the *MDSSA* process only so that the T_x approaches saturation value even after 720 ks of the MA time.

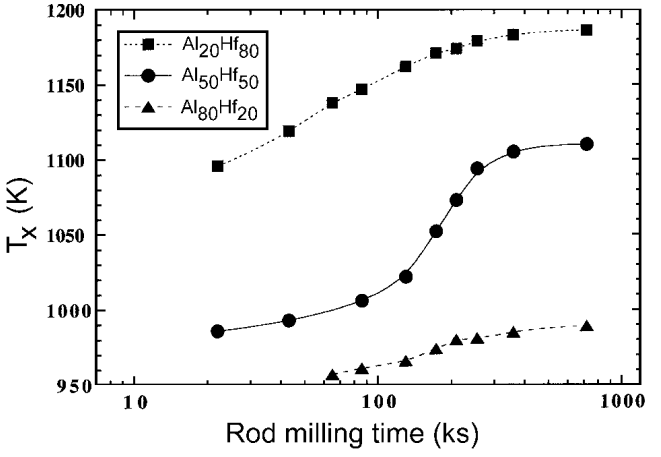

Figure 8.25. Effect of rod-milling time on the crystallization temperature, T_x, of mechanically alloyed Al_xHf_{100-x} powders. *(After El-Eskandarany.)*[33]

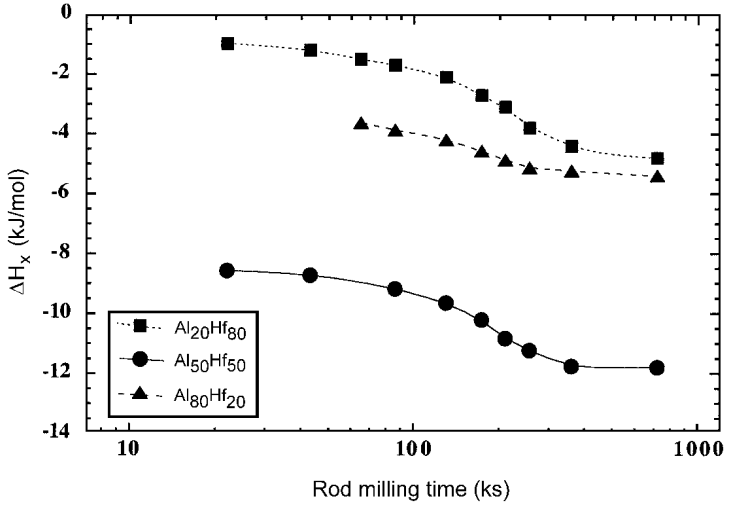

Figure 8.26. Effect of rod-milling time on the enthalpy change of crystallization, ΔH_x, of mechanically alloyed Al_xHf_{100-x} powders. *(After El-Eskandarany.)*[33]

Further information on crystallization reactions is given by ΔH_x and presented in Fig. 8.26 as a function of the rod-milling time. During the first few kiloseconds of milling, the value of ΔH_x decreases monotonically, indicating a gradual increase in the volume fraction of the formed amorphous phases. A rapid increase in the volume fraction of the formed amorphous phase is suggested by the drastic decrease of ΔH_x during the intermediate stage of milling. Towards the end of the milling process, ΔH_x tends to have saturated values, suggesting the formation of homogeneous amorphous phases.

Figure 8.27 illustrates T_x (solid line) of amorphous Al_xHf_{100-x} alloy powders after the final stage of milling (720 ks). In the figure, the melting points, T_m, of Al_xHf_{100-x} alloys based on the phase relation diagram[45] are also presented (dotted line). The dependence of T_x on T_m can be noted. In other words, T_x increases approximately in parallel with increases in the T_m. Table 8.2 shows the melting points, T_m, and the crystallization parameters (T_x, T_m/T_x ratio, ΔH_x) for amorphous Al_xHf_{100-x} alloy powders prepared by the MA method using the rod-milling technique. Obviously, the shown T_m/T_x ratio is about 0.5, in good agreement with the metallic glasses.[46]–[48]

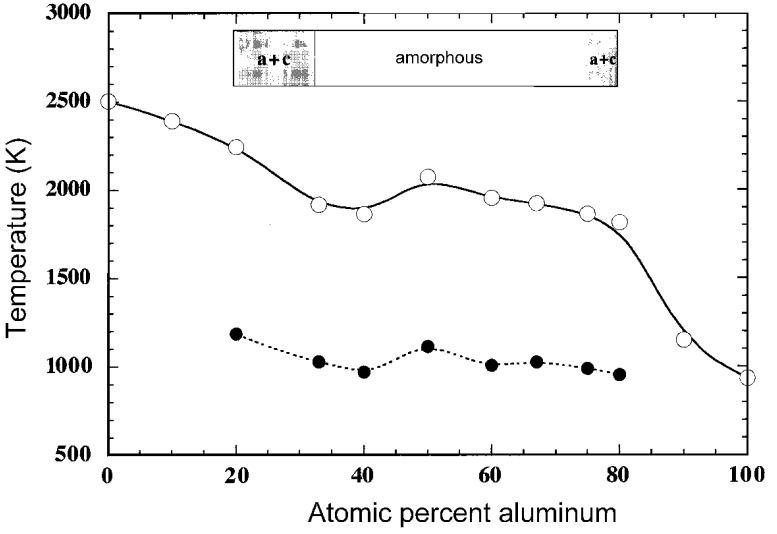

Figure 8.27. Correlation between the melting points, T_m (dotted line), and the crystallization temperatures, T_x (solid line), of Al_xHf_{100-x} powders. *(After El-Eskandarany.)*[33]

Table 8.2. The melting point, T_m,[45] crystallization temperature, T_x, T_m/T_x, and the enthalpy change of crystallization, ΔH_x, for amorphous Al_xHf_{100-x} alloy powders prepared in the present work. *(After El-Eskandarany.)*[33]

Al concentration, x (at. %)	T_m (K)	T_x (K)	$\frac{T_x}{T_m}$	ΔH_x (kJ mol^{-1})
20	2245	1186	0.528	-4.8
33	1917	1028	0.536	-9.9
40	1863	970	0.521	-10.4
50	2073	1115	0.538	-11.8
60	1953	1007	0.516	-11.3
67	1923	1025	0.533	-10.4
75	1863	989	0.531	-8.2
80	1815	952	0.524	-5.4

8.4.3.3 Mechanism

Amorphous Al_xHf_{100-x} alloy powders with wide amorphization ranges ($33 \leq x \leq 75$) have been synthesized by *TASSA* and/or *MDSSA* processes using the rod-milling technique. In the *TASSA*, the heat treatment of the composite powder particles containing a well-developed structure of fresh layers of metallic Al and Hf enhances the solid-state diffusion between these thin layers. This leads to a speed up in the rate of diffusion at the clean Al/Hf boundaries so that the free energy changes drastically from a nonstable phase (starting reactant materials) to a more stable phase (amorphous). In the *MDSSA* process, however, the solid-state reaction takes place in the same manner as occurs in the *TASSA* process, except for a lower diffusion rate and a longer MA time. This is attributed to the milling temperature which is assumed to be far below that in *TASSA* (980 K). Thus, the interdiffusion between Al and Hf layers occurs slowly. Although the two processes seem to be the same with different time-scales, they produce amorphous alloys which differ widely in thermal stability.

Amorphization via *TASSA* Process; The Early Stage of Milling. This duration of MA time (0–43 ks) refers to the first stage of milling, in which the amorphization process occurs only due to *TASSA* process.

During the first few kiloseconds of this stage (0–22 ks), almost all the initial materials of Al and Hf are agglomerated to form powder particles containing coarse layers of the metallic diffusion couples. Further milling (22–43 ks) leads to the formation of composite particles containing numerous narrow layers of Al and Hf in good arrangement as a result of the shear force generated by the rods. These intensive shear forces, accompanied by cold working, create naturally multilayered composite particles that are typical for sputtered or evaporated diffusion couples.[5] In this stage, the as-rod-milled powders are large grained mixtures of polycrystalline Al and Hf with sharp grain boundaries. It is worth saying that the formation of the amorphous phase during this stage of milling occurs only due to *TASSA*, which is conducted in DTA. During the DTA measurements of the alloy powders at this stage, two clear separate exothermic peaks appear. The first exothermic reaction occurs at about 920 K and the second reaction occurs well above this temperature. The first exothermic peak refers to *TASSA* in which the free energy of the composite Al/Hf particles decreases from the initial state to the amorphous state formed via *TASSA*. The second exothermic peak occurrs due to the crystallization of the amorphous phase that formed from the first reaction. The free energy then decreases again from the amorphous state to the equilibrium crystalline state. The DSC allow us to measure the enthalpy of amorphization via *TASSA*, ΔH_a^{TASSA}, directly.

Once the thickness of Al and Hf layers in the composite particles decreases by increasing the MA time, the number of these fresh layers (which became very narrow) increases. The increment of these layers plays a very important role for the amorphization by way of *TASSA*. The ΔH_a^{TASSA} increases drastically by increasing these layers, suggesting a dramatic increase in the volume fraction of the amorphous phase. It is worth noting that when the powder particles have no layers of the starting elements, heating them in the DTA does not lead to the formation of any amorphous phases and ΔH_a^{TASSA} becomes zero.

During the *TASSA* process, both T_x^{TASSA} and ΔH_x^{TASSA} increase drastically, suggesting a dramatic compositional change and an increase in the volume fraction of the amorphous alloy in the rod-milled powder. The crystallization process at this stage of milling involves only the crystallizing of the amorphous phase formed by *TASSA* process. It has been shown in a previous work[30] that, when the initial materials for rod-milling technique are intermetallic powders, the amorphization process or so-called mechanical disordering, MD, takes place without compositional change. This is because the final product of the milled powders has the same

composition as the starting intermetallic compound powders. It has already been established[21] that the amorphization in the MD process requires an increase in the free energy of the compound from the lowest level (most stable phase) to a higher level (less stable phase).[49] This can be performed in the ball and/or rod mills by making the crystalline compounds store energy in the form of chemical disorder and point and lattice defects,[50] which is a typical example for the *MDSSA* process. Thus, the DTA curves for MD powders[51] have shown that the exothermic peaks which are related to the *TASSA* process are absent and the processes are carried out through a single stage. During all the stages of MD process, ΔH_a refers to the heat formation of an amorphous phase by the *MDSSA* process only, i.e., ΔH_a^{MDSSA}. This value can be easily estimated at any MD processing time using Eq. (8.1).

In fact, *TASSA* is an interesting process in that an amorphous alloy can be formed simply by heating the layered-composite particles to 980 K without further milling. This phenomenon has also been shown in mechanically alloyed Ni-Ti,[21] Al-Nb,[52] Al-Ta,[51] Al-Ti,[30] and Al-Zr[31] binary systems. This process takes place in the same manner as solid-state amorphization in artificial metallic multilayered thin film.[53][54] One merit of the *TASSA* process is to shorten the milling time and this may lead to the formation of amorphous alloys with low contamination contents. However, the formed amorphous phase via *TASSA* method is rather heterogeneous, as indicated by broad crystallization peaks. Moreover, this amorphous phase has a low thermal stability, suggested by the low values of ΔH_x^{TASSA} and T_x^{TASSA}. The thermal stability and homogeneity of the amorphous phase can be improved by further milling times (see the following sections).

The Intermediate Stage of Milling; The Role of Amorphization via *TASSA* and *MDSSA* Processes. In parallel with the *TASSA* process, a *MDSSA* begins to take place at the fresh surfaces of Al/Hf layers with further MA time (86–173 ks). Thus, the amorphization reaction at this stage of milling occurs as a sum of two effects, the first is *TASSA* and the second is *MDSSA*. At the beginning of this stage, the elemental layers of Al and Hf of the composite powders become very thin and have excellent arrangement with numerous numbers of interfaces between the diffusion couples. Thus, the value of ΔH_a^{TASSA} decreases dramatically, being larger than ΔH_a^{MDSSA}. In other words, the value of ΔH_x^{TASSA} is larger than ΔH_x^{MDSSA}. Toward the middle of this stage, the elemental layers of Al and Hf gradually disappear and the amorphization process occurs mainly due to *MDSSA*. Thus, the values of ΔH_a^{MDSSA} and ΔH_x^{MDSSA} become larger than ΔH_a^{MDSSA} and ΔH_x^{TASSA}. Hence, in the amorphous phases which form by way of

TASSA plus *MDSSA* crystallizing together through a single broad exothermic peak (overlapped peak), it is very difficult to estimate the values of ΔH_a^{MDSSA}, ΔH_x^{MDSSA}, and ΔH_x^{TASSA} during this stage of MA. At the end of this stage (360 ks), the powder particles no longer have layered-structure morphology and the amorphization process starts to occur only due to *MDSSA*. Thus, the effect of the *TASSA* process in the amorphization route can be neglected.

The Final Stage of Milling; The Role of Amorphization via *MDSSA* Process. During this last stage of milling (360–1400 ks), the amorphization process occurs only due to the effect of *MDSSA*. Thus, both ΔH_a^{TASSA}, and consequently, ΔH_x^{TASSA} become negligible. The free energy change of amorphization at this stage can be directly changed from the nonstable phase (starting material) to a more stable phase (amorphous). In fact, the formed amorphous phase via the *MDSSA* process is very homogeneous, and unprocessed Al and/or Hf atoms in the final product of the alloy powders are not detected. In addition, the alloyed powders possess excellent morphological properties such as homogeneous shapes (spherical-like morphology) with fine and smooth surface relief with uniform size (less than 1 μm in diameter). During this process, the amorphous alloys crystallize through single, sharp, exothermic peaks, suggesting that the amorphous phase formed is single and homogeneous in composition. Due to the crystallization process, the free energy changes from the amorphous phase to the most stable phase (crystalline). Compared with *TASSA*, the amorphization reaction via the *MDSSA* process occurs fast and much more homogeneously. This is demonstrated by the nearly constant values of T_x^{MDSSA} and ΔH_x^{MDSSA}. One disadvantage of the *MDSSA* process is the long processing time required to change the free energy from the initial state to the amorphous state. This usually causes a rather high contamination of iron and oxygen.

8.5 THE GLASS-FORMING RANGE

As was mentioned in the preceding sections, the glass-forming range can be predicted using different models. It is worth noting that glass formed by mechanical alloying differs widely from rapid quenching; accordingly the glass-forming range for both processes differs.

Amorphization by mechanical alloying has been studied in a wide composition range for Ni-Ti,[20] Cu-Ti,[56] Fe-Zr,[56] Ni-Zr,[57]–[60] Co-Zr,[60][61] Ni-Nb,[62] Al-Nb,[34][63] Al-Ti,[30] Al-Hf,[33] and Al-Ta.[42][64]

In most cases, the XRD diffraction patterns have been used to determine the glass and/or amorphous-forming range. For example, Fig. 8.28 shows the XRD patterns of the end-product (1080 ks) for mechanically alloyed Al_xTa_{1-x}. At this stage of milling, clear halo-diffraction patterns are shown, suggesting the formation of an amorphous phase with a wide amorphization-range of $0.10 < x < 0.8$.[64]

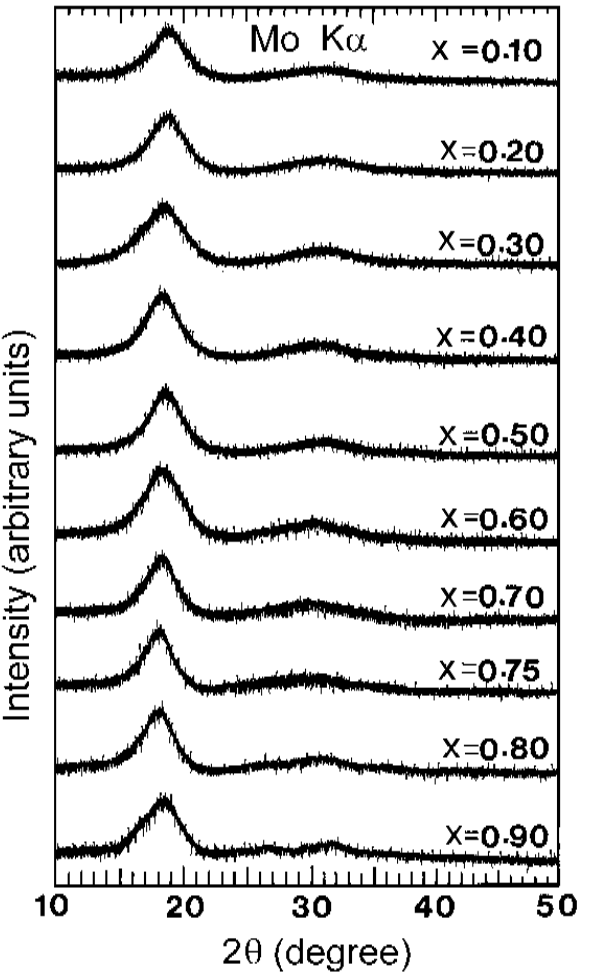

Figure 8.28. The XRD patterns of mechanically alloyed Al_xTa_{1-x} after 1080 ks (end-product) of ball-milling processing time. *(After El-Eskandarany.)*[64]

Other useful and more reliable techniques are also used to determine several physical properties of the formed amorphous phases, such as the superconducting transition temperature (Fig. 8.29), crystallization temperature, T_x (Figs. 8.27 and 8.30), enthalpy change of crystallization, ΔH_x (Figs. 8.26 and 8.31), and crystallization temperature to melting point ratio, T_x/T_m (Fig. 8.32), which are qualitative properties depending on composition within the homogeneity range of the amorphous phase and being constant in the two-phase region.

Table 8.3 lists some typical metallic amorphous binary systems that have been obtained by way of mechanical alloying and their range of amorphization.

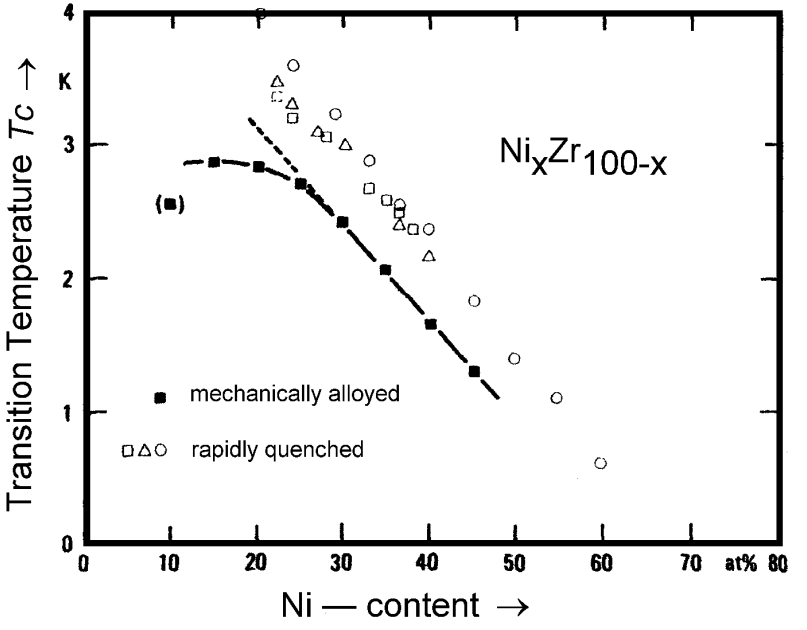

Figure 8.29. Superconducting transition temperature, T_c, of mechanically alloyed and rapidly quenched Ni_xZr_{100-x} as a function of Ni content.[65]–[67]

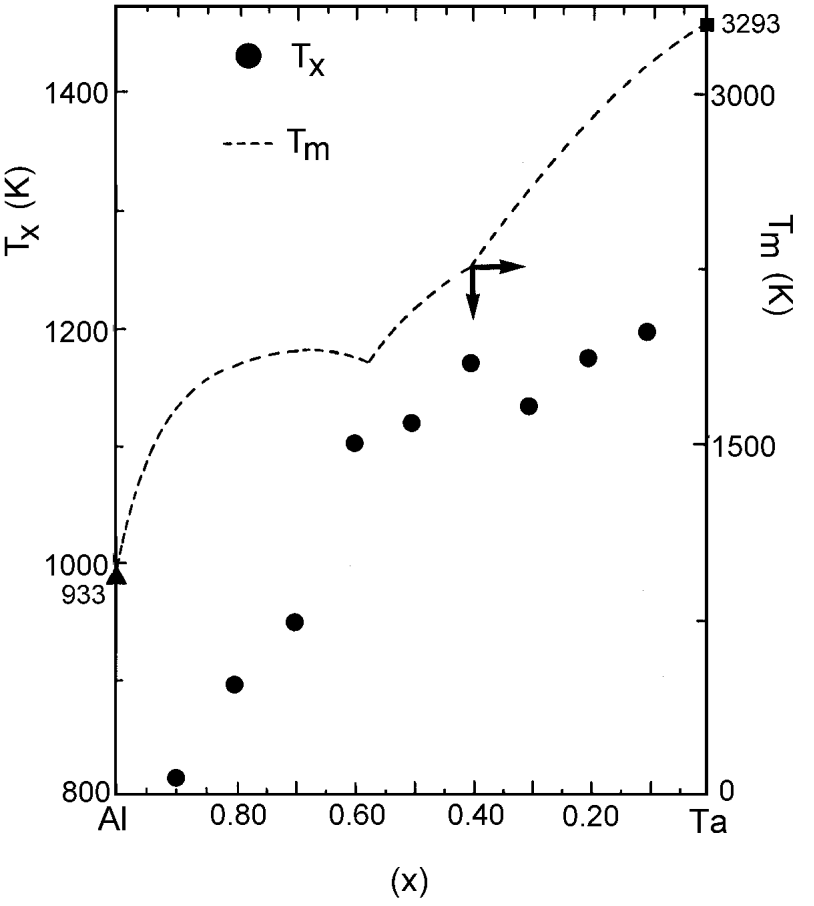

Figure 8.30. Correlation between the melting points, T_m (dotted line), and the crystallization temperatures, T_x (closed symbols), of mechanically alloyed Al_xTa_{1-x} after 1080 ks (end-product) of ball-milling processing time. *(After El-Eskandarany.)*[68]

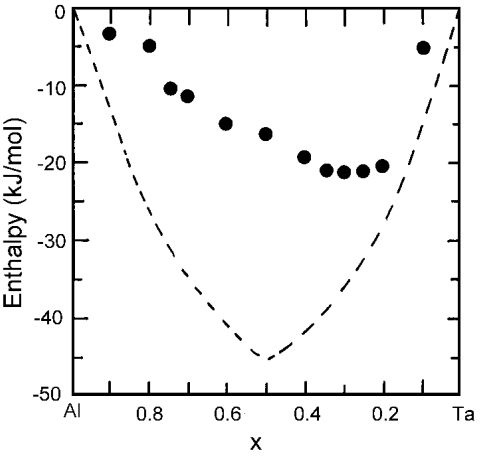

Figure 8.31. The enthalpy change of crystallization, ΔH_x, of mechanically alloyed Al_xTa_{1-x} after 1080 ks (end-product) of ball-milling processing time. *(After El-Eskandarany.)*[64]

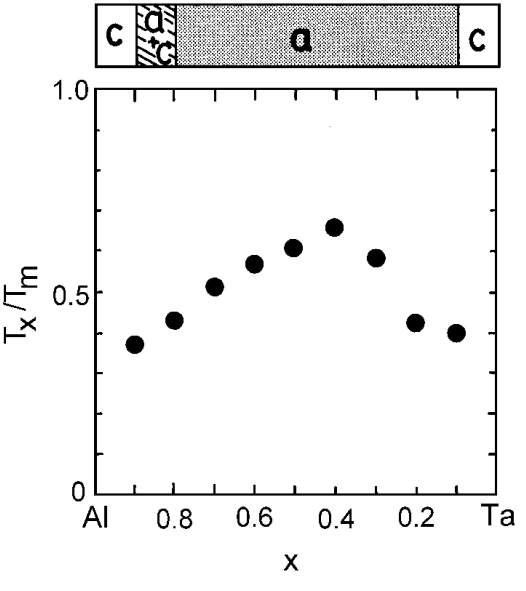

Figure 8.32. Dependence of T_x/T_m ratio of Al content, x, of mechanically alloyed Al_xTa_{1-x} after 1080 ks (end-product) of ball-milling processing time. *(After El-Eskandarany.)*[64]

Table 8.3. Glass and/or Amorphous-Forming Range of Selected Metallic Mechanically Alloyed Binary Systems and the Corresponding Mill Devices

System	Milling Device	Glass and/or Amorphous-Forming Range	References
Ag-Cu	Spex mill	$Ag_{50}Cu_{50}$	71
Al-Fe	Planetary mill	$50 \leq Al \leq 80$	72
Al-Hf	Rod mill	$20 \leq Al \leq 80$	33
Al-Nb	Planetary mill Rod mill	$Al_{50}Nb_{50}$	63 35
Al-Ta	Ball mill Rod mill	$10 \leq Al \leq 80$ $10 \leq Al \leq 75$	68 42
Al-Ti	Spex mill Rod mill	$12.5 \leq Al \leq 26$ $20 \leq Al \leq 75$	73 30
Al-Zr	Spex mill Rod mill	$17.5 \leq Al \leq 40$ $Al_{50}Zr_{50}$	74 18
Au-La	Vibratory mill	$Au_{55}La_{45}$	75
B-Fe	High-energy ball mill	B = 50, 60	76
Co-Nb	Attritor	$Co \leq 85$	77
Co-Ti	Planetary mill	$Co_{50}Ti_{50}$, $Co_{75}Ti_{25}$	78, 79, 80
Co-V	Planetary mill	$40 \leq Co \leq 67$	81
Co-Zr	Planetary mill	$27 \leq Co \leq 92$ $75 \leq Co \leq 90$	61 82
Cr-Nb	Planetary mill	$25 \leq Cr \leq 80$	83
Cu-Hf	Planetary mill	$30 \leq Cu \leq 70$	84
Cu-Ta	Planetary mill	$Cu_{30}Ta_{70}$	85
Cu-Ti	Planetary mill	$10 \leq Cu \leq 87$	55
Cu-V	Planetary mill	$Cu_{50}Ta_{50}$	86
Cu-Zr	Spex mill	Cu = 40, 50, 60	87
Fe-Nb	Vibratory mill	$Fe_{52}Nb_{48}$	28

Table 8.3. *(Cont'd.)*

System	Milling Device	Glass and/or Amorphous-Forming Range	References
Fe-Si	Planetary mill	$Fe_{75}Si_{25}$	88
Fe-Ti	Spex mill	$Fe_{60}Ti_{40}$	89
Fe-Zr	Planetary mill	$20 \leq Fe \leq 80$	27, 90
Fe-W	Ball mill	$Fe_{50}W_{50}$	91
Mn-Nb	Planetary mill	$45 \leq Mn \leq 55$	83
Mn-Zr	Planetary mill	$Mn_{60}Zr_{40}$	92
Nb-Ni	Spex mill	$20 \leq Ni \leq 83$	93
Ni-Ti	Spex mill	$35 \leq Ni \leq 80$	94
Ni-V	Planetary mill	$Ni_{40}V_{60}$	95
Ni-Zr	Planetary mill	$27 \leq Ni \leq 83$	59
Pd-Ti	Vibratory mill	$15 \leq Pd \leq 85$	96
Pd-Zr	Vibratory mill	$45 \leq Pd$	97
Si	Planetary mill	Si amorphous phase	98
Si-Ti	Planetary mill	$70 \leq Si \leq 80$	99
V-Zr	Vibratory mill	$V_{29}Zr_{71}$	100

The formation of enthalpy of crystalline compounds can be estimated using Miedema's semi-empirical model.[69] This model can be applied to estimate the formation enthalpy of an amorphous alloy with chemical short-range order.[70] The formation enthalpy of an alloy of a transition metal, *A*, in a transition metal, *B*, is given by the model as:

Eq. (8.7) $$\Delta H_f = xA\int_B^A \Delta H_{sol}^{A\,in\,B}$$

where $\Delta H_{sol}^{A\ in\ B}$ is the solution enthalpy of *A* in *B* per mol *A*, *x* is the atomic fraction and $\int_B^A$ is the degree by which an *A* atom is surrounded by *B* atoms. For ordered crystalline alloys, $\int_B^A$ is defined as;

Eq. (8.8) $$\int_B^A = c_B^s\left[1 + 8\left(c_A^s c_B^s\right)^2\right]$$

with c_B^s the surface concentration of *B* atoms:

Eq. (8.9) $$c_B^s = \frac{x_B V_B^{2/3}}{x_A V_A^{2/3} + x_B V_B^{2/3}}$$

For amorphous alloys with chemical-short-range order, the order parameter is given as:[70]

Eq. (8.10) $$\int_B^A = c_B^s\left[1 + 5\left(c_A^s c_B^s\right)^2\right]$$

For the formation enthalpy of the alloys, a weighted average of the formation enthalpies of *A* in *B* and *B* in *A* is taken:

Eq. (8.11) $$\Delta H_f = x_A x_B\left(\int_B^A \Delta H_{sol}^{A\ in\ B} + \int_A^B \Delta H_{sol}^{B\ in\ A}\right)$$

Equations (8.10) and (8.11) are used to calculate the formation enthalpy of an amorphous alloy from the crystalline elements. This enthalpy (in J/mol) is estimated following Miedema and Niessen:

Eq. (8.12) $$\Delta H = CT_m$$

where T_m is the melting temperature (in K) of the element and C is a constant for which an average value of 3.5 J/(mol K) will be used. From the difference in formation enthalpy of amorphous and crystalline phases calculated by Eqs. (8.8), (8.10), (8.11), and (8.12), the crystallization enthalpy of an amorphous phase can be estimated.

8.6 AMORPHIZATION VIA MECHANICAL ALLOYING WHEN ΔH^{for} = ZERO; MECHANICAL SOLID-STATE AMORPHIZATION OF $Fe_{50}W_{50}$ BINARY SYSTEM

The production of amorphous FeW alloys that have a heat of formation, ΔH^{for}, equal to zero[101] is difficult by melt quenching, sputter deposition and thermal evaporation methods and few reports have been published on its amorphous formation.[102]–[104] This is due to the differences in the melting points and vapor pressure between Fe and W. The possibility of amorphous phase formation was suggested earlier by Boldrick et al.[105] when they milled pure W powders in a stainless steel ball mill. Because of the hardness of W powders, contamination and later alloying with Fe from abrasion of the stainless steel balls result in the amorphous phase. An amorphous-like Fe-W coexisting with unprocessed W powders was obtained after 180 ks, using a high-energy ball mill.[105]

In 1997, El-Eskandarany et al.[91] reported the formation of a single phase of $Fe_{50}W_{50}$ amorphous alloy powders via MA process using a low-energy ball mill operated under purified argon gas atmosphere at room temperature.

8.6.1 Structural Changes with the Milling Time

The XRD patterns of mechanically alloyed $Fe_{50}W_{50}$ powders after selected MA times are presented in Fig. 8.33. In contrast to the intact mixture of polycrystalline bcc-Fe and bcc-W powders [Fig. 8.33(*a*)], after 86 ks of MA time [Fig. 8.33(*b*)], the Bragg peaks of α-W reflections become weak and broad, whereas, the peak positions do not change. On the other hand, the peak positions of α-Fe, taking Fe (110) as a typical example, shift to the low angle side. This suggests a solid-state diffusion of W atoms in the Fe matrix to form bcc Fe-W solid solution. The number of the W atoms that migrated to the Fe lattice increase with increasing MA time. Obviously, the intensity of the Bragg peaks for α-W decreases drastically after 173 ks of MA time, as shown in Fig. 8.33(*c*). In parallel, the Bragg peaks of α-Fe shift to the low angle side and become broad. After 360 ks of MA time [Fig. 8.33(*d*)], no remarkable change in the peak position of α-Fe can be noted, indicating the completion of the solid-state reaction. After 720 ks of the MA time, the Bragg peaks of α-Fe surprisingly disappear, while a broad halo peak which overlaps those of α-W appears, as shown in

Fig. 8.33(*e*). This indicates the formation of amorphous FeW coexisting with a small fraction of unprocessed W powders. After 1440 ks of MA time, a solid-state amorphization reaction takes place between the amorphous phase of FeW and the W powders. The amorphous phase is characterized by a diffuse and smooth halo, as displayed in Fig. 8.33(*f*). We emphasize that this amorphous phase is stable against mechanical deformation and does not change to any other phase(s) even after milling for a longer time, up to 2400 ks.

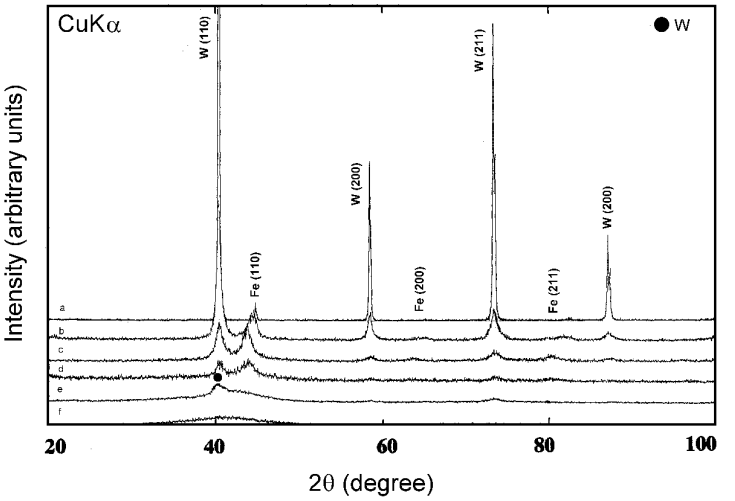

Figure 8.33. XRD patterns of mechanically alloyed $Fe_{50}W_{50}$ powders after *(a)* 0 ks, *(b)* 86 ks, *(c)* 173 ks, *(d)* 360 ks, *(e)* 720 ks, and *(f)* 1440 ks of MA time. *(After El-Eskandarany et al.)*[91]

Figure 8.34 displays the lattice parameter (a_0) of α-Fe as a function of the MA time. The a_0 monotonically increases with increasing the MA time. Increasing the MA time enhances the solid-state reaction so that the W atoms begin to migrate to the Fe lattice and this leads to a monotonical expansion in the value of a_0 for pure Fe. After 540 ks of MA time, the a_0 of α-Fe has a value of about 0.2915 nm, which is larger than that for pure Fe (0.2866 nm). This solid-solution phase transforms to a metastable phase (amorphous) after 720 ks of MA time, as presented in Fig. 8.33.

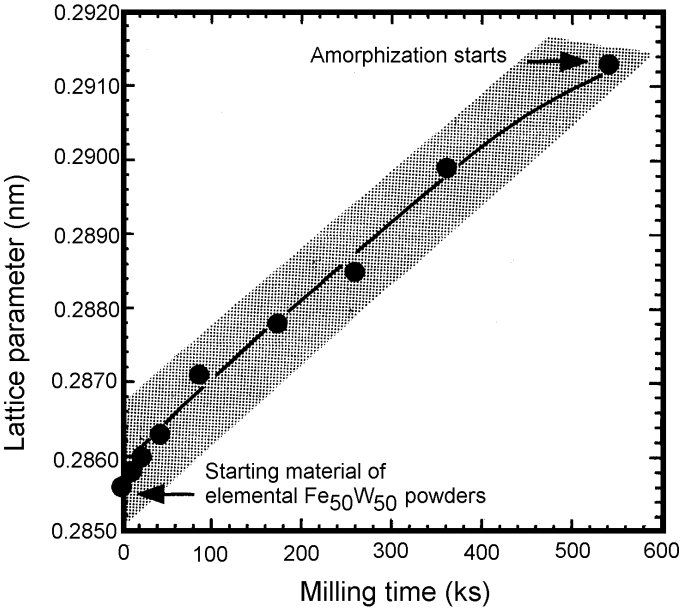

Figure 8.34. Correlation between the milling time and the lattice parameter, a_0, of a bcc Fe phase during milling of $Fe_{50}W_{50}$ powders. *(After El-Eskandarany et al.)*[91]

The TEM/EDS technique has been used to detect the local structural and compositional variations in mechanically alloyed $Fe_{50}W_{50}$ powders after several stages of milling. Figure 8.35 summarizes the local (nanoscale) EDS analyses of mechanically alloyed $Fe_{50}W_{50}$ powders during several stages of milling. After 4 ks of MA time, the particles are either rich or poor in Fe content. After 22 ks of MA time, the solubility of W in Fe increases, and the particles have a very wide compositional distribution. At the intermediate stage of milling (22 to 173 ks), the particles are heterogeneous in composition. After 720 ks of MA time, the number of grains that have an average composition of $Fe_{70}W_{30}$ become predominant. Toward the end of the MA time (1440 ks), the composition of the powder particles approach the nominal composition, indicating the formation of a homogeneous alloy.

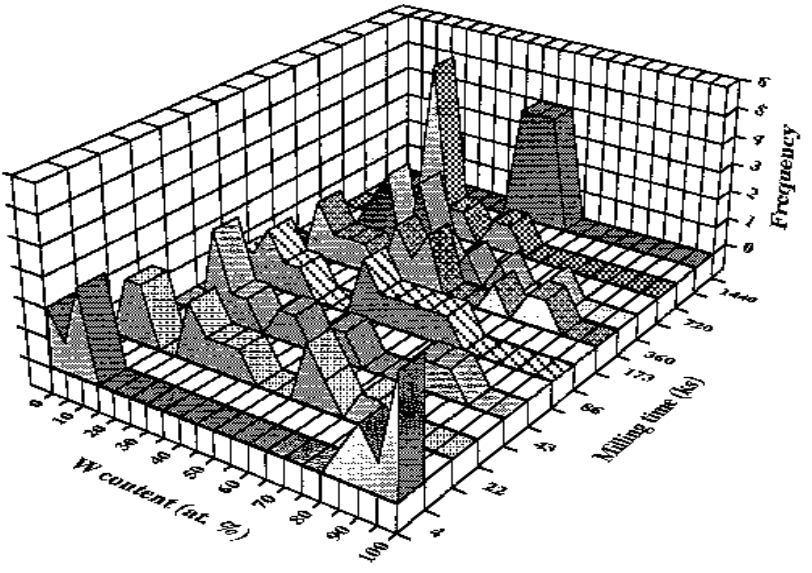

Figure 8.35. Correlation between the MA time, W content, and frequency of mechanically alloyed $Fe_{50}W_{50}$ powders. *(After El-Eskandarany et al.)*[91]

8.6.2 Magnetic Studies

The magnetization of mechanically alloyed $Fe_{50}W_{50}$ powders at room temperature is plotted as a function of the MA time in Fig. 8.36. The rapid decrease in the magnetization during the early and the intermediate stages of milling suggests a dramatic decrease of pure Fe particles. Further milling (173 to 720 ks) enhances the solubility of W in Fe lattice and this is translated to a monotonical decrease in the magnetization, as shown in Fig. 8.36. No dramatic change in the magnetization could be observed in samples milled for longer times (1080 to 1440 ks) and magnetization becomes constant at about 1.5 emu/g and still shows a saturation behavior, although FeW amorphous alloys are paramagnetic.[104] We suppose that this finite magnetization is attributable to the presence of Fe and Ni fine grains that came from the milling tools (balls and vial). It has also been reported[106] that the magnetization of mechanically alloyed FeV, surprisingly, increases towards the end of the MA time. Such increments have also been attributed to the presence of Fe contamination that came from the milling tools.

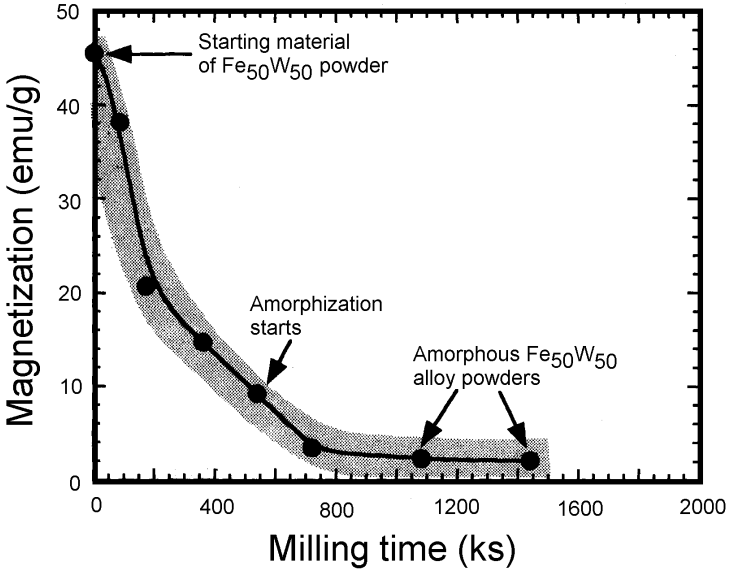

Figure 8.36. Dependence of magnetization, measured at room temperature for mechanically alloyed $Fe_{50}W_{50}$ powders, on the MA time. *(After El-Eskandarany et al.)*[91]

8.6.3 Thermal Stability

The typical DTA thermogram of mechanically alloyed $Fe_{50}W_{50}$ powders is presented in Fig. 8.37 after selected MA times. The measurements were made at a constant heating rate of 0.67 K/s under flow of argon gas. All the samples were heated to 1300 K (first run) and cooled to about 300 K. Then, second heating runs (dashed lines) were performed, in order to get a base line. After 360 ks of MA time, an exothermic reaction takes place widely at about 580 K, suggesting amorphous-crystalline transformation, as shown in Fig. 8.37(*a*). This broad exothermic peak shifts to the higher temperature side (about 785 K) and becomes pronounced after 720 ks of the MA time, as presented in Fig. 8.37(*b*). After 1440 ks of the MA time, this crystallization reaction takes place at higher temperature, characterized by a single sharp exothermic peak centered at about 870 K, as shown in Fig. 8.37(*c*).

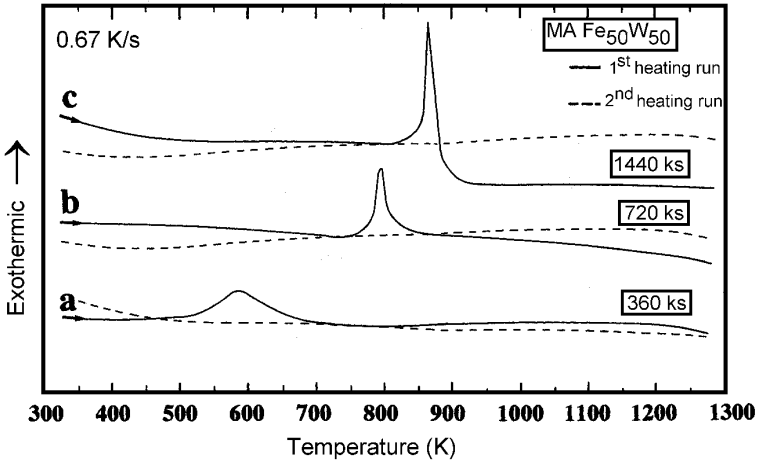

Figure 8.37. DTA curves of mechanically alloyed $Fe_{50}W_{50}$ powders after *(a)* 360 ks, *(b)* 720 ks, and *(c)* 1440 ks of MA time. *(After El-Eskandarany et al.)*[91]

The crystallization characteristics of amorphous $Fe_{50}W_{50}$ alloy powders indexed by the crystallization temperature, T_x (temperature of the exothermic crystallization reaction), and the enthalpy change of crystallization, ΔH_x (total area under the exothermic crystallization reaction), are presented as a function of the MA time in Figs. 8.38 and 8.39, respectively. It can be seen in Fig. 8.38 that the T_x of amorphous $Fe_{50}W_{50}$ alloy increases dramatically during the early and intermediate stages of milling. This is attributed to a continuous change in the composition of the amorphous phase. During the final stage of milling, the T_x approaches a saturation value of nearly 860 K, suggesting the formation of a single phase amorphous alloy.

Further information on the crystallization reaction for amorphous $Fe_{50}W_{50}$ alloy powders is given by ΔH_x and presented in Fig. 8.39 as a function of the MA time. During the early and intermediate stages, the value of ΔH_x decreases monotonically with increasing MA time. At the end of the milling process (1080 to 1440 ks) ΔH_x saturates at a value of about -9 kJ/mol, suggesting that the milled powders contain a single phase of amorphous $Fe_{50}W_{50}$ alloy. These calorimetric studies clearly demonstrate that the amorphous phase becomes chemically and topologically homogeneous with increasing MA time.

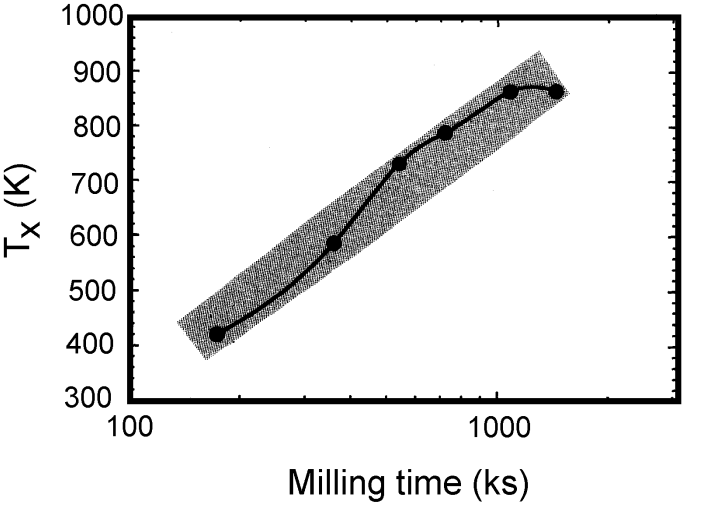

Figure 8.38. Effect of the ball milling time on the crystallization temperature, T_x, of mechanically alloyed $Fe_{50}W_{50}$ powders. *(After El-Eskandarany et al.)*[91]

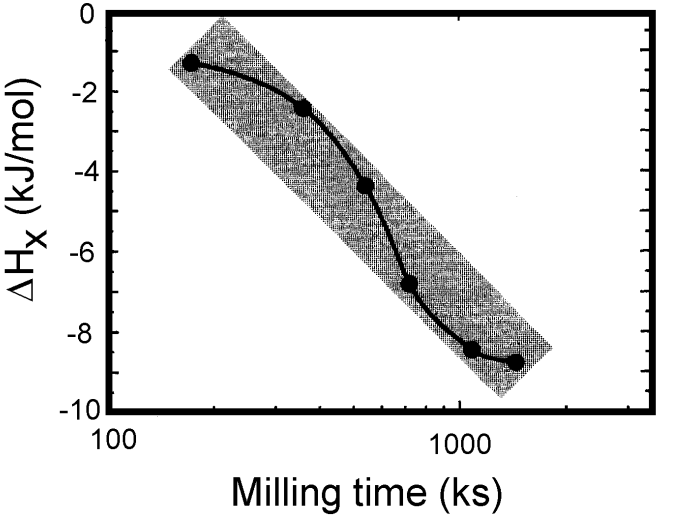

Figure 8.39. Effect of ball milling time on the enthalpy change of crystallization, ΔH_x, of mechanically alloyed $Fe_{50}W_{50}$ powders. *(After El-Eskandarany et al.)*[91]

8.6.4 Mechanism

As described in the previous section, a single phase of amorphous $Fe_{50}W_{50}$ powders has been synthesized by the milling of elemental Fe and W in a tumbling-ball mill. In this section, we discuss the amorphization process of the Fe-W binary system via MA. According to the characteristic properties of the alloy powders, the milling process is classified into the following three stages.

8.6.4.1 The Stage of Composite FeW Powder Particles Formation

During MA time of 0–360 ks (the first stage), the initial powders of Fe and W are agglomerated to form large particles containing many layers of the reactant elements. In contrast to some of the other metallic binary systems,[34][35] annealing these multilayered composite powders does not lead to the formation of any amorphous phases. This is attributed to the null value of the heat of formation for the Fe-W binary system. Accordingly, no chemical driving force to lower the free energy is a priori present in this system. At the beginning of this stage (0–86 ks), the milled powders contain large grains of polycrystalline Fe and W. During the next duration of MA time (86–360 ks), the powders are subjected to heavy deformations, leading to a large amount of lattice and point defects. During this stage, the W atoms start to migrate to the Fe lattice to form a bcc Fe-W solid solution with finer grains. Towards the end of this stage (360 ks), a small fraction of an amorphous phase is formed by a mechanically driven solid-state amorphization (*MDSSA*). This amorphous phase is heterogeneous in its composition and structure: the local structure and composition differ widely from one particle to another and even within the particle itself. Moreover, the crystallization reaction takes place at low temperature and the exothermic peak of the amorphous phase formed at this stage is broad, indicating the low stability of this amorphous phase.

An empirical rule for the amorphous phase formation is proposed by the classical elastic continuum model. A large size difference in constituent elements makes substitutional atom packing unstable[107] and gives rise to the formation of an amorphous phase.[108] By calculating the local volume strain energy in an A matrix caused by introducing a B solute with a different atomic size for the $Fe_{50}W_{50}$ binary system, the critical concentration of A primary solid solution and an amorphous phase, x_B^{min} is expressed as:[108]

Eq. (8.13) $$x_B^{min} = 0.1V_A / \left| V_B - V_A \right|$$

where V_A and V_B are the atomic volumes of *A* and *B*, respectively. The x_B^{min} values are 0.38 for the Fe-rich primary solid solution and 48 for the W-rich primary solid solution. The present $Fe_{50}W_{50}$ alloy just satisfies this condition.

The forming abilities of an amorphous phase and a solid solution have also been discussed in terms of an alloy formation enthalpy, ΔH^{for}, and a difference in outer electron concentration of constituent elements, Δn:[109] an amorphous phase is favorable as ΔH^{for} is negative and the absolute values of ΔH^{for} and Δn become smaller. Since $\Delta H^{for} = 0$[110] and $\Delta n = -2$ for Fe-W alloys, this empirical relation predicts a wide range of Fe-W crystalline solid solutions in contrast to the present experimental results. However, random solid solutions such as an amorphous phase is stabilized by a free energy gain of the mixing entropy, because the metallic powder is mechanically milled at ambient temperature. In this context, the milled Fe-W is a ternary system of Fe, W, and defects.

8.6.4.2 The Stage of Formation of FeW Solid Solution

This stage of MA (360 to 540 ks) refers to the second stage of milling in that the number of W atoms that migrate to the Fe lattice are increased. Increasing the MA time enhances the solid-state reaction between the diffusion couples of Fe and W. This reaction is supported by a remarkable expansion of the lattice parameter of Fe accompanied by a drastic decrease in the magnetization. The T_x of the amorphous phase of this stage increases drastically, suggesting a continuous change in the composition. Moreover, the value of ΔH_x decreases monotonically with increasing MA time, suggesting an increase in the volume fraction of the amorphous phase against the crystalline phase of the milled powders. Toward the end of this stage, the alloy powders contain fine grains of bcc Fe-W solid solution coexistent with the residual W powders.

8.6.4.3 The Stage of Amorphous FeW Formation

During this last stage of milling (360 to 1440 ks), the bcc Fe-W solid solution formed during the early and the intermediate stages transforms completely to an amorphous phase. The rapid diffusion process is enhanced by the several defects piled up in the milled powders. The

amorphous phase coexists with a small fraction of unprocessed W powders. The W powders react with the FeW amorphous phase to produce a single amorphous phase of FeW powders. The local structures and compositions of these particles are homogeneous, as indicated by the EDS analyses. As the W content in the amorphous FeW matrix increases, both T_x and ΔH_x increase.

8.7 SPECIAL SYSTEMS AND APPLICATIONS

8.7.1 Amorphous Austenitic Stainless Steel

Traditionally, steel and steel alloys are prepared by conventional melting and casting techniques. In 1994, El-Eskandarany and Ahmed[111] proposed an attractive technique for preparing austenitic stainless steel ($Fe_{74}Cr_{18}Ni_8$) by rod milling elemental powders of Fe, Cr, and Ni, at room temperature. The end-product (after 1800 ks of milling) was a single amorphous alloy (see Fig. 8.40). The thermal stability indexed by the crystallization temperature, T_x, of this amorphous alloy shows that the amorphous austenitic stainless steel is very stable up to temperatures as high as 1240 K. At this temperature (see Fig. 8.41), the amorphous $Fe_{74}Cr_{18}Ni_8$ is transformed into an order phase of fcc $Fe_{74}Cr_{18}Ni_8$ (the typical structure of austenitic stainless steel), as shown in Fig. 8.41.

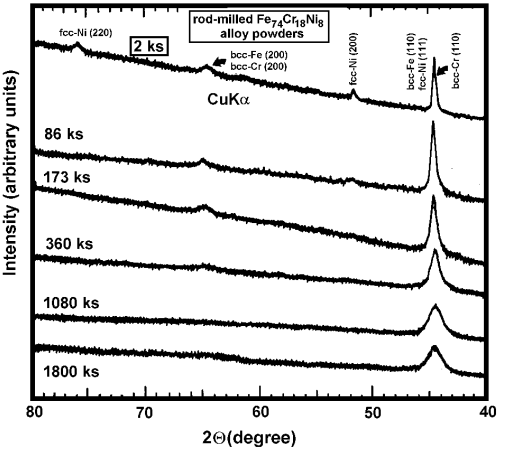

Figure 8.40. Effect of the rod-milling time on the structure of mechanically alloyed $Fe_{74}Cr_{18}Ni_8$ powders. *(After El-Eskandarany and Ahmed.)*[111]

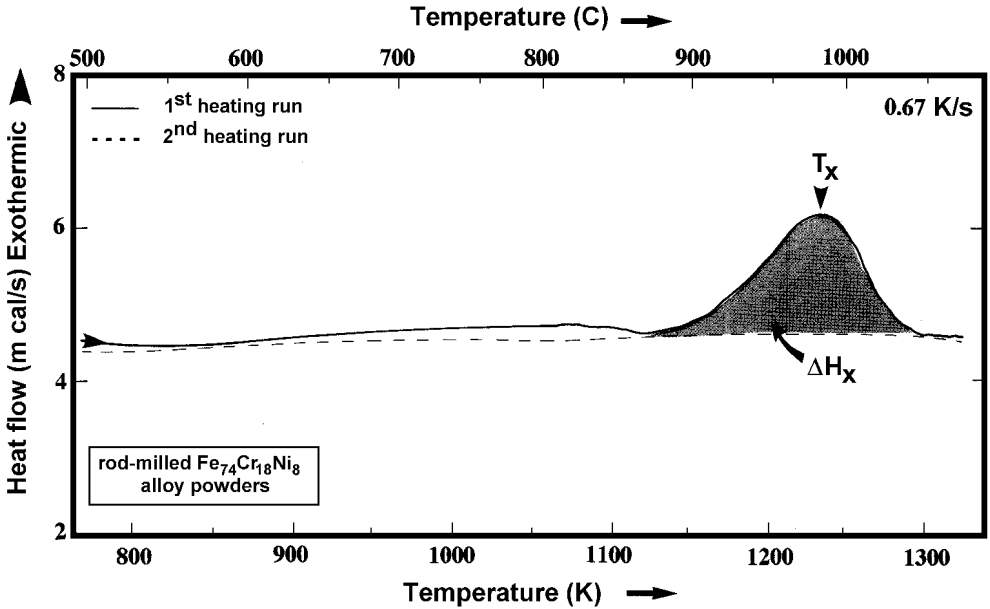

Figure 8.41. DTA curve of the end-product for amorphous $Fe_{74}Cr_{18}Ni_8$ alloy powders as rod milled for 1800 ks. *(After El-Eskandarany and Ahmed.)*[111]

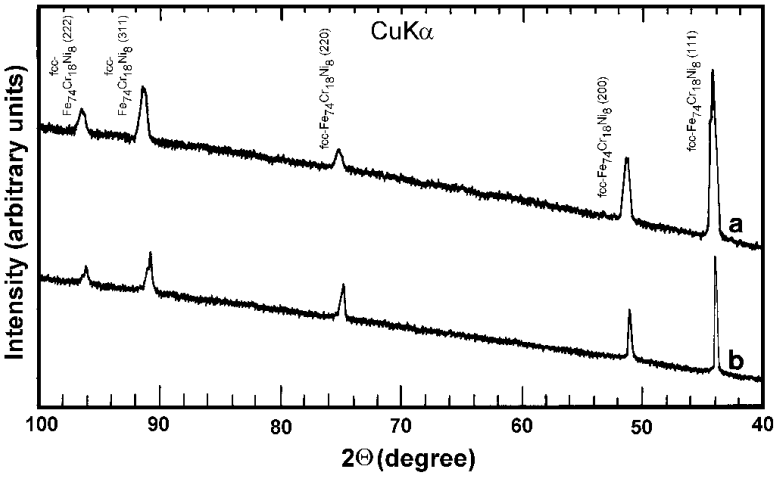

Figure 8.42. XRD patterns of *(a)* amorphous $Fe_{74}Cr_{18}Ni_8$ alloy powders as rod milled for 1800 ks, then heated to 1300 K during DTA measurements and *(b)* standard sample of austenitic stainless steel. *(After El-Eskandarany and Ahmed.)*[111]

One significant potential technological attraction of this method of fabrication is its simplicity. Moreover, the end-product of amorphous steel powder and/or annealed stainless steel (fcc structure) can be used as a powder for high corrosion resistant coatings, or can be consolidated by hot pressing, or HIPing technique, thereby offering the prospect of manufacturing bulk metallic alloys made from amorphous (below crystallization temperature) and/or crystalline (above the crystallization temperature) steel phases by a simple and powerful technique.

8.7.2 Fabrication Amorphous $Fe_{52}Nb_{48}$ Special Steel

Niobium is one of the most important alloying elements for the steel industry. It has a very strong chemical affinity for carbon and is used as a grain-refiner. The mechanical properties of steel, such as yield strength, tensile strength, and creep strength, are monotonically raised by the addition of elemental Nb. Unfortunately, the maximum solubility of Nb in α-Fe was reported to range from 0.095 to 0.330 at. % Nb at 873 to 1123 K, respectively.[112] Moreover, iron-niobium alloys with high Nb content

(>45 at. %) cannot be obtained easily by the traditional method of liquid metallurgy, due to the remarkable gap differential in the melting points between pure Fe (1809 K) and Nb (2742 K) metals. This poor solubility and the difficulties in using the liquid metallurgy method restrict the fabrication of these technological alloys that could find a wide range of applications.

In 1999, El-Eskandarany et al.[28] proposed a room temperature ball-milling technique for fabrication of $Fe_{52}Nb_{48}$ amorphous alloy, using the mechanical alloying method. A single amorphous phase is formed after 144 ks of milling elemental Fe and Nb powders in a high-energy ball mill. The XRD patterns of mechanically alloyed $Fe_{52}Nb_{48}$ powder are presented in Fig. 8.43 after selected MA times. In spite of the intact mixture of polycrystalline bcc Fe and Nb powders that were taken after 7 ks of MA time [Fig. 8.43(*a*)], the Bragg peaks of Nb become broadened after 18 ks of milling [Fig. 8.43(*b*)]. Moreover, the intensities of the Bragg peaks for elemental Fe are markedly decreased, indicating a partial solubility of α-Fe in the Nb matrix. Towards the end of this early stage of MA (54 ks), a broad peak is overlapping the major Bragg peaks of Nb(110) and Fe(110), suggesting the existence of a major amorphous phase [Fig. 8.43(*c*)]. This first halo peak becomes more pronounced at the beginning of the intermediate stage of MA (72 ks), suggesting an increase in the amorphous phase and a decrease in the unreacted powders, as displayed in Fig. 8.43(*d*). All the minor Bragg peaks of the elemental starting materials [Nb(200), Fe(200) and Nb(211)] have completely disappeared, and a second diffuse halo pattern has appeared [Fig. 8.43(*e*)]. At this stage of milling, a small mole fraction of metallic Nb and Fe powders is coexisting with the obtained amorphous phase, as suggested by the presence of Nb(110) and Fe(110) reflections in the first halo pattern. These peaks are hardly seen after 108 ks of MA time (final stage), and the material is completely in an amorphous phase, as shown in Fig. 8.43(*g*). At the end of the milling (144 ks), a single homogeneous amorphous phase is obtained, characterized by smooth diffuse halos, as displayed in Fig. 8.43(*h*).

This single amorphous phase transforms into an order phase (μ phase) upon heating at 1088 K (crystallization temperature, T_x) with enthalpy change of crystallization, ΔH_x, of -8.3 kJ mol^{-1}. The end-product of this amorphous phase can be consolidated far below or well above its crystallization temperature to obtain either bulk amorphous or nanocrystalline full dense compacts.

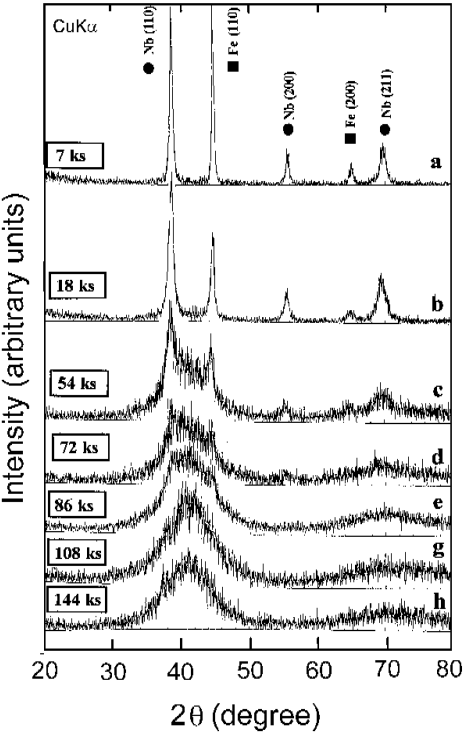

Figure 8.43. XRD patterns of mechanically alloyed $Fe_{52}Nb_{48}$ alloy powder after selected ball-milling time. *(After El-Eskandarany et al.)*[28]

8.7.3 Fe-Zr-B System

This important commercial system has been studied by L. Schultz et al.[16][113] In their experiments, elemental Fe, Zr, and submicrons of amorphous B powders were milled together, and the milled powders, during the early stage of milling, show a layered microstructure of Fe and Zr. The undeformed amorphous boron particles are caught by the colliding Fe and Zr particles and are embedded in the Fe/Zr interfaces. Further milling leads to refinement of this layered microstructure until, finally, the Fe and Zr layers react to form amorphous Fe-Zr (see Fig. 8.44).

An additional solid-state reaction process (7.2 ks at 728 K) enables the boron to diffuse into the Fe-Zr, forming amorphous Fe-Zr-B (Fig. 8.44). The boron addition to amorphous Fe-Zr also increases the crystallization temperature.[16]

The Fe-Zr-B samples have also been studied by Mössbauer spectroscopy.[114] Figure 8.45 shows the average quadrupole splitting, $\overline{QS}$, vs. the boron content for the as-milled and the reacted (annealed samples, 7.2 ks, 728 K) state. The $\overline{QS}$ increases during annealing because of the boron addition. However, the increase of $\overline{QS}$ with boron content for the as-milled samples shows that there is some boron [~ 5 at. % B for the $(Fe_{0.75}Zr_{0.25})_{85}B_{15}$ sample] dissolved in the amorphous Fe-Zr during mechanical alloying.

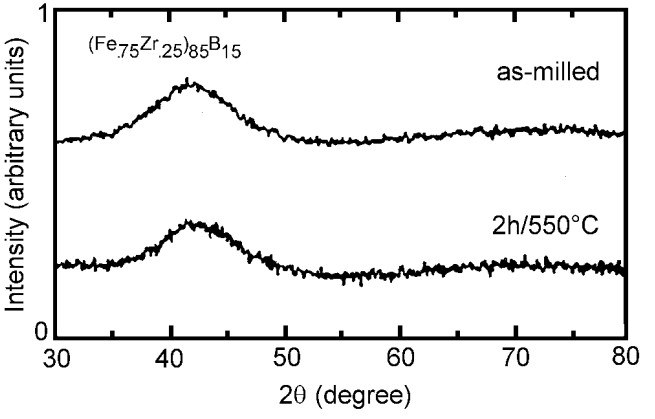

Figure 8.44. XRD patterns of $(Fe_{0.75}Zr_{0.25})_{85}B_{15}$ samples in the as-milled state and after 7.2 ks annealing at 728 K. *(After L. Schultz.)*[16]

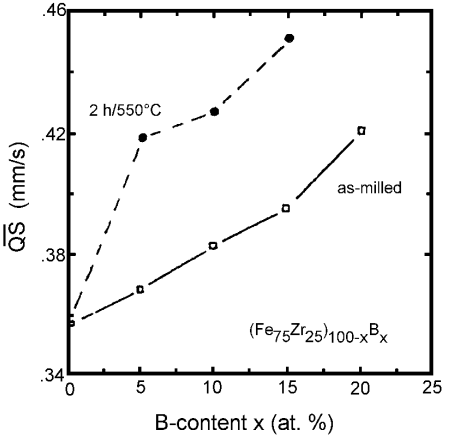

Figure 8.45. Average quadrupole splitting, $\overline{QS}$, vs. the boron content for the as-milled and the reacted (annealed samples, 7.2 ks, 728 K) state. *(After L. Schultz.)*[16]

8.8 DIFFERENCE BETWEEN MECHANICAL ALLOYING AND MECHANICAL DISORDERING IN THE AMORPHIZATION REACTION OF $Al_{50}Ta_{50}$ IN A ROD MILL

8.8.1 Background

There are only two categories of amorphization by ball milling and/or rod milling, that is to say, mechanical alloying (MA) and mechanical grinding (MG). The terms mechanical grinding,[115] or mechanical milling[116] are usually used to express the crystal-to-amorphous transformation without compositional change. Here, we are going to use mechanical disordering (MD)[49] as a more suitable terminology, which reflects the mechanism of crystal-to-amorphous transformation in much better understanding. As mentioned previously, the MA process synthesizes amorphous alloy powders by reacting elemental crystalline powders and/or intermetallic compound powders, with a negative heat of formation.[117] In the MD process, however, crystalline alloy or compound powders are transformed into the amorphous solid state by relaxing the short-range order without compositional changes.[118] The MA and MD processes are reactions going in thermodynamically opposite directions of each other, as illustrated in Fig. 8.46,[117] which is a schematic free-energy diagram for the phases involved in the mechanical alloying and mechanical disordering processes. In the figure, *A* and *B* are the starting materials (before MA or MD), with three compositions (*A*-rich, equiatomic, and *B*-rich). The starting elemental crystalline state (*c*), the amorphous state (*a*), and the order state are assumed to have the same composition. The initial state is just a mixture of crystals of pure *A* and *B* so that the free energy of this state (point 1 in Fig. 8.46) is located along the straight line that is joining the free energies of the pure elemental powders of *A* and *B*. Point 2 is the free energy of the single amorphous phase (a-AB) that is formed by milling the elemental powders of *A* and *B* for a certain period of time. Point 3 is the free energy of the single crystalline intermetallic alloy with the same composition. The mechanical solid-state amorphization reaction takes place at a constant temperature that is sufficiently high enough to allow for the mechanical interdiffusion of *A* in *B* and/or *B* in *A*, but too low for promoting the nucleation and/or growth of the crystalline alloy. This kinetic selection of the reaction path is possible in binary systems in which the elements have largely different diffusivities in each other and in the amorphous phase.[5][21]

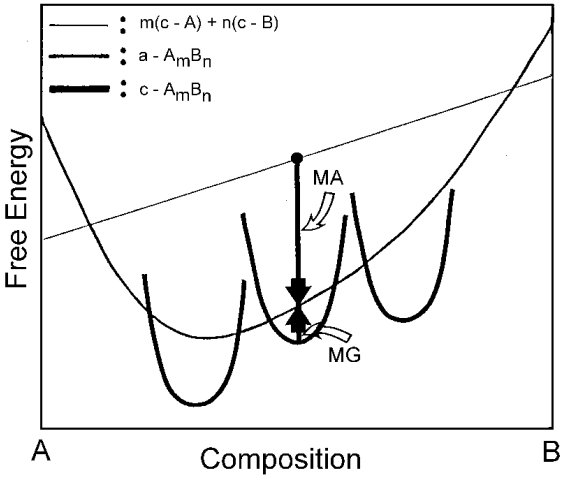

Figure 8.46. Thermodynamical processes of mechanical alloying (MA) and mechanical grinding (MG). *(After Suzuki.)*[118]

8.8.2 Procedure

In the MA process, elemental powders of aluminum (-325 mesh, 99.999%) and tantalum (-150 mesh, 99.99%) were mixed in a glove box under a purified argon gas atmosphere to give the desired average composition. On the other hand, the starting material for the MD process was prepared by arc-melting nominal amounts of 99.999% pure aluminum and 99.999% pure tantalum in an argon gas atmosphere (O_2 less than 0.2 ppm), purified with a titanium getter. The ingot was remelted five times, reweighed, and checked metallographically. After the ingot had been crushed to powder using a stainless steel (SUS 304) mortar and pestle, the powder was classified in diameter to less than 50 μm, using screen analysis, and then analyzed, using the ICP emission method. The MA and MD processes were performed by the rod-milling technique.

8.8.3 Structural Changes with Milling Time

The XRD patterns of mechanically alloyed and mechanically disordered $Al_{50}Ta_{50}$ are shown as a function of rod-milling time in Fig. 8.47(*a*) and (*b*), respectively. As shown in Fig. 8.47(*a*), the intensities of the Bragg peaks for pure Al and Ta powders decrease simultaneously with

increases in the MA time. At the intermediate stage of MA (720 ks) all of the minor Bragg peaks from elemental Al and Ta crystals decrease with increasing MA time. After 86 ks of milling, the Bragg peaks from elemental fcc Al(200), (220) and (311) reflections disappear. In addition, the intensities of the Bragg peaks from elemental bcc Ta decrease quickly. During the intermediate stage (360 to 720 ks) of MA time, the major Bragg peaks from pure Al(111) and Ta(110) and (211) reflections become wider, indicating the formation of an amorphous phase. Furthermore, the other Bragg peaks of pure Al and Ta have almost disappeared. Towards the end of the MA time (1440 ks), a homogeneous amorphous phase is formed, characterized by broad and smooth peaks.

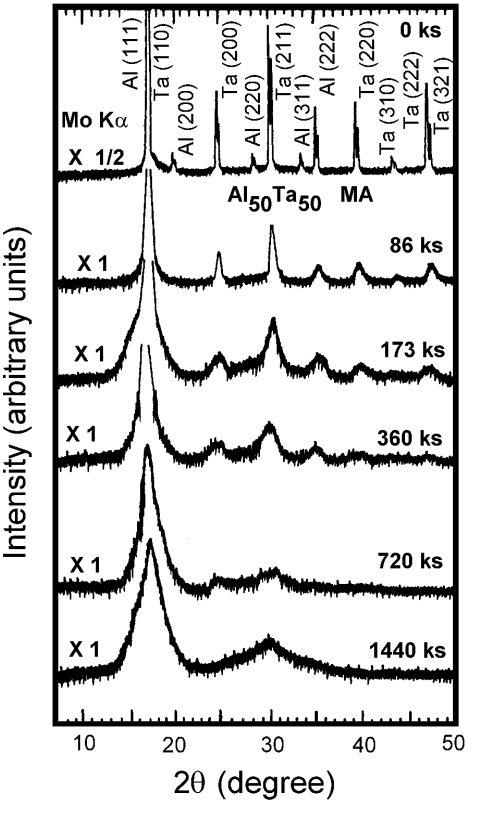

(a)

Figure 8.47. XRD patterns of $Al_{50}Ta_{50}$ alloy powders as a function of *(a)* MA time and *(b)* MD time. *(After El-Eskandarany et al.)*[49]

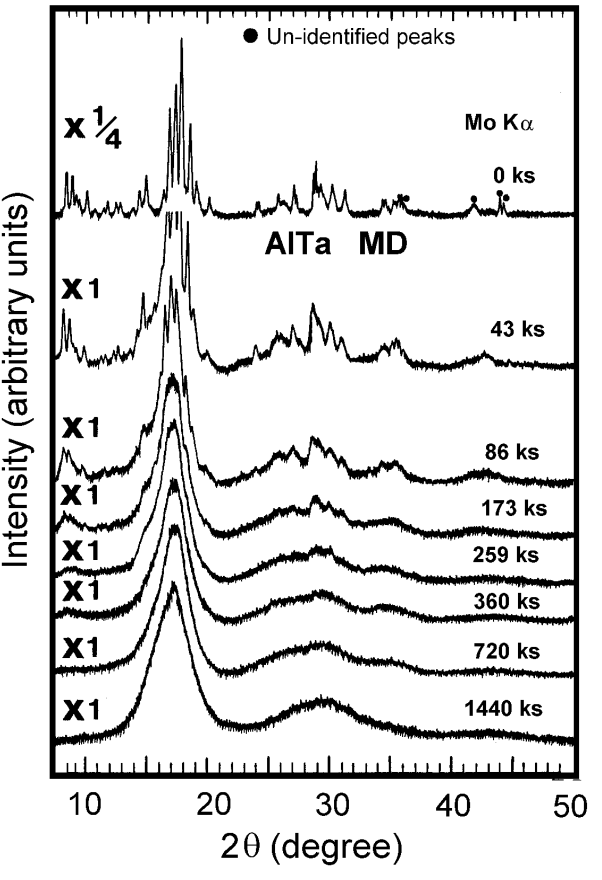

(b)

Figure 8.47. *(Cont'd.)*

As presented in Fig. 8.47(*b*), the starting powders of a AlTa intermetallic compound have an XRD pattern with sharp Bragg peaks. The intensities of these peaks decrease by increasing the MD time. A halo pattern with no sharp Bragg peaks was obtained after 360 ks of MD time. At the final stage of milling (1440 ks), a homogeneous amorphous phase was formed, because small angle scattering at 2θ less than 10 degrees completely disappeared.

8.8.4 Morphological Changes with Milling Time

Figure 8.48 shows the scanning electron micrographs of the MA and MD $Al_{50}Ta_{50}$ powders after selected rod-milling times. The typical starting powders at 0 ks of MA and MD are shown in Fig. 8.48(*a*) and (*b*), respectively. At the starting stage, the MD particles are blocky while the MA particles have a flake-like morphology. After 22 ks of MA time, the powder particles tend to agglomerate in size extending to more than 300 μm in diameter. In contrast, after 22 ks of MD, the particles' size is reduced to less than 20 μm in diameter, and the shape of the starting materials has been changed to a globe-like morphology.

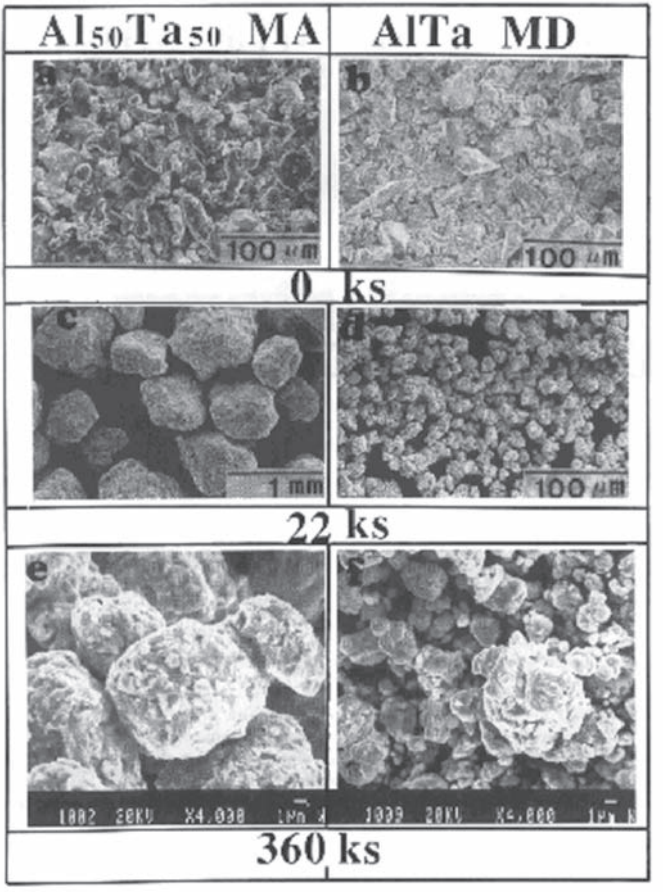

Figure 8.48. Scanning electron micrographs of $Al_{50}Ta_{50}$ alloy powders as a function of MA and MD time. *(After El-Eskandarany et al.)*[49]

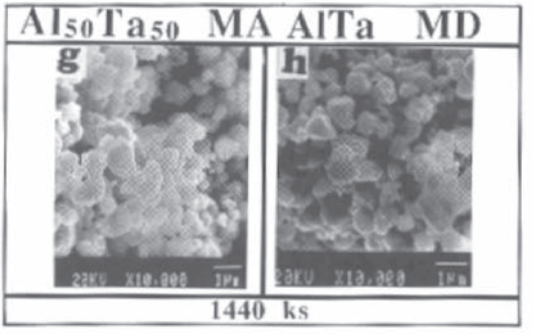

Figure 8.48. *(Cont'd.)*

Figure 8.49 shows the change of particle size for MA and MD $Al_{50}Ta_{50}$ powders as a function of the rod-milling time. The sizes of the powders were determined from the SEM observations. The process for forming alloy powders differs for MA and MD.

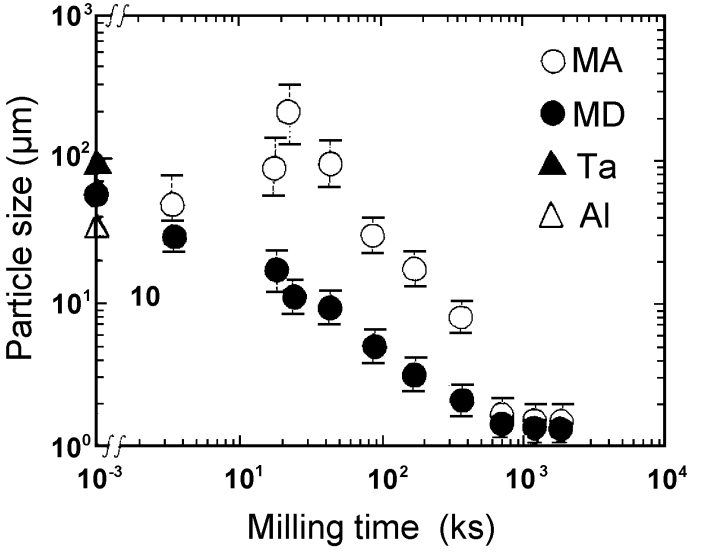

Figure 8.49. Particle size distribution of $Al_{50}Ta_{50}$ alloy powders as a function of MA and MD time. *(After El-Eskandarany et al.)*[49]

The milling process performed by the MA process can be classified into three stages. At the initial stage (4 to 22 ks), which is called the agglomeration stage, the starting elemental powders of Al and Ta agglomerate during this early stage of milling to form powders of greater diameters; as large as several hundred micrometers peaking at almost 300 μm after 22 ks of milling, as shown in Fig. 8.48(*c*). During this stage of milling, the characteristic structure containing Al and Ta layers appears, as shown in Fig. 8.50(*a*). Using an electron microscope analysis, it was found that the gray parts are Al layers and the dark matrix is Ta rich. In the middle stage corresponding to the MA time from 22 to 360 ks, fragmentation with amorphizing reaction proceeds drastically by the atomic diffusion through the interface between the layers. Moreover, the powder particles are subjected to continuous disintegration, until the size of the powders is reduced to less than 10 μm in diameter, as shown in Figs. 8.48(*e*) and 8.49.

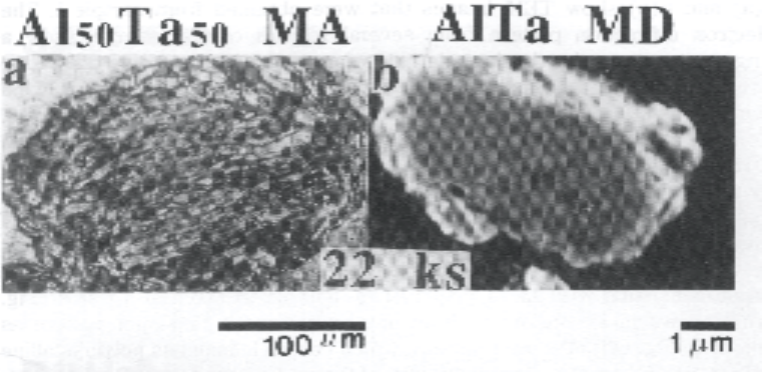

Figure 8.50. Morphology of the powder particles as a function of MA and MD processes after 22 ks of milling *(a)* optical micrographs of MA $Al_{50}Ta_{50}$ powders and *(b)* scanning electron micrographs of MD AlTa powders. *(After El-Eskandarany et al.)*[49]

The MD process leads to a different behavior for the variation in powder diameters. The starting powders of an AlTa intermetallic compound are continuously reduced in size without any agglomerations or layer-structure morphology, to form fine powders of about 10 μm in diameter after only 22 ks, as shown in Fig. 8.48(*f*). Furthermore, in the MD, however, the size reduction of the particles proceeds at a high rate to provide a narrow size distribution, as shown in Fig. 8.49.

8.8.5 Thermal Stability

Figure 8.51 shows the DTA curves for $Al_{50}Ta_{50}$ alloy powders as a function of the MA time. At 0 ks of milling, a sharp endothermic peak appears at about 930 K, due to the melting of aluminum in the starting material of $Al_{50}Ta_{50}$ powders. Then, this melt reacts with tantalum powders in the mixture, characterized by an exothermic peak which appears above 1190 K, as shown in Fig. 8.51. During the first few kiloseconds of the MA time (4 to 22 ks) there is no significant difference in the thermal properties between the alloy powders and the starting materials. Therefore, the process at this stage has the appearance of just blending the two elemental metal powders. Both the exothermic and the endothermic peaks disappear through the second heating runs, as illustrated by the dashed lines in Fig. 8.51. Contrary to this, a single broad exothermic peak appears at around 650 K, and the exothermic reaction peak disappears after 43 ks of MA time. After 86 ks of milling, another broad exothermic peak appears above 800 K, and the first exothermic peak becomes sharper. This second exothermic peak is shifted to an elevated temperature, and becomes sharp towards the end of the MA process (1440 ks). The temperature of the first exothermic peak, however, does not change with the milling time, as shown in Fig. 8.51. These reactions, which take place at the low temperature, occur due to so-called thermally assisted solid-state amorphization reaction[52] that was described in detail previously (see Sec. 8.4.3.1, Amorphization Process).

In MD alloy powders, however, the exothermic reaction peaks, which are attributed to a solid-state amorphizing reaction at the fresh surfaces of Al/Ta boundaries, are absent, as shown in Fig. 8.52.

Figure 8.53 shows the correlation between T_a, T_x, and the milling times of MA and MD. The value of T_a for MA alloy powders is independent of the milling time, which suggests that the amorphization by a solid-state reaction occurs simultaneously. Contrary to this, the T_x increases drastically with increasing the MA time in the early and the intermediate stages of milling, indicating a continuous change of the composition of the amorphous phase. The T_x approaches a saturation value (1210 K) during the final stage of the MA time. In MD alloy powders, however, there is no big change in T_x, suggesting that the process occurs homogeneously, without compositional change, as illustrated in Fig. 8.53.

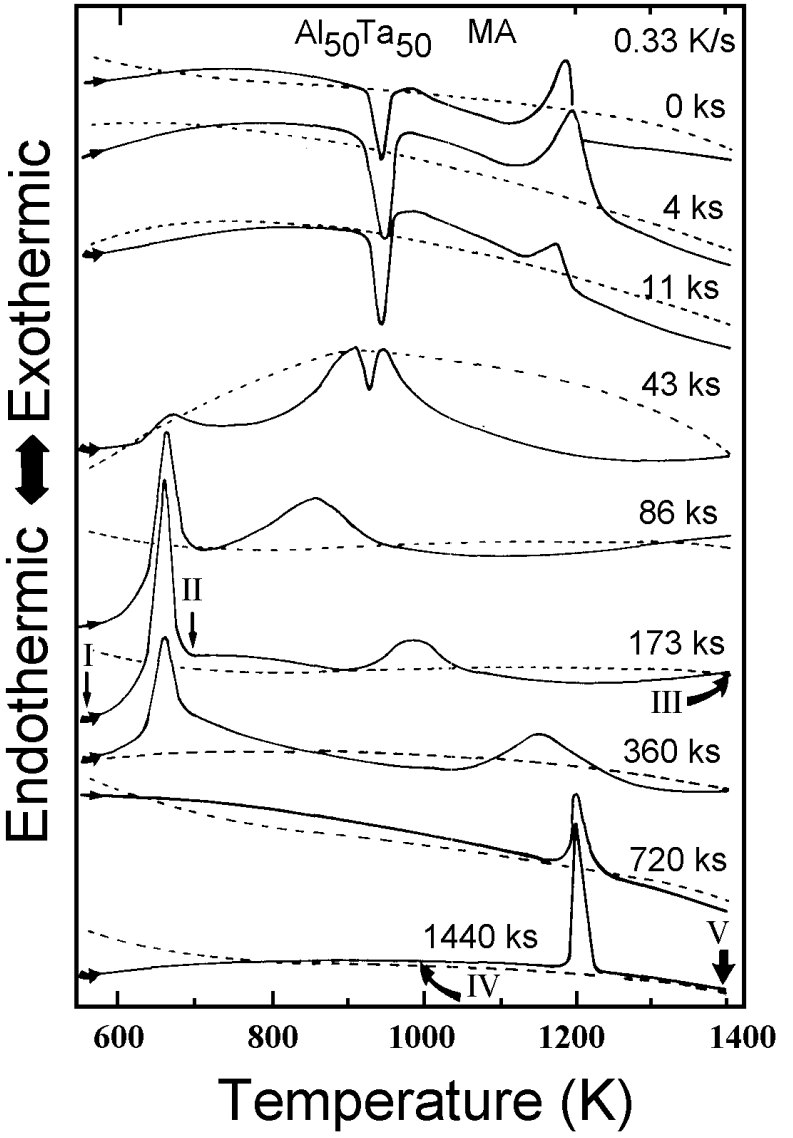

Figure 8.51. DTA curves of $Al_{50}Ta_{50}$ alloy powders as a function of MA time. *(After El-Eskandarany et al.)*[49]

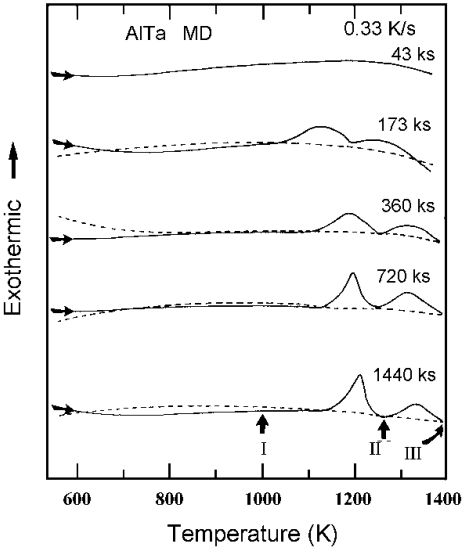

Figure 8.52. DTA curves of $Al_{50}Ta_{50}$ alloy powders as a function of MD time. *(After El-Eskandarany et al.)*[49]

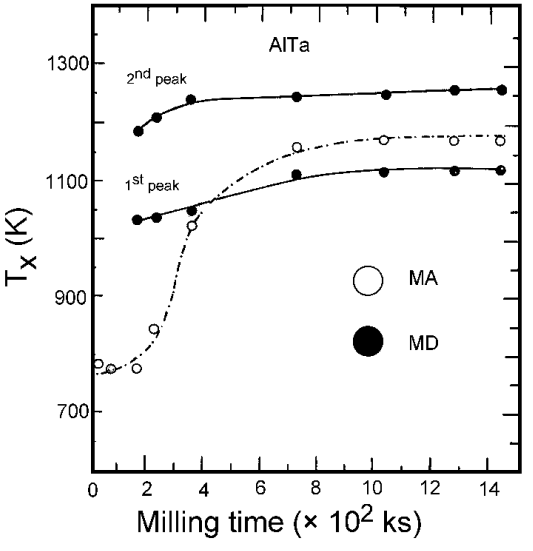

Figure 8.53. Crystallization temperature, T_x, and amorphization temperature, T_a, of $Al_{50}Ta_{50}$ alloy powders as a function of the rod-milling time. *(After El-Eskandarany et al.)*[49]

8.8.6 Mechanism of Formation of Amorphous $Al_{50}Ta_{50}$ via MD Method

The MA and MD processes are similar in appearance, but differ completely in their mechanism. The MD process differs from the MA process in that the amorphization of a crystalline AlTa alloy requires an increase in its free energy from a lower level (more stable) to a higher level (less stable). By rod milling, the crystalline compound stores energy in the form of chemical disorder, and point and lattice defects. The crystal-to-amorphous transformation requires releasing of that stored energy to approach a specified value. In addition, the MD process is carried out through only one stage, in which the powder particles are continuously disintegrated without agglomeration or formation of layer-structure morphology of the particles. This is because the starting material here is an intermetallic compound by itself, so the solid-state amorphizing reaction can not be considered in this case.

Moreover, the MD technique differs from the MA technique in the rate of amorphization. The amorphization process by MD occurs fast and much more homogeneously than that by MA. This is demonstrated by the nearly constant values of T_x and ΔH_x at the intermediate and final stages of milling (360 to 1440 ks).

Furthermore, the DTA curves of mechanically disordered AlTa alloy powders have shown that the exothermic peaks, which are related to a solid-state amorphizing reaction, are absent. However, the XRD patterns of the DTA sample for MD AlTa which was milled for 1440 ks and then annealed to 1400 K, did not show a clear difference in the Bragg peaks between them and those obtained in the case of the MA process. In addition, there is no significant difference in the Bragg peaks of as-cast AlTa crystalline compounds and as-annealed MA and MD powders at 1400 K which were milled for 1440 ks. This may suggest that the amorphization by MA and MD leads to the formation of almost the same amorphous phase regardless of the great difference in the mechanism between the two processes. Furthermore, the two exothermic peaks, which appear in the DTA curves of the 1440 ks alloy, show that the crystallization of MD alloy powders occur in two stages. This may be attributed to nucleation and growth morphology of the heated alloy powders.

In addition, the iron contamination content in the MD powders is higher than it is in the MA powders. The higher iron contamination in MD powders can be attributed to the high hardness of the used intermetallic

compound powders. Generally, intermetallic compounds are harder than their constituent elements. Therefore, the high iron contamination seems to be a general disadvantage in the MD process.

8.9 MECHANICALLY-INDUCED CYCLIC CRYSTALLINE-AMORPHOUS TRANSFORMATIONS DURING MECHANICAL ALLOYING

Since the amorphous phase is a metastable one, it inherently possesses the possibility of transforming into a more stable crystalline phase. This phase transformation usually takes place when an amorphous alloy is heated to a certain temperature (crystallization temperature, T_x), which usually ranges between 0.4 to 0.6 of its melting point, T_m. Trudeau et al.[120] suggested that some iron-based amorphous ribbons crystallize during high-energy ball milling. They mainly attributed this amorphous-crystalline phase transformation to the presence of hcp-Co, which enhances the crystallization reaction. They also discussed the effect of surface oxidation on the crystallization reaction. Eckert et al.[58] attributed the phase changes that occurred upon ball milling elemental $Al_{65}Cu_{20}Mn_{15}$ powder, to the presence of a high local effective temperature during the milling process.

The phase changes (if any) beyond these transformations were not reported until 1997 when El-Eskandarany et al.[121][122] reported the first novel technique for the possibility of a cyclic phase transformation that can occur during the high-energy ball milling of elemental Co and Ti. In addition, they investigated to prove that such cycloidal transformations were not unique to a single system (Co-Ti), and also could be observed during milling an elemental powder mixture of $Al_{50}Zr_{50}$.[123] Moreover, the effect of the milling speed (I) on such cyclic phase transformations has been studied.[123]

8.9.1 Co-Ti Binary System

Pure elemental powders (99.9%) of Co (70 μm) and Ti (50 μm) were mixed to give the nominal composition of $Co_{50}Ti_{50}$ or $Co_{75}Ti_{25}$ (at. %) in a glove box under purified argon atmosphere and sealed in a stainless steel vial (SUS 316, 250 ml in volume) together with fifty stainless steel

balls (SUS 316, 10 mm in diameter). The ball-to-powder weight ratio was maintained as 17:1. The MA process was performed in a high-energy planetary ball mill (Fritsch P5) at a rotation speed of 4.2 s^{-1}. The temperature of the vial was measured periodically, every 1.8 ks of MA time, and found to be about 320 K. In order to avoid a further temperature increase, the MA experiments were stopped periodically (every 1.8 ks) and resumed when the temperature of the vial decreased to about 300 K. When the vial was charged with the milling media only and operated for 1.8 ks, the vial's temperature reached to about 310 K. The MA experiments were performed under the same experimental conditions three times to confirm the reproducibility of the present investigation and to avoid any accidental results.

8.9.1.1 Structural Changes with the Milling Time

Figure 8.54 shows the XRD patterns of mechanically alloyed $Co_{75}Ti_{25}$ powder after selected milling times. In contrast to the initial mixture of polycrystalline hcp-Co and hcp-Ti [Fig. 8.54(*a*)] after 11 ks of MA time [Fig. 8.54(*b*)], a broad, diffuse, and smooth halo appears, suggesting the formation of an amorphous phase. The XRD pattern of the sample milled for 11 ks then annealed, well above its crystallization temperature (874 K), reveals an fcc structure corresponding to the equilibrium phase of Co_3Ti,[124] as shown in Fig. 8.55(*a*). This amorphous phase is not stable against the impact and shear forces generated by the milling media (balls) and, surprisingly, transforms into bcc-Co_3Ti upon milling for 86 ks, as shown in Fig. 8.54(*c*). The lattice parameter, a_0, of this new bcc-Co_3Ti phase was calculated to be 0.2855 nm, being smaller than that for the ordered phase of bcc-CoTi (0.2987 nm). After 173 ks of the MA time [Fig. 8.54(*d*)] the Bragg peaks for bcc-Co_3Ti become broader, suggesting the existence of an amorphous phase. The XRD pattern of the sample, milled for 173 ks then heated to 1300 K, reveals an fcc structure corresponding to fcc-Co_3Ti coexisting with bcc-Co_3Ti. After 360 ks of the MA time, the bcc-Co_3Ti phase transformed completely to an amorphous $Co_{75}Ti_{25}$, as illustrated in Fig. 8.54(*e*). Increasing the MA time to 540 ks leads again to the formation of nanocrystalline bcc-Co_3Ti coexisting with an amorphous phase, as presented in Fig. 8.54(*f*). This bcc-Co_3Ti returns to the same amorphous phase of $Co_{75}Ti_{25}$ after 720 ks of MA time, as shown in Fig. 8.54(*g*). The XRD pattern of the as-annealed 720 ks alloy at 1300 K reveals an fcc structure corresponding to fcc-Co_3Ti. It is worth noting that such transformations were observed for all the samples, which were milled on three different milling runs.

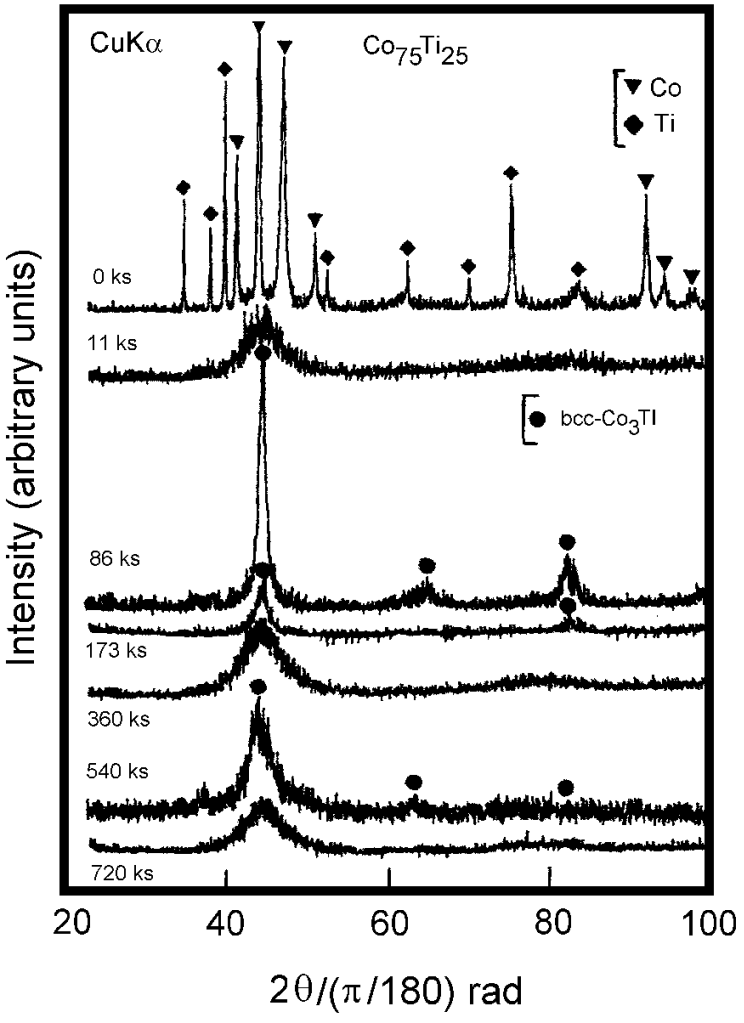

Figure 8.54. XRD patterns of mechanically alloyed $Co_{75}Ti_{25}$ powder milled for *(a)* 0 ks, *(b)* 11 ks, *(c)* 86 ks, *(d)* 173 ks, *(e)* 360 ks, *(f)* 540 ks, and *(g)* 720 ks of the MA time. *(After El-Eskandarany et al.)*[121]

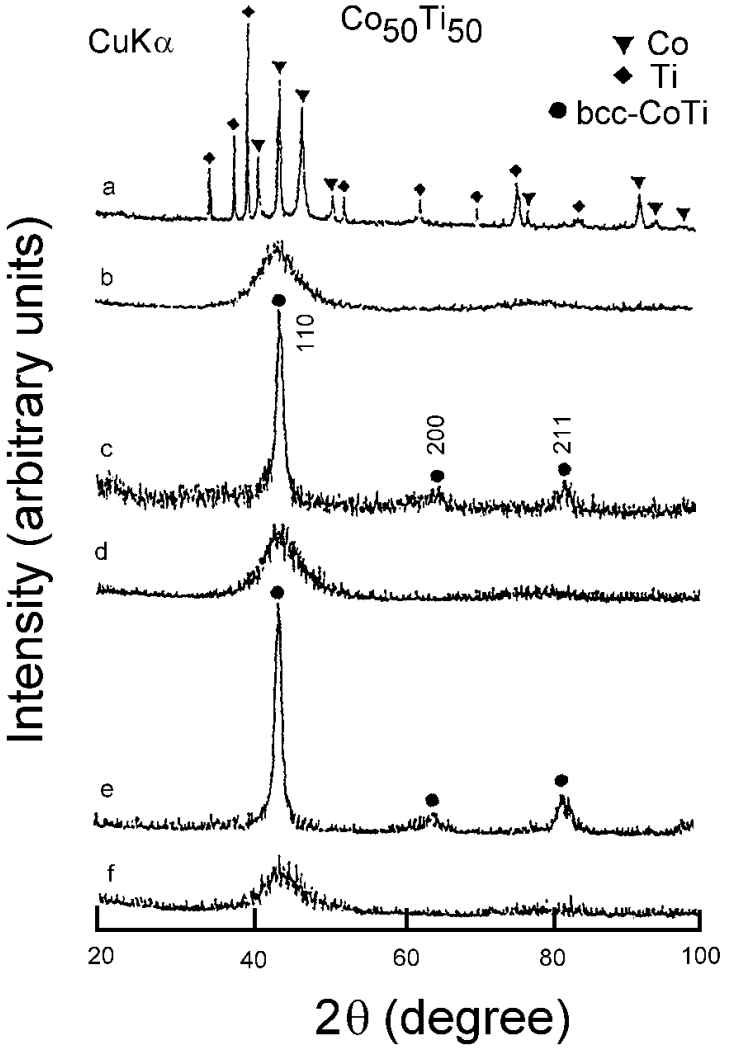

Figure 8.55. XRD patterns of mechanically alloyed $Co_{50}Ti_{50}$ powder after *(a)* 0 ks, *(b)* 22 ks, *(c)* 86 ks, *(d)* 360 ks, *(e)* 540 ks, and *(f)* 720 ks of the MA time. *(After El-Eskandarany et al.)*[122]

Figure 8.55 shows the XRD patterns of mechanically alloyed $Co_{50}Ti_{50}$ powder after selected milling times. A broad, diffuse, and smooth halo appears after 22 ks of MA time [Fig. 8.55(*b*)], suggesting the formation of an amorphous phase. The amorphous phase formed at this stage is not stable against the impact and shear forces generated by the milling media (balls) and, surprisingly, crystallizes into bcc-$Co_{50}Ti_{50}$ upon milling for 86 ks, as shown in Fig. 8.55(*c*). The lattice parameter, a_0, of this bcc-$Co_{50}Ti_{50}$ phase was calculated to be 0.2982 nm, being in agreement with the reported value (0.2987 nm). After 360 ks of the MA time, this bcc phase transforms again to an amorphous phase, suggested by the halo that is presented in Fig. 8.55(*d*). This phase transformation occurs due to the accumulation of several lattice imperfections, such as point and lattice defects, which raise the free energy from a stable phase to a less stable phase.

Further milling (540 ks) leads again to crystallization of the amorphous phase into nanocrystalline bcc-CoTi, as presented in Fig. 8.55(*e*). This bcc-$Co_{50}Ti_{50}$ returns to the same amorphous phase of $Co_{50}Ti_{50}$ after 720 ks of MA time, as shown in Fig. 8.55(*f*). These cyclic phase transformations have been observed for all the samples which were milled for three (and sometimes four) different milling runs. Thus, the sequence of the phase transformation with MA time in ball-milled $Co_{50}Ti_{50}$ is

$$\text{Co} + \text{Ti} \xrightarrow{22\text{ ks}} \text{amorphous} \xrightarrow{86\text{ ks}} \text{bcc} \xrightarrow{360\text{ ks}} \text{amorphous}$$

$$\xrightarrow{540\text{ ks}} \text{bcc} \xrightarrow{720\text{ ks}} \text{amorphous}$$

Figure 8.56 shows the bright field images (BFIs) and the corresponding selected area diffraction patterns (SADPs) of mechanically alloyed $Co_{50}Ti_{50}$ powder after selected MA times. After a few kiloseconds of MA (3.6 ks), the Co powder (dark layers) embedded into the Ti matrix, forming composite Co/Ti particles, as shown in Fig. 8.56(*a*). The SADP [inset of Fig. 8.56(*a*)] shows sharp spot patterns (Laue spots) that corresponds to polycrystalline Co and Ti. Figure 8.56(*b*) presents the BFI and the corresponding SADP of a sample milled for 22 ks of the MA time. Overall, the sample appears to have a homogeneous fine structure with no dominant facet structure. Moreover, the SADP shows a typical halo pattern of an

amorphous phase in good agreement with the XRD pattern presented in Fig. 8.55(*b*). The BFI of the powder that milled for 86 ks of MA time is presented, together with the corresponding indexed SADP, in Fig. 8.56(*c*). The powder consists of nano-size grains of polycrystalline bcc-$Co_{50}Ti_{50}$, as indicated by the Debye-Scherrer rings. In a cyclic crystalline-amorphous phase transformation, this bcc-$Co_{50}Ti_{50}$ phase returns to an amorphous phase after 360 ks of MA time. The formed amorphous phase has a fine and homogeneous structure with a clear halo diffuse pattern, as presented in Fig. 8.56(*d*).

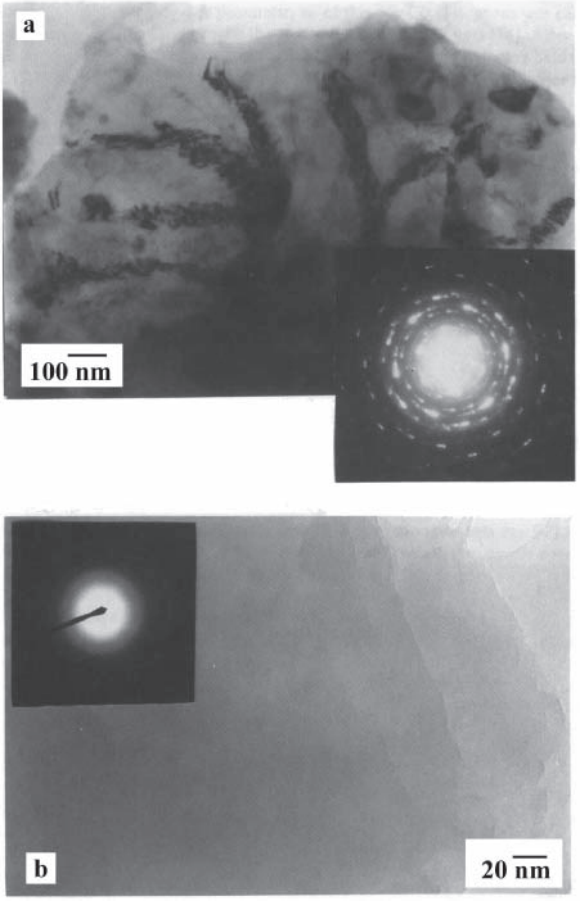

Figure 8.56. BFIs and the corresponding SADPs of mechanically alloyed $Co_{50}Ti_{50}$ powder after *(a)* 3.6 ks, *(b)* 22 ks, *(c)* 86 ks, and *(d)* 360 ks of the MA time. *(After El-Eskandarany et al.)*[122]

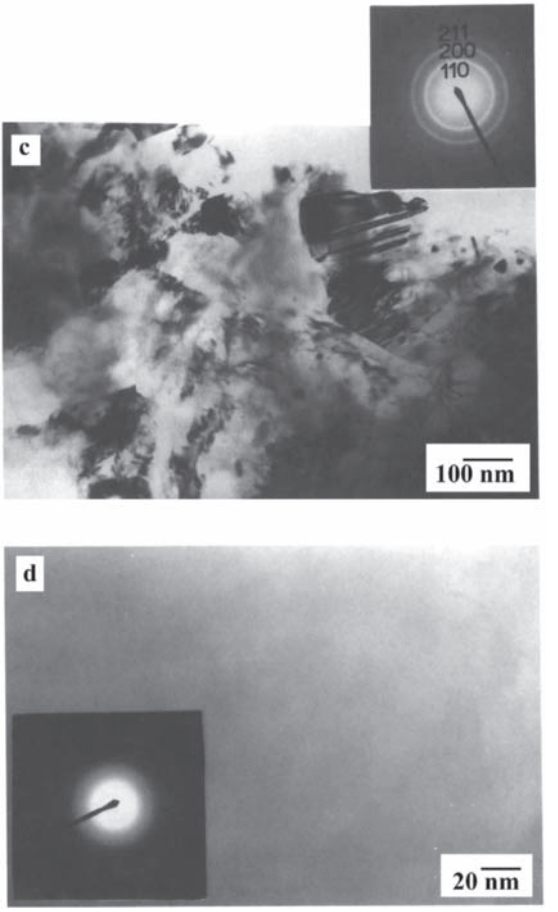

Figure 8.56. *(Cont'd.)*

The magnetization of the milled powder at room temperature is plotted as a function of the MA time in Fig. 8.57. The magnetization of the starting materials (does not appear in Fig. 8.57) is measured to be 74 emu/g. After 22 ks, the magnetization of the alloyed powder decreases dramatically, suggesting a decrease of pure Co particles in the mixture of $Co_{50}Ti_{50}$ powder, and formation of an amorphous phase. During the next stage of MA (43–86 ks), the magnetization of the milled powder decreases, to have a value of less than 2.5 emu/g, suggesting the formation

of bcc-$Co_{50}Ti_{50}$. The magnetization of the mechanically alloyed powder tends to increase upon further MA time (173–360 ks), indicating the formation of an amorphous phase. Increasing the MA time (450–540 ks) leads to a remarkable decrease in the magnetization. This is attributed to the crystallization of the amorphous alloy and the formation of crystalline bcc-$Co_{50}Ti_{50}$ phase. Towards the end of the MA time (630–720 ks), crystalline-to-amorphous phase transformation is observed, and the yielded amorphous phase has almost the same magnetic properties of the 22 ks and 360 ks MA amorphous alloys, indicating cyclic phase transformations. It is worth noting that the magnetization of the amorphous samples that annealed well above their crystallization temperatures (976 K), have almost the same magnetization values of the samples which milled for 86 and 540 ks. This may prove the similarity of the structure for these samples.

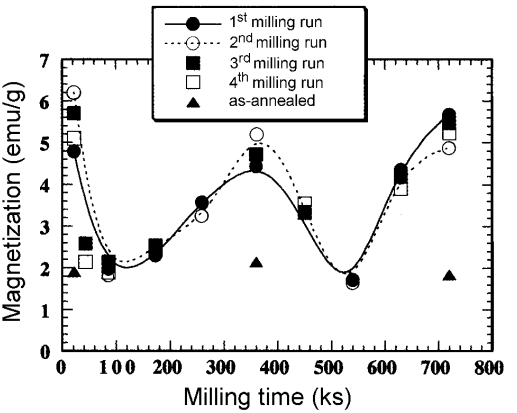

Figure 8.57. Dependence of the magnetization, measured at room temperature of mechanically alloyed $Co_{50}Ti_{50}$ powder, on the MA time. *(After El-Eskandarany et al.)*[122]

8.9.1.2 Thermal Stability

The DTA curves of mechanically alloyed $Co_{50}Ti_{50}$ powder are presented in Fig. 8.58, after selected MA time. The measurements were performed at a constant heating rate of 0.33 K/s under an argon gas

atmosphere. All the samples were heated to 1200 K (first run) and cooled to about 400 K. Then, second heating runs (dashed lines) were performed in order to get the base line. After 22 ks of the MA time [Fig. 8.58(*a*)], a single sharp exothermic peak appears at 968 K. This exothermic reaction is attributed to an amorphous-crystalline phase transformation (crystallization). The XRD patterns of the sample heated up to 1300 K shows the formation of an equilibrium bcc-$Co_{50}Ti_{50}$ phase. After 86 ks of MA time, this exothermic reaction disappears and no other reactions can be detected, as illustrated in Fig. 8.58(*b*). This suggests the amorphous-crystalline (bcc-$Co_{50}Ti_{50}$) phase transformation of the as-milled sample. No remarkable changes in the crystallization temperature (the peak temperature of the exothermic peak) can be detected in the sample that was milled for 22 ks. This bcc-$Co_{50}Ti_{50}$ phase transforms to a single amorphous phase after 360 ks of MA time, suggested by the sharp exothermic reaction which appears at 976 K in Fig. 8.58(*c*). The crystallized sample reveals a structure of bcc-CoTi phase. After 540 ks of MA time [Fig. 8.58(*d*)], no reactions can be noted, suggesting that the milled powder has a stable phase of bcc-$Co_{50}Ti_{50}$. After 720 ks of MA time, the bcc-$Co_{50}Ti_{50}$ phase transforms to an amorphous $Co_{50}Ti_{50}$ powder, which crystallizes through a single exothermic reaction peak [Fig. 8.58(*e*)].

8.9.2 Al-Zr Binary System

In order to understand the effect of the milling speed on the cyclic phase transformations, several samples of mechanically alloyed $Al_{50}Zr_{50}$ were prepared, using milling speed, 90 rpm (I = 2), 180 rpm (I = 4), 270 rpm (I = 6), and 360 rpm (I = 8). In all experiments the temperature of the vial, T_v, was measured every 30 minutes. It is worth noting that when the samples were milled with a low milling speed (I = 2 and 4), T_v does not increase remarkably, (307 or less). For those experiments run at I = 6 and 8, however, T_v increases rapidly with increasing MA time, and is found to be about 320 K after 30 minutes of MA time. In order to minimize the temperature effect in the study of the cyclic transformations, the ball-milling experiments were stopped periodically (every 30 minutes) and resumed when the temperature of the vial decreased to about 300 K. This on/off mode was also applied to those samples milled at a low milling speed. It is worth noting that when the vial was charged with milling media only and operated at I = 8 for 30 minutes, the vial's temperature increased to about 310 K. In order to study the reproducibility of this work, all the milling experiments were repeated, under the same experimental conditions, three times.

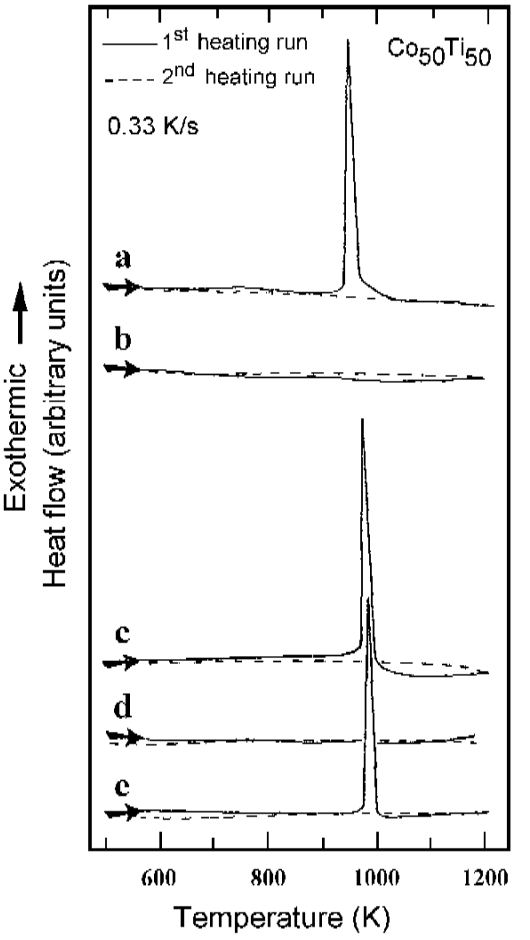

Figure 8.58. DTA curves of mechanically alloyed $Co_{50}Ti_{50}$ powder after *(a)* 22 ks, *(b)* 86 ks, *(c)* 360 ks, *(d)* 540 ks, and *(e)* 720 ks of the MA time. *(After El-Eskandarany et al.)*[122]

8.9.2.1 Structural Changes with the Milling Time

Here, unexpected results can be seen in Fig. 8.59, which shows the effect of the MA time on the structural changes of $Al_{50}Zr_{50}$ powder milled at I = 8. In contrast to the starting reactant materials of polycrystalline

fcc-Al and hcp-Zr [Fig. 8.59(*a*)], a nanocrystalline metastable phase of fcc-AlZr solid solution is obtained after 12 h of the MA time [Fig. 8.59(*b*)]. Increasing the MA time (24 h) transforms this phase into an amorphous phase of $Al_{50}Zr_{50}$, characterized by a broad, diffuse, and smooth halo, as displayed in Fig. 8.59(*c*). This amorphous phase is not stable against further mechanical deformation. It crystallizes into the most stable phase of orthorhombic-AlZr upon milling for 48 h as in Fig. 8.59(*d*). In a cyclic crystalline-amorphous phase transformation and after 72 h of MA time, the crystalline phase transforms to an amorphous phase coexisting with nanocrystalline grains of AlZr [Fig. 8.59(*e*)]. Presumably, this phase transformation takes place due to the accumulation of several lattice imperfections, such as point and lattice defects, which raise the free energy from a stable phase (orthorhombic-AlZr) to a less stable phase (amorphous-AlZr). Further milling (100 h) leads, again, to crystallization of a large fraction of the amorphous phase, and the product of this stage of milling is a composite nanocrystalline/amorphous powder [Fig. 8.59(*f*)]. Finally, at an MA processing time of 150 h, the nanocrystalline phase transforms again to the amorphous phase [Fig. 8.59(*g*)]. These cyclic phase transformations have been observed for all the samples milled on three different milling runs, using I = 8. It has been shown in a previous study[18] that when a mixture of $Al_{50}Zr_{50}$ powders were milled for a long-milling run (400 h), using a low-energy ball mill and/or rod mill, no mechanically induced crystallization and/or cyclic phase transformations were observed, and the final-products of those experiments were amorphous $Al_{50}Zr_{50}$ powders. Increasing the low-energy ball milling time[14] does not lead to the crystallization of the amorphous phase, even after a very long milling time (800 h). We can then conclude that the kinetic energy of the ball mill, which is affected by the milling speed, plays an important role in the incidence of cyclic transformations.

In contrast to the results shown in Fig. 8.59, the XRD patterns of the samples milled for different MA times, but at lower milling speed (I = 4) (Fig. 8.60), show a slow solid-state amorphization reaction taking place between the diffusion couples of Al and Zr with the absence of the cyclic phase transformations. It is worth noting that, even for samples milled at this low milling speed at longer milling times (400 h, 450 h, 500 h, 550 h, and 600 h), the cyclic reactions do not appear. The end-product for each milling run is the same as that shown in Fig. 8.60(*f*).

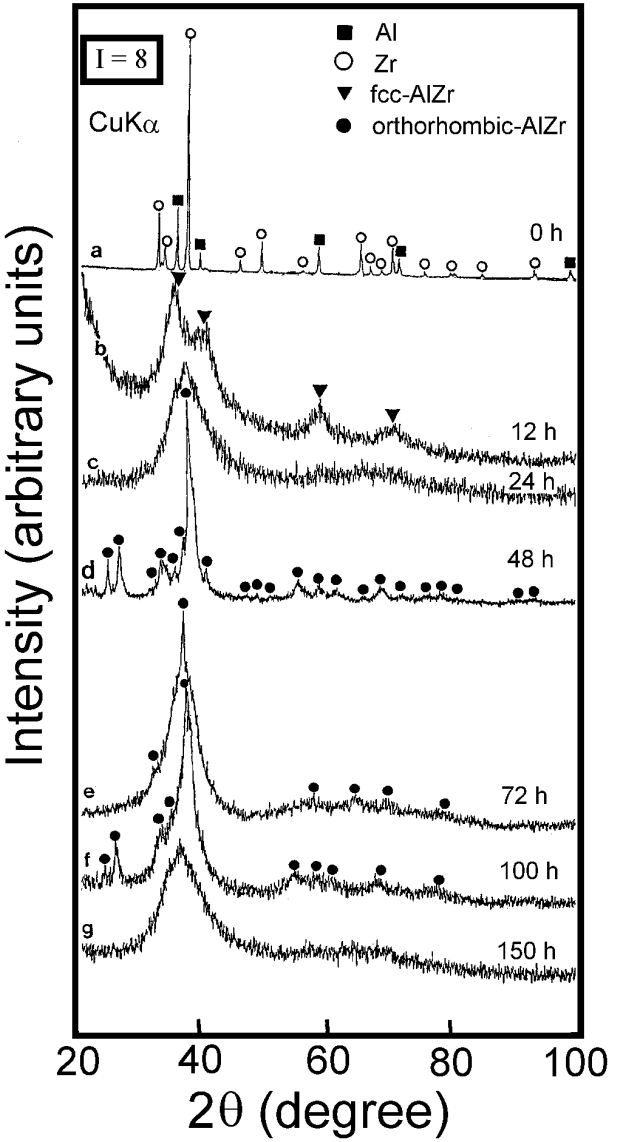

Figure 8.59. XRD patterns of $Al_{50}Zr_{50}$ powder that were ball-milled at milling speed of 8 after *(a)* 0 h, *(b)* 12 h, *(c)* 24 h, *(d)* 48 h, *(e)* 72 h, *(f)* 100 h, and *(g)* 150 h of the MA time. *(After El-Eskandarany et al.)*[123]

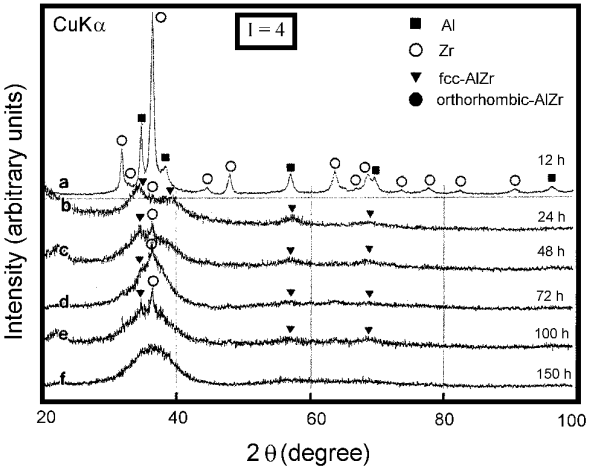

Figure 8.60. XRD patterns of $Al_{50}Zr_{50}$ powder that were ball-milled at milling speed of 4 after *(a)* 12 h, *(b)* 24 h, *(c)* 48 h, *(d)* 72 h, *(e)* 100 h, and *(f)* 150 h. *(After El-Eskandarany et al.)*[123]

8.9.2.2 Thermal Stability

The crystallization characteristics indexed by the enthalpy change of crystallization, ΔH_x, of amorphous $Al_{50}Zr_{50}$ powder that were milled at different milling speeds, I, are plotted in Fig. 8.61 as a function of the MA time. For I = 8 [Fig. 8.61(*a*)], a rapid increase in the value of ΔH_x occurs during the first stage of milling (0–12 h). This indicates a decrease of pure elemental Al and Zr in the milled powder, and the formation of an amorphous phase. After 24 h of MA time, these values increase again, ranging from -36 kJ/mol to -38 kJ/mol. During the next stage of milling (24 h–48 h), the values of ΔH_x for the as-milled powder decrease remarkably, suggesting mechanically induced amorphous-crystalline phase transformation. After 72 h of milling time, however, the values of ΔH_x for the milled powder tend to increase again, due to the formation of amorphous $Al_{50}Zr_{50}$ alloy. Again, the ΔH_x tends to have lower values during further MA time (72 h–100 h), indicating a second amorphous-crystalline phase transformation, as shown in Fig. 8.61(*a*). After longer milling (100 h–150 h), the value of ΔH_x increases to have almost the same values as those milled for 24 h.

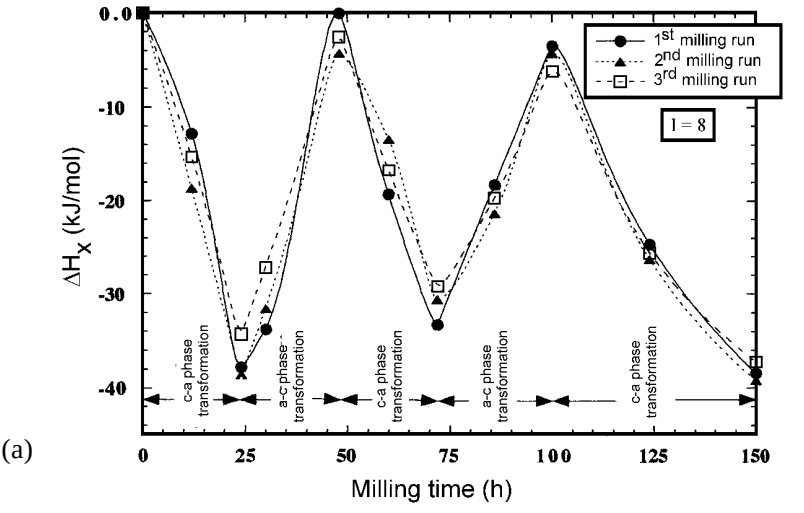

(a)

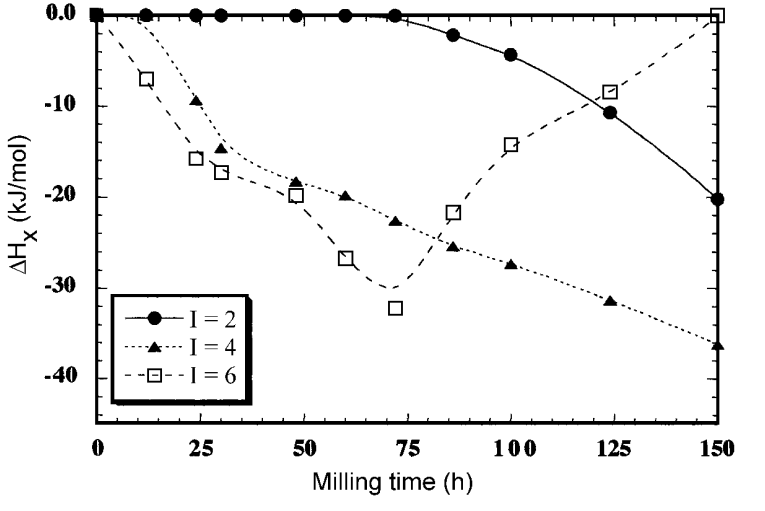

(b)

Figure 8.61. Correlation between the enthalpy change of crystallization, ΔH_x, for amorphous $Al_{50}Zr_{50}$ alloy powders that were ball milled at *(a)* high speed of milling and *(b)* low speed of milling. *(After El-Eskandarany et al.)*[123]

The characteristics of the mechanically alloyed powders seem to be very sensitive to the milling speed, I, as suggested by the behavior of ΔH_x with the I and MA time [see Fig. 8.61(*b*)]. For I = 4 and 6, the value of ΔH_x increases monotonically with increasing MA time, indicating an increasing fraction of the amorphous alloy. At I = 6, this amorphous phase gradually transforms into a stable phase when milled for 72 h–150 h. Based on the results of the present study, the crystalline phase formed after 150 h of milling is transformed to an amorphous phase after milling for 440 h. No cyclic phase changes could be observed for those samples milled at I = 4 [see Fig. 8.61(*b*)], and the end-product is an amorphous phase, even after long milling runs, as long as 600 h. Contrary to the samples milled at I = 4, the end-product (150 h) of the samples milled at I = 2 are an amorphous phase coexisting with a considerable fraction of elemental reactant powders, as indicated by the low value in ΔH_x [Fig. 8.61(*b*)].

8.9.3 Mechanism of Amorphous-Crystalline-Amorphous Cyclic Phase Transformations During Ball Milling

One possible factor which may lead to such cyclic crystalline-amorphous transformations of Co-Ti or Al-Zr binary systems, is the introduction of contamination in the ball-milled powder. The iron and gas (oxygen, nitrogen, and hydrogen) contaminating contents of the milled powder are plotted in Fig. 8.62 (for mechanically alloyed $Co_{50}Ti_{50}$) as a function of the milling time. During the first stage of MA, the iron, which comes from the stainless steel milling tool, increases drastically, to about 0.40 at. %. The gas contamination content, that may be introduced to the milled powder during the ball-milling process and/or handling of the sample outside the glove box, increases during this stage of milling. This is attributed to the formation of active-fresh surfaces of the elemental powders (especially Ti and Zr), which are able to react with the surrounding atmosphere. As the MA time increases, the milling tools are coated with the milled powder, which is wear-resistant to iron. These coated balls play an important role to prevent introduction of further iron contamination to the milled powder. The iron contamination content of the end-product is about 0.50 at. %. In addition, no remarkable changes in the gas content can be detected for the samples that milled for longer times. These values of the contaminating contents in the milled powder are almost negligible and cannot be considered to be responsible for the cyclic phase transformations of Co_xTi_{100-x} or $Al_{50}Zr_{50}$ during the ball-milling process.

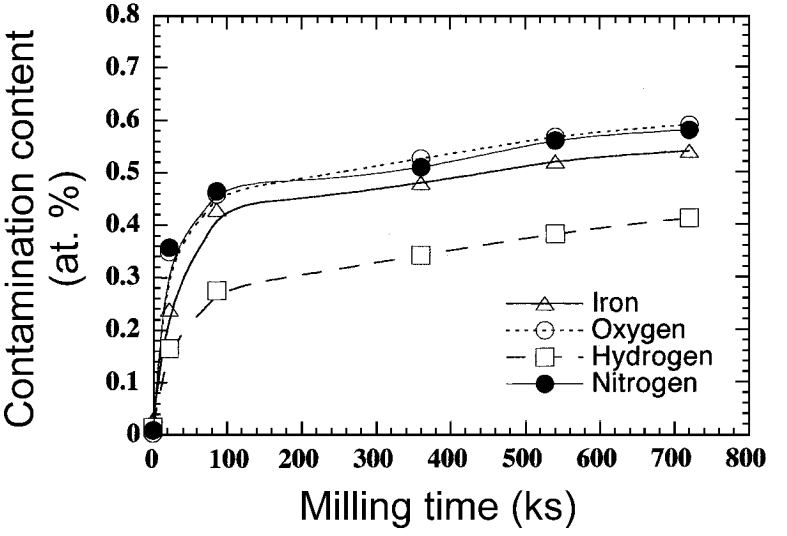

Figure 8.62. Dependence of the contamination content of mechanically alloyed $Co_{50}Ti_{50}$ powder on the MA time. *(After El-Eskandarany et al.)*[122]

Another possible factor which can lead to cyclic phase transformations, is excessive temperature during milling. To avoid such a factor, the ball-milling process was interrupted when the temperature of the vial reached about 320 K (almost every 1.8 ks of continuous milling) and then resumed when the temperature decreased to 300 K. In order to realize the effect of the temperature increase on the structure of the powder during milling, the samples that milled for 22 ks (amorphous phase of Co_xTi_{100-x} or AlZr alloys) and 86 ks (bcc-$Co_{50}Ti_{50}$) were heated separately in the DTA to 700 K (well above the measured temperature of the vial). The XRD patterns of these samples prove that no phase transformation takes place, even at this relatively high temperature. However, the amorphous $Co_{50}Ti_{50}$ alloy is transformed to a crystalline bcc-$Co_{50}Ti_{50}$ upon heating to about 968 K. We can then conclude that the temperature which was recorded during the ball-milling process is far below the required temperature that can cause structural changes in the milled powder. The same results were obtained from the samples which were milled separately for the second and third milling runs.

REFERENCES

1. Buckel, W., and Hilsch, R., *Z. Phys.*, 138:109 (1954)
2. Duwez, P., Willens, R. H., and Klement, W., Jr., *J. Appl. Phys.*, 31:1136 (1960)
3. Vegard, J., *Phil. Mag.*, 32:20 (1916)
4. Herd, S. R., Tu, K. N., and Ahn, K. Y., *Appl. Phys. Lett.*, 42:597 (1983)
5. Schwarz, R. B., and Johnson, W. L., *Phys. Rev. Lett.*, 51:415 (1983)
6. Blatter, A., and von Allmen, M., *Phys. Rev. Lett.*, 54:2103 (1985)
7. Yeh, X. L., Samwer, K., and Johnson, W. L., *Appl. Phys. Lett.*, 42:242 (1983)
8. Aoki, K., Nagano, M., Yanagitani, A., and Masumoto, T., *J. Appl. Phys.*, 62:3314 (1987)
9. Aoki, K., Yanagitani, A., and Masumoto, T., *Appl. Phys. Lett.*, 52:2212 (1988)
10. Cheng, Y. T., Johnson, W. L., and Nicolet, M. A., *Appl. Phys. Lett.*, 47:800 (1985)
11. Schroder, H., Samwer, K., and Koster, U., *Phys. Rev. Lett.*, 54:197 (1985)
12. White, R. L., *The Use of Mechanical Alloying in the Manufacture of Multifilamentary Superconductor Wire*, Ph.D. Thesis, Stanford University (1979)
13. Koch, C. C., Cavin, O. B., McKamey, C. G., and Scarbrough, J. O., *Appl. Phys. Lett.*, 43:1017 (1983)
14. El-Eskandarany, M. S., Aoki, K., and Suzuki, K., *J. Less-Common Met.*, 167:113 (1990)
15. Schwarz, R. B., Wong, K. L., Johnson, W. L., and Clements, B. M., *J. Non-Cryst. Solids*, 61–62:129 (1984)
16. Schultz, L., *J. Less-Common Met.*, 145:233 (1988)
17. Johnson, W. L., *Prog. Mater. Sci.*, 30:81 (1986)
18. El-Eskandarany, M. S., Aoki, K., and Suzuki, K., *Metall. Trans A.*, 23:2131 (1992)
19. Schwarz, R. B., *MRS Bull.*, p. 55 (May/June 1986)
20. Schwarz, R. B., Petrich, R. R., and Saw, C. K., *J. Non-Cryst. Solids*, 76:281 (1985)
21. Schwarz, R. B., and Petrich, R. R., *J. Less-Common Met.*, 140:171 (1988)
22. Weeber, A. W., and Bakker, H., *Physica B*, 153:93 (1988)

23. Weeber, A. W., Haag, W. J., Wester, A. J. H., and Bakker, H., *J. Less-Common Met.*, 140:119 (1988)
24. Weeber, A. W., Bakker, H., Heijligers, H. J. M., and Bastin, G. F., *Europhys. Lett.*, 3:1261 (1987)
25. Eckert, J., Schultz, L., and Urban, K., *J. Mater. Res.*, 6:1874 (1991)
26. Petzoldt, F., Scholz, B., and Kunze, H. D., *Mater. Sci. Eng.*, 97:25 (1988)
27. Hellstern, E., and Schultz, L., *J. Appl. Phys.*, 63:1408 (1988)
28. El-Eskandarany, M. S., Bahgat, A. A., Gomaa, N. S., and Eissa, N. A., *J. Alloys Comp.*, 290:181 (1999)
29. El-Eskandarany, M. S., Aoki, K., and Suzuki, K., *Mater. Sci. Forum*, 88–90:81 (1992)
30. El-Eskandarany, M. S., *J. Alloys Comp.*, 234:67 (1996)
31. El-Eskandarany, M. S., Aoki, K., and Suzuki, K., *Metall. Trans. A*, 23:2131 (1992)
32. El-Eskandarany, M. S., Aoki, K., Masumoto, T., and Suzuki, K., *J. Alloys Comp.*, 209:71 (1994)
33. El-Eskandarany, M. S., *J. Alloys Comp.*, 284:295 (1999)
34. El-Eskandarany, M. S., Aoki, K., and Suzuki, K., *J. Appl. Phys.*, 71:2924 (1992)
35. El-Eskandarany, M. S., Aoki, K., and Suzuki, K., *J. Appl. Phys.*, 72:2665 (1992)
36. El-Eskandarany, M. S., Aoki, A., and Suzuki, K., *J. Jpn Society of Powder and Powder Metallurgy*, 38:59 (1991)
37. El-Eskandarany, M. S., Aoki, K., Itoh, H., and Suzuki, K., *J. Less-Common Met.*, 169:235 (1991)
38. El-Eskandarany, M. S., Suzuki, H., Aoki, K., and Suzuki, K., *J. Jpn Society of Powder and Powder Metallurgy*, 38:96 (1991)
39. El-Eskandarany, M. S., Aoki, K., and Suzuki, K., *J. Non-Cryst. Solids*, 150:472 (1992)
40. El-Eskandarany, M. S., Sumiyama, K., Aoki, K., and Suzuki, K., *J. Jpn Society of Powder and Powder Metallurgy*, 39:836 (1992)
41. El-Eskandarany, M. S., in: *Proceeding of The 6th International Mining, Petroleum and Metallurgical Engineering Conference* (MPM), p. 119, Organized by Faculty of Engineering, Cairo University (Feb. 20–24, 1999)
42. El-Eskandarany, M. S., Aoki, K., and Suzuki, K., *J. Alloys Comp.*, 186:15 (1992)

43. Henaff, M. P., Colinet, C., Pasturel, A., and Buschow, K. H. J., *J. Appl. Phys.*, 56:307 (1984)
44. Miedema, A. R., *J. Less-Common Met.*, 32:117 (1973)
45. Massalski, T., *Binary Alloy Phase Diagrams*, 1st Printing, 1:157, 1st Ed., ASM (1986)
46. Davies, H. A., *Phys. Chem. Glasses*, 17:159 (1976)
47. Johnson, W. L., Poon, S. J., Durand, J., and Duwez, P., *Phys. Rev. B*, 18:201 (1978)
48. Buschow, K. H. J., *J. Phys. F*, 14:593 (1984)
49. El-Eskandarany, M. S., Aoki, K., and Suzuki, K., *J. Alloys Comp.*, 177:229 (1991)
50. Suzuki, K., *J. Non-Cryst. Solids*, 112:23 (1989)
51. El-Eskandarany, M. S., *Metall. Trans. A*, 27:3267 (1996)
52. El-Eskandarany, M. S., Aoki, K., and Suzuki, K., *Scripta Metall.*, 25:1695 (1991)
53. van Rossum, M., Nicolet, M. A., and Johnson, W. L., *Phys. Rev. B*, 29:549 (1984)
54. Cotts, E. J., Wong, G. C., and Johnson, W. L., *Phys. Rev. B*, 37:9049 (1988)
55. Politis, C., and Johnson, W. L., *Appl. Phys. Lett.*, 60:1147 (1986)
56. Hellstern, E., and Schultz, L., *Appl. Phys. Lett.*, 49:1163 (1986)
57. Schultz, L., Hellstern, E., and Thomä, A., *Europhys. Lett.*, 3:921 (1987)
58. Eckert, J., Schultz, L., and Urban, K., *J. Appl. Phys.*, 64:3224 (1988)
59. Eckert, J., Schultz, L., and Urban, K., *J. Less-Common Met.*, 145:283 (1988)
60. Thomä, A., Saemann-Ischenko, G., Schultz, L., and Hellstern, E., *Jpn. J. Appl. Phys.*, 26:977 (1987)
61. Hellstern, E., Schultz, L., and Eckert, J., *J. Less-Common Met.*, 140:93 (1988)
62. Lee, P. Y., and Koch, C. C., *J. Non-Cryst. Solids*, 94:88 (1988)
63. Hellstern, E., Schultz, L., Bormann, R., and Lee, D., *Appl. Phys. Lett.*, 53:1399 (1986)
64. El-Eskandarany, M. S., Aoki, K., and Suzuki, K., *Sci. Rep. Ritu*, Tohoku University, A39:103 (1994)
65. Babic, E., Ristic, R., Miljak, M., Scott, M. G., and Cregan, G., *Solid State Commun.*, 39:139 (1981)
66. Altounian, Z., and Strom-Olsen, J. O., *Phys. Rev. B*, 27:4149 (1983)

67. Karkut, M. G., and Hake, R. R., *Phys. Rev. B,* 28:1396 (1983)
68. El-Eskandarany, M. S., Itoh, F., Aoki, K., and Suzuki, K., *J. Non-Cryst. Solids,* 118:729 (1990)
69. Miedema, A. R., de Châtel, P. F., and de Boer, F. R., *Physica B,* 100:1 (1980)
70. Weeber, A. W., *J. Phys. F,* 17:809 (1987)
71. Richards, T. G., and Johari, G. P., *Philos. Mag. B,* 58:445 (1988)
72. Dong, Y. D., Wang, W. H., Liu, L., Xiao, K. Q., Tong, S. H., and He, Y. Z., *Mater. Sci. Eng. A,* 134:867 (1991)
73. Lerf, R., and Morris, D. G., *Mater. Sci. Eng. A,* 128:119 (1990)
74. Fecht, H. J., and Johnson, W. L., *J. Non-Cryst. Solids,* 117–118:704 (1990)
75. Loeff, P. I., and Bakker, H., *Europhys. Lett.,* 8:35 (1989)
76. Radinski, A. P., and Calka, A., *Mater. Sci. Eng. A,* 134:1376 (1991)
77. Kimura, H., Takada, F., and Myung, W. N., *Sci. Eng. A,* 97:125 (1988)
78. Hellstern, E., and Schultz, L., *Mater. Sci. Eng. A,* 93:213 (1987)
79. El-Eskandarany, M. S., Aoki, K., Sumiyama, K., and Suzuki, K., *Scripta Metall.,* 36:1001 (1997)
80. El-Eskandarany, M. S., Aoki, K., Sumiyama, K., and Suzuki, K., *Appl. Phys. Lett.,* 70:1679 (1997)
81. Eckert, J., Schultz, L., and Urban, K., *J. Less-Common Met.,* 166:293 (1990)
82. Kimura, H., Kimura, M., and Takada, F., *J. Less-Common Met.,* 140:113 (1988)
83. Schänzer, M., and Mehrer, H., *J. Phys., Coll. Phys. C4, Supp. 14,* 51:87 (1990)
84. Thompson, J. R., Politis, C., and Kim, T. C., *Mater. Sci. Eng. A,* 97:31 (1988)
85. Fukunaga, T., Nakamura, K., Suzuki, K., and Mizutani, U., *J. Non-Cryst. Solids,* 117–118:700 (1990)
86. Fukunaga, T., Mori, M., Inou, K., and Mizutani, U., *Mater. Sci. Eng. A,* 134:863 (1991)
87. Jang, J. S. C., and Koch, C. C., *Scripta Metall.,* 20:669 (1986)
88. Martin, V. E., Garcia-Escorial, A., Martin, A., Carmona, F., Cebollada, F., Adeva, P., and Gonzalez, J. M., *J. Phys., Coll. Phys. C4, Supp. 14,* 51:198 (1990)
89. Lee, P. Y., Jang, J., and Koch, C. C., *J. Less-Common Met.,* 140:73 (1988)

90. Ennas, G., Magini, M., Boffito, G., and Licheri, G., *J. Mater. Sci.*, 24:3053 (1988)

91. El-Eskandarany, M. S., Sumiyama, K., and Suzuki, K., *Acta Metall.*, 45:1175 (1997)

92. Hellstern, E., and Schultz, L., *Philos. Mag. B*, 56:443 (1987)

93. Lee, P. Y., and Koch, C. C., *J. Non-Cryst. Solids*, 94:88 (1987)

94. Boldrick, M. S., Lee, D., and Wagner, C. N. J., *J. Non-Cryst. Solids*, 106:60 (1988)

95. Fukunaga, T., Homma, Y., Misawa, M., and Mizutani, U., *J. Non-Cryst. Solids*, 117–118:721 (1990)

96. Thompson, J. R., and Politis, C., *Europhys. Lett.*, 3:199 (1985)

97. Loeff, P. I., Spit, F. H., and Bakker, H., *J. Less-Common Met.*, 145:271 (1988)

98. Gaffet, E., and Harmelin, M., *J. Less-Common Met.*, 157:201 (1990)

99. Gaffet, E., and Harmelin, M., *J. Phys., Coll. Phys. C4, Supp. 14*, 51:139 (1990)

100. Weeber, A. W., and Bakker, H., *Z. Phys. Chem. N. F.*, 157:221 (1988)

101. de Boer, F. R., Boom, R., Mattens, W. C. M., Miedema, A. R., and Niessen, A. K., *Cohesion in Metals-Transition Metal Alloys*, North-Holland, Amsterdam, 1st Ed., 1:224, (1988)

102. Wang, R., Merz, M. D., Brimhall, J. L., and Dahlgren, S. D., *Rapidly Quenched Metals III*, Metals Society, London, 1:420 (1978)

103. Maissel, L. I., Mauer, F. A., Piermarini, G. I., and Block, S., *J. Appl. Phys.*, 54:5698 (1983)

104. Sumiyama, K., Hirata, M., and Teshima, W., *Jpn J. of Appl. Phys. A*, 30:2839 (1991)

105. Boldrick, M. S., Yang, E., and Wagner, C. N. J., *J. Non-Cryst. Solids*, 150:478 (1992)

106. Koyano, T., Chatani, K., Fukunaga, T., and Mizutani, U., *Mater. Sci. Eng. A*, 181–182:1277 (1994)

107. Darken, L. S., and Curry, R. W., *Physical Chemistry of Metals*, p. 50, McGraw-Hill, New York (1953)

108. Egami, T., and Waseda, Y., *J. Non-Cryst. Solids*, 64:113 (1984)

109. Güntherod, H. J., Oelhafen, P., Hausera, E., Greuter, F., Lapka, R., Rösel, F., Jacobs, R., d'Albuquerque e Castro, J., Kübler, J., Hague, C. F., Bennemann, K. H., Fairlie, R. H., Temmermann, W. M., and Gyoffy, B. L., *Inst. Phys. Conf. Ser.*, 55:619 (1981)

110. de Boer, F. R., Boom, R., Mattens, W. C. M., Miedema, A. R., and Niessen, A. K., *Cohesion in Metals-Transition Metal Alloys*, 1:224, 1st Ed., North-Holland, Amsterdam (1988)

111. El-Eskandarany, M. S., and Ahmed, H. A., *J. Alloys Comp.*, 216:213 (1994)

112. Abrahamson, E. P., and Lopata, S. L., *Trans.*, AIME, 236:76 (1966)

113. Schultz, L., Hellstern, E., and Zone, G., *Z. Phys. Chem.*, 157:203 (1988)

114. Michaelsen, C., and Schultz, L., *Acta Metall. Mater.*, 39:987 (1991)

115. Ermakov, A. E., Yurchikov, E. E., and Barinov, V. A., *Phys. Met. Metall.*, 52:50 (1981)

116. Jang, J. S. C., and Koch, C. C., *J. Mater. Res.*, 5:498 (1990)

117. Suzuki, K., *J. Non-Cryst. Solids*, 117/118:1 (1990)

118. Suzuki, K., *J. Non-Cryst. Solids*, 112:23 (1989)

119. Subramanian, P. R., Miracle, D. B., and Mazdiyasni, S., *Metall. Trans. A*, 21:539 (1990)

120. Trudeau, M. L., Schulz, R., Dussault, D., and Neste, A. V., *Phys. Rev. Lett.*, 64:99 (1990)

121. El-Eskandarany, M. S., Aoki, K., Sumiyama, K., and Suzuki, K., *Appl. Phys. Lett.*, 70:1679 (1997)

122. El-Eskandarany, M. S., Aoki, K., Sumiyama, K., and Suzuki, K., *Scripta Metall.*, 36:1001 (1997)

123. El-Eskandarany, M. S., Aoki, K., Sumiyama, K., and Suzuki, K., *Metall. Trans. A*, 30:1877 (1999)

124. *ASTM* card No. 15-806

Index

Activated reactive evaporation 95
Advanced materials 2
Agglomerated particles 98, 100, 108
Agglomerated powder particles
  disintegration stage 49
Agglomeration stage 157
Al 5
  concentration 164
  isochemical line 155
  layers 173
  reflections 153
Al matrix 49
Al-Mg alloys 29
Al-Nb binary system 4
Al-Ta binary system 4, 19
Al_2O_3 dispersion 28
$Al_{50}Hf_{50}$
  rod-milled powders 161
Al_xHf_{100-x}
  alloy powders 171
Alloy powders 120
Alloys
  WC 129
$Al_{30}Ta_{70}$
  ball-milled powders 146
  rod-milled powders 146
$Al_{50}Ta_{50}$
  alloy powders 205
  mechanically alloyed 199
  mechanically disordered 199
AlTaN 4
$Al_{50}Zr_{50}$
  effect of MA time 218
AlZr alloys
  amorphous phase 224
Amorphization
  enthalpy 166
  free energy change 175
  process 174, 205
  ratios 168
  reaction 167, 184
Amorphous 55
Amorphous alloy
  FeW 183
  heterogeneous 164
  preparation methods 143
  single phase 144, 188

Amorphous layer
growth rate 144
Amorphous materials 19
synthesis techniques 143
Amorphous phase 4, 174, 176
empirical rule 190
free-energy curve 150
Amorphous state 146
Amorphous-AlZr
less stable 219
Amorphous-crystalline phase
transformation 209, 217
Annealed stainless steel 194
Apacitors 19
Application of milling 5
Archimedes' principle 96
Argon sparging 23
Artificial oxidation 47
As-annealed 720 ks alloy
XRD pattern 210
As-consolidated
samples 41, 96, 103
contamination content 106
hardness 109
nitrogen content 105
As-leached powder 131, 135
As-milled powders 131
As-milled samples 41, 96
contamination content 106
nitrogen content 105
As-milled state 197
Attritor or attrition ball mill 7
Austenitic stainless steel 192
Automotive structures 46

Back scattering micrograph 54
Ball collisions 17
Ball mill 84, 86, 95, 105, 128, 146
high-energy 47, 108, 119, 183, 195
low-energy 183
Ball-mill charge
kinetic energy 15
Ball-milled alloy powders 11
Ball-milling 1, 2
amorphization process 150
experiments 130, 217
high energy 4, 209
process 12, 23, 223, 224
technique 37, 47, 58, 59
time 38
Ball-to-powder weight ratio 14, 39, 66
Bcc-CoTi phase 217
Bcc-Co_3Ti phase
lattice parameters 210
Bcc-$Co_{50}Ti_{50}$ 217, 224
Bcc-Nb powders 109
Bcc-Ta powder 112
BFI 71, 78, 90, 102, 124, 133, 162. *See also* Bright field image
Binary systems 198
Binding material 129
BM. *See* Ball-milled
BN 113
Bragg peaks 14, 39, 48, 68, 96, 113, 120, 131, 183, 195, 200, 210
Bright field image 52, 71, 133, 154, 213
Brittle-to-ductile transformation 63
Bulk density 81, 103, 109
Bulk modulus 57, 105
elastic moduli 82
Bulk samples 131

Carbides 62
Casting techniques 192
Ceramics 63
composites 86
materials 91

Chemical processing 36
Chemical vapor deposition 86
  atmospheric pressure 95
Coated fine oxide production 23
Cold pressing technique 89
Cold welding 16, 37, 58, 98, 108, 137, 157
Cold working technique 37
Cold-wall technique 86
Complex oxide alloys
  dispersion-strengthened 4
Composite powders 136
Consolidated sample 131
  hardness 108
  mechanical properties 96
  microstructure 102
Consolidation of milled powders 41
Consolidation procedure 136
Consolidation step via the PAS
  three important factors 41
Corrosive atmosphere 27
Covalent glasses 143
Co_xTi_{100-x}
  amorphous phase 224
Crystal lattice
  shear instability 37
Crystalline compounds
  enthalpy 181
Crystalline intermetallic phase 148
Crystallization
  characteristics 188
  enthalpy 165, 177, 182, 221
  parameters 171
  process 169
  reaction 187
  reactions 171
  temperature 177, 192, 209
Crystallization of amorphous phases 36
Cu
  diffraction peaks 122
Cu_2O 119, 120, 125, 126
Cu_2O-Ti powders 124
Cutting tools 63, 129
CVD 86. *See also* Chemical vapor deposition
Cyclic crystalline-amorphous transformations 223
Cyclic phase transformations 209, 216, 219, 223
  milling speed 217

Dark field image 97, 113, 133
DC pulse voltage 60
Debye-Scherrer rings 72, 214
Developing countries 65
DFI 113, 133. *See also* Dark field image
Differential scanning calorimetry 145
Direct alloying 129
Disintegration 49
Disintegration stage 157
Dispersoid powders 17
Dispersoids 25
Drilling tools 64
DSC. *See* Differential scanning calorimetry
DTA
  curves 146
  curves and traces 126
  measurements 165, 173
  technique 111
  thermograph 187

EDS
  analyses 164, 192
  measurements 154
Elastic moduli 82, 103
Electrodeposition 36
Electron microscope analysis 204
Elemental crystalline state 198
Endothermic 111
Endothermic reaction 126, 162

Engineering composite material
mechanism for synthesis 58
Equiaxed grains 102
Equilibrium crystalline state 146
Equilibrium phase diagram 86
Etching time 102
Eutectic melting 150
Exothermic peak 173, 205, 217
Exothermic reaction 162, 173, 187, 217
Extractive metallurgy 129

Fcc-NbN alloy powders
metastable phase 109
Fcc-$NiTiH_3$ 113
Fcc-TiC
fully reacted 78
Fcc-TiC grains 72
α-Fe 194
lattice parameter 184
Fe-Zr-B 196
Fe_4N 4
$Fe_{50}W_{50}$
powders 183, 185
$Fe_{74}Cr_{18}Ni_8$ 192. *See also* Austenitic stainless steel
FeN 113
FeW matrix 192
Fine powder formation 53
Fine-grained material 35
First heating run 126
Formation 68
Forward reaction 128
Fracture toughness 131, 139
Fracturing 16
Fusion-thermal conductivity method 130

G_0. *See* Initial crystalline state
G_a. *See* Amorphous state
Gas condensation 37
Gas turbine engine blades 27
Gas turbine vanes 25
Glass 143
Glass-forming range 175
Globe-like morphology 202
Good oxidation resistance 63
Good thermal shock resistance 63
Grain boundaries 38
Grain boundary fringes 154
Grain growth 54, 60
Grain size 68
distribution 90
Grain size reduction
stage one 37
stage two 38
stage three 38
Graphite 129, 130
Graphite aluminum alloys 23
process for manufacturing 2
Great hardness values 62
G_x. *See* Equilibrium crystalline state

Hall-Petch assumption 81
Hall-Petch equation 35
Halo peak 195
Halo-diffraction patterns 176
Hcp-Co 209, 210
Hcp-Nb_4N_3
mixed phases 110
Hcp-NbN
mixed phases 110
Hcp-Ti 72, 210
crystals 97
powder 96
Hcp-WC
refractory phase 131
single phase 131
Helium carrier fusion-thermal conductivity 66
Hf layers 173
Hf reflections
Bragg peaks 153

High-energy ball mill 66
High-resolution transmission electron microscope 130
High-resolution transmission electron microscopy 66
High temperatures 65
Homogeneous alloy 185
Homogeneous and uniform powders 11
Homogeneous nanocrystalline 65
Homogenization 59, 161
Hot pressing technique 89
Hot-wall technique 86
HRTEM 66, 130
  micrograph 68
  observations 36, 73
Huge 58
Hydrogen atoms 143

ICP. *See* Induction coupled plasma emission method 199
Impact 59
INCO. *See* International Nickel Company
INCOLOY alloy MA 956 27
INCONEL alloys 24
INCONEL MA 6000 25
Increases linearly 56
Induction coupled plasma emission method 120, 130
Induction coupled plasma emission 66
Industrial scale at room temperature 58
Inert gas condensation 36
Initial crystalline state 147
Intensity ratios 68
Interdiffusion reaction 17, 149
Interface formation 58
Intermediate phase 55
Intermetallic compound(s) 16
International Nickel Company 2
Interstitial hcp-TiC solid solution 68
Ionic glasses 143
Iron contamination 128
Iron-resistance wear 106

Kneading action 24

Lamellar 17
Light optical microscope 120
Liquid metallurgy 4, 46, 58
  traditional method 195
Longitudinal optical (LO)-like phonon mode 86

μ phase. *See* Order phase
MA 65, 175, 198. *See also* Mechanical alloying
  alloy powders 205
  early stage 195
  processing 119
  refining stage 85
  technique 128, 208
MA Al-Mg powders
  microstructures 30
MA method 37, 83, 126, 171
  main process 16
MA process 2, 38, 68, 157, 183, 199, 205
  adding control agent 30
  applied torque 7
  different stages 76
  ductile metal 5
  end point 30
  flattening 29
  mechanism and nature 4
  refining stage 77

MA time 78, 84, 137, 153, 169, 183, 186, 190, 216, 219, 223
Magnesium 128
Matrix 49, 54, 58
  metallic 45
MD 198. *See also* Mechanical disordering
  alloy powders 205
  powders 208
  process 174
  technique 208
  time 201
MDSSA 166, 167, 175. *See also* Mechanically driven solid-state amorphization
MDSSA process 167, 168, 172, 174, 175
Mechanical alloying 2, 37, 144, 197, 198
  amorphization 149, 175
  carbide synthesis 86
  unique process 19
Mechanical alloying process
  controlling factors 6
Mechanical deformation 184
Mechanical disordering 173, 198
Mechanical grinding 198
Mechanical milling 198
Mechanical mixing
  second stage 59
  third stage 59
Mechanical solid-state amorphization reaction 198
Mechanical solid-state reduction 119
Mechanical-mixing
  first stage 58
Mechanically alloyed $Co_{50}Ti_{50}$ powder
  DTA curves 216
  XRD pattern 213
Mechanically alloyed $Co_{75}Ti_{25}$ powder 210
Mechanically alloyed $Fe_{52}Nb_{48}$ powder
  XRD patterns 195
Mechanically alloyed FeV
  magnetization 186
Mechanically alloyed powders 41
  characteristics 223
  magnetization 216
Mechanically disordered AlTa alloy powders
  DTA curves 208
Mechanically driven solid-state amorphization. 190. *See also* MDSSA
Mechanically milled 191
Melt 111
Melt spinning 150
Melting point 62, 63, 171
Melting techniques 192
Melting temperature 182
Metal carbides 19
  chemical stability 63
  fabrication 65
Metal hydrides 113
Metal matrix composites 45
Metal nitrides 19
Metal-coated zirconium oxide 23
Metallic binary systems 177, 190
Metallic glasses 171
Metallic powders 16
Metallographical examination 163
Metals 63
Metastable phase 184
  diagram 150
MG 198. *See also* Mechanical grinding
Mg 128, 129, 130. *See also* Magnesium
MgO 130
  light gray region 136
Miedema's model 167
  semi-empirical 181

Milled powders
BFI 134
compositional change 169
end product consolidated 5
gas contamination content 223
magnetization 215
metallographic characterizations 120
properties 6
Milling 1, 96, 113, 188, 201, 213
amorphization reaction 174
experiments 130
final stage 167
first stage 172
in air 145
in helium 145
intermediate stage 167
magnetization 186
media 49, 84, 210
process 39, 58, 171
refining stage 76
several stages 185
speed 209
temperature 16
time 137, 163, 223
tools 186
Mills
high-energy 5
MMC 45. *See also* Metal matrix composites
Modified phase diagram 150
More advanced properties 65
Morphological properties 175
Morphology 98, 119, 208
cabbage leaf-like 157
nearly spherical-like 157
spherical-like 50
Mössbauer spectroscopy 197
MSSR 119, 120, 128, 130, 137. *See also* Mechanical solid-state reduction
MSSR method
pre-reduction stages 129
MSSR process 120, 122, 131
intermediate stage 124

NaCl 102
NaCl type 68
NaCl-TiC 68
Nanocomposite 47, 58
powders 47
SiC_p/Al material 48
Nanocomposite materials 5, 19, 129, 139
ceramic/ceramic 5
Nanocrystalline 68
bulk material 81
character 54
compacts 58, 60
spherical grains 73
TiN 96
Nanocrystalline fcc alloys 38
Nanocrystalline materials 5, 19, 34
mechanical properties 35
mechanism for formation 37
Nanocrystalline WC 129
Nanophase materials 34
Nanophase powder 130
Nanoscale 65
reinforcements 47
Nanostructure 78
refractory materials 65
Nanostructured material 35
Narrow size distribution 204
NbN 4
Ni powders 113
$Ni_{60}Nb_{40}$
exothermic crystallization peaks 145
powders 144
$Ni_{60}Nb_{40}$ amorphous alloy
first novel technique 4

Nickel coating 2
Nickel-based superalloy 23
NiTi powders 113
$NiTiH_3$
  Bragg peaks 116
  final product 116
Nitrides 4, 95
Nitrogen gas flow 4
NiZrN 113
No-stable phase 175
Non-radioactive dispersoid 25
Nonequilibrium phase 109

Objectives of milling 5
Obsidian 143
ODS. *See* Complex oxide alloys: dispersion-strengthened; Oxide dispersion strengthening
ODS alloys 4, 28
ODS superalloy 25
Optical microscopy 96
Order phase 195
Orthorhombic-AlZr
  more stable 219
Overall composite properties
  undesirable effects 46
Oxidation-reduction reaction 128
Oxide dispersion strengthening 22
Oxide glasses
  naturally occuring 143

Particle size 119
  distribution 85
Particulate-filled composites 47
PAS 48, 59, 66. *See also* Plasma activated sintering
  important factor 60
  method 41, 53, 96
  technique 41, 102
PCA. *See* Processing control agent
Phase diagram 150
Phase transformation 213
Physical chemistry
  principles 128
Physical vapor deposition 95
Planetary ball mill 8
Plasma 41
Plasma activated sintering 41, 48, 66
Plasma activation 59
Plasma spray method 95
Plastic deformation 38
Poisson's ratio 82, 103
Polycrystalline material
  size of grain 35
Polycrystalline metal carbides 64
Poor wettability 46
Powder metallurgy 4, 23, 64
Powder particles
  metallographical examination 98
  polished and etched 125
Principles of physics 128
Process control agent
  stearic acid or methanol 29
Processing control agent 16
Promote wetting 58
PSA technique
  sintering step 78
Pulse-echo overlap ultrasonic technique 48, 131
Pure graphite crystals
  Braggs peak 68
Pure metals
  grain reduction 38
Purified argon atmosphere 47
Purified nitrogen gas 95
Pyrophoricity 24

RA. *See* Reducing agent
Rapid diffusion process 191
Rapid solidification 36

Rate of amorphization 15
RBM 95, 96, 98, 100. *See also* Reactive ball milling
  experiment 96
  process 108
  time 103, 106
RBS. *See* Rutherford back-scattering spectroscopic marker
Reactant materials
  Braggs peak 68
Reactant mixed powders
  welding, fracture, rewelding 5
Reactant powders 124
Reactants 120
Reacted state 197
Reaction layers 54
Reaction rate
  increase 119
Reactive ball-milling 4, 16, 95
Reactive milling 95
Reactive product(s) 54
Reactive sputtering technique 95
Reducing agent 126
Refined microstructure 17
Refractory materials 63
Reinforcement materials 134
Reinforcements
  fibers and particles 46
Resistance heating 59
Ring-spot pattern 124
RM. *See* Rod-milled; Rod-milling
Rod mill 120
Rod-milled 146
Rod-milling 2, 122, 128, 208
  amorphization process 150
  increased time 166
  room temperature technique 119
  technique 12, 126, 157, 173, 199
  time 126, 171, 202
Rutherford back-scattering spectroscopic marker 144
SADP 71, 78, 97, 102, 124, 133, 154, 162. *See also* Selected area diffraction patterns; Selected-area diffraction patterns
  clear FCC-rings 73
SAP. *See* Sintered Al Powder
SAP products 28
SARR 146
Scanning electron micrographs 202
Scanning electron microscope 130
Scanning electron microscopy 48, 66, 96
Scherrer equation 90
Second heating run 126
Selected area diffraction pattern 52, 71, 97, 133, 213
Self propagating combustion method 95
Self propagating high-temperature synthesis 64
SEM 66, 96, 98, 130. *See also* Scanning electron microscopy
  detailed observations 157
  micrograph 102, 139
  observations 157, 203
  technique 49, 76
Shear moduli 140
Shear modulus 57, 82, 105
SHS. *See* Self-propagating high-temperature synthesis
Si addition 47
β-SiC 5, 86
SiC/Al 46
  interfaces 48
SiC_{10}/Al_{90}
  BFI 54
  composite 50
  mechanically mixed 49
  SADP 54
SiC_x/Al_{100-x}
  composite 56
Sintered Al powder 27

Sintering
  procedure 41
  step 78
  technique 130
Sintering techniques
  forging 41
  HIPing 41
  hot extrusion 41
  hot pressing 41
Solid-state amorphization reaction 146
  two requirements 144
Solid-state chemical reactions 119
Solid-state diffusion 68
Solid-state reaction 66, 77, 85, 131
  process 196
  room temperature 2
Solids
  physical chemistry 35
Spherical-like morphology 175
Sputtering 36
SSR 131, 137. *See also* Solid-state reaction
Stable crystalline phase 209
Stable phase 175
  diagram 150
Stage of RBM
  early stage 108
  second stage 108
  intermediate stage 109
  final stage 109
Stainless steel vial 209
Starting reactant materials 68, 131, 136
Steel alloys 192
Stoichiometric β-SiC powders 86
Stress rupture tests
  negligible coarsening 27
Superconducting transition temperature 177
Szigvari attritor grinding mill 7
TaC 62
TASSA 164, 167, 175
  method 174
  process 164, 167, 168, 172, 173
  reaction 163
TEM 36, 66, 96, 110, 120, 130. *See also* Transmission electron microscopy
  analyses 154
  detailed analyses 68
  techniques 39, 52, 54, 73
TEM/EDS technique 185
Temperature 48, 64
Ternary system 191
Thermal conductivity 63
Thermal expansion coefficients 46
Thermocouple 66
Thermodynamically stable phases 150
Thin veins 71
Ti
  crystals 120
  diffraction peaks 122
Ti and C
  reactant materials 76
Ti crystals 72
Ti particles 108
Ti powder 95, 98, 108, 113, 119, 126
  as-received 106
Ti-C 83
Ti/TiN compact 100
Ti/TiN composite 108
$Ti_{44}C_{56}$ 83
$Ti_{44}C_{56}$ powders
  ball-milled 68
  mechanically alloyed 73
TiC
  as-consolidated 67
  as-milled 67
  brittle phase 82
  bulk material 78

fully dense 81
powder 68
small mole fraction 85
TiH_2 113
TiN 4, 95, 96, 102. *See also* Titanium nitride
NaCl-type 97
particles 100
powder 100, 102
single phase 102
Titanium 24
Titanium nitride 95
TM. *See* Transition-metal
T_m/T_x ratio 171
Transfer of electrons 127
Transition-metal 62
Transmission electron microscope 120, 130
Transmission electron microscopy 48, 96, 144
Transverse optical (TO)-like phonon mode 86
Tumbler ball mill 10
useful kinetic energy 10
Tumbling ball mill 190
Tumbling mills 10
low energy 5
Typical nanocomposite material 53

Ultrasonic detector 48, 131
Undesired grain growth 130
Unreacted metallic Ti 78

Values of density 92
Vibratory ball mill 9
Vibratory mill 23
Vickers hardness 56
indentation 139
measurements 100
value 81
Vickers indenter 67, 96
VN 113
Voids 55

$W_b:W_p$ ratio 15
WC
chemically stable 130
dark region 136
particles 129
small mole fraction 137
WC alloys
hexagonal phase 129
WC powder
as-consolidated 131
hcp phase 88
pure 130, 131
WC/MgO 119, 130
composite material 140
nanocomposite material 129
Wear resistant parts 64, 129
Welding 23, 30
Wet milling 16
Whiskers 46
WO_3 130

X-ray diffraction 48, 66, 120, 130
patterns 14
X-ray line broadening 36
XRD 48, 66, 110, 120, 126, 130. *See also* X-ray diffraction patterns
analysis 96
diffraction pattern 90, 176
patterns 48, 53, 86, 108, 109, 111, 113, 116, 120, 131, 145, 152, 154, 163, 214
techniques 39

Y_2O_3 25
YAG. *See* Yttrium-aluminum garnet
Young's moduli 140
Young's modulus 57, 63, 82
Yttrium aluminates 25
Yttrium-aluminum garnet 25

$Zr_{56}C_{44}$
  nanocrystalline powders 89
ZrC powders 89
ZrN 113